ISSN 2074-272X

науково-практичний
журнал
2024/5

Електротехніка і Електромеханіка

Electrical Engineering & Electromechanics

Електричні машини та апарати
Електротехнічні комплекси та системи
Промислова електроніка
Теоретична електротехніка
Інженерна електрофізика.
Техніка сильних електричних та магнітних полів
Електричні станції, мережі і системи
Електричний транспорт

Журнал включено до найвищої категорії «А»
Переліку фахових видань України

З 2019 р. журнал індексується у Scopus

З 2015 р. журнал індексується
у Web of Science Core Collection:
Emerging Sources Citation Index

Electrical Engineering & Electromechanics

Scientific Journal was founded in 2002
Founder – National Technical University «Kharkiv Polytechnic Institute» (Kharkiv, Ukraine)

EDITORIAL BOARD

Sokol Ye.I.	**Editor-in-Chief**, Professor, Corresponding member of NAS of Ukraine, Rector of National Technical University «Kharkiv Polytechnic Institute» (NTU «KhPI»), **Ukraine**
Korytchenko K.V.	**Deputy Editor,** Professor, NTU «KhPI», **Ukraine**
Rozov V.Yu.	**Deputy Editor,** Professor, Corresponding member of NAS of Ukraine, Anatolii Pidhornyi Institute of Power Machines and Systems of NAS of Ukraine, Kharkiv, **Ukraine**
Bolyukh V.F.	**Deputy Editor,** Professor, NTU «KhPI», **Ukraine**
Abu-Siada A.	Professor, Curtin University, Perth, **Australia**
Aman M.M.	Professor, NED University of Engineering & Technology, Karachi, **Pakistan**
Babak V.P.	Professor, Academician of NAS of Ukraine, General Energy Institute of NAS of Ukraine, Kyiv, **Ukraine**
Baltag O.	Professor, Grigore T. Popa University Medicine and Pharmacy, **Romania**
Baranov M.I.	Professor, Research and Design Institute «Molniya» of NTU «KhPI», **Ukraine**
Batygin Yu.V.	Professor, Kharkiv National Automobile and Highway University, **Ukraine**
Bíró O.	Professor, Institute for Fundamentals and Theory in Electrical Engineering, Graz, **Austria**
Bouktir T.	Professor, Ferhat Abbas University, Setif 1, **Algeria**
Buriakovskyi S.G.	Professor, NTU «KhPI», **Ukraine**
Butkevych O.F.	Professor, Institute of Electrodynamics of NAS of Ukraine, Kyiv, **Ukraine**
Colak I.	Professor, Nisantasi University, Istanbul, **Turkey**
Cruz S.	Professor, University of Coimbra, **Portugal**
Doležel I.	Professor, University of West Bohemia, Pilsen, **Czech Republic**
Féliachi M.	Professor, Technological Institute of Saint-Nazaire, University of Nantes, **France**
Guerrero J.M.	Professor, Aalborg University, **Denmark**
Gurevich V.I.	PhD, Honorable Professor, Central Electrical Laboratory of Israel Electric Corporation, Haifa, **Israel**
Hajjar A.A.	Professor, Tishreen University, Latakia, **Syrian Arab Republic**
Hammarström T.	Professor, Chalmers University of Technology, **Sweden**
Ida N.	Professor, The University of Akron, Ohio, **USA**
Izykowski J.	Professor, Wroclaw University of Science and Technology, **Poland**
Kildishev A.V.	Associate Research Professor, Purdue University, **USA**
Klepikov V.B.	Professor, NTU «KhPI», **Ukraine**
Korzeniewska E.	Professor, Lodz University of Technology, **Poland**
Ktena A.	Professor, National and Kapodistrian University of Athens, **Greece**
Kuznetsov B.I.	Professor, Anatolii Pidhornyi Institute of Power Machines and Systems of NAS of Ukraine, Kharkiv, **Ukraine**
Kyrylenko O.V.	Professor, Academician of NAS of Ukraine, Institute of Electrodynamics of NAS of Ukraine, Kyiv, **Ukraine**
Malik O.P.	Professor, University Of Calgary, **Canada**
Maslov V.I.	Professor, National Science Center «Kharkiv Institute of Physics and Technology», **Ukraine**
Mikhaylov V.M.	Professor, NTU «KhPI», **Ukraine**
Miljavec D.	Professor, University of Ljubljana, **Slovenia**
Milykh V.I.	Professor, NTU «KhPI», **Ukraine**
Nacke B.	Professor, Gottfried Wilhelm Leibniz Universitat, Institute of Electrotechnology, Hannover, **Germany**
Oleschuk V.	Professor, Institute of Power Engineering of Technical University of Moldova, **Republic of Moldova**
Petrushin V.S.	Professor, Odessa National Polytechnic University, **Ukraine**
Podoltsev A.D.	Professor, Institute of Electrodynamics of NAS of Ukraine, Kyiv, **Ukraine**
Reutskiy S.Yu.	PhD, Anatolii Pidhornyi Institute of Power Machines and Systems of NAS of Ukraine, Kharkiv, **Ukraine**
Rezinkin O.L.	Professor, NTU «KhPI», **Ukraine**
Rezinkina M.M.	Professor, NTU «KhPI», **Ukraine**
Shcherbak Ya.V.	Professor, NTU «KhPI», **Ukraine**
Sikorski W.	Professor, Poznan University of Technology, **Poland**
Strzelecki R.	Professor, Gdansk University of Technology, **Poland**
Suemitsu W.	Professor, Universidade Federal Do Rio de Janeiro, **Brazil**
Trichet D.	Professor, Institut de Recherche en Energie Electrique de Nantes Atlantique, **France**
Vaskovskyi Yu.M.	Professor, National Technical University of Ukraine «Igor Sikorsky Kyiv Polytechnic Institute», Kyiv, **Ukraine**
Vazquez N.	Professor, Tecnológico Nacional de México en Celaya, **Mexico**
Vinnikov D.	Professor, Tallinn University of Technology, **Estonia**
Yagup V.G.	Professor, Kharkiv National Automobile and Highway University, **Ukraine**
Yatchev I.	Professor, Technical University of Sofia, **Bulgaria**
Zagirnyak M.V.	Professor, Member of NAES of Ukraine, Kremenchuk M.Ostrohradskyi National University, **Ukraine**
Zgraja J.	Professor, Lodz University of Technology, **Poland**
Grechko O.M.	**Executive Managing Editor,** PhD, NTU «KhPI», **Ukraine**

From no. 1 2019 Journal «Electrical Engineering & Electromechanics» is indexing in **Scopus**
and from no. 1 2015 Journal is indexing in **Web of Science Core Collection: Emerging Sources Citation Index (ESCI)**

Also included in DOAJ (Directory of Open Access Journals), in EBSCO's database, in ProQuest's databases – Advanced Technologies & Aerospace Database and Materials Science & Engineering Database, in Gale/Cengage Learning databases.

Editorial office address:
National Technical University «Kharkiv Polytechnic Institute», Kyrpychova Str., 2, Kharkiv, 61002, Ukraine
phones: +380 57 7076281, +380 67 3594696, **e-mail:** a.m.grechko@gmail.com (**Grechko O.M.)**

ISSN (print) 2074-272X
ISSN (online) 2309-3404

© National Technical University «Kharkiv Polytechnic Institute», 2024

Printed 19 August 2024. Format 60 × 90 ⅛. Paper – offset. Laser printing. Edition 50 copies.
Printed by Printing house «Madrid Ltd» (18, Gudanova Str., Kharkiv, 61024, Ukraine)

Electrical Engineering & Electromechanics
Scientific Journal

no. 5, 2024

Table of Contents

Electrical Machines and Apparatus

Electrotechnical Complexes and Systems

Industrial Electronics

Theoretical Electrical Engineering

Engineering Electrophysics. High Electric and Magnetic Fields Engineering

Power Stations, Grids and Systems

Electric Transport

UDC 621.313.13 https://doi.org/10.20998/2074-272X.2024.5.01

V.A. Volkov, N.L. Antonov

Refined calculation of energy modes of a frequency-regulated induction motor

Purpose. *To obtain analytical dependencies for the precise calculation of the stator current of a frequency-regulated three-phase short-circuited induction motor and to estimate the components of its main electrical power losses, which are spent on the transportation magnetic power losses (to the magnetization circuit) and additional power losses (through the motor air gap), as well as with using the obtained refined dependencies to research the electromagnetic processes and energy modes of the frequency-regulated induction motor when its speed and load change.* ***Methodology.*** *The method of generalized vectors is used for the refined calculation of the electromagnetic processes and energy modes of the frequency-regulated induction motor.* ***Results.*** *Based on the catalog data and parameters of the induction motor's equivalent replacement circuit, also the specified values of its useful rotational torque and speed, refined analytical dependencies were obtained for the calculation of the main electromagnetic power losses of the frequency-regulated induction motor, which take into account the influence of all types of power losses, which present in it, as well as – power losses spent on transporting magnetic losses (to the magnetization circuit) and additional losses (through the air gap of the motor). With the help of the obtained dependencies, the energy modes (including main power consumption and electromagnetic power losses, efficiency factor, power factor) of the frequency-regulated induction motor in the driving and generator modes of its operation in relation to the first (at speeds not higher than the nominal) and the second (at speeds above the nominal) speed control zones for the operating ranges of the motor useful rotational torque and speed changes were calculated.* ***Originality.*** *A refined analytical calculation dependence has been obtained for determining the active projection of the generalized stator current vector of a frequency-regulated induction motor, which takes into account the presence of additional power losses and the component of electrical losses caused by the transportation of additional power losses through the air gap of the motor; an analytical dependence is also proposed for determining the increment of the mentioned active projection, which is due to the transportation of magnetic power losses to the motor magnetization circuit.* ***Practical value.*** *Analytical calculation dependencies are proposed for the quantitative assessment of errors (as a percentage of mentioned values) in steady-state modes for determining the main electromagnetic power losses of the frequency-regulated induction motor, caused by the absence (in comparison with relevant studies from known publications) of taking into account additional and magnetic power losses, as well as – the influence of electrical component losses caused by the transportation of the mentioned power losses through the air gap or to the magnetization circuit of the motor, respectively.* References 16, tables 5, figures 2.

Key words: **induction motor, frequency regulation, electromagnetic power losses, steady-state energy modes.**

Мета. *Отримати аналітичні залежності для уточненого розрахунку статорного струму частотно-регульованого трифазного короткозамкненого асинхронного двигуна і оцінити складові його основних електричних втрат потужності, котрі викликані транспортуванням магнітних втрат потужності (до контуру намагнічування) і додаткових втрат потужності (через повітряний проміжок двигуна), а також дослідити з використанням отриманих уточнених залежностей усталені електромагнітні процеси й енергетичні режими частотно-регульованого асинхронного двигуна при зміні його швидкості та навантаження.* ***Методологія.*** *При уточненому розрахунку електромагнітних процесів та енергетичних режимів частотно-регульованого асинхронного двигуна застосовано метод узагальнених векторів.* ***Результати.*** *Виходячи з каталожних даних та параметрів еквівалентної схеми заміщення асинхронного двигуна, а також заданих значень його корисного обертового моменту та швидкості, отримані для розрахунку основних електромагнітних втрат потужності частотно-регульованого асинхронного двигуна уточнені аналітичні залежності, в яких враховується вплив усіх видів присутніх у ньому втрат потужності, а також – втрат потужності, що викликані транспортуванням магнітних втрат (до контуру намагнічування) та додаткових втрат (через повітряний проміжок двигуна). За допомогою отриманих залежностей були розраховані енергетичні режими (у тому числі – основні споживана потужність та електромагнітні втрати потужності, коефіцієнт корисної дії, коефіцієнт потужності) частотно-регульованого асинхронного двигуна при двигуневому та генераторному режимах його роботи стосовно першої (при швидкостях не вище номінальної) і другої (при швидкостях вище номінальної) зон регулювання швидкості для робочих діапазонів зміни корисного обертового моменту і швидкості двигуна.* ***Наукова новизна.*** *Отримано уточнену аналітичну розрахункову залежність для визначення активної проекції узагальненого вектора статорного струму частотно-регульованого асинхронного двигуна, в котрої враховується наявність в ньому додаткових втрат потужності та складової електричних втрат, яка викликана транспортуванням додаткових втрат потужності через повітряний проміжок двигуна; також запропонована аналітична залежність для визначення прирощення вказаної активної проекції, яке обумовлено транспортуванням магнітних втрат потужності до контуру намагнічування двигуна.* ***Практична цінність.*** *Запропоновано аналітичні розрахункові залежності для кількісної оцінки в усталених режимах похибок (у відсотках від уточнених значень) щодо визначення основних електромагнітних втрат потужності частотно-регульованого асинхронного двигуна, обумовлених при розрахунку цих втрат відсутністю (в порівнянні з відповідними дослідженнями з відомих публікацій) урахування додаткових і магнітних втрат потужності, а також – впливу електричних складових втрат, викликаних транспортуванням згаданих втрат потужності через повітряний проміжок або до контуру намагнічування двигуна відповідно.* Бібл. 16, табл. 5, рис. 2.

Ключові слова: **асинхронний двигун, частотне регулювання, електромагнітні втрати потужності, усталені енергетичні режими**.

Introduction. As a result of the widespread industrial implementation of frequency-regulated (f-r) short-circuited induction motors (IMs) in various branches of the economy today and due to the observed increase in the price of electric energy, the task of precise definition has become very relevant and practically in demand (including with the use of modern powerful computing means) of instantaneous energy indicators (power losses and their components, consumed power, efficiency) for the above motors in the operating ranges of changes in their speed and load. Only by solving this task will it become possible to develop and further implement energy-efficient control (which ensures the minimization of power losses or energy consumption) for the specified motors.

Despite the existing considerable number of well-known publications devoted to the calculation and research of the energy modes of the f-r IMs, all of them do not fully take into account the presence of all components of power losses, which are actually present in a real induction motor. In particular, in the monographs [1, 2], an idealized representation of the f-r IM is considered, in which magnetic and additional motor power losses are not taken into account at all. In monographs [3–7] and well-known articles [8, 9], only additional motor power losses are not taken into account when calculating and researching energy modes of the IM; moreover, when assessing the impact of magnetic power losses, the component of electrical losses caused by them is also taken into account, which is spent on transporting magnetic power losses to the magnetization circuit of the motor. In contrast to the publications listed above, in the article [10], which investigates the energy modes of the f-r IM in start-braking modes, at the same time, all existing (including magnetic and additional) motor power losses are taken into account in the calculations; however, this does not take into account components of electrical losses spent on transporting magnetic and additional power losses to the magnetization circuit or through the motor air gap.

In contrast to all previous publications, in the article [11], devoted to the study of the energy modes of the f-r IM during acceleration and braking, all types of power losses present in it (including magnetic and additional) are simultaneously taken into account, as well as the component of electrical losses is taken into account which is spent on transporting magnetic power losses to the magnetization circuit; however, this does not take into account the component of electrical losses spent on transporting additional power losses through the air gap of the motor.

Known publications [12, 13] present calculation analytical dependencies for determining additional IM power losses, which in the nominal mode of operation of the motor make up 0.5 % of its input power consumption, and in modes different from the nominal, are characterized by their change in proportion to the second degree of module of the generalized motor stator current vector.

According to the monograph [4], additional IM power losses are created by the joint action of two components: «no load stray losses» and «load stray losses». Known methods discussed in [14, 15] are used for the experimental determination of these components. Permissible values of additional power losses for induction motors are set by International Standards: IEEE112 – for the USA; IEC34-2 – for Europe and IEC37 – for Japan [16].

It follows from the conducted analysis that at present there are no refined analytical dependencies for the calculation and study of the energy modes of the f-r IMs, which would simultaneously take into account all types of power losses (electrical in the stator and rotor windings, mechanical, magnetic and additional) of the motor and all components of its electrical losses in the stator winding (which are spent on the creation of electromagnetic torque and motor power and the aforementioned transportation of magnetic and additional motor power losses). Also, currently there are no analytical dependencies for the refined calculation of the stator current, which take into account the influence of these components of the stator current, which are spent on transporting magnetic and additional power losses to the magnetization circuit or through the air gap of the IM.

The goal of the article. To obtain analytical dependencies for the refined calculation of the stator current of a frequency-regulated three-phase short-circuited induction motor and to estimate the components of its electrical power losses, which are spent on the transportation of magnetic power losses (to the magnetization circuit) and additional power losses (through the air gap of the motor), as well as to investigate with using the obtained refined dependencies, the steady-state electromagnetic processes and energy modes of the frequency-regulated induction motor with changes in its speed and load.

Obtained results. During the calculations and studies, the assumption was made:

a) the three-phase stator winding of the motor is symmetrical;

b) the air gap of the motor is the same along the entire inner circuit of the stator;

c) the magnetization curve of steel is linear (that is, the value of the internal inductances of the motor does not depend on the currents);

d) the internal parameters of the induction motor (inductances and active resistances brought to its calculated operating temperature [12]) were considered unchanged;

e) the main (caused by the first harmonic components of the phase stator currents) power losses of the f-r IM are taken into account, which include the following loss components [12]:

- electrical $\Delta P_{\text{e.s}}$ in the three-phase stator winding;
- electrical $\Delta P_{\text{e.r}}$ in short-circuited rotor winding;
- magnetic $\Delta P_{\text{i.r}}$ (in the steel of the stator and rotor core);
- mechanical ΔP_{ad} (spent on friction in bearings and self-ventilation);
- additional ΔP_{ad} (caused by pulsations of magnetic flux density in the teeth of the stator and rotor).

In order to further simplify the analytical dependencies describing the electromechanical and energy parameters of the f-r IM mode, we will use the method of generalized vectors [1] and the relative system of units generally accepted for AC electric machines [4, 10, 11].

Mentioned electrical (in stator $\Delta P_{\text{e.s}}$ and rotor $\Delta P_{\text{e.r}}$ windings), magnetic $\Delta P_{\text{i.r}}$, mechanical ΔP_{mech} and additional ΔP_{ad} types of main power losses, as well as main electromagnetic ΔP_{em} and total ΔP_{m} IM power losses (which will be called simply «losses» below) are determined from known analytical dependencies [1, 10, 11]:

$$\begin{cases} \Delta P_{\text{e.s}} = R_{\text{s}} \cdot I_{\text{s}}^2, \quad \Delta P_{\text{e.r}} = \beta \cdot T_{\text{em}} = k_{\text{r}}^2 \cdot R_{\text{r}} \cdot I_{1\Sigma\text{y}}^2, \\ \Delta P_{\text{ir}} = \Delta P_{\text{ir.n}} \cdot \left(\Psi_{\text{m}}/\Psi_{\text{mn}}\right)^2 \cdot \left(\omega_1/\omega_{1\text{n}}\right)^{\lambda}, \\ \Delta P_{\text{ad}} \approx \Delta P_{\text{ad.n}} \cdot \left(I_{\text{s}}/I_{\text{sn}}\right)^2 = R_{\text{ad}} \cdot I_{\text{s}}^2, \ \ \beta = \omega_1 - \omega, \\ \Delta P_{\text{ad.n}} = \dfrac{0.005 \cdot P_{2\text{n}}}{\eta_{\text{n}}}, \quad R_{\text{ad}} = \dfrac{\Delta P_{\text{ad.n}}}{I_{\text{sn}}^2}, \\ \Delta P_{\text{mech}} = \Delta P_{\text{mech.n}} \cdot \left(\omega/\omega_{\text{n}}\right)^2, \\ \Delta P_{\text{em}} = \Delta P_{\text{e.s}} + \Delta P_{\text{e.r}} + \Delta P_{\text{ir}} + \Delta P_{\text{ad}}, \\ \Delta P_{\text{m}} = \Delta P_{\text{em}} + \Delta P_{\text{mech}}, \ \ k_{\text{r}} = L_{\text{m}}/\left(L_{\text{m}} + L_{\sigma\text{r}}\right), \end{cases} \qquad (1)$$

where R_{s} is the active resistance of the IM phase stator winding; R_{r} is the equivalent (reduced to the three-phase winding) phase active resistance of the short-circuited rotor winding of the motor; I_{s} and I_{sn} are, respectively, the instantaneous and nominal value of the module of the generalized vector of the IM stator current (and in the adopted relative system of units: I_{sn} = 1 pu [4]); k_{r} is the coupling factor of the rotor [1]; L_{m} and $L_{\sigma\text{r}}$ are the magnetization inductance and dissipation inductance of the IM rotor, respectively; R_{ad} is the equivalent active resistance to take into account additional motor losses [10, 11]; $P_{2\mathrm{n}}$ and η_n are the nominal values of the useful power on the motor shaft and its efficiency, respectively; ω_1 and $\omega_{1\mathrm{n}}$ are the current and nominal value of the angular frequency of rotation of the IM stator magnetic field, respectively (and, in the adopted relative system of units: $\omega_{1\mathrm{n}} = 1$ pu [10, 11]); ω and ω_n are the current and nominal value of the angular frequency of rotation (speed) of the rotor of the motor, respectively; $\Delta P_\mathrm{ir.n}$, $\Delta P_\mathrm{ad.n}$ and $\Delta P_\mathrm{mech.n}$ are the nominal values (inherent in the nominal operating mode of the IM) of magnetic, additional and mechanical losses of the motor, respectively; $I_{1\Sigma\mathrm{y}}$ is the component of the active projection I_sy of the generalized stator current vector $\boldsymbol{I}_\mathrm{s}$ (on the imaginary axis «*y*» of the rotational orthogonal coordinate system (ROCS) «*x-y*», connected by the real axis «*x*» to the generalized rotor flux linkage vector $\boldsymbol{\Psi}_\mathrm{r}$ of the motor), which creates the electromagnetic torque and electromagnetic power in the air gap of the f-r IM; Ψ_m and Ψ_mn are, respectively, the current and nominal value of the module of the generalized vector of the magnetic (in the air gap) flux $\boldsymbol{\Phi}_\mathrm{m}$ of the IM; λ is the coefficient that takes into account the changes in magnetic losses ΔP_ir of the f-r IM from the angular frequency ω_1 of the stator magnetic field (for general industrial IMs: $\lambda = 1.3$ [10–12]); T_em and β are the current values of the electromagnetic torque (created by the motor in the air gap) and the absolute slip of the f-r IM, respectively.

The instantaneous value of the module Φ_m of the generalized magnetic flux vector is determined from known dependencies [10]:

$$\begin{cases} \Phi_\mathrm{m} = \sqrt{\Phi_\mathrm{mx}^2 + \Phi_\mathrm{my}^2}\,, \\ \Phi_\mathrm{mx} = k_\mathrm{r} \cdot \left(\Psi_\mathrm{r} + L_{\sigma\mathrm{r}} I_\mathrm{sx}\right), \;\; \Phi_\mathrm{my} = k_\mathrm{r} \cdot L_{\sigma\mathrm{r}} I_{1\Sigma\mathrm{y}} \end{cases}, \quad (2)$$

where Φ_mx and Φ_my are the projections of the generalized magnetic flux vector $\boldsymbol{\Phi}_\mathrm{m}$ on the «*x-y*» axis of the ROCS, oriented with its real «*x*» axis along the generalized vector of the rotor flux linkage $\boldsymbol{\Psi}_\mathrm{r}$; Ψ_r is the current value of the module of the generalized flux linkage vector of the rotor $\boldsymbol{\Psi}_\mathrm{r}$ of the motor; $L_{\sigma\mathrm{r}}$ is the dissipation inductance of the IM rotor.

The energy balance of the f-r IM is characterized by the following known dependencies [12]:

$$\begin{cases} P_1 = P_\mathrm{e.s} + \Delta P_\mathrm{i\,r} + P_\mathrm{em}; \\ P_\mathrm{em} = \Delta P_\mathrm{e.\,r} + P_\mathrm{mech}; \\ P_\mathrm{mech} = \Delta P_\mathrm{mech} + \Delta P_\mathrm{ad} + P_2, \\ \Delta P_\mathrm{e.\,r} = P_\mathrm{em} - P_\mathrm{mech}, \end{cases} \quad (3)$$

where: P_1 and P_em are the main consumed and electromagnetic (transmitted through the IM air gap) power of the motor, respectively; P_mech and P_2 are the main mechanical and useful shaft power of the motor, respectively.

The relationship between energy values and torques created in the f-r IM is described by well-known relations [12]:

$$\begin{cases} P_\mathrm{mech} = \omega \cdot T_\mathrm{em} = \omega \cdot \left(T + \Delta T_\mathrm{mech}\right) + \Delta P_\mathrm{ad}; \\ P_2 = \omega \cdot T; \quad P_\mathrm{em} = \omega_1 \cdot T_\mathrm{em} = P_1 - \Delta P_\mathrm{e.s} - \Delta P_\mathrm{i\,r}; \\ \omega_1 T_\mathrm{em} = \Delta P_\mathrm{e.r} + \omega T_\mathrm{em}; \;\; \Delta T_\mathrm{mech.n} = \Delta P_\mathrm{mech.n} / \omega_\mathrm{n}; \\ \Delta T_\mathrm{mech} = \Delta P_\mathrm{mech} / \omega = \Delta T_\mathrm{mech.n} \cdot \left(\omega / \omega_\mathrm{n}\right), \end{cases} \quad (4)$$

where T is the useful torque of the f-r IM transmitted to the working mechanism (equal to the static torque T_s of the drive applied to the motor shaft in steady-state conditions); ΔT_mech and $\Delta T_\mathrm{mech.n}$ are, respectively, the instantaneous and nominal value of the mechanical losses of the IM torque; $(T + \Delta T_\mathrm{mech.n})$ is the motor torque.

Speed n_1[rpm] and angular frequency of rotation ω_1[pu] of the magnetic field of the stator, speed n[rpm] and angular frequency of rotation ω[pu] of the rotor, absolute slip β[pu] of the f-r IM are found from known expressions [12]:

$$\begin{cases} n_1[\mathrm{rpm}] = \dfrac{60 \cdot f_1}{z_\mathrm{p}}; \; n_{1\mathrm{n}} = \dfrac{60 \cdot f_{1\mathrm{n}}}{z_\mathrm{p}}; \; \omega_1 = \dfrac{n_1}{n_{1\mathrm{n}}}; \\ \omega = \dfrac{n}{n_{1\mathrm{n}}}; \; \Delta n\,[\mathrm{rpm}] = n_{1\mathrm{n}} - n; \; \beta = \dfrac{\Delta n}{n_{1\mathrm{n}}} = \omega_1 - \omega, \end{cases}, \quad (5)$$

where f_1 and $f_{1\mathrm{n}} = 50$ Hz are, respectively, the instantaneous and nominal value of the frequency of the main harmonics of the phase stator voltages (or currents) of the f-r IM; z_p is the number of motor pole pairs.

According to [1, 2], the instantaneous value of the torque $(T + \Delta T_\mathrm{mech})$ of the idealized f-r IM (which does not take into account magnetic and additional power losses) is determined as:

$$T + \Delta T_\mathrm{mech} = \Phi_\mathrm{m} \cdot I_{1\mathrm{q}} \quad \text{or} \quad T + \Delta T_\mathrm{mech} = k_\mathrm{r} \Psi_\mathrm{r} I_{1\mathrm{y}}\,, \quad (6)$$

where Φ_m and Ψ_r are the modules of the generalized vectors of the magnetic (in the air gap) flux $\boldsymbol{\Psi}_\mathrm{m}$ and flux linkage of the motor rotor $\boldsymbol{\Psi}_\mathrm{r}$, respectively; $I_{1\mathrm{q}}$ is the active (torque-generating) projection of the generalized vector of the stator current $\boldsymbol{I}_1$ of the f-r IM on the imaginary axis «*q*» of the ROCS «*d-q*», which is oriented with the real axis «*d*» in the direction of the generalized vector of the magnetic flux $\boldsymbol{\Phi}_\mathrm{m}$; $I_{1\mathrm{y}}$ is the active (torque-generating) projection of the generalized vector of the stator current $\boldsymbol{I}_1$ of the idealized IM on the imaginary axis «*y*» of the ROCS «*x-y*», which is oriented with the real axis «*x*» in the direction of the generalized vector of the rotor flux linkage $\boldsymbol{\Psi}_\mathrm{r}$.

At the *first stage* of research for a real (non-idealized) f-r IM through the magnetizing I_sx and active projections I_sy, $I_{1\Sigma\mathrm{y}}$, $I_{1\mathrm{y}}$ of the generalized vectors $\boldsymbol{I}_\mathrm{s}$, $\boldsymbol{I}_{1\Sigma}$, $\boldsymbol{I}_{1\mathrm{y}}$ of the stator current (on the «*x*» and «*y*» axis of the ROCS « *x-y*», which is oriented with the real axis «*x*» along the generalized rotor flux linkage vector $\boldsymbol{\Psi}_\mathrm{r}$) we give the calculation relationships for the modules I_s, $I_{1\Sigma}$, $I_{1\mathrm{y}}$ of these vectors in the form:

$$\begin{cases} I_\mathrm{s} = \sqrt{I_\mathrm{sx}^2 + I_\mathrm{sy}^2}; \quad I_{1\Sigma} = \sqrt{I_\mathrm{sx}^2 + I_{1\Sigma\mathrm{y}}^2}; \\ I_{1\mathrm{y}} = \sqrt{I_\mathrm{sx}^2 + I_{1\mathrm{y}}^2}; \quad I_1 = I_\mathrm{sx} + \mathrm{j} I_{1\mathrm{y}}; \\ I_{1\Sigma} = I_\mathrm{sx} + \mathrm{j} I_{1\Sigma\mathrm{y}}; \quad I_\mathrm{s} = I_\mathrm{sx} + \mathrm{j} I_\mathrm{sy}; \\ I_\mathrm{sy} = I_{1\Sigma\,\mathrm{y}} + \Delta I_\mathrm{sy}; \quad I_{1\Sigma\mathrm{y}} = I_{1\mathrm{y}} + \Delta I_{1\mathrm{y}}. \end{cases} \quad (7)$$

In (7), the generalized vectors $\boldsymbol{I}_{1\Sigma}$ and $\boldsymbol{I}_1$ are mathematically formed from the generalized vector $\boldsymbol{I}_\mathrm{s}$ of the stator current of the real f-r IM, if the active projection I_sy of this vector does not take into account the increment ΔI_sy or simultaneously two increments ΔI_sy and $\Delta I_{1\mathrm{y}}$, respectively; the value of the active projection $I_{1\mathrm{y}}$ is found from the second relation in (6) through the value of the torque $T + \Delta T_\mathrm{mech}$ and the module Ψ_r of the generalized flux linkage vector of the motor rotor. The indicated increments ΔI_sy and $\Delta I_{1\mathrm{y}}$ are caused by the transportation (transmission) of magnetic ΔP_ir and additional ΔP_ad losses to the magnetization circuit or through the air gap of this motor, respectively. Figure 1 shows a diagram illustrating the distribution, according to the relations in (7), of the increments ΔI_sy, $\Delta I_{1\mathrm{y}}$ of the stator current between the active projections I_sy, $I_{1\Sigma\mathrm{y}}$ and $\Delta I_{1\mathrm{y}}$ of the generalized vectors $\boldsymbol{I}_\mathrm{s}$, $\boldsymbol{I}_{1\Sigma}$ and $\boldsymbol{I}_1$ of the f-r IM, respectively.

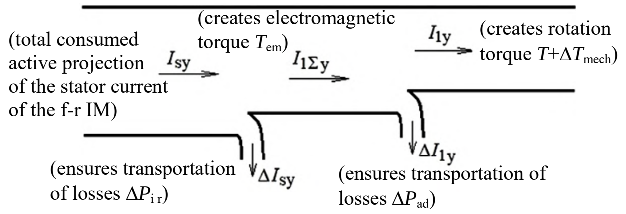

Fig. 1. Diagram of the distribution of increments ΔI_{sy} and $\Delta I_{1\text{y}}$ of the stator current between the active projections I_{sy}, $I_{1\Sigma\text{y}}$, $I_{1\text{y}}$ of the generalized vectors $\boldsymbol{I}_{\text{s}}$, $\boldsymbol{I}_{1\Sigma}$, $\boldsymbol{I}_{1}$ in the real f-r IM (the purpose of the projections and their increments is indicated in parentheses)

Based on the second and last relations in (1), we obtain, similarly to the second relation from (6), the calculation expressions (through the active projection $I_{1\Sigma\text{y}}$ of the generalized stator current vector $\boldsymbol{I}_{1\Sigma}$, the module Ψ_{r} of the generalized rotor flux linkage vector $\boldsymbol{\Psi}_{\text{r}}$ and the active resistance R_{r} of the rotor winding) to find the value of the electromagnetic torque T_{em} created in the air gap of the f-r IM

$$T_{\text{em}} = k_{\text{r}} \Psi_{\text{r}} I_{1\Sigma\,\text{y}}, \tag{8}$$

as well as the absolute slip β and the angular frequency of rotation ω_1 of the stator magnetic field:

$$\beta = \Delta P_{\text{e.r}} / T_{\text{em}} = k_{\text{r}} R_{\text{r}} I_{1\Sigma\text{y}} \quad \text{and} \quad \omega_1 = \omega + \beta\,. \tag{9}$$

At the *second stage*, we obtain an analytical dependence for determining the active projection $I_{1\Sigma\text{y}}$ of the generalized stator current vector $\boldsymbol{I}_{1\Sigma}$ of the f-r IM. Before that, we recall that the increment ΔI_{sy}, which is part of the active projection I_{sy} of the generalized stator current vector $\boldsymbol{I}_{\text{s}}$, is caused by the transport of magnetic power losses to the magnetization circuit of the motor (where these losses are dissipated in the stator core [4, 12]). As a result, the specified increment ΔI_{sy} of the stator current does not physically affect, according to (4), the electromagnetic power P_{em} transmitted through the IM air gap (and, therefore, it also does not affect the mechanical power P_{mech} and the additional losses ΔP_{ad} included in it).

Therefore, in order to increase the accuracy of the determination of the additional losses of the f-r IM, we will below calculate them (in contrast to the known calculation relationship from (1) for them [12, 13]) in a different way, excluding the mentioned increment ΔI_{sy} from the composition of the module I_{s} of the stator current. Namely, it is proportional to the second degree of the module $I_{1\Sigma}$ of the generalized vector $\boldsymbol{I}_{1\Sigma}$ of the stator current from the following expressions:

$$\begin{cases} \Delta P_{\text{ad}} = R^{*}_{\text{ad}} \cdot I^{2}_{1\Sigma} = R^{*}_{\text{ad}} \cdot \left(I^{2}_{\text{sx}} + I^{2}_{1\Sigma\,\text{y}} \right); \\ R^{*}_{\text{ad}} = \dfrac{\Delta P_{\text{ad.n}}}{I^{2}_{\text{sx.n}} + I^{2}_{1\Sigma\,\text{y.n}}} = \dfrac{\Delta P_{\text{ad.n}}}{I^{2}_{1\Sigma\text{.n}}} = R_{\text{ad}} \cdot \left(\dfrac{I_{\text{s.n}}}{I_{1\Sigma\text{.n}}} \right)^{2} \end{cases} \tag{10}$$

through the value of the specified module $I_{1\Sigma}$, magnetizing I_{sx} and active $I_{1\Sigma\text{y}}$ projections of the generalized vector $\boldsymbol{I}_{1\Sigma}$ on the ROCS «*x-y*» axis. In (10), R^{*}_{ad} is the refined value of the equivalent (intended for the calculation of additional losses) active resistance of the motor, which is calculated from the nominal (i.e., corresponding to the nominal IM mode) values of additional losses $\Delta P_{\text{ad.n}}$, as well as of the module $I_{1\Sigma\text{.n}}$, magnetizing $I_{\text{sx.n}}$ and active projection of the generalized $I_{1\Sigma\text{y.n}}$ vector of the stator current $\boldsymbol{I}_{1\Sigma\text{.n}}$ of the motor.

Substituting the expression for the electromagnetic torque T_{em} from (8) and the expression (10) for additional losses into the first relation from (4), we convert this relation to the following dependence:

$$\omega \cdot \left(k_{\text{r}} \Psi_{\text{r}} I_{1\Sigma\,\text{y}} \right) = \omega \cdot \left(T + \Delta T_{\text{mech}} \right) + R^{*}_{\text{ad}} \cdot \left(I^{2}_{\text{sx}} + I^{2}_{1\Sigma\,\text{y}} \right), \tag{11}$$

which, in turn, we reduce by equivalent transformations to the form of an algebraic equation of the second order:

$$R^{*}_{\text{ad}} I^{2}_{1\Sigma\,\text{y}} - \omega k_{\text{r}} \Psi_{\text{r}} I_{1\Sigma\,\text{y}} + \omega \cdot \left(T + \Delta T_{\text{mech}} \right) + R^{*}_{\text{ad}} I^{2}_{\text{sx}} = 0\,. \tag{12}$$

The solution of (12) is the following analytical dependence:

$$I_{1\Sigma\,\text{y}} = \left(k_{\text{r}} \Psi_{\text{r}} / 2R^{*}_{\text{ad}} \right) \cdot \left\{ \omega - \left(\omega^{2} - \left(\frac{2R^{*}_{\text{ad}}}{k_{\text{r}} \Psi_{\text{r}}} \right)^{2} \cdot \left[\frac{\omega \cdot \left(T + \Delta T_{\text{mech}} \right)}{R^{*}_{\text{ad}}} + I^{2}_{\text{sx}} \right] \right)^{0.5} \right\}. \tag{13}$$

It allows to determine the value of the active projection $I_{1\Sigma\text{y}}$ of the generalized vector of the stator current of the f-r IM through the instantaneous values of the parameters of the motor mode: the speed ω of the rotor, the torque ($T+\Delta T_{\text{mech}}$), the module Ψ_{r} of the generalized vector of the flux linkage of the rotor and the magnetizing projection I_{sx} of the generalized stator current vector.

We determined from the second relation from (6) the active projection $I_{1\text{y}}$ of the stator current and based on the obtained dependence (13) and the last relation from (7), we find for the real IM the increment $\Delta I_{1\text{y}}$ as part of the active projection $\Delta I_{1\Sigma\text{y}}$ of the generalized stator current vector $\boldsymbol{I}_{1\Sigma}$ from the expression:

$$\Delta I_{1\text{y}} = I_{1\Sigma\,\text{y}} - I_{1\text{y}}, \tag{14}$$

caused by the transport of additional power losses ΔP_{ad} through the motor air gap.

Thus, a refined analytical calculation dependence (13) was obtained for determining the active projection $I_{1\Sigma\text{y}}$ of the generalized stator current vector $\boldsymbol{I}_{1\Sigma}$ of the f-r IM and expressions in the form of: formula (14) and the last relation from formula (7), – for finding the increment ΔI_{1} of the active projection $I_{1\text{y}}$ of the stator current. With the help of this increment, the effect of the electrical component of losses, which is caused by the transportation of additional power losses through the air gap of the motor, is taken into account.

At the *third stage*, we obtain an analytical calculation dependence for determining the increment ΔI_{sy}, which is caused by the transport of magnetic losses ΔP_{ad} to the magnetization circuit of the motor and is part of the active projection I_{sy} of the generalized vector of the stator current $\boldsymbol{I}_{\text{s}}$ of the real f-r IM.

From [4], the classical method of determining the specified increment ΔI_{sq} of the active projection I_{sq} (on the «*q*» axis of the «*d-q*» ROCS, which is oriented with the real axis «*d*» along the generalized magnetic flux vector $\boldsymbol{\Phi}_{\text{m}}$ of the IM) is known, in which this projection is founded based on of the energy balance between the additional electric power supplied to the magnetizing circuit of the motor and equal to the product $E_{\text{m}} \cdot \Delta I_{\text{sq}}$, and the magnetic losses $\Delta P_{\text{i r}}$, which are dissipated in the stator core:

$$E_{\text{m}} \cdot \Delta I_{\text{sq}} = \Delta P_{\text{i r}}, \tag{15}$$

where E_{m} is the instantaneous value of the module of the generalized magnetizing electromotive force vector $\boldsymbol{E}_{\text{m}}$.

From (15), the instantaneous increment ΔI_{sq} of the active projection I_{sq} of the IM stator current is determined in the form:

$$\Delta I_{\text{sq}} = \Delta P_{\text{i r}} / E_{\text{m}} = \Delta P_{\text{i r}} / \omega_1 \Phi_{\text{m}}, \text{ where } E_{\text{m}} = \omega_1 \Phi_{\text{m}}\,. \tag{16}$$

In another (known from [11]) method, the aforementioned increment ΔI_{sq} of the stator current (caused by the transport of magnetic power losses to the magnetization circuit of the f-r IM) is proposed to be determined in the form of the increment ΔI_{sq} of the active projection I_{sq} of the generalized motor stator current vector after being added to the motor shaft of the static fictitious torque T_f. According to the first relation in (6), the indicated increment ΔI_{sq} of the active projection of the stator current is founded in the form:

$$\Delta I_{sq} = T_f / \Phi_m. \qquad (17)$$

After equating the increments ΔI_{sq} calculated from (16) and (17), we determine the required value of the fictitious torque T_f, taking into account the third relation in (1):

$$T_f = \Delta P_{i\,r} / \omega_1 = \Delta P_{i\,r.n} \cdot \left(\frac{\Phi_m}{\Phi_{m.n}}\right)^2 \cdot \frac{\omega_1^{\lambda-1}}{\omega_{1n}^{\lambda}}, \qquad (18)$$

in which, in the second method, the value of the increment ΔI_{sq} of the active projection of the stator current is calculated, which is completely identical to the first (classical) method.

Let's pay attention to the well-known simplification of vector automatic control systems and calculation of energy modes of the f-r IMs when using for them ROCS «x-*y*», which is oriented with the real axis «*x*» along the generalized vector of flux linkage of the rotor [2, 3, 10]. Taking this into account, the second method (using the fictitious torque) is more appropriate in practice. With this method, increment ΔI_{sy} of the active projection I_{sy} of the stator current (on the «*y*» axis of the «*x-y*» ROCS, which is connected by the real «*x*» axis to the direction of the generalized rotor flux linkage vector $\boldsymbol{\Psi}_r$) is determined after substituting expression (18) in the second relation from (6) in the form:

$$\Delta I_{sy} = \frac{T_f}{k_r \Psi_r} = \frac{\Delta P_{i\,r.n}}{k_r \Psi_r} \cdot \left(\frac{\Psi_m}{\Psi_{mn}}\right)^2 \cdot \frac{\omega_1^{\lambda-1}}{\omega_{1n}^{\lambda}}. \qquad (19)$$

Thus, a theoretical justification of the refined analytical dependence (19) is given for determining the increment ΔI_{sy} caused by the transport of magnetic power losses to the motor magnetization circuit, which is part of the active projection I_{sy} of the generalized stator current vector $\boldsymbol{I}_s$ of the f-r IM.

It should be noted that the very form of the previously obtained active projection $I_{1\Sigma y}$ of the stator current of the calculation dependence (13) indicates that in the range of very low values of the motor speeds ω it is possible to reach a negative value in the radical expression of this dependence. In particular, as shown by the researches of the AT250L4U2 motor, negative values in the subdued expression of dependence (13) occur at speeds: $\omega \leq (0.02 - 0.03)\omega_n$. This situation is explained, obviously, by the impossibility of applying in practice the known mathematical expression from (1) or the one proposed from the relation from (10) for calculating additional losses ΔP_{ad} of the f-r IM in the range of very low motor speeds. Therefore, in order to find a refined calculation dependence for the active projection $I_{1\Sigma y}$ of the stator current in this low speed range of the f-r IM, it is necessary to preliminary obtain (on the basis of additional experimental studies or recommendations of electrical machine designers) a refined analytical calculation dependence $\Delta P_{ad} = f\,(I_{sx}, I_{1\Sigma y}, \omega)$ for additional power losses of the f-r IM in relation to its low speed range.

At the *fourth stage*, setting the values of the speed ω and the useful torque T, from the previously obtained calculation dependencies, let's calculate for the f-r IM AT250L4U2 (which is characterized by the nominal parameters and basic values presented in Table 1) the electromagnetic and energy processes of this motor in the motor (at $T > 0$) and generator (at $T < 0$) steady-state modes for the first (when $n \leq n_n$) and the second (when $n > n_n$) speed zones. The results of these calculations are shown in Table 2, 3.

Table 1

Nominal parameters of the f-r IM AT250L4U2 and its basic values for the relative system of units

I. Nominal parameters, dimensions	Value
Useful power, kW	120
Active linear stator voltage, V	400
Active phase stator current, A	202.5
Stator voltage frequency, Hz	50
Number of pole pairs	2
Slip, %	1.5
Maximum speed, rpm	4000
Efficiency, %	94
Power factor	0.91
Multiplicity of the maximum torque	3.5
Multiplicity of the starting torque	3.5
Connection of phase stator windings	Y
Electrical power losses in the stator winding, kW	2.625
Electrical power losses in the rotor winding, kW	1.849
Magnetic power losses, kW	1.800
Additional power losses, kW	0.638
Mechanical power losses, kW	0.748
Module Φ_m of the generalized magnetic flux vector, pu	0.9562
Modulus Ψ_r of the generalized rotor flux linkage vector, pu	0.9574
Useful torque T_n, pu	0.8684
II. Parameters of the «T»-shaped substitution circuit	
Active resistance of the phase stator winding, pu	0.01871
Equivalent resistance of the phase rotor winding, pu	0.01569
Active resistance of the magnetization circuit, pu	71.3
Magnetization inductance, pu	2.6421
Dissipation inductance of the stator winding, pu	0.06850
Dissipation inductance of the rotor winding, pu	0.07633
III. Base values for the relative system of units:	
- for voltage, V	326.6
- for current, A	286.4
- for active and inductive resistance, Ω	1.1404
- for power, kW	140.296
- for torque, N·m	893.15
- for magnetic flux and flux linkage, Wb	1.0396
- for inductances, mH	3.630
- for angular frequency of rotation, rad/s	157.08
- for time, ms	3.183

The reliability of the performed calculations of electromagnetic processes and energy modes is confirmed by comparing their values with the corresponding values calculated in the MATLAB software package (the relative deviation does not exceed 0.2 %).

From the analysis of the computational data given in Table 2, 3, it was found that in the motor mode of operation of the f-r IM at equal speeds n and the same (by absolute value) useful torques T of the motor, the values of the modules of the stator current I_s and stator voltage U_s of the motor exceed their corresponding values in the generator mode of operation.

Table 2

Results of the refined calculation in the first speed zone at steady-state motor (at $T > 0$) and generator (at $T < 0$) modes of electromagnetic and energy quantities for the f-r IM AT250L4U2 depending on the speed and relative useful torque T/T_n

n	$\frac{T}{T_n}$	$\frac{I_s}{I_{sn}}$	Δn	ω_1	$\frac{\Psi_m}{\Psi_{mn}}$	$\Delta P_{e.s}$	$\Delta P_{e.r}$	$\Delta P_{i\,r}$	ΔP_{ad}	ΔP_{mech}	ΔP^*_{em}	$\frac{P_1}{P_{1n}}$	η	$\cos\varphi$	$\frac{U_s}{U_{sn}}$
rpm	–	–	rpm	pu	–	kW	kW	kW	kW	kW	kW	–	%	–	–
1477.5	0.5	0.566	11.32	0.993	0.998	0.842	0.467	1.775	0.205	0.748	3.289	0.502	93.70	0.825	0.977
	1	1	22.55	1	1	2.625	1.853	1.800	0.638	0.748	6.916	1.000	94.00	0.910	1
	1.5	1.459	33.83	1.008	1.003	5.585	4.170	1.829	1.358	0.748	12.94	1.517	92.93	0.921	1.028
	2	1.986	45.17	1.015	1.008	9.739	7.431	1.865	2.368	0.748	21.40	2.054	91.55	0.915	1.061
	–0.5	0.531	–10.98	0.978	0.998	0.739	0.439	1.740	0.180	0.748	3.098	–0.440	93.59	–0.798	0.945
	–1	0.954	–22.05	0.970	1	2.387	1.771	1.730	0.581	0.748	6.468	–0.884	93.99	–0.900	0.937
	–1.5	1.400	–33.07	0.963	1.003	5.147	3.984	1.724	1.252	0.748	12.11	–1.309	92.86	–0.912	0.937
	–2	1.852	–44.04	0.956	1.008	9.004	7.066	1.722	2.190	0.748	19.98	–1.718	91.36	–0.904	0.933
1000	0.5	0.563	11.27	0.674	0.998	0.832	0.462	1.073	0.202	0.342	2.570	0.340	93.55	0.825	0.666
	1	0.998	22.53	0.682	1	2.613	1.849	1.093	0.636	0.342	6.192	0.687	92.67	0.911	0.687
	1.5	1.459	33.88	0.689	1.003	5.588	4.180	1.117	1.359	0.342	12.24	1.052	90.71	0.923	0.711
	2	1.930	45.30	0.697	1.008	9.781	7.476	1.144	2.379	0.342	20.78	1.437	88.55	0.917	0.739
	–0.5	0.534	–11.03	0.659	0.998	0.749	0.443	1.043	0.182	0.342	2.417	–0.297	93.48	–0.798	0.635
	–1	0.956	–22.07	0.652	1	2.399	1.774	1.032	0.583	0.342	5.788	–0.589	92.59	–0.898	0.624
	–1.5	1.400	–33.03	0.645	1.003	5.148	3.975	1.023	1.252	0.342	11.40	–0.863	90.45	–0.910	0.617
	–2	1.849	–43.92	0.637	1.007	8.972	7.028	1.017	2.182	0.342	19.20	–1.120	88.04	–0.901	0.612
500	0.5	0.561	11.27	0.341	0.998	0.827	0.463	0.442	0.201	0.086	1.933	0.174	91.19	0.829	0.341
	1	1.001	22.66	0.348	1	2.629	1.870	0.457	0.639	0.086	5.595	0.362	87.84	0.916	0.360
	1.5	1.471	34.21	0.356	1.003	5.676	4.263	0.473	1.380	0.086	11.79	0.570	83.75	0.928	0.380
	2	1.954	46.93	0.364	1.008	10.03	7.686	0.492	2.438	0.086	20.64	0.798	79.71	0.923	0.402
	–0.5	0.536	–11.03	0.326	0.998	0.754	0.443	0.417	0.183	0.086	1.797	–0.145	91.01	–0.793	0.310
	–1	0.957	–21.96	0.319	1	2.388	1.756	0.407	0.581	0.086	5.131	–0.278	87.29	–0.892	0.297
	–1.5	1.391	–32.74	0.312	1.003	5.078	3.905	0.397	1.235	0.086	10.62	–0.394	82.53	–0.901	0.286
	–2	1.829	–43.39	0.304	1.007	8.783	9.859	0.389	2.136	0.086	18.17	–0.494	77.60	–0.889	0.276
150	0.5	0.568	11.52	0.108	0.998	0.846	0.483	0.099	0.206	0.008	1.634	0.061	78.85	0.851	0.114
	1	1.033	23.53	0.116	1	2.801	2.017	0.109	0.681	0.008	5.608	0.139	68.48	0.932	0.132
	1.5	1.551	36.23	0.124	1.004	6.313	4.782	0.121	1.535	0.008	12.75	0.243	58.90	0.944	0.151
	2	2.110	49.76	0.133	1.010	11.69	9.020	0.134	2.842	0.008	23.68	0.376	50.71	0.941	0.142
	–0.5	0.531	–10.81	0.093	0.998	0.739	0.426	0.082	0.180	0.008	1.426	–0.037	76.57	–0.757	0.083
	–1	0.930	–21.27	0.086	1	2.268	1.648	0.074	0.552	0.008	4.542	–0.060	62.72	–0.849	0.069
	–1.5	1.337	–31.34	0.079	1.003	4.689	3.577	0.067	1.140	0.008	9.474	–0.069	48.16	–0.831	0.056
	–2	1.736	–41.05	0.726	1.006	7.909	6.138	0.060	1.923	0.008	16.03	–0.065	34.21	–0.754	0.045

Moreover, by using vector control [2, 3], constant values of the rotor flux linkage module Ψ_r and the magnetizing projection I_{sx} of the generalized stator current vector (equal to their nominal values $\Psi_{r.n} = 0.9574$ pu and $I_{sx.n} = 0.288$ pu) were set for the f-r IM in the first zone:

$$\Psi_r = \Psi_{r\,n} = \text{const}; \quad I_{sx} = I_{sx.n} = \text{const}, \tag{20}$$

and in the second zone, the values of the module Ψ_r the generalized rotor flux linkage vector and the magnetizing projection I_{sx} of the generalized stator current vector changed inversely proportional to the angular frequency of rotation ω_1 of the IM stator magnetic field [10]:

$$\Psi_r = \Psi_{r\,n} / \omega_1; \quad I_{sx} = I_{sx.n} / \omega_1. \tag{21}$$

According to the results of the calculations for the steady-state motor mode (at $T > 0$), Fig. 2 presents constructed (relative to the considered IM AT250L4U2) graphical dependencies of the following energy quantities: I_s/I_{sn}, U_s/U_{sn}, P_1/P_{1n}, η, $\cos\varphi$, $\Delta P^*_{em}/\Delta P^*_{em.n}$ – functions of change in speed n and relative torque T/T_n of the f-r IM. Moreover, in the mentioned quantities, which are given in the form of fractions, the instantaneous value of the quantity is indicated in the numerator, and the value (indicated by the additional index «*n*») of this quantity corresponding to the nominal mode of operation of the motor is indicated in the denominator.

In steady-stable modes, the values of the efficiency η, the power factor $\cos\varphi$ and the module U_s of the generalized vector of the stator voltage of the f-r IM were determined from known dependencies [1, 12]:

$$\begin{cases} U_{sx} = R_s \cdot I_{sx} - \omega_1 \cdot L_\sigma \cdot I_{sy}; \\ U_{sy} = R_s \cdot I_{sy} + \omega_1 \cdot L_\sigma \cdot I_{sx} + \omega_1 \cdot k_r \cdot \Psi_r; \\ U_s = \sqrt{U_{sx}^2 + U_{sy}^2}; \quad \cos\varphi = \cos(\Theta_U - \Theta_I); \\ \Theta_I = \text{sign}(I_{sx}) \cdot \arcsin\left(\dfrac{I_{sy}}{I_s}\right) + \dfrac{\pi}{2} \cdot [1 - \text{sign}(I_{sx})]; \\ \Theta_U = \text{sign}(U_{sx}) \cdot \arcsin\left(\dfrac{U_{sy}}{U_s}\right) + \dfrac{\pi}{2} \cdot [1 - \text{sign}(U_{sx})]; \\ L_\sigma = L_{\sigma s} + k_r \cdot L_{\sigma r}; \quad \eta = P_2 / P_1; \\ \text{sign}(I_{sx}) = \begin{cases} 1, & I_{sx} \ge 0; \\ -1, & I_{sx} < 0; \end{cases} \text{sign}(U_{sx}) = \begin{cases} 1, & U_{sx} \ge 0; \\ -1, & U_{sx} < 0, \end{cases} \end{cases} \tag{22}$$

where L_σ is the total dissipation inductance of the motor; sign( ) is the mathematical operation for determining the sign of an algebraic value shown in parentheses.

Based on the analysis of graphical dependencies in Fig. 2, let's compare the values shown on these graphs for the first and second speed control zones in relation to the f-r IM operating in motor mode:

Table 3

Results of the refined calculation in the second speed zone at steady-state motor (at $T > 0$) and generator (at $T < 0$) modes of electromagnetic and energy quantities for the f-r IM AT250L4U2 depending on the speed n and relative useful torque T/T_n

n	$\frac{T}{T_n}$	$\frac{I_s}{I_{sn}}$	Δn	ω_1	Ψ_r	$\frac{\Psi_m}{\Psi_{mn}}$	$\Delta P_{e.s}$	$\Delta P_{e.r}$	$\Delta P_{i\,r}$	ΔP_{ad}	ΔP_{mech}	ΔP^*_{em}	$\frac{P_1}{P_{1n}}$	η	$\cos\varphi$	$\frac{U_s}{U_{sn}}$
rpm	–	–	rpm	pu	pu	–	kW	kW	kW	kW	kW	kW	–	%	–	–
2000	0.5	0.687	20.65	1.347	0.711	0.742	1.238	0.856	1.459	0.301	1.371	3.854	0.677	93.96	0.904	0.993
	1	1.318	41.95	1.361	0.703	0.739	4.560	3.459	1.469	1.109	1.371	10.60	1.366	93.14	0.916	1.030
	1.5	1.980	64.35	1.376	0.696	0.740	10.29	7.964	1.494	2.501	1.371	22.24	2.094	91.16	0.888	1.084
	2	2.665	87.96	1.392	0.688	0.745	18.64	14.55	1.537	4.533	1.371	39.26	2.863	88.88	0.845	1.156
	–0.5	0.631	–19.05	1.321	0.725	0.757	1.046	0.758	1.479	0.255	1.371	3.538	–0.598	93.96	–0.889	0.969
	–1	1.212	–37.62	1.308	0.732	0.768	3.857	3.012	1.505	0.938	1.371	9.311	–1.189	93.42	–0.912	0.979
	–1.5	1.791	–55.42	1.296	0.739	0.782	8.422	6.656	1.541	2.048	1.371	18.67	–1.752	91.78	–0.890	1.000
	–2	2.360	–72.51	1.285	0.745	0.798	14.62	11.60	1.586	3.556	1.371	31.36	–2.289	89.92	–0.855	1.031
2500	0.5	0.835	32.59	1.688	0.567	0.594	1.830	1.357	1.254	0.445	2.142	4.887	0.850	93.53	0.919	1.008
	1	1.646	66.51	1.711	0.560	0.596	7.108	5.505	1.287	1.729	2.142	15.63	1.730	91.95	0.883	1.084
	1.5	2.493	102.7	1.735	0.552	0.606	16.32	12.76	1.353	3.969	2.142	34.41	2.672	89.29	0.813	1.199
	2	3.378	141.5	1.761	0.544	0.624	29.95	23.52	1.461	7.284	2.142	62.21	3.685	86.32	0.734	1.353
	–0.5	0.760	–29.49	1.647	0.581	0.608	1.517	1.168	1.274	0.369	2.142	4.327	–0.745	93.63	–0.913	0.976
	–1	1.493	–58.05	1.628	0.588	0.624	5.850	4.632	1.318	1.423	2.142	13.22	–1.470	92.43	–0.887	1.011
	–1.5	2.211	–85.18	1.610	0.595	0.643	12.83	10.20	1.381	3.121	2.142	27.53	–2.153	90.26	–0.829	1.069
	–2	2.911	–111.0	1.593	0.601	0.666	22.25	17.69	1.462	5.411	2.142	46.82	–2.798	87.94	–0.764	1.145
3000	0.25	0.524	23.87	2.016	0.475	0.496	0.720	0.511	1.102	0.175	3.084	2.508	0.521	91.59	0.911	0.993
	0.5	0.996	47.41	2.032	0.471	0.497	2.602	1.984	1.116	0.633	3.084	6.334	1.028	92.82	0.909	1.033
	1	1.985	97.25	2.065	0.464	0.507	10.35	8.080	1.186	2.516	3.084	22.13	2.106	90.62	0.822	1.174
	1.5	3.026	151.2	2.101	0.456	0.529	24.03	18.87	1.323	5.843	3.084	50.06	3.279	87.31	0.711	1.388
	–0.25	0.454	–20.83	1.986	0.482	0.503	0.541	0.401	1.112	0.132	3.084	2.186	–0.436	91.35	–0.897	0.973
	–0.5	0.896	–42.07	1.972	0.486	0.511	2.108	1.658	1.134	0.513	3.084	5.413	–0.888	93.03	–0.910	0.991
	–1	1.774	–82.58	1.945	0.492	0.531	8.261	6.566	1.205	2.009	3.084	18.04	–1.743	91.33	–0.837	1.068
	–1.5	2.626	–120.7	1.920	0.499	0.558	18.10	14.40	1.310	4.403	3.084	38.22	–2.540	88.70	–0.742	1.185
4000	0.25	0.689	43.38	2.696	0.355	0.374	1.246	0.944	0.912	0.303	5.483	3.405	0.706	90.14	0.913	1.021
	0.5	1.334	86.10	2.724	0.352	0.380	4.674	3.639	0.957	1.137	5.483	10.41	1.397	91.09	0.843	1.130
	0.75	2.002	131.0	2.754	0.348	0.394	10.52	8.243	1.042	2.558	5.483	22.36	2.127	89.75	0.748	1.293
	1	2.691	178.4	2.786	0.344	0.414	19.01	14.94	1.170	4.623	5.483	39.74	2.899	87.78	0.653	1.502
	–0.25	0.577	–36.19	2.643	0.362	0.380	0.873	0.683	0.919	0.212	5.483	2.688	–0.572	89.94	–0.914	0.988
	–0.5	1.171	–73.39	2.618	0.366	0.392	3.602	2.864	0.965	0.876	5.483	8.306	–1.165	91.51	–0.859	1.053
	–0.75	1.756	–109.1	2.594	0.369	0.408	8.089	6.440	1.035	1.967	5.483	17.53	–1.728	90.55	–0.776	1.155
	–1	2.327	–143.3	2.571	0.372	0.428	14.22	11.32	1.126	3.458	5.483	30.12	–2.266	89.04	–0.692	1.280

- with the same values of the torque T, the corresponding values of the module I_s of the generalized stator current vector and the electromagnetic power losses ΔP^*_{em} in the first speed zone (when $n \leq n_n$) are significantly smaller than in the second zone (when $n > n_n$);

- extreme (maximum) values are characteristic of graphic dependencies for the efficiency η and the power factor $\cos\varphi$ of the f-r IM in the first and second zones;

- values of motor efficiency η with increasing speed: in the first zone – increase, while in the second zone – decrease;

- the optimal value of the motor torque (corresponding to the maximum value of the efficiency) with increasing speed: in the first zone – it increases, while in the second zone – on the contrary, it decreases.

At the *fifth stage*, we quantitatively estimate the possible errors regarding the main (caused by the first harmonic components of the phase stator voltages and currents) electromagnetic losses ΔP_{em}, if additional and magnetic power losses, as well as components of electrical losses caused by the transport of these power losses through the air gap or to the magnetization circuit of the motor were not taken into account (as, for example, in well-known publications [1–11]).

The calculated analytical dependence for the main electromagnetic power losses (MEPL) ΔP^*_{em} of the short-circuited f-r IM (which simultaneously takes into account: all types of power losses present in the motor, as well as the above-mentioned electrical components of losses associated with the mentioned transportation of additional and magnetic power losses) obtained based on the diagram in Fig. 1 and formulas (1), (10), (13), (14), (19) is refined and has the following form:

$$\begin{aligned}\Delta P^*_{em} = {} & R_s\cdot\left[I_{sx}^2 + \left(I_{1y}+\Delta I_{1y}+\Delta I_{sy}\right)^2\right] + \Delta P_{i\,r} + \\ & + k_r^2 R_r\cdot\left(I_{1y}+\Delta I_{1y}\right)^2 + R^*_{ad}\cdot\left[I_{sx}^2+\left(I_{1y}+\Delta I_{1y}\right)^2\right].\end{aligned} \qquad (23)$$

In this dependence: the first term is the calculation relation for the main electrical power losses in the stator winding (which take into account, according to (23), the magnetizing I_{sx} and active I_{1y} projections of the generalized stator current vector $\boldsymbol{I}_1$, as well as the increments ΔI_{sy} and ΔI_{1y} of the stator current, caused by the transportation of magnetic and additional losses; the second term is the magnetic losses $\Delta P_{i\,r}$, which are calculated from (1); the third term is the calculation relation for the main electrical losses in the rotor winding (calculated through the active projection I_{1y} of the stator current and the increment ΔI_{1y} pf the stator current, which is calculated from (14) and is caused by the transport of additional power losses through the air gap of the motor), and the fourth one is the additional motor power losses ΔP_{ad}, calculated from (10).

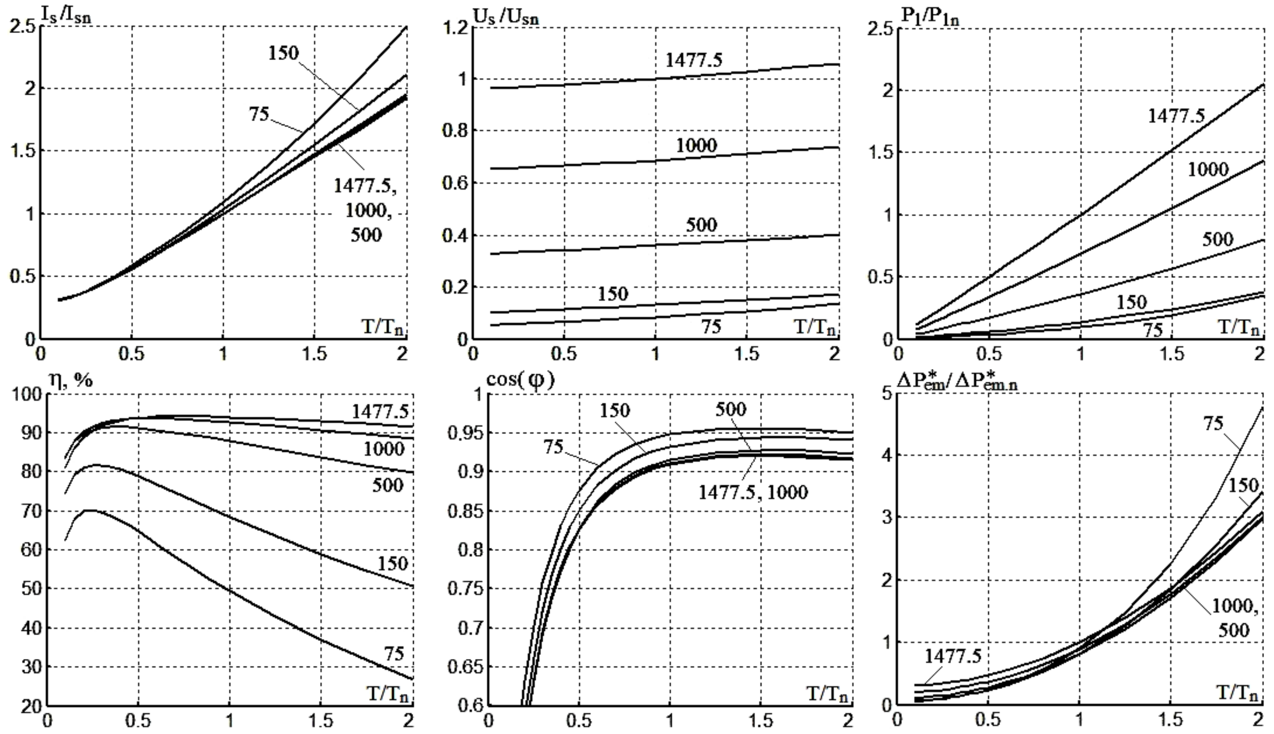

a) with $n \leq n_n$

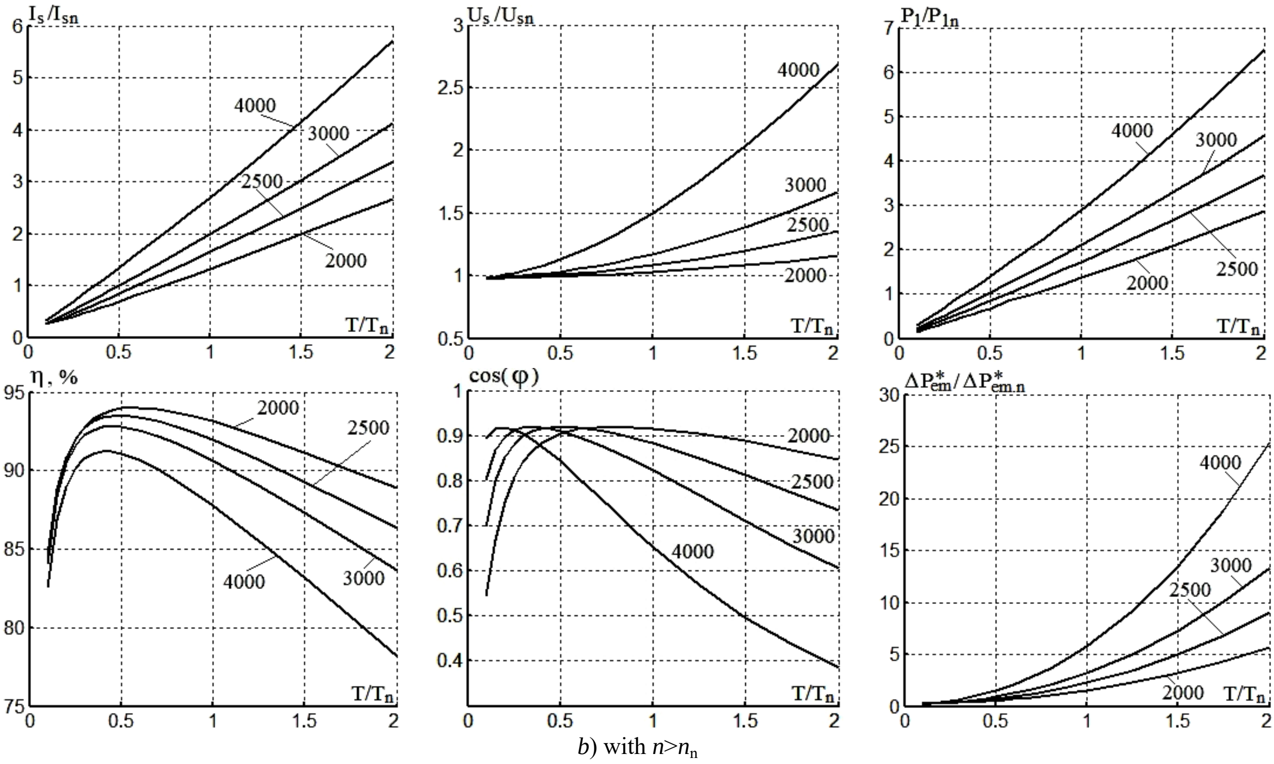

b) with $n > n_n$

Fig. 2. Graphical dependencies illustrating the change in the motor mode of operation in the first (*a*) and second (*b*) speed zones of: the modules of the generalized vectors of the stator current I_s/I_{sn} and voltage U_s/U_{sn}, the efficiency η and the power factor $\cos\varphi$, the main electromagnetic power losses $\Delta P^*_{em}/\Delta P^*_{em.n}$ and the main consumed active power P_1/P_{1n}, – for the f-r IM AT250L4U2 depending on the useful torque T/T_n (at speeds n equal to 75, 150, 500, 1000 and 1477.5 rpm for the first zone, or 2000, 2500, 3000 and 4000 rpm for the second zone)

The importance of obtaining for practice the proposed dependence (23) for the refined calculation of MEPL ΔP^*_{em} is explained by the direct effect of these power losses on motor heating (as a result, the use of this dependence can warn the designers of f-r induction electric drives about motor overheating during operation).

The values of MEPL, which are calculated from inaccurate dependencies (in which there is no taking into account of at least one type of motor power losses, or at least one of the electrical components spent on transporting additional or magnetic losses), are denoted without an asterisk from above in the form: $\Delta P_{em.1}$, $\Delta P_{em.2}$, $\Delta P_{em.3}$, $\Delta P_{em.4}$ or $\Delta P_{em.5}$. Based on (23) and the accepted notation, we obtain calculation dependencies for determining errors in the calculation of the MEPL of the f-r IM:

$$\Delta P_{\delta 1}=\Delta P_{\mathrm{em}}^{*}-\Delta P_{\mathrm{em.1}}=R_{\mathrm{s}}\cdot\left[\left(I_{1\mathrm{y}}+\Delta I_{1\mathrm{y}}+\Delta I_{\mathrm{sy}}\right)^{2}-\right.$$
$$\left.-\left(I_{1\mathrm{y}}+\Delta I_{\mathrm{sy}}\right)^{2}\right]+k_{\mathrm{r}}^{2}R_{\mathrm{r}}\cdot\left[\left(I_{1\mathrm{y}}+\Delta I_{1\mathrm{y}}\right)^{2}-I_{1\mathrm{y}}^{2}\right], \tag{24}$$

– in relation to the dependence for $\Delta P_{\mathrm{em.1}}$, which is obtained from (23) when $\Delta I_{1\mathrm{y}}=0$ and does not take into account the electrical component of losses caused by the transportation of additional power losses through the air gap of the motor (according to [11]);

$$\Delta P_{\delta 2}=\Delta P_{\mathrm{em}}^{*}-\Delta P_{\mathrm{em.2}}=R_{\mathrm{s}}\cdot\left[\left(I_{1\mathrm{y}}+\Delta I_{1\mathrm{y}}+\Delta I_{\mathrm{sy}}\right)^{2}-I_{1\mathrm{y}}^{2}\right]+$$
$$+k_{\mathrm{r}}^{2}R_{\mathrm{r}}\cdot\left[\left(I_{1\mathrm{y}}+\Delta I_{1\mathrm{y}}\right)^{2}-I_{1\mathrm{y}}^{2}\right], \tag{25}$$

– in relation to the dependence for $\Delta P_{\mathrm{em.2}}$, which is obtained from (23) when $\Delta I_{1\mathrm{y}}=0$, $\Delta I_{\mathrm{sy}}=0$ and does not take into account the components of electrical losses due to the transportation of additional losses through the air gap and of magnetic power losses to the motor magnetization circuit (according to [10]);

$$\Delta P_{\delta 3}=\Delta P_{\mathrm{em}}^{*}-\Delta P_{\mathrm{em.3}}=\Delta P_{\delta 1}+R_{\mathrm{ad}}^{*}\cdot\left(I_{\mathrm{sx}}^{2}+I_{1\Sigma\,\mathrm{y}}^{2}\right)=$$
$$=R_{\mathrm{s}}\cdot\left[\left(I_{1\mathrm{y}}+\Delta I_{1\mathrm{y}}+\Delta I_{\mathrm{sy}}\right)^{2}-\left(I_{1\mathrm{y}}+\Delta I_{\mathrm{sy}}\right)^{2}\right]+$$
$$+k_{\mathrm{r}}^{2}R_{\mathrm{r}}\cdot\left[\left(I_{1\mathrm{y}}+\Delta I_{1\mathrm{y}}\right)^{2}-I_{1\mathrm{y}}^{2}\right]+R_{\mathrm{ad}}^{*}\cdot\left(I_{\mathrm{sx}}^{2}+I_{1\Sigma\,\mathrm{y}}^{2}\right), \tag{26}$$

– in relation to the dependence for $\Delta P_{\mathrm{em.3}}$, which is obtained from (23) when $\Delta I_{1\mathrm{y}}=0$, $R^{*}_{\mathrm{ad}}=0$ and does not take into account additional losses and the electrical component of losses caused by their transportation through the air gap of the motor (according to [3–9]);

$$\Delta P_{\delta 4}=\Delta P_{\mathrm{em}}^{*}-\Delta P_{\mathrm{em.4}}=R_{\mathrm{s}}\cdot\left[\left(I_{1\mathrm{y}}+\Delta I_{1\mathrm{y}}+\Delta I_{\mathrm{sy}}\right)^{2}-I_{1\mathrm{y}}^{2}\right]+$$
$$+k_{\mathrm{r}}^{2}R_{\mathrm{r}}\cdot\left[\left(I_{1\mathrm{y}}+\Delta I_{1\mathrm{y}}\right)^{2}-I_{1\mathrm{y}}^{2}\right]+R_{\mathrm{ad}}^{*}\left(I_{\mathrm{sx}}^{2}+I_{1\Sigma\,\mathrm{y}}^{2}\right), \tag{27}$$

– in relation to the dependence for $\Delta P_{\mathrm{em.4}}$, which is obtained from (23) when $I_{\mathrm{sy}}=0$, $\Delta I_{1\mathrm{y}}=0$, $R^{*}_{\mathrm{ad}}=0$ and does not take into account additional losses, as well as components of electrical losses due to the transportation of magnetic and additional power losses;

$$\Delta P_{\delta 5}=\Delta P_{\mathrm{em}}^{*}-\Delta P_{\mathrm{em.5}}=\Delta P_{\delta 4}+\Delta P_{\mathrm{i\,r}}=$$
$$=R_{\mathrm{s}}\cdot\left[\left(I_{1\mathrm{y}}+\Delta I_{1\mathrm{y}}+\Delta I_{\mathrm{sy}}\right)^{2}-I_{1\mathrm{y}}^{2}\right]+\Delta P_{\mathrm{i\,r}}+$$
$$+k_{\mathrm{r}}^{2}R_{\mathrm{r}}\cdot\left[\left(I_{1\mathrm{y}}+\Delta I_{1\mathrm{y}}\right)^{2}-I_{1\mathrm{y}}^{2}\right]+R_{\mathrm{ad}}^{*}\left(I_{\mathrm{sx}}^{2}+I_{1\Sigma\,\mathrm{y}}^{2}\right) \tag{28}$$

– in relation to the dependence for $\Delta P_{\mathrm{em.5}}$, which is obtained from (23) when $\Delta I_{\mathrm{sy}}=0$, $\Delta I_{1\mathrm{y}}=0$, $R^{*}_{\mathrm{ad}}=0$, $\Delta P_{\mathrm{i.r}}=0$ and does not take into account magnetic and additional losses, as well as components of electrical losses for their transportation to the magnetization circuit or through the air gap of the motor, respectively (which, as is known, is characteristic of the idealized representation of the IM [1, 2]).

Results of calculations carried out by (24) – (28) of absolute values of errors $\Delta P_{\delta 1}$, $\Delta P_{\delta 2}$, $\Delta P_{\delta 3}$, $\Delta P_{\delta 4}$, $\Delta P_{\delta 5}$, as well as relative values of these errors $\Delta P_{\delta 1}/\Delta P^{*}_{\mathrm{em}}$, $\Delta P_{\delta 2}/\Delta P^{*}_{\mathrm{em}}$, $\Delta P_{\delta 3}/\Delta P^{*}_{\mathrm{em}}$, $\Delta P_{\delta 4}/\Delta P^{*}_{\mathrm{em}}$ i $\Delta P_{\delta 5}/\Delta P^{*}_{\mathrm{em}}$ are given in Table 4, 5, from the analysis of which it follows that:

Table 4

Calculated ratios of electromagnetic and energy quantities, as well as absolute values of errors $\Delta P_{\delta 1}$, $\Delta P_{\delta 2}$, $\Delta P_{\delta 3}$, $\Delta P_{\delta 4}$, $\Delta P_{\delta 5}$ for the f-r IM AT250L4U2 in the first speed zone (when $n \le n_{\mathrm{n}}$)

n	$\frac{T}{T_{\mathrm{n}}}$	$\frac{I_{\mathrm{s}}}{I_{1\Sigma}}$	$\frac{I_{\mathrm{s}}}{I_1}$	$\frac{I_{1\Sigma}}{I_1}$	$\frac{\Delta I_{\mathrm{sy}}}{I_{\mathrm{sn}}}$	$\frac{\Delta I_{1\mathrm{y}}}{I_{\mathrm{sn}}}$	$\frac{\Delta P_{\delta.1}}{\Delta P^{*}_{\mathrm{em}}}$	$\frac{\Delta P_{\delta.2}}{\Delta P^{*}_{\mathrm{em}}}$	$\frac{\Delta P_{\delta.3}}{\Delta P^{*}_{\mathrm{em}}}$	$\frac{\Delta P_{\delta.4}}{\Delta P^{*}_{\mathrm{em}}}$	$\frac{\Delta P_{\delta.5}}{\Delta P^{*}_{\mathrm{em}}}$	$\Delta P_{\delta 1}$	$\Delta P_{\delta 2}$	$\Delta P_{\delta 3}$	$\Delta P_{\delta 4}$	$\Delta P_{\delta 5}$
rpm	–	–	–	–	%	%	%	%	%	%	%	kW	kW	kW	kW	kW
1477.5	0.5	1.021	1.024	1.002	1.370	0.153	0.210	1.258	6.341	7.389	60.31	0.007	0.041	0.209	0.243	1.983
	1	1.013	1.018	1.005	1.378	0.484	0.624	1.614	9.855	10.84	35.88	0.043	0.112	0.682	0.750	2.481
	1.5	1.009	1.017	1.007	1.391	1.037	1.069	1.866	11.64	12.44	25.78	0.138	0.242	1.507	1.610	3.336
	2	1.007	1.017	1.010	1.407	1.815	1.508	2.156	12.71	13.35	21.42	0.323	0.462	2.720	2.858	4.584
	–0.5	0.979	0.977	0.998	1.363	0.146	–0.201	–1.250	6.019	4.970	62.19	–0.006	–0.039	0.187	0.154	1.927
	–1	0.987	0.982	0.995	1.366	0.464	–0.619	–1.640	8.850	7.830	35.59	–0.040	–0.106	0.573	0.507	2.302
	–1.5	0.991	0.984	0.993	1.371	0.992	–1.065	–1.890	9.756	8.931	23.99	–0.129	–0.229	1.181	1.081	2.905
	–2	0.993	0.984	0.991	1.380	1.728	–1.501	–2.173	9.918	9.246	18.54	–0.300	–0.434	1.982	1.848	3.704
1000	0.5	1.019	1.022	1.004	1.220	0.224	0.391	1.576	8.177	9.362	49.95	0.010	0.041	0.210	0.241	1.284
	1	1.012	1.019	1.007	1.229	0.713	1.026	2.007	11.32	12.30	28.98	0.064	0.124	0.701	0.762	1.794
	1.5	1.008	1.019	1.011	1.241	1.535	1.672	2.422	12.88	13.63	22.00	0.205	0.297	1.577	1.669	2.694
	2	1.007	1.021	1.014	1.257	2.698	2.308	2.904	13.91	14.51	19.42	0.480	0.603	2.891	3.014	4.034
	–0.5	0.981	0.978	0.997	1.212	0.217	–0.386	–1.591	7.648	6.443	50.79	–0.009	–0.038	0.185	0.156	1.228
	–1	0.988	0.981	0.993	1.212	0.687	–1.027	–2.044	9.574	8.558	27.40	–0.060	–0.118	0.554	0.495	1.586
	–1.5	0.992	0.982	0.990	1.216	1.463	–1.670	–2.449	9.800	9.021	18.78	–0.190	–0.279	1.117	1.028	2.140
	–2	0.994	0.980	0.987	1.222	2.540	–2.296	–2.916	9.527	8.906	14.82	–0.441	–0.560	1.829	1.710	2.846
500	0.5	1.015	1.023	1.007	0.994	0.448	1.036	2.311	11.40	12.67	34.28	0.020	0.045	0.220	0.245	0.663
	1	1.010	1.024	1.014	1.005	1.441	2.294	3.179	13.80	14.69	21.97	0.128	0.178	0.772	0.822	1.229
	1.5	1.007	1.028	1.021	1.018	3.129	3.550	4.187	15.41	16.04	19.42	0.419	0.494	1.817	1.892	2.290
	2	1.005	1.034	1.029	1.035	5.544	4.803	5.296	16.80	17.30	19.19	0.991	1.093	3.469	3.570	3.960
	–0.5	0.985	0.978	0.993	0.981	0.434	–1.042	–2.363	9.755	8.434	32.98	–0.019	–0.043	0.175	0.152	0.593
	–1	0.990	0.977	0.987	0.978	1.361	–2.296	–3.224	9.552	8.624	17.48	–0.118	–0.165	0.490	0.443	0.897
	–1.5	0.993	0.974	0.980	0.977	2.877	–3.517	–4.191	8.592	7.918	12.34	–0.373	–0.445	0.912	0.841	1.309
	–2	0.995	0.969	0.974	0.979	4.961	–4.816	–5.242	7.485	6.959	9.626	–0.857	–0.952	1.360	1.264	1.749
150	0.5	1.011	1.035	1.024	0.704	1.542	4.248	5.311	16.90	17.96	22.96	0.069	0.087	0.276	0.294	0.375
	1	1.007	1.058	1.051	0.722	5.148	8.318	8.951	20.62	21.26	22.57	0.466	0.502	1.157	1.192	1.266
	1.5	1.005	1.085	1.080	0.743	11.65	12.57	13.00	24.82	25.25	25.76	1.603	1.658	3.165	3.219	3.285
	2	1.004	1.117	1.113	0.769	21.62	16.99	17.31	29.23	29.55	29.79	4.025	4.100	6.922	6.998	7.056
	–0.5	0.989	0.968	0.978	0.673	1.407	–4.229	–5.376	8.991	7.845	14.70	–0.060	–0.077	0.128	0.112	0.210
	–1	0.993	0.952	0.958	0.659	4.282	–8.055	–8.764	4.583	3.874	6.210	–0.366	–0.398	0.208	0.176	0.282
	–1.5	0.995	0.935	0.940	0.647	8.818	–11.84	–12.34	0.636	0.135	1.342	–1.122	–1.169	0.060	0.013	0.127
	–2	0.996	0.919	0.922	0.635	14.84	–15.58	–15.97	–3.170	–3.558	–2.794	–2.497	–2.559	–0.508	–0.570	–0.448

Table 5

Calculated ratios of electromagnetic and energy quantities, as well as absolute values of errors $\Delta P_{\delta 1}$, $\Delta P_{\delta 2}$, $\Delta P_{\delta 3}$, $\Delta P_{\delta 4}$, $\Delta P_{\delta 5}$ for the f-r IM AT250L4U2 in the second speed zone (when $n > n_n$)

n	$\frac{T}{T_n}$	$\frac{I_s}{I_{1\Sigma}}$	$\frac{I_s}{I_1}$	$\frac{I_{1\Sigma}}{I_1}$	$\frac{\Delta I_{sy}}{I_{sn}}$	$\frac{\Delta I_{1y}}{I_{sn}}$	$\frac{\Delta P_{\delta.1}}{\Delta P^*_{em}}$	$\frac{\Delta P_{\delta.2}}{\Delta P^*_{em}}$	$\frac{\Delta P_{\delta.3}}{\Delta P^*_{em}}$	$\frac{\Delta P_{\delta.4}}{\Delta P^*_{em}}$	$\frac{\Delta P_{\delta.5}}{\Delta P^*_{em}}$	$\Delta P_{\delta 1}$	$\Delta P_{\delta 2}$	$\Delta P_{\delta 3}$	$\Delta P_{\delta 4}$	$\Delta P_{\delta 5}$
rpm	–	–	–	–	%	%	%	%	%	%	%	kW	kW	kW	kW	kW
2000	0.5	1.016	1.019	1.003	1.118	0.226	0.357	1.338	8.132	9.114	46.00	0.014	0.052	0.313	0.352	1.773
	1	1.009	1.015	1.007	1.125	0.853	0.978	1.695	11.54	12.26	25.41	0.104	0.180	1.223	1.299	2.692
	1.5	1.006	1.016	1.010	1.145	1.955	1.615	2.140	13.03	13.55	19.75	0.359	0.476	2.898	3.015	4.393
	2	1.004	1.018	1.014	1.177	3.593	2.268	2.680	14.02	14.43	17.94	0.890	1.052	5.504	5.666	7.041
	–0.5	0.983	0.981	0.997	1.133	0.200	–0.318	–1.327	7.319	6.310	49.12	–0.011	–0.047	0.259	0.223	1.738
	–1	0.991	0.985	0.994	1.153	0.718	–0.871	–1.655	9.666	8.882	25.83	–0.081	–0.154	0.900	0.827	2.405
	–1.5	0.994	0.985	0.992	1.181	1.545	–1.395	–1.992	10.02	9.422	18.28	–0.260	–0.372	1.870	1.759	3.411
	–2	0.995	0.984	0.989	1.215	2.652	–1.884	–2.369	9.878	9.394	14.93	–0.591	–0.743	3.098	2.946	4.684
2500	0.5	1.011	1.016	1.004	0.961	0.338	0.528	1.363	9.671	10.51	35.34	0.026	0.067	0.473	0.513	1.727
	1	1.006	1.014	1.008	0.986	1.343	1.315	1.851	12.54	13.07	20.77	0.206	0.289	1.959	2.043	3.246
	1.5	1.004	1.017	1.013	1.037	3.139	2.118	2.506	13.87	14.25	17.80	0.729	0.862	4.770	4.904	6.124
	2	1.003	1.021	1.018	1.119	5.857	2.958	3.271	14.90	15.21	17.25	1.840	2.035	9.271	9.465	10.73
	–0.5	0.988	0.984	0.996	0.976	0.286	–0.464	–1.349	8.508	7.623	37.95	–0.020	–0.058	0.368	0.330	1.642
	–1	0.993	0.986	0.993	1.010	1.079	–1.146	–1.746	10.05	9.451	20.02	–0.152	–0.231	1.329	1.250	2.647
	–1.5	0.995	0.985	0.990	1.058	2.331	–1.769	–2.219	9.982	9.531	15.00	–0.487	–0.611	2.748	2.624	4.130
	–2	0.996	0.983	0.987	1.120	3.991	–2.351	–2.721	9.608	9.238	12.73	–1.101	–1.274	4.498	4.325	5.960
3000	0.25	1.016	1.018	1.002	0.844	0.131	0.246	1.127	7.195	8.076	51.14	0.006	0.028	0.181	0.203	1.283
	0.5	1.009	1.014	1.005	0.855	0.484	0.704	1.395	10.79	11.48	28.40	0.045	0.088	0.683	0.727	1.799
	1	1.005	1.015	1.010	0.908	1.971	1.649	2.070	13.22	13.64	18.58	0.365	0.458	2.924	3.018	4.110
	1.5	1.003	1.019	1.016	1.014	4.670	2.628	2.944	14.53	14.85	17.18	1.316	1.474	7.275	7.434	8.599
	–0.25	0.983	0.980	0.998	0.852	0.104	–0.194	–1.086	6.213	5.321	57.10	–0.004	–0.024	0.136	0.116	1.248
	–0.5	0.991	0.986	0.996	0.868	0.395	–0.611	–1.362	9.303	8.552	30.25	–0.033	–0.074	0.504	0.463	1.637
	–1	0.995	0.987	0.992	0.923	1.512	–1.403	–1.883	10.15	9.670	16.83	–0.253	–0.340	1.831	1.744	3.036
	–1.5	0.996	0.984	0.988	1.003	3.262	–2.122	–2.488	9.797	9.430	13.22	–0.811	–0.951	3.744	3.604	5.054
4000	0.25	1.010	1.014	1.003	0.699	0.230	0.430	1.157	9.386	10.11	36.17	0.015	0.039	0.320	0.344	1.232
	0.5	1.006	1.012	1.007	0.733	0.880	1.052	1.539	12.14	12.63	21.34	0.110	0.160	1.264	1.315	2.221
	0.75	1.004	1.014	1.010	0.798	2.007	1.677	2.047	13.33	13.70	17.99	0.375	0.458	2.981	3.063	4.022
	1	1.003	1.017	1.014	0.896	3.675	2.320	2.634	14.19	14.50	17.13	0.922	1.047	5.638	5.762	6.807
	–0.25	0.988	0.985	0.997	0.704	0.165	–0.329	–1.115	7.976	7.190	42.18	–0.009	–0.030	0.214	0.193	1.134
	–0.5	0.994	0.988	0.994	0.739	0.667	–0.886	–1.436	10.08	9.528	21.70	–0.074	–0.119	0.837	0.791	1.802
	–0.75	0.996	0.987	0.992	0.792	1.479	–1.399	–1.820	10.23	9.807	16.13	–0.245	–0.319	1.793	1.719	2.828
	–1	0.996	0.986	0.989	0.863	2.573	–1.882	–2.236	9.993	9.639	13.73	–0.567	–0.673	3.010	2.904	4.136

- due to taking into account the mentioned increment ΔI_{1y}, the accuracy of determining the module $I_{1\Sigma}$ of the stator current in the motor mode of the f-r IM (in comparison with the module I_1 of the stator current, in which this increment is not taken into account) increases, according to the relations $I_{1\Sigma}/I_1$, by (0.2 – 11.3) %, where the largest values of these relations refer to low speeds and increased values of the useful torque T, and smaller values to increased speeds and reduced values of this torque T;

- according to the calculated values of the relationships $I_s/I_{1\Sigma}$, as a result of taking into account the mentioned increment ΔI_{sy}, the accuracy of the calculation of the module I_s of the generalized vector of the stator current $\boldsymbol{I}_s$ in the motor mode of the f-r IM increases by (0.3 – 2.1) %;

- in the motor mode, in the first speed zone, the value of increment $\Delta I_s/I_{sn}$ of the active projection of the stator current of the f-r IM increases with an increase in speed n, and in the second zone, on the contrary, they decrease;

- the relative errors $\Delta P_{\delta 3}/\Delta P^*_{em}$, $\Delta P_{\delta 4}/\Delta P^*_{em}$ and $\Delta P_{\delta 5}/\Delta P^*_{em}$ always have only positive values which indicates the underestimated values of MEPL from (26) – (28): $\Delta P_{em.3}<\Delta P^*_{em}$, $\Delta P_{em.4}<\Delta P^*_{em}$ i $\Delta P_{em.5}<\Delta P^*_{em}$ – in comparison with their refined value ΔP^*_{em};

- at the same speed and equal (in absolute value) values of the useful torque of the motor, the lowest values in absolute value among all considered types of errors are inherent, according to Table 4, 5, relative errors $\Delta P_{\delta 1}/\Delta P^*_{em}$ and $\Delta P_{\delta 2}/\Delta P^*_{em}$ (the algebraic signs of which are positive in motor mode and negative in generator mode); as a result of the latter, in the generator mode, the values of the calculated power losses $\Delta P_{em.1}$ and $\Delta P_{em.2}$ exceed the refined values of ΔP^*_{em} MEPL calculated from (23);

- in the first and second speed zones in motor and generator modes, the absolute value of all relative errors: $\Delta P_{\delta 1}/\Delta P^*_{em}$, $\Delta P_{\delta 2}/\Delta P^*_{em}$, $\Delta P_{\delta 3}/\Delta P^*_{em}$, $\Delta P_{\delta 4}/\Delta P^*_{em}$, $\Delta P_{\delta 5}/\Delta P^*_{em}$ – with a decrease in speed and an increase (by absolute value) of the useful torque, of the f-r IM increases, which is caused by the influence of the electrical loss component, which is due to the transportation of additional power losses through motor air gap.

We note that (despite the obtained identical type of calculation dependencies for electromagnetic processes and energy parameters of the real f-r IM mode in relation to the motor and generator modes of its operation) with the same absolute value, but with the opposite algebraic sign of the values of the useful torque T, it is observed (according to the calculated data from Tables 2 – 5) the difference in motor and generator operating modes in the calculated values: module I_s of the stator current, electromagnetic torque $|T_{em}|$, refined MEPL ΔP^*_{em}, calculation errors $\Delta P_{\delta 1}$, $\Delta P_{\delta 2}$, $\Delta P_{\delta 3}$,

$\Delta P_{\delta 4}$, $\Delta P_{\delta 5}$ and other motor mode parameters. This is explained by the fact that: firstly, in the motor mode, the directions of action of the useful torque T and the mechanical losses of the torque ΔT_{mech} are opposite to each other (and in the generator mode, they coincide); secondly, in the motor mode, the algebraic sign of the component of the active projection I I_{1y} of the generalized stator current vector coincides with the signs of the increments ΔI_{1y}, ΔI_{sy} of the stator current caused by the transportation of additional and magnetic power losses (while in the generator mode, the algebraic sign of the projection I_{1y} is opposite to the signs of the specified increments ΔI_{1y} and ΔI_{sy}).

The results of the research carried out in the article are recommended to scientists and engineers who are engaged in the research of electromagnetic and energy processes of the f-r IMs and the design of energy-efficient control (which ensures the minimization of electromagnetic power losses or consumed active electric power) for these motors.

Conclusions. Analytical calculation dependencies are obtained to determine the increments of the active projection of the generalized stator current vector of the frequency-regulated induction motor, caused by the transportation of additional and magnetic power losses through the air gap or to the magnetization circuit of the motor, respectively. With the use of these dependencies, refined calculations of the main electromagnetic power losses, the main consumed active power, the efficiency and the power factor of the mentioned motor in steady-state motor and generator modes were performed.

Conflict of interest. The authors declare no conflict of interest.

REFERENCES

1. Kovacs K.P., Racz I. *Transiente vorgange in wechselstrommaschinen.* Budapest, Verlag der ungarischen akademie der wissenschaften, 1959. 514 p. (Ger).

2. Leonhard W. *Control of Electrical Drives.* Springer Berlin, Heidelberg, 2001. 460 p. doi: https://doi.org/10.1007/978-3-642-56649-3.

3. Bose B.K. *Modern power electronics and AC drives.* New Jersey, Prentice Hall RTR, 2002. 711 p.

4. Say M.G. *Alternating current machines. Fourth Edition.* Edinburgh, Heriot-Watt University, a Pitman international text. 1976. 543 p.

5. Pyrhonen J., Jokinen T., Hrabovcoca V. *Design of rotating electrical machines.* John Wiley & Sons, Ltd. 2008. 512 p.

6. Kothari D.P., Nagrath I.J. *Electric Machines. Fourth Edition.* New Delhi, Tata McGraw Hill Education Private Limited, 2010. 759 p.

7. Sahdev S.K. *Electrical machines.* Cambridge University Press, 2018. 954 p.

8. Kirschen D.S., Novotny D.W., Suwanwisoot W. Minimizing Induction Motor Losses by Excitation Control in Variable Frequency Drives. *IEEE Transactions on Industry Applications*, 1984, vol. IA-20, no. 5, pp. 1244-1250. doi: https://doi.org/10.1109/TIA.1984.4504590.

9. Aswathy M.S, Beevi M.W. High performance induction motor drive in field weakening region. *2015 International Conference on Control Communication & Computing India (ICCC)*, 2015, pp. 242-247. doi: https://doi.org/10.1109/ICCC.2015.7432899.

10. Volkov V.A. Energy-saving tachograms of acceleration (deceleration) of a frequency-regulated asynchronous engine. *Naukovyi Visnyk Natsionalnoho Hirnychoho Universytetu*, 2019, no. 4, pp. 55-62. doi: https://doi.org/10.29202/nvngu/2019-4/11.

11. Volkov V. Minimization of electrical consumption of a frequency-regulation induction motor with a fan load in start-braking regimes. *Electromechanical and Energy Saving Systems*, 2021, vol. 4, no. 56, pp. 8-24. doi: https://doi.org/10.30929/2072-2052.2021.4.56.8-24.

12. Ostashevsky M.O. *Electric machines and transformers.* Kyiv, Caravela Publ., 2018. 452 p. (Ukr).

13. Hrabko V.V., Rozvodyuk M.P., Levytskyi S.M., Kazak M.O. *Experimental studies of electric machines. Part III. Induction machines.* Vinnytsia, VNTU Publ., 2007. 197 p. (Ukr).

14. Schwarz K.K. Survey of basic stray losses in squirrel-cage induction motors. *Proceedings of the Institution of Electrical Engineers*, 1964, vol. 111, no. 9, pp. 1565-1574. doi: https://doi.org/10.1049/piee.1964.0258.

15. Agamloh E.B. An Evaluation of Induction Machine Stray Load Loss From Collated Test Results. *IEEE Transactions on Industry Applications*, 2010, vol. 46, no. 6, pp. 2311-2318. doi: https://doi.org/10.1109/TIA.2010.2070474.

16. Boglietti A., Cavagnino A., Lazzari M., Pastorelli M. International Standards for the Induction Motor Efficiency Evaluation: A Critical Analysis of the Stray-Load Loss Determination. *IEEE Transactions on Industry Applications*, 2004, vol. 40, no. 5, pp. 1294-1301. doi: https://doi.org/10.1109/TIA.2004.834034.

Received 11.02.2024
Accepted 25.05.2024
Published 20.08.2024

V.A. Volkov[1]*, PhD, Associate Professor,*
N.L. Antonov[1]*, PhD, Dean of Electrical Engineering Faculty,*
[1] National University «Zaporizhzhia Polytechnic»,
64, Zhykovskii Str., Zaporizhzhia, 69063, Ukraine,
e-mail: green_stone@ukr.net (Corresponding Author);
nickanto@zp.edu.ua

How to cite this article:
Volkov V.A., Antonov N.L. Refined calculation of energy modes of a frequency-regulated induction motor. *Electrical Engineering & Electromechanics*, 2024, no. 5, pp. 3-13. doi: https://doi.org/10.20998/2074-272X.2024.5.01

UDC 621.3.013 https://doi.org/10.20998/2074-272X.2024.5.02

B. Nemouchi, S.E. Rezgui, H. Benalla, K. Nebti

Fractional-based iterative learning-optimal model predictive control of speed induction motor regulation for electric vehicles application

Introduction. *A new control strategy based on the combination of optimal model predictive control (OMPC) with fractional iterative learning control (F-ILC) for speed regulation of an induction motor (IM) for electric vehicles (EVs) application is presented. OMPC uses predictive models to optimize speed control actions by considering the dynamic behavior of the IM, when integrated with the F-ILC, the system learns and refines the speed control iteratively based on previous iterations, adapting to the specific characteristics of the IM and improving performance over time. The synergy between OMPC and F-ILC named F-ILC-OMPC enhances the precision and adaptability of speed control for IMs in EVs application, and optimizes the energy efficiency and responsiveness under varying driving conditions.* ***The novelty*** *lies in the conjunction of the OMPC with the ILC-based on the fractional calculus to regulate the speed of IMs, which is original.* ***Purpose.*** *The new control strategy provides increased performance, robustness and adaptability to changing operational conditions.* ***Methods.*** *The mathematical development of a control law that mitigates the disturbance and achieves accurate and efficient speed regulation. The effectiveness of the suggested control strategy was assessed via simulations in MATLAB conducted on an IM system.* ***Results.*** *The results clearly show the benefits of the F-ILC-OMPC methodology in attaining accurate speed control, minimizing steady-state error and enhanced disturbance rejection.* ***Practical value.*** *The main perspective lies in the development of a speed control strategy for IMs for EVs and the establishment of reliable and efficient electrical systems using ILC-OMPC control. This research has the prospect of a subsequent implementation of these results in experimental prototypes.* References 24, tables 2, figures 9.

Key words: **optimal model predictive control, iterative learning control, induction motor, speed control, electric vehicles.**

Вступ. *Представлено нову стратегію керування, яка базується на поєднанні прогнозного керування оптимальною моделлю (OMPC) з дробовим ітеративним навчальним керуванням (F-ILC) для регулювання швидкості асинхронного двигуна (АД) для застосування в електромобілях. OMPC використовує прогнозні моделі для оптимізації дій керування швидкістю, враховуючи динамічну поведінку АД. При інтеграції з ILC на основі дробів система вивчає та вдосконалює керування швидкістю ітеративно на основі попередніх ітерацій, адаптуючись до конкретних характеристик АД та підвищення продуктивності з часом. Синергія між OMPC і F-ILC під назвою F-ILC-OMPC підвищує точність і адаптивність регулювання швидкості для АД в електромобілях, а також оптимізує енергоефективність і чутливість за різних умов руху.* ***Новизна*** *полягає в поєднанні OMPC з ILC на основі дробового числення для регулювання швидкості АД, що є оригінальним.* ***Призначення.*** *Нова стратегія управління забезпечує підвищену продуктивність, надійність і адаптивність до мінливих умов експлуатації.* ***Методи.*** *Математичний розвиток закону керування, який пом'якшує збурення та досягає точного та ефективного регулювання швидкості. Ефективність запропонованої стратегії керування була оцінена за допомогою моделювання у MATLAB, проведеного на системі АД.* ***Результати.*** *Результати чітко показують переваги методології F-ILC-OMPC у досягненні точного контролю швидкості, мінімізації стаціонарної помилки та покращеного усунення перешкод.* ***Практична цінність.*** *Основна перспектива полягає в розробці стратегії регулювання швидкості АД для електромобілів і створення надійних і ефективних електричних систем з використанням керування ILC-OMPC. Дане дослідження має перспективу подальшого впровадження цих результатів в експериментальні прототипи.* Бібл. 24, табл. 2, рис. 9.

Ключові слова: **оптимальна модель прогнозного керування, ітераційне навчальне керування, асинхронний двигун, керування швидкістю, електромобілі.**

Abbreviations

DTC	Direct Torque Control	IM	Induction Motor
EV	Electric Vehicle	ILC	Iterative Learning Control
FCS-PTC	Finite Control Set-Predictive Torque Control	MPC	Model Predictive Control
F-ILC	Fractional Iterative Learning Control	OMPC	Optimal Model Predictive Control
IFOC	Indirect Field-Oriented Control	SVM	Space Vector Modulation

Introduction. EV is a vehicle that uses one or more electric motors for propulsion. In contrast to traditional vehicles that rely only on internal combustion drive fueled by gasoline or diesel, EVs include reduced greenhouse gas emissions, lower operating costs due to lower maintenance and electricity costs compared with gasoline, and the potential for using renewable energy sources to charge batteries.

Several types of electric motors are commonly employed in these vehicles. The choice of motor depends on factors such as vehicle type, performance requirements, and cost. IMs offer several advantages when used in EVs, contributing to their widespread adoption in the automotive industry. It has a simple and robust design, and the simplicity of the IMs results in lower maintenance requirements. In addition, IMs can operate at high efficiency levels and are self-starting, eliminating the need for additional starting mechanisms.

The motor's driver (traction inverter and controller) is a crucial component of an EV. It regulates the power supplied to the electric motor based on the driver's input and other factors. It can adjust the voltage and current to control the speed of the electric motor. Speed control is part of a larger vehicle control system that manages various aspects, including safety, stability, and efficiency. This overarching system integrates inputs from multiple sensors and subsystems to ensure a smooth and controlled driving experience.

There are many methods for controlling the speed of EVs that can be applied to a variety of electric motors. One can site some of them, like the PID controller which involves proportional, integral and derivative components to regulate the system. It helps in achieving the desired speed regulation of EV motors [1].

In [2], authors proposed a back-stepping control technique with SVM strategy for IM. A load torque observer was designed to enhance speed tracking, and system stability was studied using Lyapunov theory.

The authors [3] have used a model reference adaptive system observer to ensure the continuity of the drive of a permanent magnet synchronous motor and improve its reliability by eliminating the speed sensor. The performance and robustness of the system were tested using real driving scenarios.

Other researchers have used the zeta converters in improving the speed control of brushless DC motors for small EVs. The goal was to develop EVs that reduce emissions by utilizing renewable fuels. The study proposed the use of a PI controller assisted by a hysteresis current controller to regulate the motor's speed [4].

The paper [5] presented a new approach for estimating the speed of in-wheel EV with two independent rear drives. This study focused on the use of variable-speed IMs. The objective is to improve the dynamic performance of the control system using type-1 and type-2 fuzzy logic controllers in a model reference adaptive system.

The authors of [6] have developed and tested a DTC control for EVs for a six-phase motor with adaptive speed estimator, and extensive SVM.

Another DTC scheme with a predictive speed and flux control of an IM for an EV was used in [7], authors proposed also a sliding mode observer to accomplish a sensorless estimation technique in aim to achieve efficient torque control and higher efficiency. The design has included the implementation of the sliding mode observer, with stator currents transformation, and flux angle estimation.

The main work in [8] was the design of a speed-sensorless control based on finite control set-predictive torque control (FCS-PTC) in IM drive system. An adaptive fading-based extended Kalman filter observer was used to estimate the angular speed and the flux that are required for the FCS-PTC algorithm. The load torque is estimated to improve speed estimation performance, and it is used in the feed-forward control loop to enhance load disturbance rejection. It was shown that FCS-PTC offers advantages such as easy implementation, handling of nonlinearities, and inclusion of constraints.

The fractional PID controller is a type of control system that extends the traditional PID controller by introducing fractional-order calculus into the proportional, integral, and derivative terms [9]. This type of controller has attracted great interest from researchers thanks to its advantages.

In [10] the authors address the issue of torque ripples generated by a motor when using a PID controller, which can lead to increased noise in the system. They proposed a fractional-order-based PID control scheme that offers faster tracking and reduces the magnitude of torque ripples compared to traditional PID control. Authors of [11] have applied a new controller for EV speed control which was based on a fuzzy fractional-order PID algorithm and the Ant Colony Optimization technique for parameter's tuning was used. The controller's performance was evaluated using the new European driving cycle.

The goal of the paper is the design of a new strategy for speed control of an IM using a combination of OMPC and ILC. The objective is to achieve accurate and efficient speed regulation of the motor in EVs application. OMPC leverages predictive models to optimize speed control actions, it provides a real-time optimization approach that predicts future motor behavior and generates control signals accordingly. When combined with ILC, the system benefits from iterative learning, enabling it to refine speed control based on previous experiences, which enables the system to learn from previous iterations and improve performance over time. The ILC uses the error information from previous control cycles to update the control inputs and reduce tracking errors in subsequent iterations. The proposed control strategy was evaluated through simulations of an IM system. The results demonstrate the effectiveness of the OMPC–ILC approach in achieving precise speed control with reduced steady-state error and improved disturbance rejection compared with other control methods.

IM model and theory of the control. The powertrain of an EV is a system that propels the vehicle by converting electrical energy from the battery into mechanical energy for driving (Fig. 1). It typically consists of several key components that work together to achieve efficient and controlled vehicle movement [12, 13].

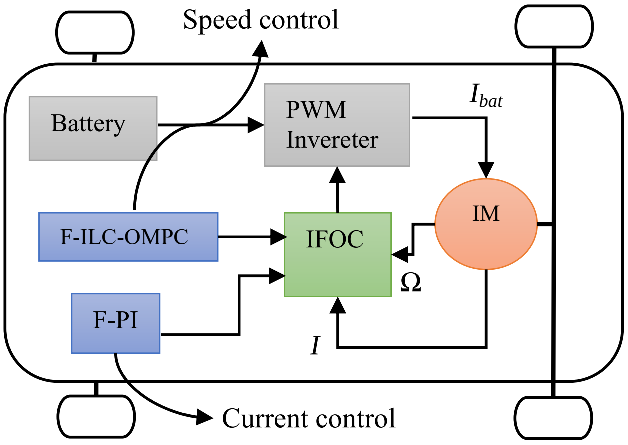

Fig. 1. EV powertrain

IM belongs to electric motors which are predominant in EVs, thanks to its simplicity, reliability, and robustness. The mathematical model of the motor's electric and mechanical dynamics is given by the equations (1)–(4) [14]:

$$\begin{cases} v_{ds} = R_s i_{ds} + \dfrac{\mathrm{d}\varphi_{ds}}{\mathrm{d}t} - \omega_e \varphi_{qs}; \\ v_{qs} = R_s i_{qs} + \dfrac{\mathrm{d}\varphi_{qs}}{\mathrm{d}t} - \omega_e \varphi_{ds}; \\ v_{dr} = R_r i_{dr} + \dfrac{\mathrm{d}\varphi_{dr}}{\mathrm{d}t} - (\omega_e - \omega_r)\varphi_{qs}; \\ v_{qr} = R_r i_{qr} + \dfrac{\mathrm{d}\varphi_{qr}}{\mathrm{d}t} + (\omega_e - \omega_r)\varphi_{qs}; \end{cases} \tag{1}$$

$$\begin{cases} \varphi_{ds} = L_s i_{ds} + L_m i_{dr}; \\ \varphi_{qs} = L_s i_{qs} + L_m i_{qr}; \\ \varphi_{dr} = L_r i_{dr} + L_m i_{ds}; \\ \varphi_{qr} = L_r i_{qr} + L_m i_{qs}; \end{cases} \tag{2}$$

$$J\frac{\mathrm{d}\Omega}{\mathrm{d}t} = T_{em} - T_L - f\,\Omega; \tag{3}$$

$$T_{em} = p\left(\varphi_{ds} i_{qs} - \varphi_{qs} i_{ds}\right), \tag{4}$$

where v_d, v_q, i_d, i_q, φ_d and φ_q are the dq components of the rotor (symbol «*r*») and stator (symbol «*s*») voltage, current and flux linkage, respectively; L_r, L_s, R_r, R_s are the rotor and stator self-inductances and resistances; p is the pairs number of poles; ω is the angular speed; L_m is the magnetizing inductance; J is the motor moment inertia; Ω is the speed; T_{em} is the motor torque; T_L is the load torque; f is the viscous friction coefficient

Indirect field-oriented control. Also known as vector control, it's a popular control strategy used in the field of electric motor control. The primary objective of IFOC is to control the stator currents of a three-phase AC IM in a manner that simplifies the control task. Speed control is achieved by regulating the torque-producing current based on the desired speed (Fig. 2).

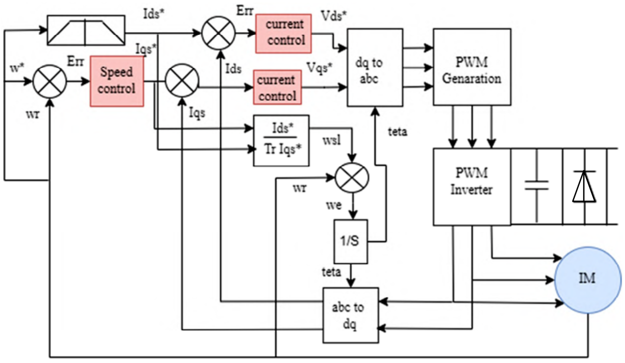

Fig. 2. Block diagram of control strategy IFOC

IFOC provides several advantages, including high dynamic performance, efficient torque control, and the ability to operate over a wide speed range. It is widely used in applications where precise control of motor performance is crucial, such as in EVs.

Iterative learning control. The control law within the framework of ILC is presented as the mathematical relationship or the algorithm that determines how to adjust control inputs at each iteration to reduce errors and enhance performance over time. The underlying objective of this control law is to assimilate insights derived from errors encountered in previous iterations and to make adjustments to control inputs for a more efficient convergence towards the desired performance. The PID-type ILC control law is given as follows [15, 16]:

$$U_{k+1}(t) = U_k(t) + K_p e_k(t) + K_i \int e_k(t)\mathrm{d}t + K_d \dot{e}_k(t), \tag{5}$$

where $U_k(t)$ is the control input at the current iteration; $U_{k+1}(t)$ is the control input at the next iteration; $e_k(t)$ is the error between the desired and actual outputs at the current iteration.

In (5), the control input for the next iteration $U_{k+1}(t)$ is modified based on the current control input $U_k(t)$ and the error $e_k(t)$ observed in the current iteration. This adjustment is scaled by the learning parameter (K_p, K_i and K_d) that determine the magnitude of the control input adjustment. It is worth highlighting that the actual structure of the control law may be more intricate and could encompass additional terms or considerations depending on the unique attributes of the system and the task at hand. The selection of the learning (K_p, K_i and K_d) is pivotal and may necessitate tuning to attain optimal performance in a specific application.

Optimal model predictive control. MPC is an advanced control strategy used in various industries to optimize the performance of dynamic systems. OMPC is an extension of MPC that emphasizes finding an optimal control policy while considering system constraints, dynamic models, and performance objectives [17, 18].

These models are used to predict the future behavior of the system based on current and past states and inputs.

The dual mode represents a control strategy that relies on predictions using two distinct modes. The first mode is applied when the system is distant from the steady state, while the second mode comes into play as the system approaches the desired operating point.

The control law can be elaborated as [17, 19]:

$$U_k = -KX_k + C_k \cdot K \le n_c; \tag{6}$$

$$U_k = -KX_k \cdot K > n_c, \tag{7}$$

where n_c is the control horizon; C_k is the perturbations; X_k is the state space model; K is the state feedback gain, it can be determined by using the MATLAB command [K] = dlqr (A, B, Q, R), where Q and R are the real symmetric matrices, semi-positive definite, and positive definite, respectively.

The cost function is expressed as:

$$J = X_k^T S_k X_k + C_{\to k}^T S_{cx} C_{\to k} + 2X_k^T S_{cx} C_{\to k}, \tag{8}$$

where S_k, S_c and S_{cx} are the parameters of the cost function after solving using a standard Lyapunov identity to form the predicted cost.

To ensure good performance and tracking of the reference r, we propose setting ($Y_k = r$), we added some terms (X_{ss}) and (U_{ss}) at each step k, that express the desired stable state as follows ($X_k = \widehat{X}_k + X_{ss}$) and ($U_k = \widehat{U}_k + U_{ss}$):

$$Y_k = CX_x; \tag{9}$$

$$X_{ss} = AX_x + BU_{ss}; \tag{10}$$

$$\begin{bmatrix} Y_{ss} \\ 0 \end{bmatrix} = \begin{bmatrix} C & 0 \\ A-I & B \end{bmatrix} \begin{bmatrix} X_{ss} \\ U_{ss} \end{bmatrix}; \tag{11}$$

$$\begin{bmatrix} X_{ss} \\ U_{ss} \end{bmatrix} = \begin{bmatrix} C & 0 \\ A-I & B \end{bmatrix}^{-1} \begin{bmatrix} r \\ 0 \end{bmatrix}. \tag{12}$$

We define:

$$\begin{bmatrix} X_{ss} \\ U_{ss} \end{bmatrix} = \begin{bmatrix} M_x \\ M_u \end{bmatrix} \begin{bmatrix} r \\ 0 \end{bmatrix}. \tag{13}$$

Therefore, we have:

$$X_{ss} = M_x \cdot r; \tag{14}$$

$$U_{ss} = M_u \cdot r. \tag{15}$$

By substituting X_{ss} and U_{ss} into (6):

$$U_k - U_{ss} = -K(X_k - X_{ss}) + C_k; \tag{16}$$

$$U_k = -KX_k - K\,M_x \cdot r + M_u \cdot r + C_k. \tag{17}$$

So:

$$U_k = -KX_k + (K\,M_x - M_u) \cdot r + C_k, \tag{18}$$

where A, B, and C are the matrices that define the system dynamics and relationships between state, input, and output:

$$\begin{cases} \dot{X} = AX + BU; \\ Y = CX + DU, \end{cases} \qquad (19)$$

where X is the state vector of dimension n; U is the system input (or control) of dimension m; Y is the system output of dimension r; A is the state matrix (or evolution matrix) dim $[A(.)] = n \times n$; B is the input matrix dim $[B\,(.)] = n \times m$; C is the output matrix (or observation matrix) dim $[C\,(.)] = r \times n$; D is the feed forward matrix dim $[D\,(.)] = r \times m$.

Design of the combination of F-ILC and OMPC (F-ILC-OPMC). Now we will elaborate the proposed control strategy for the speed control of an IM using the proposed combination of OMPC and iterative learning control.

From the OMPC we substitute the control law formulation of U_k determined in (15) into the ILC (5); so one can find the new ILC control law as follows:

$$U_{k+1}(t) = \alpha + \beta\,, \qquad (20)$$

where:

$$\alpha = \left[-KX_k + \left(KM_x - M_u\right)\cdot r + C_k\right]; \qquad (21)$$

$$\beta = K_p e_k(t) + K_i \int e_k(t)\mathrm{d}t + K_d \dot{e}_k(t). \qquad (22)$$

The second term of (20) named β constitutes the PID-type ILC as defined in its original form in (5). In our case, we propose a fractional order controller which is FOP ID-type of ILC as it is illustrated in Fig. 3.

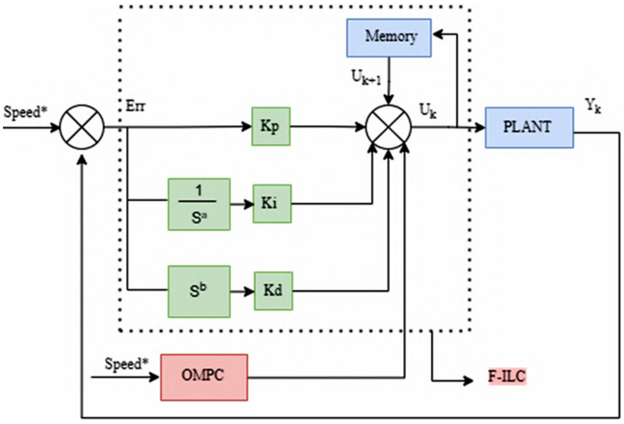

Fig. 3. Block diagram of the fractional control law F-ILC-OMPC

In standard PID controllers, the order of the terms is restricted to integer values (1 for proportional, integral, and derivative). However, fractional-order PID controllers allow the use of fractional orders, which allow additional degrees of freedom for tuning and optimizing control systems [20].

In addition, the use of fractional orders allows more flexibility in shaping the frequency response and adapting the controller to specific system dynamics. For this purpose, we use it in the ILC law control:

$$\beta = \left[K_p + \frac{K_i}{s^{\lambda}} + K_d s^{\gamma}\right] e_k(t), \qquad (23)$$

where λ, γ are the fractional orders for the integral and derivative terms, respectively; s is the Laplace variable.

The full controller is depicted in Fig. 3.

Simulation and analysis. The regulation of the IM's speed relies on the subsequent closed-loop equations:

$$G(s) = \frac{1}{Js + f}\,; \qquad (24)$$

$$H(s) = \frac{G}{G+1}\,, \qquad (25)$$

where H is the closed-loop speed; G is the open loop speed transfer function.

In a state-space representation, a dynamic system is described by a set of first-order differential or difference equations, so that H is transformed in state-space and we use A, B, and C to determine the control law.

The F-ILC-OMPC is injected in the speed loop of the IFOC (Fig. 4). The IM parameters are reported in Table 1 [21].

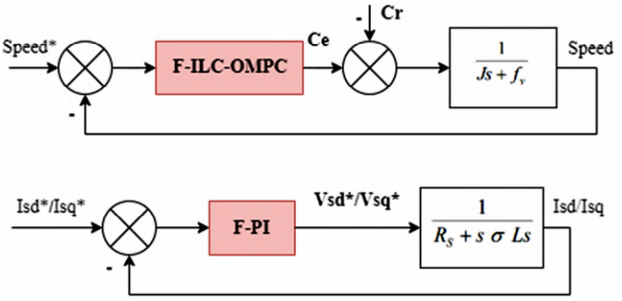

Fig. 4. Control loop of speed with F-ILC-OMPC and current with F-PI

Table 1

IM's parameters

Rated shaft power P_n, kW	3
Line-to-line voltage V_n, V	220 / 380
Rated speed N_n, rpm	1500
Pairs number of poles	2
Stator self-inductance L_s, mH	261
Rotor self-inductance L_r, mH	261
Magnetizing inductance L_m, mH	249
Stator resistance R_s, Ω	2.3
Rotor resistance R_r, Ω	1.55
Machine inertia J, kg·m^2	0.0076
Viscous friction coefficient f, kg·m^2/s	0.0007

Performance assessment is conducted using MATLAB simulations to illustrate the responses of the rotor speed, electromagnetic torque and stator phase current under the F-ILC-OMPC controller.

The system's speed tracking response is examined under the conditions of a multi-step speed references with [400, 900, 1500, –1500] rpm at [0 s, 0.5 s, 1 s, 1.5 s]. A load torque of 7 N·m disturbs the system at time 0.7 s.

Figures 5, 6 show the pursuing curve of the actual speed compared to its reference, in addition, the stability of the system is tested when it's disturbed by the application of the resisting torque. With this scenario, it's clear that the system ensures a stable and efficient tracking performance since the rise time is about 0.0243 s and with an overshoot about only 0.33 %.

The behavior of the electromagnetic torque is shown in Fig. 7. This curve shows a fast dynamic response during the regulation process, the goal is typically to ensure that the motor operates at the desired torque level (7 N·m), and maintaining stability and efficiency.

The direct and quadratic components of the stator currents of the IM (Fig. 8) refers to the controlled or adjusted current flowing through the stator windings of the motor during the test scenario. A simple two F-PI regulators was sufficient to achieve the desired stator currents regulation and no sharp peaks was induced (Fig. 9).

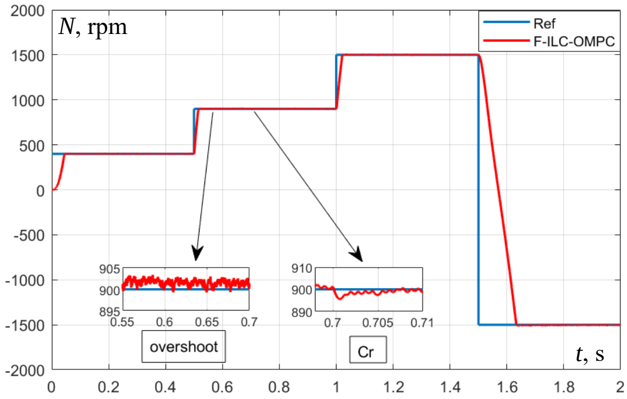

Fig. 5. Speed response of IM with F-ILC-OMPC controller

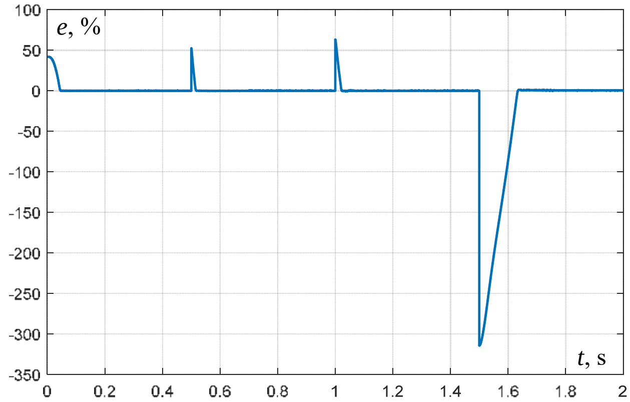

Fig. 6. Error between the actual speed and the reference

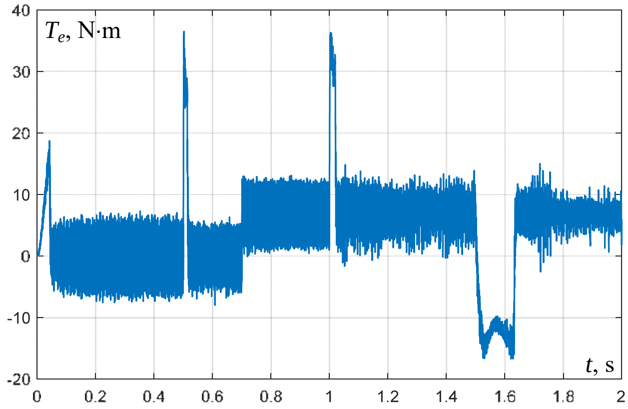

Fig. 7. Electromagnetic torque response

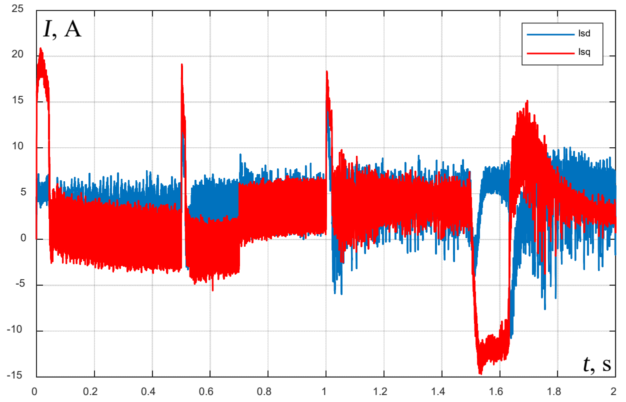

Fig. 8. Currents I_{sq}, I_{sd} of IM with ILC-OMPC controller

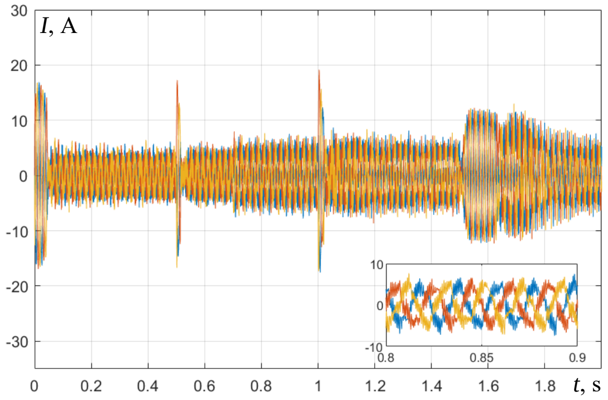

Fig. 9. Three phase stator currents of IM

The results obtained using our proposed method is juxtaposed with other references in Table 2. Various controllers were used for the control of electrical machines, and we have endeavored to make the comparison as fair as possible.

Table 2

Comparison with other references

Controller	Rise time, s	Overshoot, %	Settling time, s	Disturbance rejection time, s	Ref.
DTC-slide mode NPC	0.9	10	2	–	[7]
MFPCC	0.7	6	2	1	[22]
ASMC-MPTC	0.25	–	0.3	0.4	[23]
FPIM-OESW	0.38	2	0.5	–	[24]
F-ILC-OMPC	0.0243	0.33	0.048	0.071	Proposed method

Conclusions. The proposed F-ILC-OMPC approach was evaluated through simulations using an IM. The results demonstrated that the combination of F-ILC and OMPC yields higher speed control performance compared with other control methods. It achieves faster response times, better tracking accuracy and improved disturbance rejection. As expected, OMPC with F-ILC strategy offers an effective solution for the speed control of IMs and can be exploited in EVs application. It leverages predictive modeling, real-time optimization, and iterative learning to achieve precise and efficient speed regulation in the electrical motored system.

In summary, the combination of OMPC and F-ILC offers a promising approach for speed control of IMs, providing enhanced performance, robustness, and adaptability to varying operating conditions.

Conflict of interest. The authors declare that they have no conflicts of interest.

REFERENCES

1. Zhu Q. Speed regulation of electric vehicle motor based on PID control. *Theoretical and Natural Science*, 2023, vol. 9, no. 1, pp. 91-99. doi: https://doi.org/10.54254/2753-8818/9/20240723.

2. Bacha S., Saadi R., Ayad M.Y., Sahraoui M., Laadjal K., Cardoso A.J.M. Autonomous Electric-Vehicle Control Using Speed Planning Algorithm and Back-Stepping Approach. *Energies*, 2023, vol. 16, no. 5, art. no. 2459. doi: https://doi.org/10.3390/en16052459.

3. Bendjedia B., Chouireb S. MRAS based speed sensorless control of PMSM Drive for urban electric vehicle. *Romanian*

Journal of Information Technology and Automatic Control, 2023, vol. 33, no. 3, pp. 29-42. doi: https://doi.org/10.33436/v33i3y202303.

4. Hafidh M.Y., Wibawa U., Nurwati T., Wakama E.T. Enhancing Speed Control of BLDC Motors Using Zeta Converter for Small Electric Vehicles. *Jurnal EECCIS (Electrics, Electronics, Communications, Controls, Informatics, Systems)*, 2023, vol. 17, no. 1, pp. 27-33. doi: https://doi.org/10.21776/jeeccis.v17i1.1648.

5. Khemis A., Boutabba T., Drid S. Model reference adaptive system speed estimator based on type-1 and type-2 fuzzy logic sensorless control of electrical vehicle with electrical differential. *Electrical Engineering & Electromechanics*, 2023, no. 4, pp. 19-25. doi: https://doi.org/10.20998/2074-272X.2023.4.03.

6. Listwan J., Oleszczyszyn P. Analysis of the Drive of the Electric Vehicle with Six-Phase Induction Motor. *Power Electronics and Drives*, 2023, vol. 8, no. 1, pp. 252-274. doi: https://doi.org/10.2478/pead-2023-0017.

7. Priya S., Kumar P.V., Karthikeyan, Subramaniyam S. Predictive Speed And Flux Control Based Sensorless Sliding Mode Observer For Induction Motor Used In Electric Vehicle. *International Journal of Aquatic Science*, 2021, vol. 12, no. 3, pp. 431-440.

8. Zerdali E., Demir R. Speed-sensorless predictive torque controlled induction motor drive with feed-forward control of load torque for electric vehicle applications. *Turkish Journal of Electrical Engineering & Computer Sciences*, 2021, vol. 29, no. 1, pp. 223-240. doi: https://doi.org/10.3906/elk-2005-75.

9. Leonenko N., Podlubny I. Monte Carlo method for fractional-order differentiation. *Fractional Calculus and Applied Analysis*, 2022, vol. 25, no. 2, pp. 346-361. doi: https://doi.org/10.1007/s13540-022-00017-3.

10. Nosheen T., Ali A., Chaudhry M.U., Nazarenko D., Shaikh I. ul H., Bolshev V., Iqbal M.M., Khalid S., Panchenko V. A Fractional Order Controller for Sensorless Speed Control of an Induction Motor. *Energies*, 2023, vol. 16, no. 4, art. no. 1901. doi: https://doi.org/10.3390/en16041901.

11. George M.A., Kamat D.V., Kurian C.P. Electronically Tunable ACO Based Fuzzy FOPID Controller for Effective Speed Control of Electric Vehicle. *IEEE Access*, 2021, vol. 9, pp. 73392-73412. doi: https://doi.org/10.1109/ACCESS.2021.3080086.

12. Guizani M.A. *Approche multi-agents pour la conception optimale des systemes mecatroniques.* These de Doctorat de l'Universite de SFAX et de l'Universite Paris-Saclay, 2016. 162 p. (Fra).

13. Ibrar A., Ahmad S., Safdar A., Haroon N. Efficiency enhancement strategy implementation in hybrid electric vehicles using sliding mode control. *Electrical Engineering & Electromechanics*, 2023, no. 1, pp. 10-19. doi: https://doi.org/10.20998/2074-272X.2023.1.02.

14. Guezi A., Bendaikha A., Dendouga A. Direct torque control based on second order sliding mode controller for three-level inverter-fed permanent magnet synchronous motor: comparative study. *Electrical Engineering & Electromechanics*, 2022, no. 5, pp. 10-13. doi: https://doi.org/10.20998/2074-272X.2022.5.02.

15. Khurram A., Rehman H., Mukhopadhyay S., Ali D. Comparative analysis of integer-order and fractional-order proportional integral speed controllers for induction motor drive systems. *Journal of Power Electronics*, 2018, vol. 18, no. 3, pp. 723-735. doi: https://doi.org/10.6113/JPE.2018.18.3.723.

16. Riaz S., Qi R., Tutsoy O., Iqbal J. A novel adaptive PD-type iterative learning control of the PMSM servo system with the friction uncertainty in low speeds. *PLOS ONE*, 2023, vol. 18, no. 1, art. no. e0279253. doi: https://doi.org/10.1371/journal.pone.0279253.

17. Watson M.T., Gladwin D.T., Prescott T.J., Conran S.O. Dual-Mode Model Predictive Control of an Omnidirectional Wheeled Inverted Pendulum. *IEEE/ASME Transactions on Mechatronics*, 2019, vol. 24, no. 6, pp. 2964-2975. doi: https://doi.org/10.1109/TMECH.2019.2943708.

18. Rossiter J.A. *A First Course in Predictive Control. 2nd Edition.* CRC Press, 2018. 426 p. doi: https://doi.org/10.1201/9781315104126.

19. Darwish S., Pertew A., Elhaweet W., Mokhtar A. Advanced Boiler Control System for Steam Power Plants Using Modern Control Techniques. *2019 IEEE 28th International Symposium on Industrial Electronics (ISIE)*, 2019, pp. 461-466. doi: https://doi.org/10.1109/ISIE.2019.8781481.

20. Saleem A., Soliman H., Al-Ratrout S., Mesbah M. Design of a fractional order PID controller with application to an induction motor drive. *Turkish Journal of Electrical Engineering & Computer Sciences*, 2018, vol. 26, no. 5, pp. 2768-2778. doi: https://doi.org/10.3906/elk-1712-183.

21. Kraiem H., Flah A., Hamed M.B., Sbita L. High performances induction motor drive based on fuzzy logic control. *International Journal of Control and Automation*, 2012, vol. 5, no. 1, pp. 1-12.

22. Hussain M.A., Hati A.S., Chakrabarti P., Hung B.T., Bolshev V., Panchenko V. DSVM-Based Model-Free Predictive Current Control of an Induction Motor. *Energies*, 2023, vol. 16, no. 15, art. no. 5657. doi: https://doi.org/10.3390/en16155657.

23. Zhang Y., Yin Z., Li W., Liu J., Zhang Y. Adaptive Sliding-Mode-Based Speed Control in Finite Control Set Model Predictive Torque Control for Induction Motors. *IEEE Transactions on Power Electronics*, 2021, vol. 36, no. 7, pp. 8076-8087. doi: https://doi.org/10.1109/TPEL.2020.3042181.

24. Saad K., Abdellah K., Ahmed H., Iqbal A. Investigation on SVM-Backstepping sensorless control of five-phase open-end winding induction motor based on model reference adaptive system and parameter estimation. *Engineering Science and Technology, an International Journal*, 2019, vol. 22, no. 4, pp. 1013-1026. doi: https://doi.org/10.1016/j.jestch.2019.02.008.

Received 26.02.2024
Accepted 18.04.2024
Published 20.08.2024

B. Nemouchi[1], *PhD Student,*
S.E. Rezgui[1], *PhD, Associate Professor,*
H. Benalla[1], *Professor,*
K. Nebti[1], *PhD, Associate Professor,*
[1] Laboratory of Electrical Engineering of Constantine (LEC),
Technology Sciences Faculty,
University Freres Mentouri Constantine 1, Algeria,
e-mail: besma.nemmouchi@doc.umc.edu.dz (Corresponding Author);
rezgui.salaheddine@umc.edu.dz; benalla.hocine@umc.edu.dz;
idor2003@yahoo.fr

How to cite this article:

Nemouchi B., Rezgui S.E., Benalla H., Nebti K. Fractional-based iterative learning-optimal model predictive control of speed induction motor regulation for electric vehicles application. *Electrical Engineering & Electromechanics*, 2024, no. 5, pp. 14-19. doi: https://doi.org/10.20998/2074-272X.2024.5.02

UDC 621.314 https://doi.org/10.20998/2074-272X.2024.5.03

H. Bounechba, A. Boussaid, A. Bouzid

Experimental validation of fuzzy logic controller based on voltage perturbation algorithm in battery storage photovoltaic system

Introduction. *Solar photovoltaic (PV) has recently become very important especially in electrical power applications for countries with high luminosity because it is an effectively unlimited available energy resource. Depending on solar radiation and temperature, the PV generator has a non-linear characteristic with a maximum power point (MPP).* ***The novelty*** *is the efficiency improvement of a PV energy module, it is necessary to track the MPP of the PV array regardless of temperature or irradiation circumstances.* ***Purpose.*** *This paper presents the modeling and the digitally simulation under MATLAB/Simulink of a Fuzzy Logic Controller based on Voltage Perturbation Algorithm (FLC-VPA) applied to PV battery charging system, which consists of PV module, DC-DC boost converter, MPP tracking (MPPT) unit and battery storage.* ***Methods.*** *The DSP1104 is then used to experimentally implement this MPPT algorithm for real-time driving.* ***The obtained results*** *show the high precision of the proposed FLC-VPA MPPT around the optimal point compared to the conventional VPA under stable and changing meteorological conditions.* ***Practical value.*** *The experimental results approve the effectiveness and validity of the proposed total control system in the PV system.* References 30, tables 3, figures 17.

Key words: **maximum power point, fuzzy logic controller based on voltage perturbation algorithm, battery, boost converter.**

Вступ. *Сонячна фотоелектрична (PV) енергія останнім часом стала дуже важливою, особливо в електроенергетиці в країнах з високим сонячним освітленням, оскільки вона є фактично необмеженим доступним енергетичним ресурсом. Залежно від сонячного випромінювання та температури, PV генератор має нелінійну характеристику з точкою максимальної потужності (MPP).* ***Новизною*** *є підвищення ефективності PV енергетичного модуля, що необхідно відстежувати MPP PV батареї незалежно від температури або умов опромінення.* ***Мета.*** *У цій статті представлено моделювання та цифрове моделювання в рамках MATLAB/Simulink контролера нечіткої логіки на основі алгоритму збурення напруги (FLC-VPA), що застосовується до системи зарядки PV батарей, яка складається з PV модуля, DC-DC підвищувального перетворювача, системи MPP (MPPT) та акумуляторної батареї.* ***Методи.*** *DSP1104 використовується для експериментальної реалізації цього MPPT алгоритму для режиму реального часу.* ***Отримані результати*** *показують високу точність пропонованого FLC-VPA MPPT біля оптимальної точки порівняно з традиційним VPA у стабільних та мінливих метеорологічних умовах.* ***Практична цінність.*** *Результати експериментів підтверджують ефективність та обґрунтованість запропонованої системи контролю у PV системі.* Бібл. 30, табл. 3, рис. 17.

Ключові слова: **точка максимальної потужності, контролер нечіткої логіки на основі алгоритму збурення напруги, акумулятор, підвищувальний перетворювач.**

Abbreviations

ANN	Artificial Neural Network	MPPT	Maximum Power Point Tracking
FOCV	Fractional Open-Circuit Voltage	P&O	Perturb and Observe
FSCC	Fractional Short-Circuit Current	PV	Photovoltaic
FLC-VPA	Fuzzy Logic Controller based on Voltage Perturbation Algorithm	PWM	Pulse Width Modulated
FLC	Fuzzy Logic Controller	STC	Standard Test Conditions
INC	Incremental Conductivity	VPA	Voltage Perturbation Algorithm
MPP	Maximum Power Point		

Introduction. Renewable energies are an effective solution to eliminating greenhouse gas emissions. Among the promising resources of production (wind, hydro and so on), PV cells have become very important as they are one of the most suitable and successful renewable sources in the production of electricity due to its advantages such as no fuel cost, and no noise; and because the solar cell is a semiconductor device, it needs very little maintenance and so on.

The PV module directly converts solar energy into electricity. The output value of these PV modules varies according to environmental conditions such as radiation and the temperature (Fig 1). The solar modules have distinctive characteristics, including that the maximum value of the available energy is available only in one operating point that has a specific voltage and current, called the MPP, whose position changes as a function of radiation and temperature of the solar module so that the used load (Fig. 2).

The major drawback of PV systems is the relatively expensive cost of this kind of energy. To get rid of this problem, we must make the solar panels work at maximum power to increase the energy efficiency of these systems. This requires a tracking mechanism of this point so that the maximum power is generated continuously.

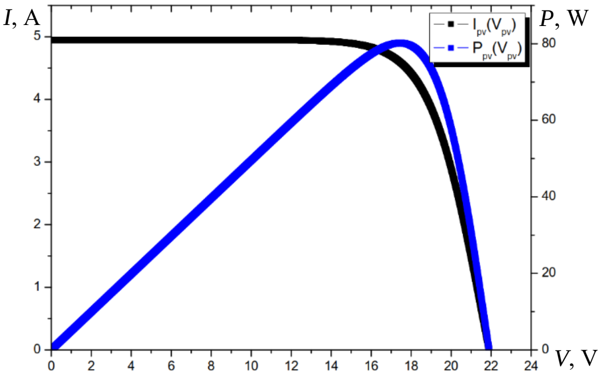

Fig. 1. Current and power curves under 1000 W/m^2 and 25 °C

MPPT enables us to control the operating point by regulating the duty cycle converter circuit connected between the PV generator and the load or battery storage.

Various MPPT methods have been developed and executed: P&O [1], INC [2], FOCV [3] and FSCC [4]. The existing methods have one or more defects, such as costly, difficult to achieve, plurality of sensors, high complexity, easy to instability. The first two are used in many PV systems more largely than others because of their simple implementation.

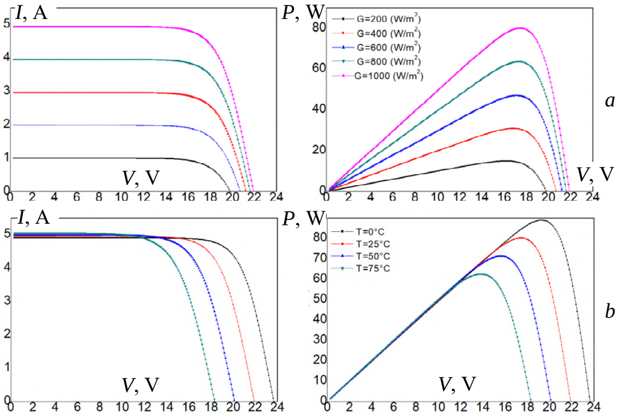

Fig. 2. Current-Voltage (*I*-*V*) and Power-Voltage (*P*-*V*) characteristics: *a* – temperature $T = 25$ °C and different levels of irradiance *G*: *b* – at irradiance $G = 1000$ W/m² and different temperatures *T*

When the control parameter is increased or decreased to a small extent (step size) in the P&O method, a disturbance occurs at the PV generator operating point. We measure the PV external energy before and after the disturbance, if there is an increase in the power, the algorithm continues to perturb order in the same way; if it is the other way around, the system will perturb in the opposite way [5], and this algorithm can be described based on the nature of the control variable you use [6]:

1) *voltage* – Voltage Perturbation Algorithm;
2) *current* – Current Perturbation Algorithm;
3) *duty cycle* – Duty Cycle Perturbation Algorithm.

To determine the unit operating point on both sides of the MPP we derive the power from the voltage and then approximate this point from the MPP by adjusting the duty cycle. This method is called the INC method.

In the presence of uniform radiation the previous two methods work effectively because there is only one MPP in this case however, boot P&O and INC become ineffective under rapid change in the atmosphere as well as power fluctuations at the MPP [7–9].

FOCV and FSCC methods are simple methods for obtaining maximum power, but they are inaccurate because they give only an approximation of the constant ratio between optimum voltage and open circuit voltage or between optimum current and short circuit current for the PV panel. This makes the efficiency of the PV system weak and energy loss, especially that the MPP varies with the level of radiation and temperature [10].

FLC and ANN are smart methods and techniques that have recently been used in the literature [11–14]. ANN presents some drawbacks despite its good performance, especially in the case of rapid fluctuations in weather conditions. Hence, its robustness requires a massive database [15]. The proposed FLC-VPA method is better than MPPT methods used in a several applications [16–20] because it is easy to design, robust and requires no exact model.

The goal of the paper expressed in proposing a fuzzy logic controller based on the principal of the well-known voltage perturbation algorithm. The last-mentioned algorithm uses a fixed step size, if it is taken to large, the power perturbation increases. The main contribution of this paper is the introduction of a FLC-VPA that uses a variable step size to avoid the large time response of VPA when the step size chosen too small.

PV module. To carry out the simulation and the experimental part we chose the STP080S-80 12/Sb PV module. The module is made up of 36 monocrystalline silicon solar cells connected in series to produce a maximum power of 80 W. Solar cells are typically studied under STC, where the mean solar spectrum value is AM1.5, and at an estimated irradiance of 1000 W/m^2, with the cell temperature set as 25 °C.

The prototypical involves a current generator to simulate the flow of incident light and a diode for the polarization of cells (Fig. 3).

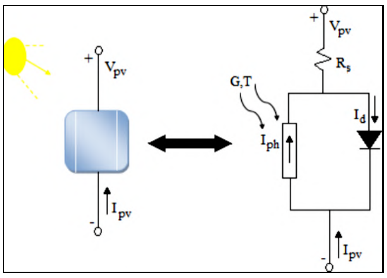

Fig. 3. Equivalent schematic of the PV cell

To account for physical phenomena at the cell level, the model is supplemented with a series resistor R$_s$. The behavior of a PV cell with a silicon based PN junction can be characterized by the equation in statics [21]:

$$I_{pv} = I_{ph} - I_d. \tag{1}$$

The diode current is given by:

$$I_d = I_s \cdot \left[\exp\left(q \cdot \frac{V_{pv} + R_s I_{pv}}{A \cdot k \cdot T} \right) - 1 \right], \tag{2}$$

where: q is the electron charge ($q = 1.602 \cdot 10^{-19}$ C); k is the Boltzmann constant ($k = 1.38 \cdot 10^{-23}$ J/K); A is the diode ideality; I_s is the reverse diode saturation current; R_s is the series resistance of the cell; T is the temperature, K; V_{pv}, I_{pv} are the output voltage and current of the solar cell, respectively.

The saturation current I_s varying with temperature, which is described as:

$$I_s = I_{so} \cdot \left(\frac{T}{T_{ref}} \right)^{\frac{3}{A}} \cdot \exp\left[\left(-\frac{E_g}{A \cdot k} \right) \cdot \left(\frac{1}{T} - \frac{1}{T_{nom}} \right) \right]; \tag{3}$$

$$I_{so} = \frac{I_{sc\_nom}}{\exp\left(q \cdot \dfrac{V_{oc\_nom}}{A \cdot k \cdot T_{nom}} \right) - 1}, \tag{4}$$

where I_{ph} is the generated photo-current, which is primarily determined by irradiance G and cell temperature T as follows:

$$I_{ph} = I_{ph\_nom} \cdot \left[1 + \alpha \left(T - T_{nom} \right) \right]; \tag{5}$$

$$I_{ph\_nom} = I_{sc\_nom} \cdot \frac{G}{G_{nom}}; \tag{6}$$

where G_{nom} is the nominal irradiance; T_{nom} is the nominal temperature; I_{sc_nom} is the nominal short circuit current; V_{oc_nom} is the nominal open circuit voltage of PV panel at STCs.

The Suntech A STP080S-12/Bb PV panel was utilized in the simulation, and the data for the PV module can be seen in Table 1.

Table 1

Parameter condition of STP080S-12/Bb PV module

Parameter	Value
Maximum power $P_{\max}$, W	80
Maximum voltage $V_{\max}$, V	17.5
Current at the maximum power $I_{\max}$, A	4.58
Open circuit voltage V_{oc}, V	21.9
Short circuit current I_{sc}, A	4.95

The maximum voltage $V_{\max}$ and maximum current $I_{\max}$ to the MPP, the open circuit voltage V_{oc}, the short circuit current I_{sc}, and the slopes of the curves *I-V* near V_{oc} and I_{sc} are used to determine the ideal factor and series resistance for a specific solar radiation and temperature [22].

DC/DC converter. A chopper is a DC/DC converter that converts DC energy at one voltage (or current) level to DC energy at a different voltage (or current). Depending on the load voltage, numerous DC/DC converters can be connected to the PV generator (buck, boost and buck boost).

The employed structure of the DC-DC boost chopper in this research is shown in Fig. 4, where S is the switch, L is the boost inductor and C is the filter capacitor.

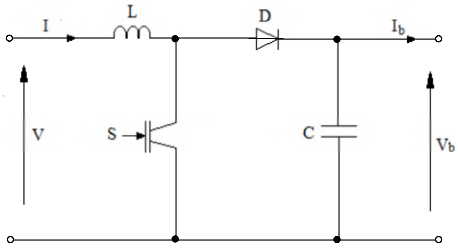

Fig. 4. Scheme of the boost converter

Equation (7) is the energy model of the used boost converter:

$$\frac{\mathrm{d}}{\mathrm{d}t}\begin{bmatrix} V_b \\ I \end{bmatrix} = \begin{bmatrix} 0 & (1-\alpha)/C \\ (\alpha-1)/L & 0 \end{bmatrix}\begin{bmatrix} V_b \\ I \end{bmatrix} + \begin{bmatrix} 0 & -1/C \\ 1/L & 0 \end{bmatrix}\begin{bmatrix} V \\ I_b \end{bmatrix}, \quad (7)$$

where *I*, *V*, V_b, I_b and *α* are the input current, input voltage, output voltage, output current and duty ratio of boost converter, respectively. Because the output voltage of a DC-DC boost converter is always higher than the input voltage, it can be used to connect low module voltages to high load/battery voltages [23].

By adjusting the switching duty cycle *α*, an IGBT can boost the PV module's output voltage:

$$V_b = V / (1 - \alpha). \quad (8)$$

When the switch S is turned on, current travels from the input source through the inductor L to the IGBT, storing energy in the inductor as a result. The energy stored in the inductor is released through the diode to the C and the load when the switch S is turned off.

The boost converter specifications are shown in Table 2.

Table 2

Boost converter parameters

IGBT	1× IRGPC60K	600 V, 41 A, 15 V at 125 °C
Schottky diode	1× GI BYW29-150 9616	150V, 8 A, 0.8 V at 150 °C
L	2× LEYBOLD 56214 parallel	0.011 mH, 2.5 A
C	2× REA series	47 µF, 400 V

Battery modeling. Batteries are complicated electrochemical devices that use chemical bonds to store electrical charge. Lead acid battery is generally used storage component in PV system. There are several lead battery models proposed, in this paper we have opted for the Thevenin model used in [24] (Fig. 5).

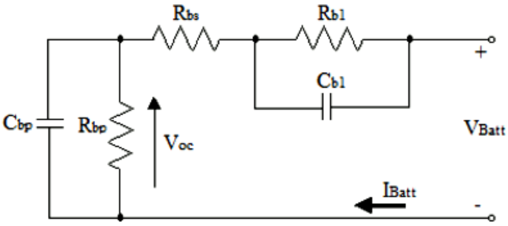

Fig. 5. Circuit diagram of the battery

The battery, on the other hand, is an energy storage element whose energy is measured in kWh. When a capacitor is used to mimic the battery unit, the following factors can be considered:

$$C_{bp} = \frac{2 \cdot E_b}{V_{\max}^2 - V_{\min}^2}, \quad (8)$$

where C_{bp} is the battery charge capacity; E_b is the energy given by the manufacturer of the battery, kWh; $V_{\max}$, $V_{\min}$ are the maximum and the minimum voltage of the battery in open circuit respectively.

The circuit in Fig. 5 describes the characteristics of a lead acid battery with a complete manner yet very simplified, this circuit expresses the input equivalent impedance Z_b by:

$$Z_b(s) = R_{bs} + \frac{R_{b1}}{R_{b1}C_{b1}s + 1} + \frac{R_{bp}}{R_{bp}C_{bp}s + 1}, \quad (9)$$

where R_{b1} and C_{b1} are the energy and voltage during charging and discharging using the parallel circuit; the resistance of R_{bp} is significant because the self-discharging current of a battery is minimal.

VPA MPPT. VPA is one of the easier online procedures can be realized by applying a disruption to the reference voltage. According to the flowchart (Fig. 6) VPA operates by periodically perturbing (increases or decreases) the module terminal voltage and estimates the power difference between the present and the past extracted power from the PV source such us $V_{pv}(n)$, $I_{pv}(n)$ and $P_{pv}(n)$ are voltage, current and power of PV panel at n^{th} iteration, respectively.

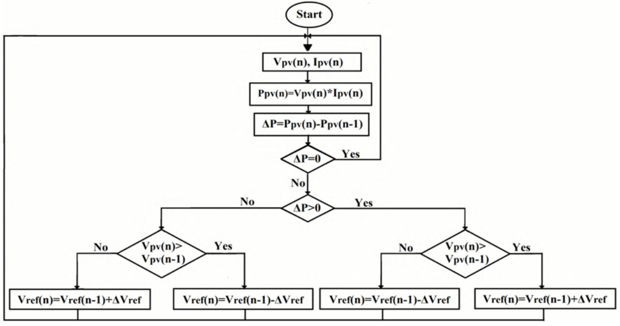

Fig. 6. Flow chart of the VPA MPPT

If the power difference is positive, the tracking is in the right direction and the perturbation direction will keep on (increase or decrease) in the next cycle.

However, the opposite perturbation direction will occur at a negative power difference; similarly, the next cycle is repeated until the MPP is tracked.

The choice of the perturbation step value (ΔV_{ref}) applied to the system, is very important because it is the responsible of oscillations and moreover the convergence speed to the final response. If a large perturbation step is used the algorithm will find the maximum value faster, nevertheless the quantity of power loss caused by the perturbation is high.

A modest perturbation step, on the other hand, can lessen the power loss caused by the perturbation while slowing down the system's tracking speed. This phenomenon is a term used to describe the trade-off between tracking speed and tracking precision [25].

FLC-VPA MPPT controller. Fuzzy systems are based on Lotfi Zadeh's fuzzy set theory and related techniques, which he pioneered in 1965. Because of their simplicity and effectiveness for both linear and nonlinear systems, they have been successfully applied in a variety of domains including control systems engineering, industrial automation, and optimization. FLCs which don't require the knowledge of an exact plant model, have recently been introduced in the following of the MPP in PV systems [26].

FLC-VPA method suggested in this research takes advantage of the VPA's simplicity as well as its ability to reduce the FLC's steady state oscillations. FLC-VPA technique examines the properties of PV panels before perturbing the operating voltage by an appropriate increment (ΔV_{ref}) to adjust the PV power. The power variation (ΔP_{pv}) might be in either a positive or negative direction.

The value of (ΔP_{pv}) can be huge or tiny. From here, the voltage variation (ΔV_{ref}) is increased or lowered in a small or large way in the direction that allows the power P_{pv} to be increased until the optimum is reached.

FLC-VPA MPPT controller, like conventional FLC, consists of 3 phases – fuzzification, rule processing unit and defuzzification (Fig. 7). The triangular and trapezoidal shapes were chosen for the fuzzy control because they consume less hardware memory and have a simpler parametric representation. The triangular version of this procedure's membership function assumes that there is only one main fuzzy subset for each input [27].

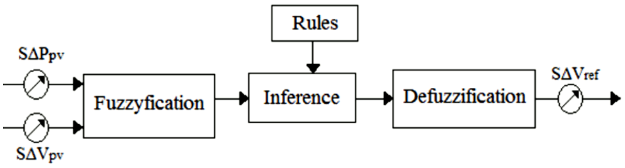

Fig. 7. Fuzzy controller structure

1. *Fuzzification*. The fuzzy control requires that variable used in describing the control rules has to be expressed in terms of fuzzy set notations with linguistic labels [28]. In this paper, the FLC-VPA MPPT method has two input variables, namely $\Delta P_{pv}(n)$, $\Delta V_{pv}(n)$, and one output variable $\Delta V_{ref}(n)$; at a sampling instant n, where the variable $\Delta P_{pv}(n)$ and $\Delta V_{pv}(n)$ are expressed as follows:

$$\Delta P_{pv} = P_{pv}(n) - P_{pv}(n-1); \qquad (10)$$

$$\Delta V_{pv} = V_{pv}(n) - V_{pv}(n-1); \qquad (11)$$

where $P_{pv}(n)$ and $V_{pv}(n)$ are the power and the voltage of the PV module.

The fuzzy sets for both inputs and output are: P (positive), N (negative), Z (zero), as shown in Fig. 8.

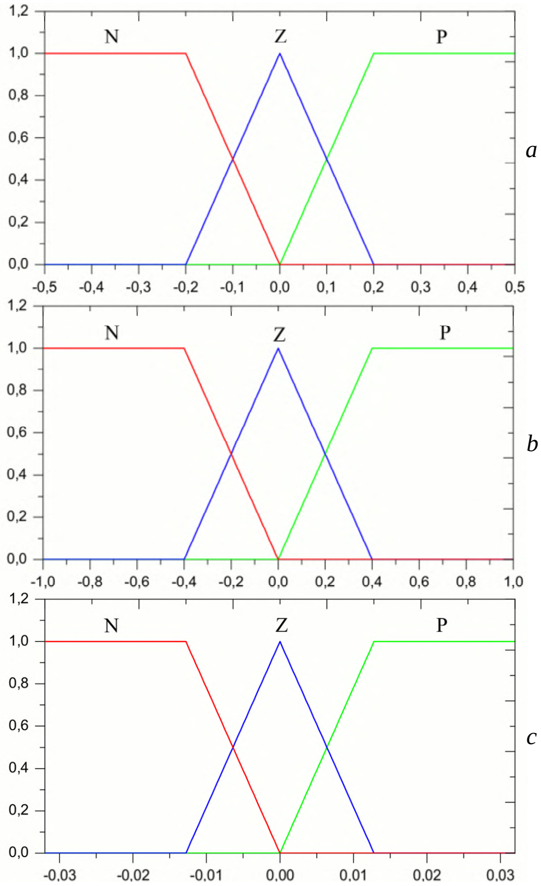

Fig. 8. Membership functions:
a – input ΔV_{pv}; *b* – input ΔP_{pv}; *c* – output ΔV_{ref}

2. *Inference method*. The inference method used to determine the output of fuzzy logic controller. Several inference methods are discussed in literature include Compositional Rule of Inference, Generalized Modus Ponens and Sugeno inference method [29].

In this study Mamdani's inference method is employed because it was the most common method used in engineering application [30].

The composition operation is the method by which a control output is generated, the commonly applied method is MAX/MIN used in this article.

The membership function of every rule is given by the MIN operator and MAX operator. The construction of control rules to relate the fuzzy input to the fuzzy output depends on the knowledge base of the system dynamics. The control rules proposed is presented in Table 3. For one example, control rule in Table 3 is expressed as follows. «IF ΔP_{pv} is P and ΔV_{pv} is P THEN ΔV_{ref} is P». This implies that «IF the power change is positive, AND the voltage variation is positive THEN the perturbation step will increase in the next cycle».

Table 3

Control rules

ΔV_{pv} / ΔP_{pv}	N	Z	P
N	P	Z	N
Z	N	Z	P
P	N	Z	P

3. *Defuzzification*. After evaluating the rules, the FLC-VPA's final step is to compute the output, which is

the perturbation step (ΔV_{ref}) with the defuzzification process.

The centroid approach, commonly known as the Center of Gravity method, is employed in this paper, because it has good averaging capabilities and gives decent results. The crisp value of the control output ΔV_{ref} is calculated as:

$$\Delta V_{ref} = \frac{\sum_{j=1}^{n} W_j \Delta V_j}{\sum_{j=1}^{n} W_j}, \tag{12}$$

where n is the maximum number of effective rules; W_j is the weighting factor; V_j is the value corresponding to ΔV_{ref} membership function.

This adjustment is added to the previous control voltage value to get the final control voltage:

$$V_{pv}(n) = V_{pv}(n-1) + \Delta V_{ref}(n). \tag{13}$$

The terminal and reference voltages were measured at each sample period, and the error $e = (V_{ref} - V_{pv})$ was determined. FLC-VPA adjusts the reference voltage (V_{ref}) for MPPT as previously stated. This voltage is the positive input (reference) to the PI controller, which conducts steady-state voltage control.

To get the terminal voltage to the desired value, a PWM generator is utilized to adjust the duty ratio of the converter. FLC-VPA controller is implemented in real-time for MPPT following the methods outlined above.

Simulation results. A simulation of a solar panel with 36 cells connected to a storage battery via a DC-DC boost converter with MPPT algorithms is used in this section. The DC input voltage is converted to the battery voltage level using a DC-DC boost converter. This research compares and contrasts the VPA and FLC-VPA MPPT algorithms for tracking of maximum power. We have combined the two improved methods shown above in Fig. 9 to evaluate their efficiency.

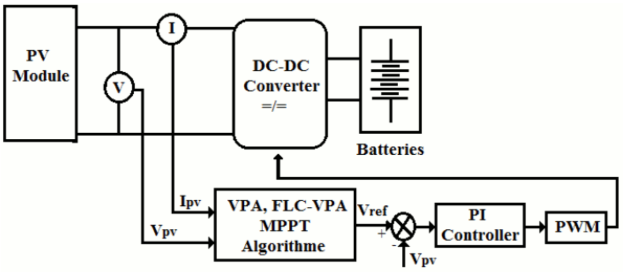

Fig. 9. Block diagram of the PV battery charging system

a) *PI controller effectiveness*. To improve the efficiency of the PI controller, the two MPPT algorithms studied in this paper was simulated under constant irradiance 1000 W/m^2 and temperature 25 °C.

Figure 10 shows that for VPA or FLC-VPA MPPT algorithms the PI loop provides overall system stability.

The error e in VPA is very large compared with the error of FLC-VPA because of the voltage reference perturbation.

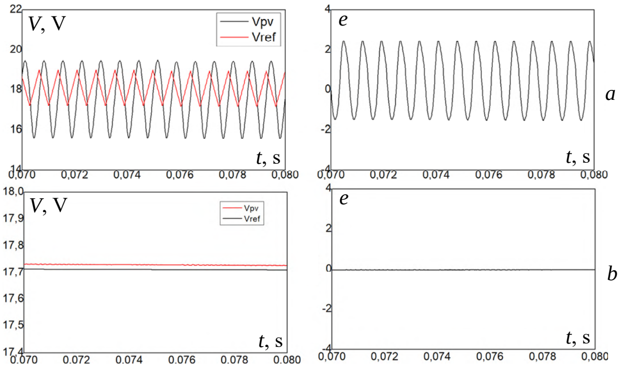

Fig. 10. PI controller efficiency for both controllers:
a – VPA; *b* – FLC-VPA

b) *Irradiation influence*. Figure 11 depicts the simulation results by changing the solar irradiation disturbance from 1000 W/m^2 to 600 W/m^2 at a constant temperature of 25 °C. When the simulation is started, both MPPT algorithms detect the maximum power available; although the detection of the maximum power is taking place, VPA and FLC-VPA generate the necessary control signals for the operation power of PV module follows the MPP with a minimum error.

The irradiation intensity abruptly rises to 600 W/m^2 at t = 0.2 s, causing a negative change, and the MPP search process is initialized to look for a new MPP. After determining the new MPP, the two MPPT algorithms investigated in this study operate the PV module at the new MPP.

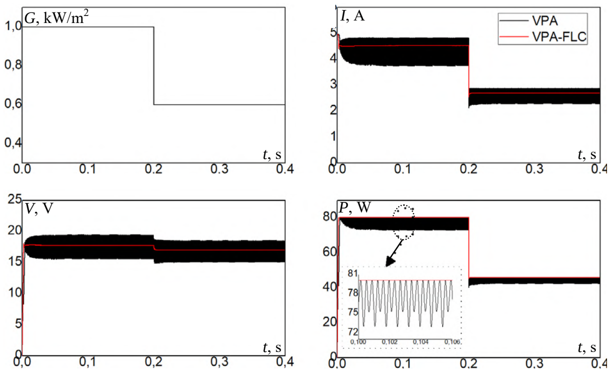

Fig. 11. Variations in irradiance have an impact on the management of both MPPT at a constant temperature of 25 °C

c) *Temperature influence*. We report in Fig. 12 the response of the two algorithms to a random variation of the temperature.

We note that for a quick variation of temperature, between a minimal value of 15 °C and a maximum value of 25 °C; it's clear that the algorithm which adapts better is FLC-VPA. Thus, with this simulation tool, we have highlighted the fact that for fast step changes in temperature, the advantages of the FLC-VPA to the VPA by achievement of the MPP which is carried out instantaneously in the good direction without additional oscillations when the MPP is reached. And what enhance our study is that the power and the voltage of the PV module follow the variation of temperature conversely what is completely the opposite in the current PV module witch stay constant under temperature variation.

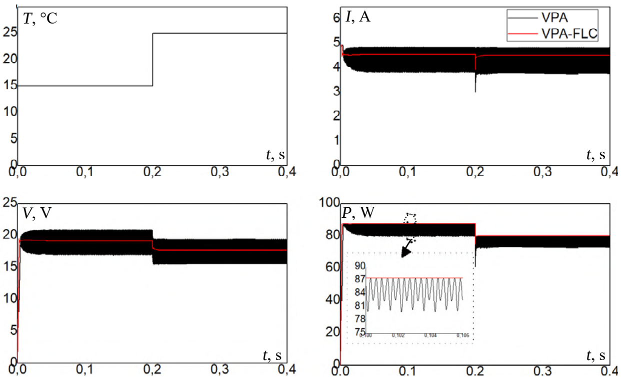

Fig. 12. The effect of temperature fluctuations on the control of both MPPT at a fixed irradiance of 1000 W/m^2

Experimental results. A prototype PV battery charging system was created and tested for experimental verification. In this study, a STP080S-12/Bb PV module with a 30° and a maximum power of 80 W in standard irradiance and temperature was used. To draw the $I_{pv}(V_{pv})$ and $P_{pv}(V_{pv})$ characteristics of STP080S-12/Bb module the circuit shown in Fig. 13 is used.

Two batteries in series each one is determined by nominal voltage of a battery (12 V_{dc}) and battery capacity (100 Ah) compose the energy storage component.

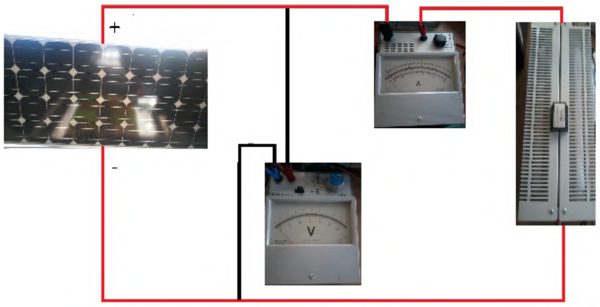

Fig. 13. Circuit measurement of $I_{pv}(V_{pv})$ and $P_{pv}(V_{pv})$ of STP080S-12/Bb module

The PV power system consists also of a DC-DC boost converter, which has the parameters summarized in Table 2 to step up the PV module voltage. Figure 14 depicts the synoptic diagram of this PV system.

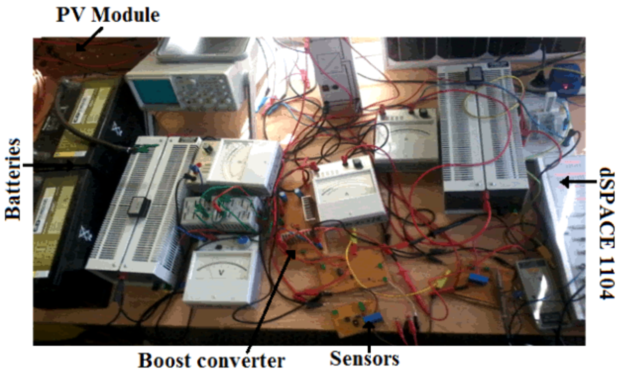

Fig. 14. Experimental setup of the PV battery charging system

The control platform for assessing MPPT algorithms was a dSPACE 1104 controller board. Allowing MATLAB/Simulink to communicate with real-world hardware. This is accomplished by utilizing dSPACE interface blocks' input/output (I/O); the inputs are analog to digital converter (ADC) and the outputs are digital to analog converter (DAC). The voltage and current of the PV module are used as inputs to the dSPACE 1104 interface for the MPPT algorithms proposed in this work, and LEM sensors (LV25-P) and (LA25-P) are employed for data processing.

On MATLAB/Simulink model the MPPT method generate the reference voltage and is compared with the sensed PV module voltage which gives the modulating wave for the PWM after real-time simulation.

The output of the dSPACE 1104 is limited by 10 V, so we utilized an amplifier circuit to boost the output voltage to a level that could feed the IGBT (15 V). When the pulses are augmented, they pass via an isolated circuit that separates the power and control circuits. For noise rejection from the module current and voltage feedback signals, low pass filters are used.

The PV array's nonlinear feature can be seen in the current and power curves (see Fig. 1). As a result, an MPPT algorithm must be implemented to force the system to function at MPP all the time.

In this paper two MPPT algorithms are carried out, therefore, to confirm the efficiency of the algorithms a real time simulation using DSP1104 is used.

Figure 15 shows the current, power and voltage of PV module under constant temperature and irradiance using VPA with 0.5 V of perturbation step. In the solar irradiation 779 W/m^2, PV output current is ranging from 1.5 A to 4 A and the rate of change of the PV module voltage is about 12 V results a PV power output perturbs between 30 W and 51 W, all this perturbation creates power loss in the PV system.

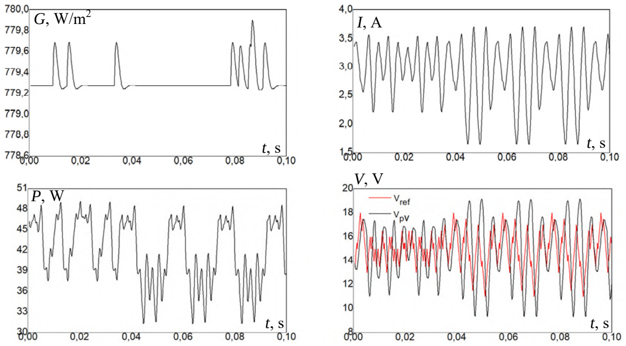

Fig. 15. Real time simulation results using VPA under constant irradiance and temperature

To reduce the perturbation, we can minimize the perturbation step value but that can provoke a divergence of the system after a few seconds of the beginning of the real time simulation.

The system is working with an average power of 51 W, which corresponds to the maximum power of the PV module under 780 W/m^2, and this power is practically constant (Fig. 16). As a result, the system's operation in this state demonstrates the FLC-VPA method's efficiency tracking.

Comparison of MPPT algorithms. The boost converter is turned on inactive mode at first. As a result, the PV module is directly connected to the two 24 V storage batteries. The operational voltage and current of the PV module are 17.5 V and 1.9 A, respectively.

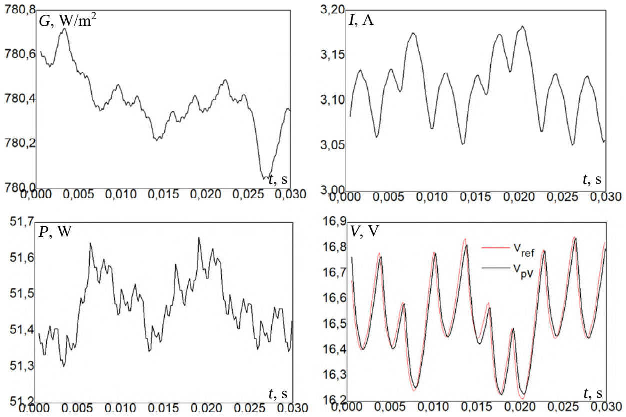

Fig. 16. Real time simulation results using FLC-VPA under constant irradiance and temperature

The irradiance measured is 473 W/m^2, both of algorithms optimize the PV system by make the PV module offer the maximum power, but the FLC-VPA is better than the VPA because this last present a very perturbed reference voltage and that's clear in the error curve.

When the FLC-VPA method is employed, the PV module power is 33.5 W, however when the VPA is applied, the power is balanced between 25 W and 32.5 W, resulting in significant power losses (Fig. 17). It should be emphasized that the VPA controls the system using oscillating signal responses, and hence may fail to achieve the optimization goal described in the introduction. The efficiency of the FLC-VPA system, as well as its ability to operate at maximum power, is demonstrated in this study.

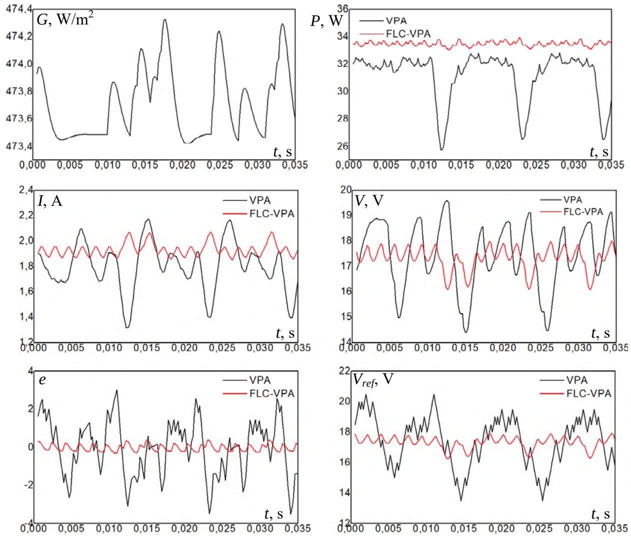

Fig. 17. Experimental results for both controllers showing system responses to a PV panel

Conclusions. In this research, we combine the traditional voltage perturbation algorithm with the fuzzy logic controller in the field of energy development with the goal of improvement the performance and maximizing the efficiency of solar modules by allowing them to operate at their maximum power. By incorporating the advantages of both algorithms, this controller increased the voltage perturbation algorithm's simplicity while also eliminating the complexity of the original fuzzy logic controller and ensuring the system's efficiency. The fuzzy logic based on voltage perturbation controller's effectiveness for system optimization is demonstrated through simulation and experimental findings utilizing the control system card dSPACE1104.

Conflict of interest. The authors declare that they have no conflict of interest.

REFERENCES

1. Hafeez M.A., Naeem A., Akram M., Javed M.Y., Asghar A.B., Wang Y. A Novel Hybrid MPPT Technique Based on Harris Hawk Optimization (HHO) and Perturb and Observer (P&O) under Partial and Complex Partial Shading Conditions. *Energies*, 2022, vol. 15, no. 15, art. no. 5550. doi: https://doi.org/10.3390/en15155550

2. Ibrahim M.H., Ang S.P., Dani M.N., Rahman M.I., Petra R., Sulthan S.M. Optimizing Step-Size of Perturb & Observe and Incremental Conductance MPPT Techniques Using PSO for Grid-Tied PV System. *IEEE Access*, 2023, vol. 11, pp. 13079-13090. doi: https://doi.org/10.1109/ACCESS.2023.3242979.

3. Hassan A., Bass O., Masoum M.A.S. An improved genetic algorithm based fractional open circuit voltage MPPT for solar PV systems. *Energy Reports*, 2023, vol. 9, pp. 1535-1548. doi: https://doi.org/10.1016/j.egyr.2022.12.088.

4. Claude Bertin Nzoundja Fapi, Wira P., Kamta M., Tchakounte H., Colicchio B. Simulation and dSPACE Hardware Implementation of an Improved Fractional Short-Circuit Current MPPT Algorithm for Photovoltaic System. *Applied Solar Energy*, 2021, vol. 57, no. 2, pp. 93-106. doi: https://doi.org/10.3103/S0003701X21020080.

5. Feroz Mirza A., Mansoor M., Ling Q., Khan M.I., Aldossary O.M. Advanced Variable Step Size Incremental Conductance MPPT for a Standalone PV System Utilizing a GA-Tuned PID Controller. *Energies*, 2020, vol. 13, no. 16, art. no. 4153. doi: https://doi.org/10.3390/en13164153.

6. Sibtain D., Gulzar M.M., Shahid K., Javed I., Murawwat S., Hussain M.M. Stability Analysis and Design of Variable Step-Size P&O Algorithm Based on Fuzzy Robust Tracking of MPPT for Standalone/Grid Connected Power System. *Sustainability*, 2022, vol. 14, no. 15, art. no. 8986. doi: https://doi.org/10.3390/su14158986.

7. Sahraoui H., Mellah H., Drid S., Chrifi-Alaoui L. Adaptive maximum power point tracking using neural networks for a photovoltaic systems according grid. *Electrical Engineering & Electromechanics*, 2021, no. 5, pp. 57-66. doi: https://doi.org/10.20998/2074-272X.2021.5.08.

8. Khan S.A., Mahmood T., Awan K.S. A nature based novel maximum power point tracking algorithm for partial shading conditions. *Electrical Engineering & Electromechanics*, 2021, no. 6, pp. 54-63. doi: https://doi.org/10.20998/2074-272X.2021.6.08.

9. Saeed H., Mehmood T., Khan F.A., Shah M.S., Ullah M.F., Ali H. An improved search ability of particle swarm optimization algorithm for tracking maximum power point under shading conditions. *Electrical Engineering & Electromechanics*, 2022, no. 2, pp. 23-28. doi: https://doi.org/10.20998/2074-272X.2022.2.04.

10. Zaimi M., El Achouby H., Ibral A., Assaid E.M. Determining combined effects of solar radiation and panel junction temperature on all model-parameters to forecast peak power and photovoltaic yield of solar panel under non-standard conditions. *Solar Energy*, 2019, vol. 191, pp. 341-359. doi: https://doi.org/10.1016/j.solener.2019.09.007.

11. Lahiouel Y., Latreche S., Khemliche M., Boulemzaoud L. Photovoltaic fault diagnosis algorithm using fuzzy logic controller based on calculating distortion ratio of values. *Electrical Engineering & Electromechanics*, 2023, no. 4, pp. 40-46. doi: https://doi.org/10.20998/2074-272X.2023.4.06.

12. Sathish C., Chidambaram I.A., Manikandan M. Intelligent cascaded adaptive neuro fuzzy interface system controller fed

KY converter for hybrid energy based microgrid applications. *Electrical Engineering & Electromechanics*, 2023, no. 1, pp. 63-70. doi: https://doi.org/10.20998/2074-272X.2023.1.09.

13. Praveen Kumar T., Ganapathy S., Manikandan M. Improvement of voltage stability for grid connected solar photovoltaic systems using static synchronous compensator with recurrent neural network. *Electrical Engineering & Electromechanics*, 2022, no. 2, pp. 69-77. doi: https://doi.org/10.20998/2074-272X.2022.2.10.

14. Bengharbi A.A., Laribi S., Allaoui T., Mimouni A. Photovoltaic system faults diagnosis using discrete wavelet transform based artificial neural networks. *Electrical Engineering & Electromechanics*, 2022, no. 6, pp. 42-47. doi: https://doi.org/10.20998/2074-272X.2022.6.07.

15. Chen Y., Song L., Liu Y., Yang L., Li D. A Review of the Artificial Neural Network Models for Water Quality Prediction. *Applied Sciences*, 2020, vol. 10, no. 17, art. no. 5776. doi: https://doi.org/10.3390/app10175776.

16. Li X., Wen H., Hu Y., Jiang L. A novel beta parameter based fuzzy-logic controller for photovoltaic MPPT application. *Renewable Energy*, 2019, vol. 130, pp. 416-427. doi: https://doi.org/10.1016/j.renene.2018.06.071.

17. Loukil K., Abbes H., Abid H., Abid M., Toumi A. Design and implementation of reconfigurable MPPT fuzzy controller for photovoltaic systems. *Ain Shams Engineering Journal*, 2020, vol. 11, no. 2, pp. 319-328. doi: https://doi.org/10.1016/j.asej.2019.10.002.

18. Ilyas A., Khan M.R., Ayyub M. FPGA based real-time implementation of fuzzy logic controller for maximum power point tracking of solar photovoltaic system. *Optik*, 2020, vol. 213, art. no. 164668. doi: https://doi.org/10.1016/j.ijleo.2020.164668.

19. Rezk H., Aly M., Al-Dhaifallah M., Shoyama M. Design and Hardware Implementation of New Adaptive Fuzzy Logic-Based MPPT Control Method for Photovoltaic Applications. *IEEE Access*, 2019, vol. 7, pp. 106427-106438. doi: https://doi.org/10.1109/ACCESS.2019.2932694.

20. Vivek K., Subbarao K.V., Routray W., Kamini N.R., Dash K.K. Application of Fuzzy Logic in Sensory Evaluation of Food Products: a Comprehensive Study. *Food and Bioprocess Technology*, 2020, vol. 13, no. 1, pp. 1-29. doi: https://doi.org/10.1007/s11947-019-02337-4.

21. Chatrenour N., Razmi H., Doagou-Mojarrad H. Improved double integral sliding mode MPPT controller based parameter estimation for a stand-alone photovoltaic system. *Energy Conversion and Management*, 2017, vol. 139, pp. 97-109. doi: https://doi.org/10.1016/j.enconman.2017.02.055.

22. Akbar F., Mehmood T., Sadiq K., Ullah M.F. Optimization of accurate estimation of single diode solar photovoltaic parameters and extraction of maximum power point under different conditions. *Electrical Engineering & Electromechanics*, 2021, no. 6, pp. 46-53. doi: https://doi.org/10.20998/2074-272X.2021.6.07.

23. Benazza B., Bendaoud A., Slimani H., Benaissa M., Flitti M., Zeghoudi A. Experimental study of electromagnetic disturbances in common and differential modes in a circuit based on two DC/DC boost static converter in parallel. *Electrical Engineering & Electromechanics*, 2023, no. 4, pp. 35-39. doi: https://doi.org/10.20998/2074-272X.2023.4.05.

24. Lu C.-F., Liu C.-C., Wu C.-J. Dynamic modelling of battery energy storage system and application to power system stability. *IEE Proceedings - Generation, Transmission and Distribution*, 1995, vol. 142, no. 4, art. no. 429. doi: https://doi.org/10.1049/ip-gtd:19951858.

25. Moradi M.H., Reisi A.R. A hybrid maximum power point tracking method for photovoltaic systems. *Solar Energy*, 2011, vol. 85, no. 11, pp. 2965-2976. doi: https://doi.org/10.1016/j.solener.2011.08.036.

26. Sheetal W. Dubewar D. Comparative Study of Photovoltaic Array Maximum Power Point Tracking Techniques. *International Journal of Engineering Research and Technology*, 2015, vol. 4, no. 2, pp. 216-223.

27. Gounden N.A., Ann Peter S., Nallandula H., Krithiga S. Fuzzy logic controller with MPPT using line-commutated inverter for three-phase grid-connected photovoltaic systems. *Renewable Energy*, 2009, vol. 34, no. 3, pp. 909-915. doi: https://doi.org/10.1016/j.renene.2008.05.039.

28. Guenounou O., Dahhou B., Chabour F. Adaptive fuzzy controller based MPPT for photovoltaic systems. *Energy Conversion and Management*, 2014, vol. 78, pp. 843-850. doi: https://doi.org/10.1016/j.enconman.2013.07.093.

29. Mabrouk Y.A., Mokhtari B., Allaoui T. Frequency analysis of stator currents of an induction motor controlled by direct torque control associated with a fuzzy flux estimator. *Electrical Engineering & Electromechanics,* 2023, no. 6, pp. 27-32. doi: https://doi.org/10.20998/2074-272X.2023.6.05.

30. Altin N., Ozdemir S. Three-phase three-level grid interactive inverter with fuzzy logic based maximum power point tracking controller. *Energy Conversion and Management*, 2013, vol. 69, pp. 17-26. doi: https://doi.org/10.1016/j.enconman.2013.01.012.

Received 06.11.2023
Accepted 26.03.2024
Published 20.08.2024

Hadjer Bounechba[1,2,3]*, Professor,*
Abdelfettah Boussaid [1,2,4]*, Professor,*
Aissa Bouzid [1,2]*, Professor,*
[1] University Freres Mentouri Constantine 1,
25000 Ain El Bey Way, Constantine, Algeria,
[2] Constantine Electrotechnical Laboratory,
[3] The Department of Electrical Engineering,
[4] Institut des Sciences et des Techniques Appliquees-ISTA,
e-mail: hadjer.bounechba@lec-umc.org (Corresponding Author);
abdlfettah.boussaid@lec-umc.org; aissa.bouzid@umc.edu.dz

How to cite this article:
Bounechba H., Boussaid A., Bouzid A. Experimental validation of fuzzy logic controller based on voltage perturbation algorithm in battery storage photovoltaic system. *Electrical Engineering & Electromechanics*, 2024, no. 5, pp. 20-27. doi: https://doi.org/10.20998/2074-272X.2024.5.03

UDC 621.314 https://doi.org/10.20998/2074-272X.2024.5.04

L. Djafer, R. Taleb, F. Mehedi

Dspace implementation of real-time selective harmonics elimination technique using modified carrier on three phase inverter

Introduction. *In the contemporary world, alternative electrical energy has become an integral part of our daily existence, with the majority of our electrical materials, electronic devices, and industrial equipment relying on this energy source. Consequently, ensuring the quality of the electrical signal obtained is of paramount importance in the process of converting and distributing electrical energy. The improvement of the output voltage inverter can be achieved through adjustments to the inverter structure or by refining the control strategy.* ***The novelty*** *of the presented research lies in an innovative approach that employs real-time modulation for efficient control over the reduction of harmonics, alongside managing the fundamental component. This approach is applicable to both bipolar and unipolar configurations, featuring quarter-wave and half-wave symmetries.* ***Purpose.*** *Employing this modulation strategy aims to enhance the durability of the switching components and enhance the voltage output of the inverter.* ***Methods.*** *The methodology is founded on a sine-sine modulation as its foundational model. It constitutes an inventive pulse width modulation technique in which a reference sinusoidal waveform, operating at the desired signal frequency, is compared to a modified carrier signal with an identical time period as the reference signal.* ***Results.*** *This paper introduces a broader and more comprehensive approach, alongside specific solutions, for the control and mitigation of harmonics in three phase voltage source inverters. The proposed method offers precise control over the reduction of harmonics and the fundamental component, and it can be implemented in extensive power electronic converters.* ***Practical value.*** *To assess the effectiveness of the given control approach, we conducted simulations as well as real-time implementation employing Dspace DS1104 controller board. The outcomes were highly favorable, confirming the effectiveness and validity of the suggested control algorithm.* References 15, tables 4, figures 7.

Key words: **voltage source inverter, real-time harmonics control, pulse width modulation technique, Dspace DS1104.**

Вступ. *У сучасному світі альтернативна електрична енергія стала невід’ємною частиною нашого повсякденного існування, і більшість наших електричних матеріалів, електронних пристроїв і промислового обладнання покладаються на це джерело енергії. Отже, забезпечення якості отриманого електричного сигналу має першочергове значення в процесі перетворення та розподілу електричної енергії. Покращення вихідної напруги інвертора може бути досягнуто шляхом коригування структури інвертора або вдосконалення стратегії керування.* ***Новизна*** *представленого дослідження полягає в інноваційному підході, який використовує модуляцію в реальному часі для ефективного контролю над зменшенням гармонік, поряд з керуванням основною компонентою. Цей підхід застосовний як до біполярних, так і до однополярних конфігурацій, що мають чвертьхвильову та напівхвильову симетрію.* ***Мета.*** *Застосування цієї стратегії модуляції спрямоване на підвищення довговічності комутаційних компонентів і підвищення вихідної напруги інвертора.* ***Методи.*** *Методологія базується на синусоїдній модуляції як базовій моделі. Він являє собою метод широтно-імпульсної модуляції за винаходом, у якій опорна синусоїдальна форма хвилі, що працює на бажаній частоті сигналу, порівнюється з модифікованим несучим сигналом з ідентичним періодом часу, що й опорний сигнал.* ***Результати.*** *Ця стаття представляє ширший і комплексний підхід, поряд із конкретними рішеннями, для контролю та пом’якшення гармонік у трифазних інверторах джерел напруги. Запропонований метод пропонує точний контроль над зменшенням гармонік і основної складової, і він може бути реалізований у потужних електронних перетворювачах.* ***Практична цінність.*** *Щоб оцінити ефективність даного підходу до управління, ми провели моделювання, а також реалізацію в реальному часі з використанням плати контролера Dspace DS1104. Результати були дуже сприятливими, підтверджуючи ефективність і валідність запропонованого алгоритму контролю.* Бібл. 15, табл. 4, рис. 7.

Ключові слова: **інвертор джерела напруги, контроль гармонік у реальному часі, метод широтно-імпульсної модуляції, Dspace DS1104.**

Abbreviations

FFT	Fast Fourier Transform	RTHC	Real-Time Harmonics Control
GA	Genetic Algorithm	RTI	Real-Time Implementation
PWM	Pulse Width Modulation	SHE-PWM	Selective Harmonic Elimination Pulse Width Modulation
RTHE	Real-Time Harmonic Elimination	SPWM	Sinusoidal Pulse Width Modulation

Introduction. Harmonics and the frequency at which switches operate present notable difficulties within power systems overall, with switching converters being particularly affected [1]. To tackle this issue, two commonly used approaches are the widely recognized SPWM and SHE-PWM [2–5].

SHE-PWM, regarded as a substitute for the SPWM approach, has been extensively studied and explored over time. When compared to SPWM and SHE-PWM provides enhanced control over the lower order harmonic and results in a reduced switching frequency, consequently prolonging the converter’s operational lifespan [6]. Another significant distinction between the two methodologies lies in the manner in which the angles of switching are computed. Within the SPWM technique, angles are continuously produced in real-time through the comparison of a sinusoidal reference with the triangular carrier. In SHE-PWM, the computations are carried out offline, rendering its implementation less resource-intensive. The primary difficulty linked with SHE-PWM lies in the resolution of the resulting system of nonlinear equations [6]. To simplify these equations, prior and contemporary studies have relied on essential assumptions that enforce quarter-wave symmetry on the output waveform [2, 3].

SHE-PWM involves a two-step procedure. In the first phase, the switching instants are determined by solving a system of nonlinear algebraic transcendental equations [7], which can be accomplished using various algorithms like the commonly used iterative method, elimination theory, and a range of optimization approaches, involving GAs and particle swarm optimization techniques. During the second phase, the computed switching instants are stored in a lookup table for real-time retrieval [7]. In practice look-up tables are electronic memories, there capacities depend on the number of harmonics desired to be eliminated and the sampling time of the modulation index. In recent times, numerous studies have put forward various SHE-PWM methods that eliminate the need for storing switching angles in memory, as discussed in references [7, 8]. The approaches introduced in references [9, 10] are regarded as significant advancements in the concept of RTHE.

The goal of the paper is analysis, simulation and implementation RTHC method on three phase inverter, this method permits the removal of chosen harmonics while also simplifying the generation and comparison of the modified sine carrier and a sinusoidal reference.

Subject of investigations. This paper presents an innovative method for managing and reducing harmonics within switching converters, known as RTHE. It is introduced as an alternate approach to SHE-PWM [11, 12]. This approach employs a modulation strategy that utilizes an altered sine carrier waveform, which is contrasted with a typical sine wave, rather than the more common triangular carrier wave [12]. As a result, RTHC streamlines the process of generating and comparing modified sine carrier and the reference sinusoid modulation signals, allowing for quick and precise execution without any precision-related concerns.

In pursuit of this objective, the switching instants are calculated by solving nonlinear algebraic transcendental equations with the use of any optimization algorithm (this paper employs GA). Then these computed angles are applied to produce the required sine carrier wave, resulting in a sine-sine modulation.

Sine-sine PWM. Figure 1,*a* shows the electrical circuit of a three phase inverter, where the input voltage is denoted as v_{dc} and 6 electronic switches. To generate a PWM signal, two sinusoidal waveforms are employed: a reference sinusoid denoted as $v_{ref} = m_i\cdot\sin(2\cdot\pi\cdot f\cdot t + \pi)$ and a sinusoidal carrier labeled as $v_{car} = m_i\cdot\sin k\cdot(2\cdot\pi\cdot f\cdot t)$ as shown in Fig. 1,*b* juxtaposed with (rather than a sinusoidal reference and a triangular carrier as in traditional SPWM). The PWM waveform that emerges from this contrast is shown in Fig. 1,*c* with a maximum amplitude of $r = 1$, a fixed value of $k = 9$ and a frequency $f = 50$ Hz. The constant k signifies the relationship between the carrier frequency and the reference signal frequency. A generalized method to compute the intersection points, as presented in Fig. 1,*b*,*c*, in the context of sine-sine PWM, involves solving (1). The angles of intersection φ_i are represented in radians for the values of $k = 5, 9, 13, 17, 21, 25, \ldots, n, n + 4$:

$$\varphi_i = \frac{i\cdot\pi}{(k+(-1)^i)},\quad i=\left[1:\frac{k-1}{2}\right],$$

$$0<\varphi_i>\frac{\pi}{2},\quad k=5,9,13,17,21\ldots n,n+4. \qquad (1)$$

Table 1 illustrates instances of intersection points in a sine-sine PWM signal for various k values ranging from 5 to 21.

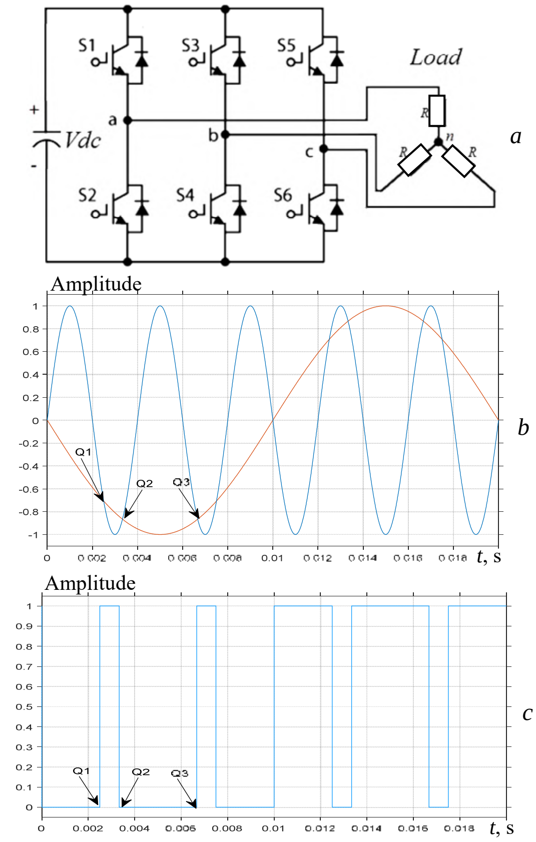

Fig. 1. Sine-sine PWM: *a* – electrical circuit of three phase inverter; *b* – sine-wave comparison; *c* – produced PWM

Table 1

Points of intersection present in a sine-sine PWM signal

	$k = 5$	$k = 9$	$k = 13$	$k = 17$	$k = 21$
φ_1	$\pi/4$	$\pi/8$	$\pi/12$	$\pi/16$	$\pi/20$
φ_2	$\pi/3$	$\pi/5$	$\pi/7$	$\pi/9$	$\pi/11$
φ_3	*	$3\pi/8$	$\pi/4$	$3\pi/16$	$3\pi/20$
φ_4	*	$2\pi/5$	$2\pi/7$	$2\pi/9$	$2\pi/11$
φ_5	*	*	$5\pi/12$	$5\pi/16$	$\pi/4$
φ_6	*	*	$3\pi/7$	$\pi/3$	$3\pi/11$
φ_7	*	*	*	$7\pi/16$	$7\pi/20$
φ_8	*	*	*	$4\pi/9$	$4\pi/11$
φ_9	*	*	*	*	$9\pi/20$
φ_{10}	*	*	*	*	$5\pi/11$

RTHE theory. The PWM signal depicted in Fig. 1,*c* exhibits both quarter-wave and half-wave symmetrical properties. To suppress N harmonics and regulate the fundamental component, (N+1) angles need to be calculated during each quarter period of the waveform.

To accomplish this objective, we will need to solve a system of transcendental equations using the Fourier series decomposition method:

$$I_1 = 1 + 2\cdot\sum_{i=1}^{N+1}(-1)^i\cos(\varphi_i - \alpha_i) - M = 0;$$

$$I_{N+1} = 1 + 2\cdot\sum_{i=1}^{N+1}(-1)^i\cos((N+1)(\varphi_i - \alpha_i)) = 0, \qquad (2)$$

for $k = 2(N + 1) + 1$ and $M = \pi\cdot m_i / 4$, where m_i is the modulation index (usually $0 \le m_i \le 1$). The term α_i is referred to as the perturbation angle and is denoted in radians. To ascertain the appropriate perturbation angles values α_i for any combination of m_i and k, it is essential to solve the set of transcendental equations as described in (2). This can be accomplished by employing various computational techniques, as introduced earlier.

In this study, we have employed the established GA algorithm. The fundamental procedures of GA are elaborated in [13]. A specific method for resolving the system of equations in (2) involves the minimization of the following constrained objective function:

$$F(\alpha_1, \alpha_2, \alpha_3, \dots \alpha_{N+1}) = 0.5\left(I_1^2, I_2^2, I_3^2, \dots, I_{N+1}^2\right), \quad (3)$$

where the constraint is defined by:

$$0 \le \varphi_1 - \alpha_1 \le \varphi_2 - \alpha_2 \le \varphi_3 - \alpha_3 \le \cdots \le \varphi_{N+1} - \alpha_{N+1} \le \pi/2 . \quad (4)$$

The perturbation angles' numerical values for $m_i = 0.8$ can be found in Table 2, where $k = 9$ and 13.

Table 2

Numerical values of α_i

α_i	$k = 9$	$k = 13$
α_1	0.1999	0.1341
α_2	0.2051	0.1477
α_3	0.4634	0.3071
α_4	0.3791	0.2899
α_5	0	0.4847
α_6	0	0.4153

To obtain the intended PWM signal, it is essential to establish a modified carrier signal using the perturbation angles computed through the minimization of (3). The carrier signal in question should have the capability to produce a PWM waveform that displays attributes of both odd and quarter-wave symmetries. It is expected to cross the horizontal axis (time axis) at the point π and 2π [14].

The altered carrier signal takes on the subsequent expression:

$$f(\theta) = A_1 \cdot \sin(k_1 \cdot \theta) + A_2 \cdot \sin(k_2 \cdot \theta) + \cdots, \quad (5)$$

where A_i and k_i represent unidentified parameters.

The given formulation of $f(\theta_i)$ in this manuscript is characterized as follows:

$$f(\theta_i) = \sum_{i=1}^{N+1} C_i \cdot A_i, \quad C_i = \sin(q_i \cdot \theta), \quad (6)$$

where C_i is the fixed value, $\theta_i = \varphi_i - \alpha_i$ and q_i is the odd number within the range of [3, k].

Thus, the sole remaining unidentified parameters comprise A_i. This transforms the system into a set of linear equations that can be solved easily using standard techniques. Compared to [14, 15], the determination of the new points of intersection θ_i is performed exclusively over a quarter of a cycle.

As an illustration, let's take the case with $k = 9$. The set of algebraic equations for deriving the parameters A_i can be expressed as:

$$\begin{aligned}
f(\theta_1) &= A_1 \sin(q_1\theta_1) + A_2 \sin(q_2\theta_1) + \\
&\quad + A_3 \sin(q_3\theta_1) + A_4 \sin(q_4\theta_1); \\
f(\theta_2) &= A_1 \sin(q_1\theta_2) + A_2 \sin(q_2\theta_2) + \\
&\quad + A_3 \sin(q_3\theta_2) + A_4 \sin(q_4\theta_2); \\
f(\theta_3) &= A_1 \sin(q_1\theta_3) + A_2 \sin(q_2\theta_3) + \\
&\quad + A_3 \sin(q_3\theta_3) + A_4 \sin(q_4\theta_3); \\
f(\theta_4) &= A_1 \sin(q_1\theta_4) + A_2 \sin(q_2\theta_4) + \\
&\quad + A_3 \sin(q_3\theta_4) + A_4 \sin(q_4\theta_4),
\end{aligned} \quad (7)$$

where

$$f(\theta_i) = \sin(\theta_i + \pi), \quad \theta_i = \varphi_i - \beta_i,$$

$$i = 1, 2, 3, 4 \text{ for } q_1 = 3, q_2 = 5, q_3 = 7, q_4 = 9.$$

In general $k = n$: $q_1 = 3$, $q_2 = 5$, $q_3 = 7, \dots, q_{(n-1)/2} = n$ (for quarter-wave symmetry).

The suggested approach can be succinctly outlined via a sequence of 5 steps, outlined as follows:

1st step: select the modulation index m_i and define the quantity of harmonics N to be regulated based on the k's value;

2nd step: employ the GA algorithm to solve the non-linear algebraic transcendental equations (2) and ascertain the perturbation angles α_i;

3rd step: utilize the calculated perturbation angles α_i to derive and solve the set of linear equations in A_i, employing (7);

4th step: create the intended modified carrier by inputting the numerical values of A_i (calculated in 3rd step) and q_i into (7); and

5th step: generate the PWM waveform.

Results and discussion. To evaluate the effectiveness of the suggested method, this section unveils the outcomes under the scenario where all harmonics until the 11th, 13th, and 17th orders are regulated in three phase inverters.

To derive the modulation signal (θ_i, $f(\theta_i)$), which represents the modified carrier waveform, it is imperative to compute the A_i values by solving a set of linear equations. Before this, the α_i perturbation angles are calculated by solving the nonlinear transcendental equations through the use of the GA. The resultant values are documented in Table 2.

The numeric values of the points of intersection θ_i and the associated modulation signal $f(\theta_i)$ for $m_i = 0.8$ and different values of k, specifically 9 and 13, can be found in Table 3. Substituting the values of (θ_i, $f(\theta_i)$) into (7) results in a set of linear equations for A_i corresponding to each k value.

The solutions for A_i with k values of 9 and 13, are detailed in Table 4. Subsequently, by replacing the q_i and A_i values into (7), the modified carrier is derived, leading to the generation of the PWM waveform.

Table 3

Coordinates of intersection points

$k = 9$		$k = 13$	
θ_i, rad	$f(\theta_i)$	θ_i, rad	$f(\theta_i)$
0.1782	–0.1772	0.1276	–0.1272
0.4434	–0.4290	0.3010	–0.2964
0.6995	–0.6438	0.4782	–0.4601
0.9008	–0.7838	0.6076	–0.5708
*	*	0.8242	–0.7340
*	*	0.9310	–0.8022

Table 4

Computed values of A_i

	$k = 9$	$k = 13$
A_1	–0.8027	–0.8524
A_2	0.5035	0.6133
A_3	–0.2283	–0.3638
A_4	0.0570	0.1694
A_5	0	–0.0559
A_6	0	0.0099

The modified carrier, the output voltage waveform and its corresponding FFT are depicted in Figs. 2–4, respectively, for a frequency $f = 50$ Hz.

It is important to highlight that in a three phase voltage system, the corresponding phase shifts are 0, $-2\pi/3$ and $2\pi/3$, respectively. Consequently, for the alignment of our system voltages in phase:

- The reference sinusoid exhibit phase shifts of 0, $-2\pi/3$ and $2\pi/3$, respectively;
- the modified carrier exhibit phase shifts of π, $-q_i\cdot 2\pi/3+\pi$ and $q_i\cdot 2\pi/3+\pi$, respectively.

Simulation results. To showcase the effectiveness of a three phase inverter under various k values (specifically, $k = 9$ and $k = 13$), custom carrier signals were generated. These custom carrier signals, along with their corresponding output voltage waveforms and resulting harmonic spectra, were simulated over a duration of 0.02 s. The simulations were carried out at a 50 Hz frequency and a DC input voltage of $V_{dc} = 100$ V.

As depicted by the simulation outcomes, the suggested approach has been effectively employed across various k values. The outcomes of the simulation distinctly demonstrate that the modified carrier possesses half-and also quarter wave symmetry. As depicted in Fig. 2, the output voltages along with their corresponding harmonics spectra for the three phase inverter are illustrated in Fig. 3, 4, respectively. In conclusion the harmonic spectra provide clear evidence of the complete elimination of all fundamental frequency harmonics.

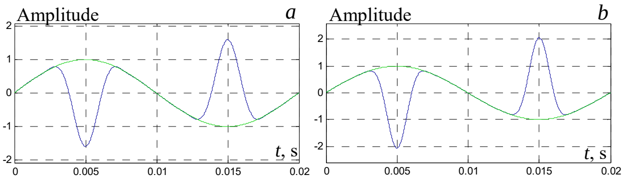

Fig. 2. The modified carrier, a sinusoidal reference in three phase inverter: *a* – $k = 9$; *b* – $k = 13$

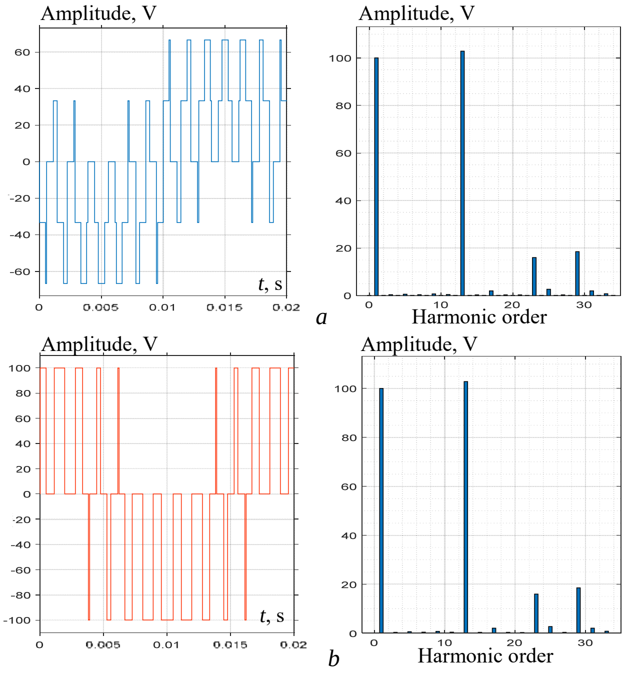

Fig. 3. Implementation of RTHE:
a – the phase-neutral output voltage waveform and FFT corresponding for $k = 9$; *b* – line-to-line output voltage waveform and FFT corresponding for $k = 9$

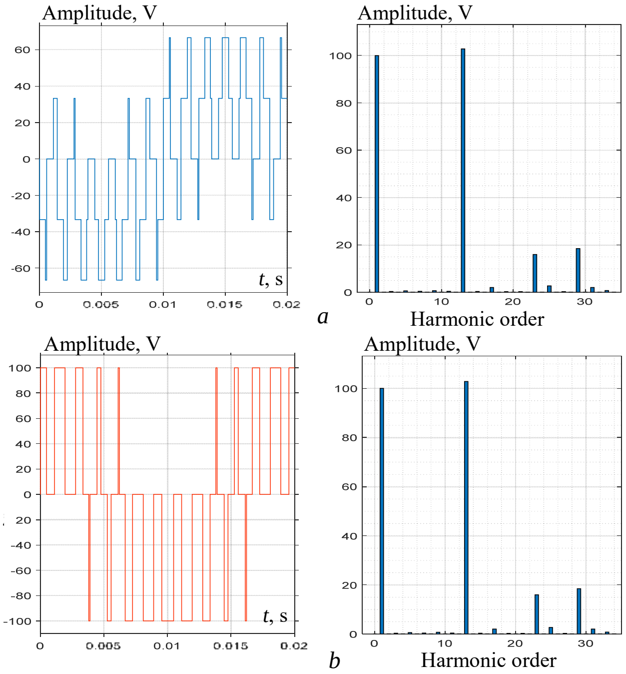

Fig. 4. Implementation of RTHE:
a – the phase-neutral output voltage waveform and FFT corresponding for $k = 13$; *b* – line-to-line output voltage waveform and FFT corresponding for $k = 13$

Experimental evaluation. The practical execution of the experiment was realized using the Dspace DS1104. Figure 5 depicts the experimental prototype of the system; its purpose was to confirm the validity of the simulation results. The model comprises a DC power supply, Dspace 1104 for producing gating signals to control the switching devices and three phase inverter consists of 6 MOSFET IRF840 switches controlled by driver circuits

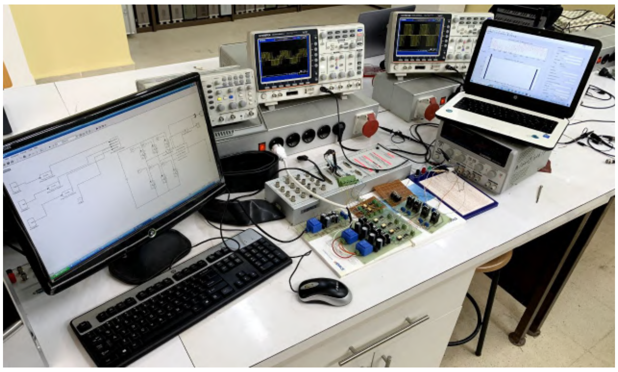

Fig. 5. Experimental prototype of the system

Figures 6,*a-c* show the experimental output voltage wave forms of the inverter, the phase-neutral voltage and the line-line voltage and their associated harmonic spectrum respectively. We note clearly that the harmonics 5th, 7th and 11th have been effectively eradicated.

Figures 7,*a-c* show the experimental output voltage wave forms of the inverter, the phase-neutral voltage and the line-line voltage and their associated harmonic spectrum respectively. We note clearly that the harmonics 5th, 7th, 11th, 13th and 17th have been effectively eradicated.

Figures 6, 7 illustrate congruence between the experimental results and simulations, providing compelling evidence to confirm the effectiveness of the proposed approach. The success in eliminating the specified harmonics clearly attests to the effectiveness of the suggested method.

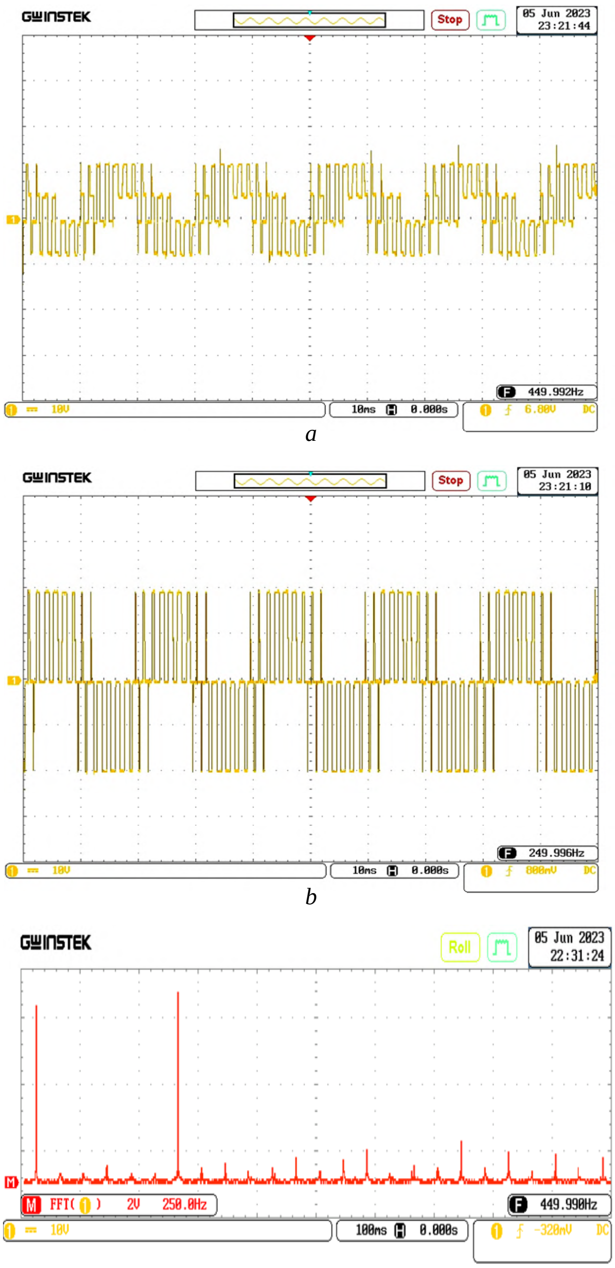

a

b

c

Fig. 6. Experimental implementation of RTHE:
a – the phase-neutral output voltage waveform for $k = 9$;
b – line-to-line output voltage waveform for $k = 9$;
c – harmonic spectrum

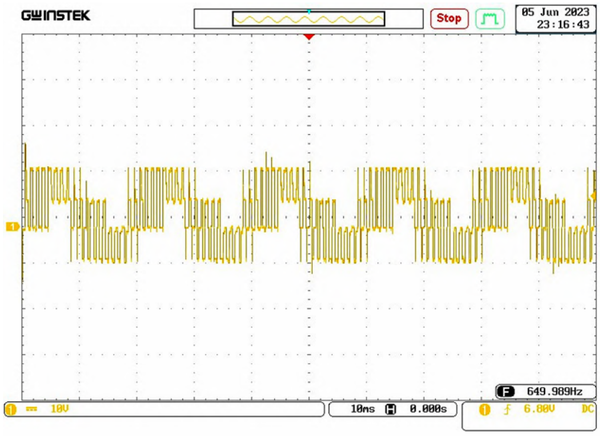

a

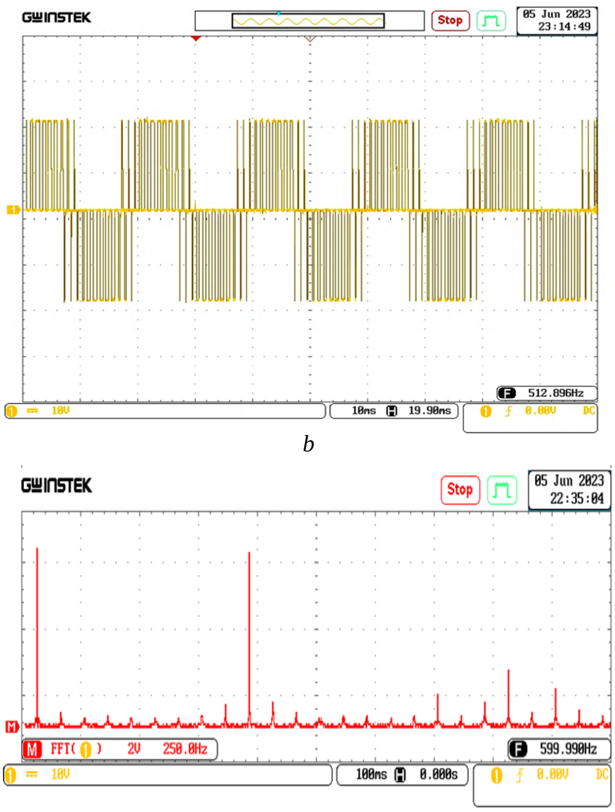

b

c

Fig. 7. Experimental implementation of RTHE:
a – the phase-neutral output voltage waveform for $k = 13$;
b – line-to-line output voltage waveform for $k = 13$;
c – harmonic spectrum

Conclusions.

1. This paper discusses a novel real-time implementation of SHE-PWM to eliminate the unwanted harmonics in the output voltage waveform of three phase inverter. This novel approach, known as RTHC, employs an alternative modulation strategy that streamlines the carrier generation process and facilitates the comparison between the carrier and the reference.

2. The suggested method commences by introducing a novel formula for the modified carrier waveform, resulting in a set of linear algebraic equations. To calculate the perturbation angles, the GA method is utilized. The perturbation angles have a crucial role in shaping the modified carrier. The proposed approach guarantees comprehensive control over both the elimination of harmonics and the fundamental component.

3. To evaluate the efficacy of the technique simulation and real-time hard ware implementations have been carried out. The simulation and experimental outcomes are highly satisfactory, conclusively demonstrating the soundness of the suggested approach. Presently, efforts are ongoing to develop solutions for the modified carrier waveform applicable across a broad spectrum in multi-level inverters.

Conflict of interest. The authors declare that they have no conflict of interest.

REFERENCES

1. Toubal Maamar A.E. Analysis and Experimental Validation of Selective Harmonic Elimination in Single-Phase Five-Level Inverter using Particle Swarm Optimization Algorithm.

Electronics, 2022, vol. 26, no. 2, pp. 65-72. doi: https://doi.org/10.53314/ELS2226065M.

2. Toubal Maamar A.E., Helaimi M., Taleb R., Mouloudj H., Elamri O., Gadoum A. Mathematical Analysis of N-R Algorithm for Experimental Implementation of SHEPWM Control on Single-phase Inverter. *International Journal of Engineering Trends and Technology*, 2020, vol. 68, no. 2, pp. 9-16. doi: https://doi.org/10.14445/22315381/IJETT-V68I2P202.

3. Parimalasundar E., Kumar N.M.G., Geetha P., Suresh K. Performance investigation of modular multilevel inverter topologies for photovoltaic applications with minimal switches. *Electrical Engineering & Electromechanics*, 2022, no. 6, pp. 28-34. doi: https://doi.org/10.20998/2074-272X.2022.6.05.

4. Hosseinzadeh M.A., Sarbanzadeh M., Salgueiro Y., Rivera M., Wheeler P. Selective Harmonic Elimination In Cascaded H-Bridge Multilevel Inverter Using Genetic Algorithm Approach. *2019 IEEE International Conference on Industrial Technology (ICIT)*, 2019, pp. 1527-1532. doi: https://doi.org/10.1109/ICIT.2019.8755089.

5. Sakri D., Laib H., Farhi S.E., Golea N. Sliding mode approach for control and observation of a three phase AC-DC pulse-width modulation rectifier. *Electrical Engineering & Electromechanics*, 2023, no. 2, pp. 49-56. doi: https://doi.org/10.20998/2074-272X.2023.2.08.

6. Yaqoob M.T., Rahmat M.K., Maharum S.M.M., Su'ud M.M. A Review on harmonics elimination in real time for cascaded H-bridge multilevel inverter using particle swarm optimization. *International Journal of Power Electronics and Drive Systems (IJPEDS)*, 2021, vol. 12, no. 1, pp. 228-240. doi: https://doi.org/10.11591/ijpeds.v12.i1.pp228-240.

7. Mohammed L.A., Husain T.A., Ibraheem T.A.M. Implementation of SHE-PWM technique for single-phase inverter based on Arduino. *International Journal of Electrical and Computer Engineering (IJECE)*, 2021, vol. 11, no. 4, pp. 2907-2915. doi: https://doi.org/10.11591/ijece.v11i4.pp2907-2915.

8. Shanono I.H., Abdullah N.R.H., Daniyal H., Muhammad A. Optimizing performance of a reduced switch multi-level inverter with moth-flame algorithm and SHE-PWM. *The Journal of Engineering*, 2023, no. 11, pp. 1-27. doi: https://doi.org/10.1049/tje2.12281.

9. Hassan E.D., Mohammed K.G., Ali I.I. Implementation of TMS320f28335 DSP code based on SVPWM Technique for Driving VSI with Induction Motor. *International Journal of Power Electronics and Drive Systems (IJPEDS)*, 2022, vol. 13, no. 3, pp. 1895-1903. doi: https://doi.org/10.11591/ijpeds.v13.i3.pp1895-1903.

10. Yan X., Guan B., Du X. Multi-mode Hybrid Modulation Strategy for Three-level Converters based on Half-wave Symmetric SHEPWM. *2021 IEEE 12th Energy Conversion Congress & Exposition - Asia (ECCE-Asia)*, 2021, pp. 349-354. doi: https://doi.org/10.1109/ECCE-Asia49820.2021.9479391.

11. Bouyakoub I., Taleb R., Mellah H., Zerglaine A. Implementation of space vector modulation for two level Three-phase inverter using dSPACE DS1104. *Indonesian Journal of Electrical Engineering and Computer Science*, 2020, vol. 20, no. 2, pp. 744-751. doi: https://doi.org/10.11591/ijeecs.v20.i2.pp744-751.

12. Maamar A.E.T., Kermadi M., Helaimi M., Taleb R., Mekhilef S. An Improved Single-Phase Asymmetrical Multilevel Inverter Structure With Reduced Number of Switches and Higher Power Quality. *IEEE Transactions on Circuits and Systems II: Express Briefs*, 2021, vol. 68, no. 6, pp. 2092-2096. doi: https://doi.org/10.1109/TCSII.2020.3046186.

13. Ganesh Babu B., Surya Kalavathi M. Hardware Implementation of Multilevel Inverter using NR, GA, Bee Algorithms. *2021 International Conference on Sustainable Energy and Future Electric Transportation (SEFET)*, 2021, pp. 1-6. doi: https://doi.org/10.1109/SeFet48154.2021.9375750.

14. Guan B., Yan X. Hybrid low switching frequency modulation strategy with high dynamic response for high-power voltage source converter. *IET Electric Power Applications*, 2023, vol. 17, no. 7, pp. 906-917. doi: https://doi.org/10.1049/elp2.12312.

15. Chatterjee S., Das A. A review on technological aspects of different PWM techniques and its comparison based on different performance parameters. *International Journal of Circuit Theory and Applications*, 2023, vol. 51, no. 5, pp. 2446-2498. doi: https://doi.org/10.1002/cta.3513.

Received 30.01.2024
Accepted 12.03.2024
Published 20.08.2024

L. Djafer[1], *PhD Student,*
R. Taleb[2], *Professor,*
F. Mehedi[3], *Associate Professor,*
[1] Electrical Engineering Department, Faculty of Technology,
Hassiba Benbouali University of Chlef,
Laboratoire Genie Electrique et Energies Renouvelables (LGEER),
Chlef, Algeria,
e-mail: lem.djafer@gmail.com (Corresponding Author)
[2] Electrical Engineering Department, Faculty of Technology,
Hassiba Benbouali University of Chlef,
Laboratoire Genie Electrique et Energies Renouvelables (LGEER),
and Unite de Recherche en Systemes Embarques de Chlef,
Centre de Recherche sur l'Information Scientifique et Technique
(CERIST), Chlef, Algeria,
e-mail: rac.taleb@gmail.com
[3] Faculty of Technology, Hassiba Benbouali University of Chlef,
Laboratoire Genie Electrique et Energies Renouvelables (LGEER),
Chlef, Algeria,
e-mail: f.mehedi@univ-chlef.dz

How to cite this article:
Djafer L., Taleb R., Mehedi F. Dspace implementation of real-time selective harmonics elimination technique using modified carrier on three phase inverter. *Electrical Engineering & Electromechanics*, 2024, no. 5, pp. 28-33. doi: https://doi.org/10.20998/2074-272X.2024.5.04

UDC 621.314 https://doi.org/10.20998/2074-272X.2024.5.05

F. Ebrahimi, N.A. Windarko, A.I. Gunawan

Wild horse optimization algorithm implementation in 7-level packed U-cell multilevel inverter to mitigate total harmonic distortion

Introduction. *Multilevel inverters (MLIs) are a popular industrial and, more especially, renewable energy application solution. This is because of its appetite for filters, low distortion class, and capacity to provide a multilayer output voltage that resembles a pure sine waveform.* ***The novelty*** *is in applying the wild horse optimization algorithm (WHOA) to adjust the sinusoidal pulse width modulation (SPWM) technique by producing the optimal reference signal parameters in a new multilevel inverter architecture known as the packed U-cell multilevel inverter (PUC-MLI).* ***Purpose.*** *This study helps with the idea of new inverter architecture and a modified pulse width modulation (MPWM) method to make the multilevel inverter smaller, cheaper, and with less total harmonic distortion (THD).* ***Methods.*** *We use the proposed approach to control a 7-level, single-phase PUC-MLI. The WHOA is used to discover the optimal parameters of the additional reference sine signal after being compared with SPWM to evaluate its performance in harmonic reduction. The simulation's outcome was validated by building a PUC-MLI prototype.* ***Results.*** *Experimental results and simulations validate the effectiveness of the suggested approach. The WHOA-improved MPWM approach achieves a significant reduction in THD on the PUC-MLI output voltage, as indicated by the results.* ***Practical value.*** *THD in MLI output voltage will be reduced without spending any cost. The suggested solution works with many MLI topologies with varying output voltage levels.* References 20, tables 6, figures 12.

Key words: **packed U-cell multilevel inverter, total harmonic distortion, modified pulse width modulation, wild horse optimization algorithm.**

Вступ. *Багаторівневі інвертори (MLIs) є популярним рішенням для застосування у промисловості та, особливо, у відновлюваних джерелах енергії. Це пов'язано з його потребою у фільтрах, низьким класом спотворень та здатністю забезпечувати багатошарову вихідну напругу, що нагадує чистий синусоїдальний сигнал.* ***Новизна*** *полягає у застосуванні алгоритму оптимізації «дикого коня» (WHOA) для налаштування методу синусоїдальної широтно-імпульсної модуляції (SPWM) шляхом створення оптимальних параметрів опорного сигналу в новій архітектурі, відомої як упакований багаторівневий інвертор U-подібного типу (PUC-MLI).* ***Мета.*** *Це дослідження допомагає реалізувати ідею нової архітектури інвертора та модифікованого методу широтно-імпульсної модуляції (MPWM), що дозволяє зробити багаторівневий інвертор меншим, дешевшим і з меншим загальним гармонічним спотворенням (THD).* ***Методи.*** *Ми використовуємо запропонований підхід для керування 7-рівневим однофазним PUC-MLI. WHOA використовується для визначення оптимальних параметрів додаткового еталонного синусоїдального сигналу після порівняння зі SPWM для оцінки його ефективності зниження гармонік. Результати моделювання були підтверджені створенням прототипу PUC-MLI.* ***Результати.*** *Експериментальні результати та моделювання підтверджують ефективність запропонованого підходу. Удосконалений WHOA підхід MPWM дозволяє досягти значного зниження THD вихідної напруги PUC-MLI, про що свідчать результати.* ***Практична цінність.*** *THD вихідної напруги MLI буде знижено без будь-яких витрат. Пропоноване рішення працює з багатьма топологіями MLI з різними рівнями вихідної напруги.* Бібл. 20, табл. 6, рис. 12.

Ключові слова: **упакований багаторівневий інвертор U-cell, повне гармонічне спотворення, модифікована широтно-імпульсна модуляція, алгоритм оптимізації «дикого коня».**

Abbreviations

CHB	Cascaded H-bridge	PUC	Packed U-cell
FFT	Fast Fourier Transform	PUC-MLI	Packed U-cell Multilevel Inverter
FLC	Flying Capacitor	PWM	Pulse Width Modulation
MPWM	Modified Pulse Width Modulation	SPWM	Sinusoidal Pulse Width Modulation
MLI	Multilevel Inverter	THD	Total Harmonic Distortion
NPC	Neutral Point Clamped	WHOA	Wild Horse Optimization Algorithm

Introduction. Afghanistan, one of the least developed nations, has serious economic problems. Industry is essential to its growth, but the lack of power impedes development because of an imbalance between supply and demand. Afghanistan has a lot of solar potential, so the government is pursuing a 2000 MW renewable energy initiative as a solution to this. By allowing the establishment of factories in isolated locations without long transmission lines, solar energy may stimulate the local economy. The factory needs electricity in the AC range. Inverters are devices that change DC voltage into AC voltage. The application of inverters is wide; however, it can be used where DC power is a supplier and AC power is the consumer; for instance, it can be used for renewable energy applications. Grid-connected or standalone systems widely use MLIs as voltage converters to provide AC loads with power from renewable energy sources such as wind turbines and solar panels [1]. High-efficiency power conversion systems achieve exceptional performance by minimizing THD and reducing conduction losses during switching; these systems can maximize their energy conversion capacities and achieve improved overall efficiency and performance by regulating these elements properly [2].

Because the MLI can generate output waveforms with lower THD and higher quality, they are becoming more and more popular. Electrical loads in the AC output voltage require a sinusoidal waveform. All the same, MLI may provide an output voltage that looks like a staircase and is almost exactly like a sine wave. The generation of switching patterns results in an output voltage from the staircase that is not a perfect sine wave. The staircase sine wave contains harmonics. Researchers have developed other MLI variants, including PUC-MLI, FLC MLI and CHB MLI to address this problem [3]. The complex structure of MLI circuits has led some academics to recommend reducing the number of components in them [4]. Even still, the PUC-MLI architecture necessitates a low quantity of devices in order to provide a high output voltage among MLIs [5] that will address the size and cost of construction of MLI issues.

The efficient control of switching patterns to reduce the THD of the output voltage is a major area of active study in MLIs, in addition to the exploration of topological solutions [6]. Space vector modulation [7], selective harmonic elimination, PWM [8] are some of the methods that have been suggested to reduce THD in MLI. Lower-order harmonic suppression in the straight-line output voltage of MLIs has been the explicit focus of several reported modulation techniques [9]. It is also standard practice to use injection techniques that include the modulated signal's integration of several reference signals [10].

In order to reduce THD in MLI, several studies have suggested novel injection techniques. The third harmonic injection space vector PWM [11], the third harmonic injection PWM [12], and the generalized discontinuous PWM [13] are a few instances of distinct PWM approaches. Each strategy significantly impacts the THD value of the output voltage.

Recently, researchers have optimized the THD of the output voltage in MLI by applying meta-heuristic methods in modulation approaches. Particle swarm optimization was used in [14] to improve the design of grid-connected photovoltaic systems. The whale optimization algorithm has been used in PUC-MLI to reduce the THD of the output voltage of MLI; the result is presented only in MATLAB simulation [15], and the researcher modified the switching pattern of MLI in order to reduce the THD in [16] focused on using evolutionary algorithms to get rid of harmonics in PUC-MLI. The result was presented through the simulation only as well; in another study, the researcher analyzed the THD of CHB MLI [17], and in another study, the grey wolf optimizer was used to improve the switching sequence of the NPC MLI in order to reduce the THD. They succeeded in reducing THD from 31.42 % to 26.44 % [18]. However, they used a grey wolf optimizer to optimize only 2 parameters of the injected signal, which are amplitude and phase shafted angle. Unfortunately, no studies have been done on the use of WHOA in PUC-MLI injection technique optimization, where the simulation result is confirmed by building a prototype PUC-MLI.

The goal of the paper. Utilizing the WHOA to optimize injection procedures in PUC-MLI has yet to be the subject of any study. This research aims to improve all parameters of the injected sine signal and lower THD in PUC-MLI by presenting a novel method that uses the WHOA. We will build and test a prototype PUC-MLI to verify the efficacy of the suggested approach. This will validate the simulation results and show how the WHOA will be used in practice to optimise switching patterns in PUC-MLI's switches.

Subject of investigations. The application of WHOA to optimize the injected signal parameters (amplitude, frequency and phase shifted angle) for a 7-level PUC-MLI is the focus of the study. Building a prototype, PUC-MLI will be used to validate the modelling outcome.

Methodology. Packed U-cell multilevel inverter. An electronic device or circuit that changes DC voltage into AC voltage is known as an inverter. Conventional inverters often offer 3 output voltage levels: zero, negative and positive states of output voltages ($-V_{dc}$ and $+V_{dc}$). An MLI is a type of special inverter that can simultaneously produce different voltage and current levels. Table 1 shows the number of devices required by different types of inverters (NPC, FLC, CHB) and PUC-MLI to achieve 7 output voltage levels.

Table 1

The number of devices corresponding to various categories of MLIs

Components	FLC	NPC	CHB	PUC
IGBTs	24	24	12	6
Capacitors	30	6	3	2
Clamping diodes	0	20	0	0
Total component	54	50	15	8

The PUC-MLI architecture requires only 8 devices to generate 7 output levels. By comparison, the NPC needs 50 devices, the FLC needs 54 and the CHB needs 15. Because of the U-shaped architecture of each unit, the inverter is called a «packed U-cell». Depending on the number of voltage sources (capacitors) and switches utilized, the voltage levels in the packed U-cell design may change. First presented the recommended inverter in 2010, which was then improved upon in 2022 [19]. The PUC-MLI design, which produces 7 output voltage levels by using 2 DC voltage sources and 6 switches, is shown in Fig. 1.

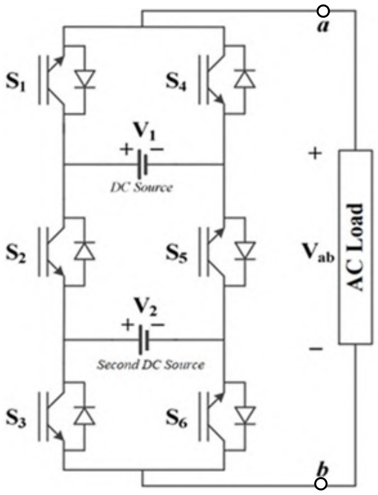

Fig. 1. PUC-MLI design

Table 2 states that this study suggests building a single-phase PUC-MLI structure with 8 output voltage states, which is constructed based on a sequence of connections between cells. As a precaution against DC bus short circuits, switches S4, S5 and S6 in Table 2 function in reverse relative to S1, S2 and S3. Even though the PUC may produce different voltage levels from different DC sources, in order to achieve maximum output voltage (V_{ab}), the second DC bus amplitude must be one-third of the first ($V_1 = 3V_2$). V_{ab} has 7 voltage levels as a result of this configuration: 0, $\pm V_2$, $\pm 2V_2$, $\pm 3V_2$.

Table 2

PUC-MLI produces voltage levels

S1	S2	S3	S4	S5	S6	V_{ab}
1	0	0	0	1	1	V_1
1	0	1	0	1	0	$V_1 - V_2$
1	1	0	0	0	1	V_2
1	1	1	0	0	0	0
0	0	0	1	1	1	0
0	0	1	1	1	0	$-V_2$
0	1	0	1	0	1	$V_2 - V_1$
0	1	1	1	0	0	$-V_1$

Modified PWM technique. The presence of harmonic distortion in the output voltage of the PUC-MLI is a direct consequence of the switching process. As such, the use of a suitable modulation approach becomes imperative in order to reduce the negative impacts of harmonic distortion. A viable remedy is presented in this research paper – the MPWM approach. While the standard method of modulation is SPWM, it compares the triangle carrier signal with the sine reference signal. In the case of PUC-MLI only a few semiconductor components are required, specifically one reference signal and 6 carrier signals. Figure 2 demonstrates the MPWM techniques.

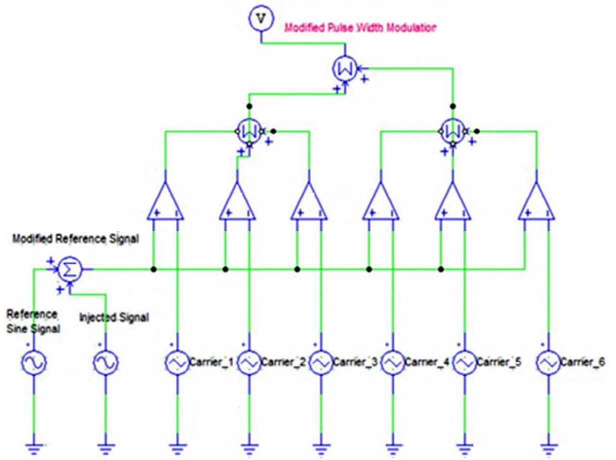

Fig. 2. The procedure for MPWM

The reference sine signal is altered when the injected sine signal and the reference sine signal are added together. The injected sine signal contains parameters for frequency, phase shift and amplitude, whereas the reference signal is a sinusoidal waveform with a fundamental frequency. The injected signal might be either a singular signal or numerous signals. The mathematical expressions representing these signals are as follows:

$$S_r(t) = A_1 \sin(2\pi f_1 t); \tag{1}$$

$$S_i(t) = \sum_{n=2}^{\infty} A_n \sin(2\pi f_n t + \theta_n), \tag{2}$$

where $S_r(t)$ is the reference signal; $S_i(t)$ is the injected signal.

Equation (1) represents a sinusoidal reference signal with amplitude A_1 of 3 and a fundamental frequency f_1 of 50 Hz. The signal in (2) represents the injected signal. The objective of the injected signal is to alter the reference waveform. The signal is characterized by its amplitude A_n, frequency f_n and phase shift θ_n. These parameters will be determined through the process of wild horse optimizer tracking to find their optimal values. Two signals are combined, yielding the mathematical expression in (3), as exemplified in (4):

$$S_M(t) = A_1 \sin(2\pi f_1 t) + \sum_{n=2}^{\infty} A_n \sin(2\pi f_n t + \theta_n); \tag{3}$$

$$S_M(t) = 3\sin(2\pi 50 t) + \sum_{n=2}^{\infty} 0.35 \sin(2\pi 999.72 t + 4.80); \tag{4}$$

where $S_M(t)$ is the modified signal.

The process of generating MPWM is depicted in Fig. 3. Figure 3,*a* depicts a sine wave that serves as a reference as stated in (1). The wave has amplitude of 3, a frequency of 50 Hz and a phase-shifted angle of 0. Figure 3,*b* shows a signal waveform that has been injected according to (2). This waveform has amplitude of 0.35 V, a frequency of 999.72 Hz and a phase shift of 271.37° (equivalent to 4.80 rad). Both signals are shown in Fig. 3,*c*. They are combined to make a new reference signal, which is shown in (3). This signal will be compared to the triangular carrier signal in the form of MPWM.

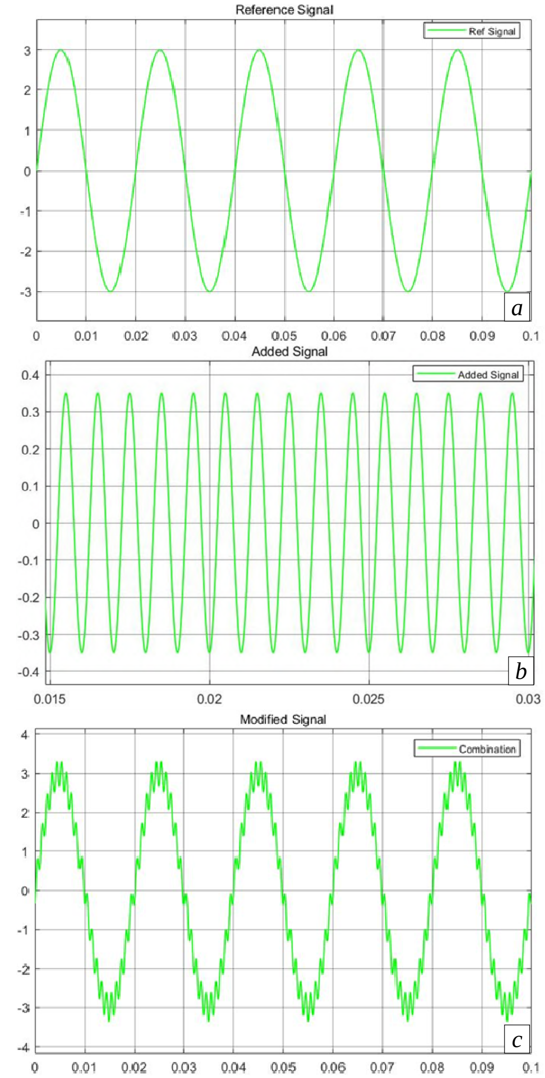

Fig. 3. MPWM signal generation process demonstrates:
a – the reference sine signal; *b* – the injected signal;
c – the modified reference signal

Wild horse optimization algorithm. The WHOA is a meta-heuristic optimization method that draws inspiration from wild horse behaviour. A dominant stallion leads a group of horses, and other horses (foals and mares) follow him. This social hierarchy and herd behaviour of wild horses are the basis for the algorithm [20]. A stallion is in charge of the herd of wild horses, which also includes mares and foals. The suggested method in this study is implemented as a flowchart (Fig. 4). According to this algorithm, like all meta-heuristic algorithms, starts with population initialization. This creates the first group of possible solutions, each represented by a set of values for the injected signal's amplitude, frequency and phase angle. Then, the fitness of each candidate solution is evaluated by injecting its corresponding signal into the reference sinusoidal signal and measuring the performance of the modified switching pattern.

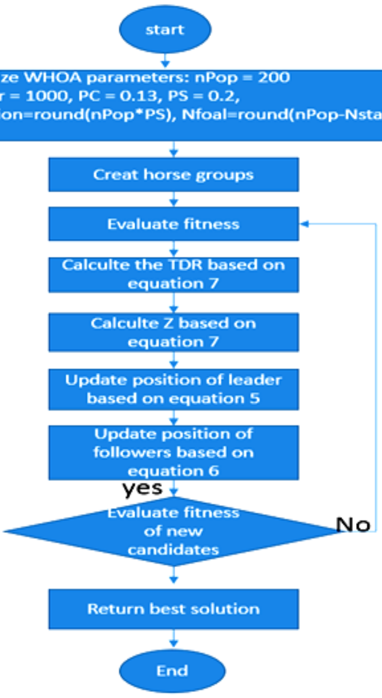

Fig. 4. Flowchart of the WHOA

After that, update the position of the leader, select the best candidate solution as the leader, and update its position using (5). Evaluate the fitness of the new candidate solutions generated using the following equations. Then repeat searching for a set number of iterations, updating the positions of the leader and followers using (6) at each iteration. Finally, return the best of the found solutions. After finding the modified value, evaluate the performance of the optimized switching pattern, add the modified signal to the reference sinusoidal signal, and measure the performance of the modified switching pattern using the MATLAB simulation FFT analyzer tool. The equations are:

$$\overrightarrow{Stallion_{Gi}} = \\ = \begin{cases} 2Z\cos(2\pi RZ)\cdot\left(WH - Stallion_{Gi}\right) + WH; \text{if } R3 > 0.5; \\ 2Z\cos(2\pi RZ)\cdot\left(WH - Stallion_{Gi}\right) - WH; \text{if } R3 \le 0.5, \end{cases} \quad (5)$$

where the subsequent location of the i group's leader, indicated as $\overrightarrow{Stallion_{Gi}}$, is established based on the present coordinates of the leader $Stallion_{Gi}$, the location of the water hole (WH), a dynamically computed adaptive mechanism (Z) utilizing (7), a uniformly distributed random number (R) ranging from –2 to 2.

Updating the positions of the followers can be done by comparing the positions of the remaining candidates based on their distance from the leader and a random term. The position of a follower is updated using (6):

$$\overrightarrow{X_{i,G}^{j}} = 2Z\cos(2\pi RZ)\cdot\left(Stallion^{j} - X_{i,G}^{j}\right) + Stallion; \quad (6)$$

$$P = \overrightarrow{R1} < TDR; IDX = P = 0; Z = R2\theta IDX + \overrightarrow{R3}\theta(\sim IDX), \quad (7)$$

where the variable $X_{i,G}^{j}$ signifies the current position of a group member, whether it's a foal or a mare. The notation $Stallion^j$ is employed to denote the location of the stallion, who serves as the group's leader. Z is a variable that dynamically changes depending on the size of the problem; it is not a continuous value. It is an essential component of the wild horse optimizer's scalability because of its function as a mechanism, which allows the algorithm to retain constant performance across various issue dimensions. It can be define as adaptive mechanism calculated through the use of (7). R is a randomly generated number with a uniform distribution within the range of [–2, 2], determining the angles at which horses graze around the group leader in a 360° fashion. Lastly, $\overrightarrow{X_{i,G}^{j}}$ indicates the updated position of a group member during grazing, as elaborated in reference [20].

Simulation results. MATLAB program is utilized for simulating the improved MPWM approach using an algorithm. The simulation utilizes the PUC-MLI with settings specified in Table 3.

Table 3
Simulation parameters for PUC-MLI

Components	Value
V_{DC1}	180
V_{DC2}	60

The initial DC supply values are 180 V for the first supply and 60 V for the second supply. To streamline the optimization process, the injected signal was treated as a singular waveform. WHOA optimizes the injected signal's frequency, amplitude and phase shift. Figure 5 displays an illustration of the outcomes of the tracking procedure for the injected signal. Figure 5,*a* represents the WHOA tracking process to find the best amplitude; Fig. 5,*b* represents the tracking process for the frequency; Fig. 5,*c* represents the tracking process for the phase shift of the added signal; and Fig. 5,*d* illustrates the THD reduction over iterations. All parameters, such as amplitude, frequency and phase shift are searched starting from 0 and then approached to their best value.

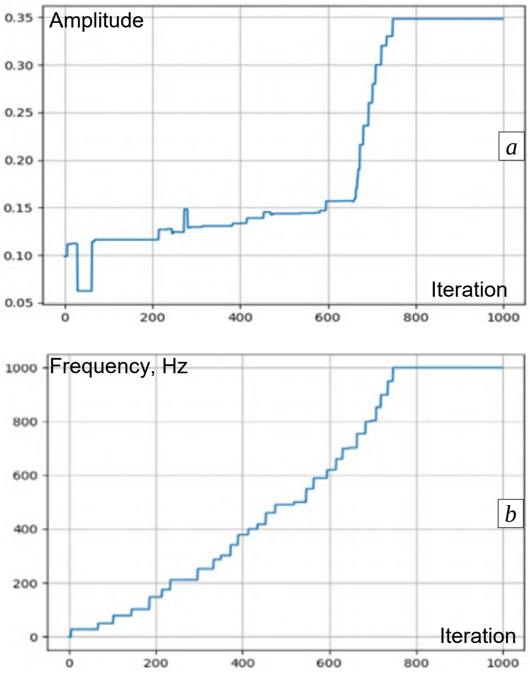

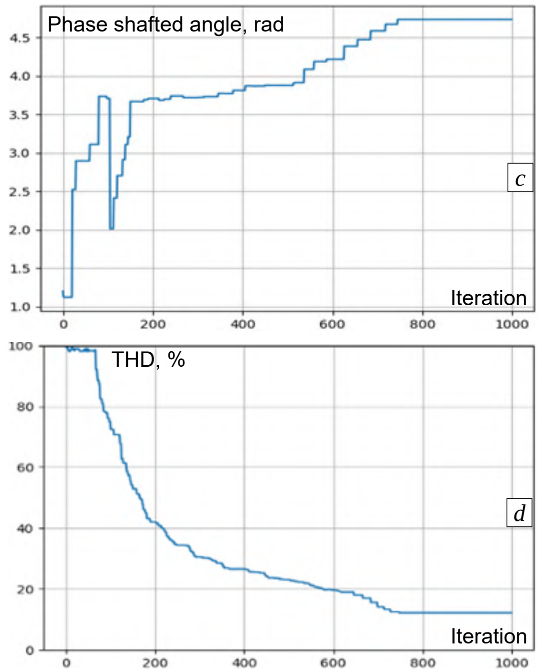

Fig. 5. Simulation results of the optimized injected signal

WHOA's performance was assessed against SPWM, resulting in a decrease in THD from 17.89 % to 12.25 %. To prevent getting trapped in local optima, WHOA was executed a hundred times, and the outcomes are presented in Fig. 6, where THD exceeds SPWM are marked as errors and highlighted with a chocolate colour bar chart. Conversely, lower THD values than SPWM signify success, but not the optimal solution, marked with a yellow colour bar chart, and the best solutions (global optima) are highlighted with a black colour bar chart. WHOA successfully attained the global optimum by reducing THD to 12.25 %. The values for amplitude, frequency, and phase-shift angle derived from WHOA were $A = 0.35$, $f = 999.72$, $\theta = 4.80$, detailed in Fig. 5,*a*–*c*.

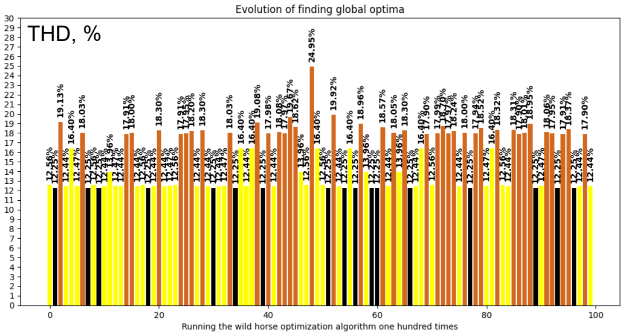

Fig. 6. The procedure for identifying global optima

The corresponding result is shown in Fig. 8,*b*. A comparison between the PUC-MLI output voltage waveform using SPWM and MPWM was conducted in MATLAB/Simulink. As both output voltages possess the same amplitude modulation, distinctions in the effects of the injected signal on MPWM can be identified by analyzing different patterns. Figure 7 demonstrates the inverter's output voltage – Fig. 7,*a* represents the inverter output in SPWM, while Fig. 7,*b* illustrates the output using MPWM.

Table 4 furnishes a comparison of THD levels in the PUC-MLI's output voltage, showing SPWM at 17.89 % and MPWM at 12.25 %.

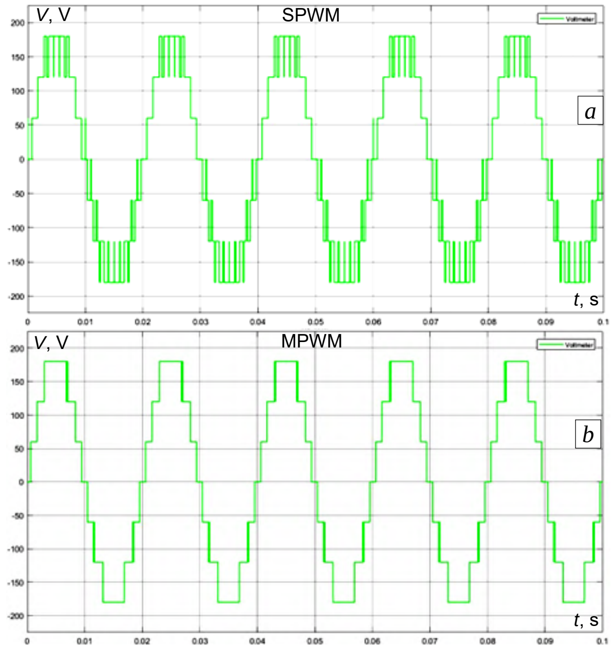

Fig. 7. Voltage output of PUC-ML

Table 4

Comparison of THD for the modulation technique

Modulation technique	THD, %
SPWM	17.89
MPWM	12.25

Furthermore, Fig. 8,*a* illustrates the harmonic spectrum of SPWM, while Fig. 8,*b* depicts the harmonic spectrum of the MPWM.

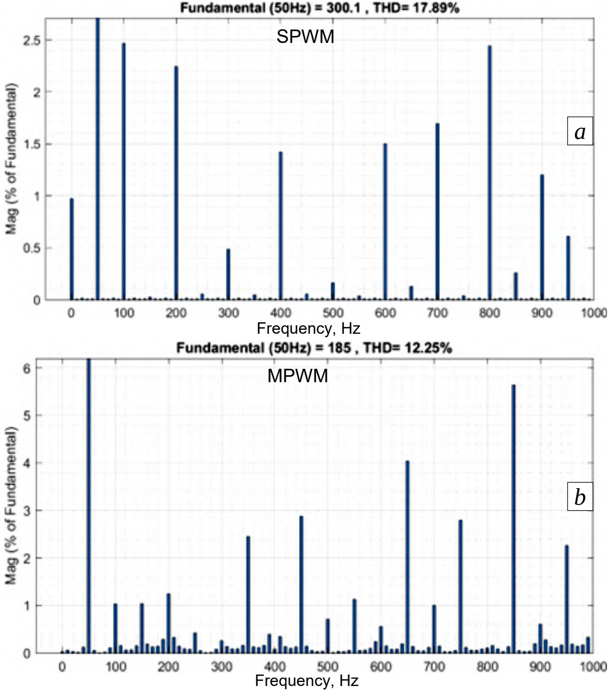

Fig. 8. Spectral analysis of harmonics

Experimental results. To confirm the WHOA's simulation findings and the recommended modulation strategy, a single-phase, 7-level PUC-MLI prototype was built. Software called AutoCAD Eagle was used to design the inverter. Table 5 lists the components that went into building PUC-MLI. Figure 9 shows the experimental system configuration and a close-up of PUC-MLI, shown in Fig. 10, respectively. For PUC-MLI switches, the

STM32F407G microcontroller on the Discovery board has generated switching pulses. This microcontroller is programmed using the C programming language and STM32CubeIDE version 1.1 software. The waveform and harmonic spectrum are measured and analyzed using a Rigol DS 1052E oscilloscope; the data from the oscilloscope is recorded, and then the amount of THD is measured using MATLAB software. Two programmable DC power sources that maintain a steady DC voltage (TDK-Lambda and GW Instek PSS-3203) supply the PUC-MLI. PUC MLI is tested with 2 DC input voltages, 20 V and 60 V, and a 500 W resistive load (see Fig. 9).

Table 5

Inventory of components utilized in the experiment

Components	Specifications
IGBT Switches	SGL160N60UFD (Faichild)
Microcontroller	Discovery STM32F407G
Optocoupler	FOD3182
Gate Drive Power Supply	DC 12V, HLK-PM12

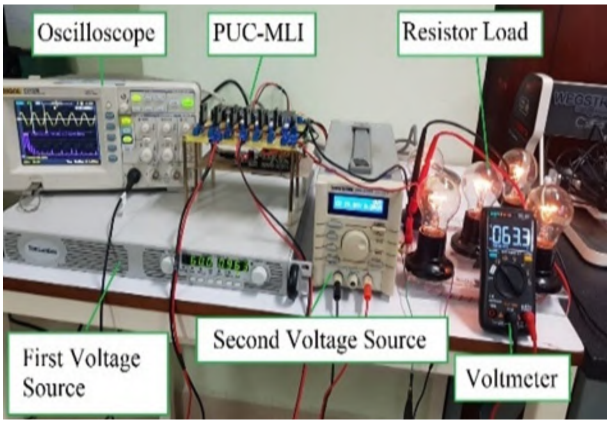

Fig. 9. Arrangement and configuration of the experimental setup

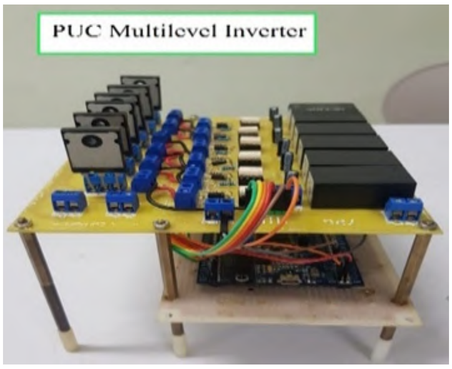

Fig. 10. PUC-MLI hardware

The prototype PUC-MLI is utilized to validate the modulation of both SPWM and MPWM techniques using the optimal parameters obtained from simulation results. Both SPWM and MPWM are applied with an amplitude modulation of 1. In addition, the MPWM incorporates a 999.72 Hz injected signal with amplitude of 0.35 V and a phase shift of 271.37°. Figures 11,*a*,*b* present the experimental comparison between the output voltage of SPWM and MPWM, which aligns with the simulation results (see Fig. 7). The THD is determined by recording the output voltage. Figure 12 illustrates the spectrum and THD results, indicating that both modulation techniques exhibit a low-level harmonic spectrum at high frequencies. This high-frequency harmonic content offers an advantage in distortion suppression by employing a compact LC filter. Notably, the THD of the MPWM, as listed in Table 6, measures 16.84 %, demonstrating that the optimized WHOA-based switching of the MPWM achieves a lower THD compared to SPWM, which has a THD of 18.44 %, which is a great success.

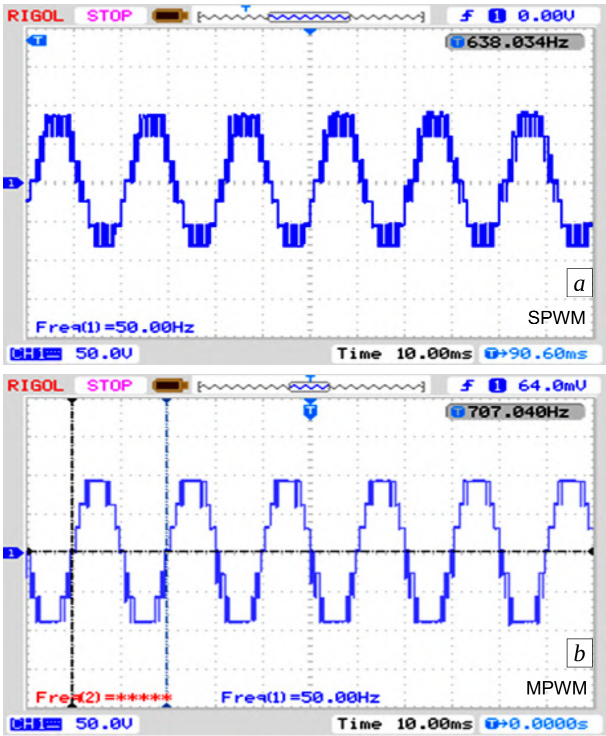

Fig. 11. The output voltage of PUC-MLI observed on the oscilloscope: *a* – SPWM; *b* – MPWM

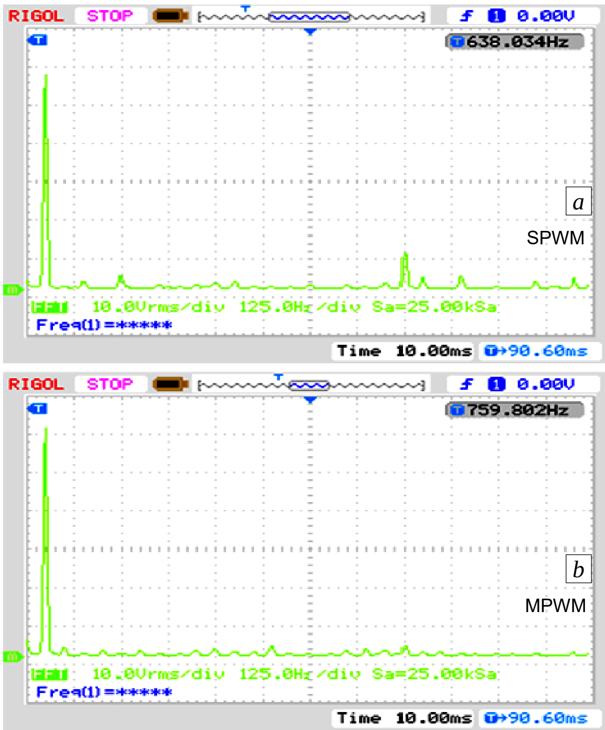

Fig. 12. Measurement of THD using the oscilloscope's FFT tools: *a* – THD of SPWM; *b* – THD of MPWM

Table 6

Experimental results for THD measurements

Method	THD, %
SPWM	18.44
MPWM	16.84

Conclusions.

1. Based on the findings of this research, the PUC topology of MLI is the best topology against other topologies of MLI, namely CHB, FLC and NPC, in order to overcome the size and cost of construction issues.
2. The WHOA can effectively reduce the THD in a PUC-MLI by improving the switching pattern of the inverter's switches. To validate this conclusion, a prototype PUC-MLI was built, and the proposed method was implemented.
3. The performance of the WHOA algorithm was compared with the SPWM in terms of THD reduction. The results indicate that the WHOA algorithm outperformed SPWM in terms of THD reduction performance. Therefore, the WHOA algorithm is a promising approach for reducing THD in PUC-MLIs.
4. Moreover, the reduced THD of PUC-MLI can support the advancement of applications for electrical vehicles in industry as well as renewable energy.

Acknowledgments. Authors would like to thank the Ministry of Education, Culture, Research, and Technology of the Republic of Indonesia for providing us with the Kemitraan Negara Berkembang (KNB) scholarship and grant for this research.

Conflict of interest. The authors declare that they have no conflict of interest.

REFERENCES

1. Bughneda A., Salem M., Richelli A., Ishak D., Alatai S. Review of Multilevel Inverters for PV Energy System Applications. *Energies*, 2021, vol. 14, no. 6, art. no. 1585. doi: https://doi.org/10.3390/en14061585.

2. Leon J.I., Vazquez S., Franquelo L.G. Multilevel Converters: Control and Modulation Techniques for Their Operation and Industrial Applications. *Proceedings of the IEEE*, 2017, vol. 105, no. 11, pp. 2066-2081. doi: https://doi.org/10.1109/JPROC.2017.2726583.

3. Harbi I., Rodriguez J., Liegmann E., Makhamreh H., Heldwein M.L., Novak M., Rossi M., Abdelrahem M., Trabelsi M., Ahmed M., Karamanakos P., Xu S., Dragičević T., Kennel R. Model-Predictive Control of Multilevel Inverters: Challenges, Recent Advances, and Trends. *IEEE Transactions on Power Electronics*, 2023, vol. 38, no. 9, pp. 10845-10868. doi: https://doi.org/10.1109/TPEL.2023.3288499.

4. Omer P., Kumar J., Surjan B.S. A Review on Reduced Switch Count Multilevel Inverter Topologies. *IEEE Access*, 2020, vol. 8, pp. 22281-22302. doi: https://doi.org/10.1109/ACCESS.2020.2969551.

5. Vahedi H., Al-Haddad K. *Method and system for operating a multilevel inverter*. US Patent, no. 20160126862, 2015.

6. Savitha M., Nagaraja Rao S. Switching angle optimization and fault analysis of a multistring-multilevel inverter for renewable-energy-source applications. *Clean Energy*, 2022, vol. 6, no. 6, pp. 907-930. doi: https://doi.org/10.1093/ce/zkac055.

7. Srinivas G., Durga Sukumar G., Subbarao M. Total harmonic distortion analysis of inverter fed induction motor drive using neuro fuzzy type-1 and neuro fuzzy type-2 controllers. *Electrical Engineering & Electromechanics*, 2024, no. 1, pp. 10-16. doi: https://doi.org/10.20998/2074-272X.2024.1.02.

8. Shanono I.H., Abdullah N.R.H., Daniyal H., Muhammad A. Selective harmonic elimination (SHE) based 3-phase multilevel voltage source inverter (VSI) for standalone applications. *SN Applied Sciences*, 2019, vol. 1, no. 12, art. no. 1670. doi: https://doi.org/10.1007/s42452-019-1726-3.

9. Muralikumar K., Ponnambalam P. Analysis of Cascaded Multilevel Inverter with a Reduced Number of Switches for Reduction of Total Harmonic Distortion. *IETE Journal of Research*, 2023, vol. 69, no. 1, pp. 295-308. doi: https://doi.org/10.1080/03772063.2020.1819450.

10. Siddique M.D., Mekhilef S., Rawa M., Wahyudie A., Chokaev B., Salamov I. Extended Multilevel Inverter Topology With Reduced Switch Count and Voltage Stress. *IEEE Access*, 2020, vol. 8, pp. 201835-201846. doi: https://doi.org/10.1109/ACCESS.2020.3026616.

11. Nishizawa K., Itoh J., Odaka A., Toba A., Umida H. Input Current Harmonic Reduction based on Space Vector PWM for Three-level Inverter Operating over a Wide Range Power Factor. *IEEJ Journal of Industry Applications*, 2020, vol. 9, no. 3, pp. 208-218. doi: https://doi.org/10.1541/ieejjia.9.208.

12. Iqbal W., Qureshi I.M., Majeed H.B.A., Khan A. Performance Evaluation of Third Harmonic Injection PWM Technique for Three Phase Multilevel Inverter. *2021 International Conference on Frontiers of Information Technology (FIT)*, 2021, pp. 78-83. doi: https://doi.org/10.1109/FIT53504.2021.00024.

13. Xu J., Soeiro T.B., Gao F., Tang H., Bauer P. Carrier-Based Generalized Discontinuous PWM Strategy for Single-Phase Three-Legs Active Power Decoupling Converters. *IEEE Transactions on Industrial Electronics*, 2021, vol. 68, no. 11, pp. 11609-11613. doi: https://doi.org/10.1109/TIE.2020.3038099.

14. Gireesh Kumar D., Venkata Sireesha N., Ganesh A., Kotb H., AboRas K.M., Zeinoddini-Meymand H., Kamel S. Design of an Optimized Asymmetric Multilevel Inverter with Reduced Components Using Newton-Raphson Method and Particle Swarm Optimization. *Mathematical Problems in Engineering*, 2023, pp. 1-18. doi: https://doi.org/10.1155/2023/9966708.

15. Ebrahimi F., Windarko N.A., Gunawan A.I. Minimizing Total Harmonic Distortion of 7-Level Packed U-Cell Multilevel Inverter Using Whale Optimization Algorithm. *Indonesian Journal of Computer Science*, 2023, vol. 12, no. 6, pp. 3217-3231. doi: https://doi.org/10.33022/ijcs.v12i6.3507.

16. Ebrahimi F., Windarko N.A., Gunawan A.I. Reducing THD of 7-Level Packed U-cell Multilevel Inverter Using Genetic Algorithm. *2023 International Electronics Symposium (IES)*, 2023, pp. 88-93. doi: https://doi.org/10.1109/IES59143.2023.10242460.

17. Ahamad I., Ansari A.J., Iqbal A. THD Analysis of 5-Level, 7-Level and 9-Level CHB-Multilevel Inverters Using SPWM Switching Approach. *Lecture Notes in Electrical Engineering*, 2021, vol. 723 LNEE, pp. 719-728. doi: https://doi.org/10.1007/978-981-33-4080-0_69.

18. Izzaqi F.A., Windarko N.A., Qudsi O.A. Minimization of total harmonic distortion in neutral point clamped multilevel inverter using grey wolf optimizer. *International Journal of Power Electronics and Drive Systems (IJPEDS)*, 2022, vol. 13, no. 3, pp. 1486-1497. doi: https://doi.org/10.11591/ijpeds.v13.i3.pp1486-1497.

19. Ait bellah F., Abouloifa A., Echalih S., Hekss Z., Naftahi K., Lachkar I. Control Design of a Seven-Level Packed U Cell Inverter. *IFAC-PapersOnLine*, 2022, vol. 55, no. 12, pp. 677-682. doi: https://doi.org/10.1016/j.ifacol.2022.07.390.

20. Naruei I., Keynia F. Wild horse optimizer: a new meta-heuristic algorithm for solving engineering optimization problems. *Engineering with Computers*, 2022, vol. 38, no. S4, pp. 3025-3056. doi: https://doi.org/10.1007/s00366-021-01438-z.

Received 11.02.2024
Accepted 25.04.2024
Published 20.08.2024

F. Ebrahimi[1]*, M. Eng.,*
N.A. Wndarko[1]*, PhD, Professor,*
A.I. Gunawan[1]*, PhD, Doctor,*
[1] Politeknik Elektronika Negeri Surabaya,
Raya ITS Str., Surabaya, 60111, Indonesia,
e-mail: faizuddin@pasca.student.pens.ac.id (Corresponding Author);
Ayub@pens.ac.id; Agus_ig@pens.ac.id

How to cite this article:
Ebrahimi F., Windarko N.A., Gunawan A.I. Wild horse optimization algorithm implementation in 7-level packed U-cell multilevel inverter to mitigate total harmonic distortion. *Electrical Engineering & Electromechanics*, 2024, no. 5, pp. 34-40. doi: https://doi.org/10.20998/2074-272X.2024.5.05

UDC 621.314 https://doi.org/10.20998/2074-272X.2024.5.06

S. Muthukaruppasamy, R. Dharmaprakash, S. Sendilkumar, E. Parimalasundar

Enhancing off-grid wind energy systems with controlled inverter integration for improved power quality

Introduction. *Off-grid wind energy systems play a pivotal role in providing clean and sustainable power to remote areas. However, the intermittent nature of wind and the absence of grid connectivity pose significant challenges to maintaining consistent power quality. The wind energy conversion system plays a central role in tapping renewable energy from wind sources. Operational parameters such as rotor and stator currents, output voltages of rectifiers and converters, and grid phase voltage variations are crucial for stable power generation and grid integration. Additionally, optimizing power conversion output through voltage gain analysis in boost converters is essential. Moreover, ensuring electricity quality via total harmonic distortion reduction in inverters is vital for grid compatibility.* ***Goal****. Enhancing the power quality of grid-integrated wind energy conversion systems.* ***Methods.*** *The proposed topology is implemented in MATLAB/Simulink with optimized control strategies for enhancing power quality in off-grid wind energy systems.* ***Results****. Control strategies with a grid-connected wind energy conversion system yields substantial improvements in power quality. This includes effectively mitigating voltage fluctuations and harmonics, resulting in smoother operation and reduced disturbances on the grid.* ***Practical value.*** *The proposed topology has proven to be extremely useful for off grid-integrated wind system.* References 18, table 1, figures 11.

Key words: **off-grid wind energy systems, power quality, optimized control strategies, voltage regulation, harmonic mitigation.**

Вступ*. Автономні вітроенергетичні системи грають ключову роль у забезпеченні екологічно чистої та сталої електроенергії віддалених районів. Однак переривчастий характер вітру та відсутність підключення до мережі створюють значні проблеми для підтримки сталої якості електроенергії. Система перетворення енергії вітру відіграє важливу роль у використанні відновлюваної енергії з джерел вітру. Робочі параметри, такі як струм ротора та статора, вихідна напруга випрямлячів і перетворювачів, а також коливання фазної напруги мережі, є вирішальними для стабільного виробництва електроенергії та інтеграції в мережу. Також важлива оптимізація вихідної потужності за допомогою аналізу посилення напруги в підвищувальних перетворювачах. Забезпечення якості електроенергії за рахунок зменшення повного гармонійного спотворення в інверторах є життєво важливим для сумісності з мережею.* ***Мета****. Підвищення якості електроенергії інтегрованих в мережу систем перетворення енергії вітру.* ***Методи****. Запропонована топологія реалізована в MATLAB/Simulink з оптимізованими стратегіями керування для підвищення якості електроенергії у автономних вітроенергетичних системах.* ***Результати****. Стратегії керування за допомогою підключеної до мережі системи перетворення енергії вітру дають суттєві покращення якості електроенергії. Це включає в себе ефективне послаблення коливань напруги та гармонік, що призводить до більш плавної роботи та зменшення завад у мережі.* ***Практична цінність****. Запропонована топологія виявилася надзвичайно корисною для автономної інтегрованої вітрової системи.* Бібл. 18, табл. 1, рис. 11.

Ключові слова: **автономні вітроенергетичні системи, якість електроенергії, оптимізовані стратегії управління, регулювання напруги, послаблення впливу гармонік.**

Abbreviations

DFIG	Doubly Fed Induction Generator	THD	Total Harmonic Distortion
ESS	Energy Storage System	VSC	Voltage Source Converter
PWM	Pulse Width Modulation	WECS	Wind Energy Conversion System
STATCOM	Static Synchronous Compensator		

1. Introduction. Off-grid wind energy systems represent a promising avenue for providing clean and sustainable power to remote areas, islands, and regions where traditional grid infrastructure is absent or unreliable. These systems harness the abundant energy of the wind to generate electricity, offering a decentralized solution to meet local energy needs. However, despite their environmental benefits and potential to promote energy independence, off-grid wind energy systems face significant challenges in maintaining consistent power quality [1, 2].

The intermittent nature of wind, coupled with the absence of grid connectivity, poses unique obstacles to ensuring stable and reliable electricity supply [3]. Fluctuations in wind speed and direction can lead to variations in power output, causing voltage and frequency instabilities within the system. Moreover, the lack of a grid connection eliminates the buffering effect typically provided by centralized power distribution networks, amplifying the impact of these fluctuations on local power quality [4].

Ensuring adequate power quality in off-grid wind energy systems is crucial for their successful operation and integration into the broader energy landscape. Poor power quality can result in voltage sags, swells, and transients, as well as harmonic distortions, which can damage equipment, disrupt operations, and compromise the performance of connected loads. Additionally, inconsistent power quality may limit the feasibility and reliability of critical applications, such as telecommunications, healthcare facilities, and industrial processes, which rely on stable electricity supply [5–7].

To address these challenges, advanced control strategies have emerged as a key solution for enhancing power quality in off-grid wind energy systems. By leveraging sophisticated control algorithms and innovative techniques, such as predictive control and adaptive filtering, these strategies aim to regulate voltage and frequency, mitigate harmonics, and improve the overall stability and reliability of the system. One of the fundamental challenges in off-grid wind power systems is the variability of wind speed and direction, which directly impacts the output power of wind turbines. To address this challenge, researchers have investigated predictive control techniques that utilize advanced algorithms to forecast wind conditions and adjust system parameters accordingly. Another area of focus in power quality enhancement is voltage regulation, which is crucial for ensuring the stability and reliability of off-grid wind power systems. Several studies have explored the use of power electronic converters, such as VSCs and STATCOMs, to regulate voltage levels and mitigate voltage fluctuations. Harmonic mitigation is another important aspect of power quality enhancement in off-grid wind power systems. Harmonic distortions can arise from the nonlinear characteristics of power electronic converters and can degrade the performance of connected loads. To address this issue, researchers have proposed various filtering techniques, such as active filters and passive filters, to suppress harmonics and improve system reliability. In addition to predictive control, voltage regulation, and harmonic mitigation, researchers have also explored the integration of ESSs to enhance power quality in off-grid wind power systems. ESS can store surplus energy during periods of high wind availability and release it during periods of low wind, thereby smoothing out power fluctuations and improving system stability [8–15].

Off-grid wind power systems often incorporate multiple renewable energy sources, energy storage devices, and power electronics components, making system integration and coordination a complex task. Advanced control techniques have to be employed to effectively manage the interactions between different system components and optimize overall system performance while ensuring power quality and reliability [16–18].

The goal of the paper is to enhance the power quality of grid-integrated wind energy conversion systems:

- Investigate the efficacy of advanced control techniques, such as predictive control and adaptive algorithms, in enhancing power quality in off-grid wind energy systems.
- Evaluate methods to enhance power generation efficiency by analyzing rotor current, stator current, and voltage gain in the boost converter.
- Investigate the impact of grid phase voltage variations on stable power generation and assess techniques such as filter integration to reduce THD in the inverter output.
- Explore ways to maximize the utilization of wind resources by analyzing parameters such as rated power, wind speed, power coefficient, and technical specifications like the number of blades and tip speed ratio.
- Identify opportunities for further improvement and refinement of control strategies to optimize power quality enhancement in off-grid wind energy systems and promote their widespread adoption in diverse applications.

2. Off grid isolated wind turbine conversion system.

Operation of isolated WECS. The off-grid wind turbine conversion system comprises several interconnected components working synergistically to convert wind energy into usable electrical power. At its core lies a DFIG directly coupled to the wind turbine, harnessing wind energy to generate AC electricity. This AC output is then rectified by a diode rectifier to convert it into DC, suitable for further processing. The DC power undergoes voltage regulation and conditioning through a DC/DC converter. This converter ensures a stable and controlled DC output, crucial for maintaining the integrity of downstream components. Control of the DC power is facilitated through PWM techniques, adjusting the duty cycle of the converter to optimize power flow and efficiency. The conditioned DC power is then fed into a three-phase inverter, where it undergoes conversion back into AC electricity. The inverter, controlled by PWM signals, ensures the quality and stability of the AC output, synchronizing it with the grid or local loads' requirements. Before the electricity is distributed, it passes through a transformer for voltage stepping to match the grid or load voltage levels. This transformer also provides isolation and impedance matching to improve system performance and reliability. Throughout the operation, various control systems play crucial roles. The wind turbine control system monitors and optimizes turbine performance, adjusting blade pitch and yaw angles to maximize energy capture efficiency. The grid operator control system oversees the integration of the wind power into the grid, managing power flow, frequency, and voltage to ensure stability and reliability. Overall, the operation of the off-grid wind turbine conversion system involves seamless coordination and control of multiple components, from the wind turbine itself to the grid connection point. Through advanced control strategies and efficient power conversion techniques, this system enables the reliable and sustainable harnessing of wind energy in remote or off-grid locations, contributing to the transition towards clean and renewable energy sources. Figure 1 illustrates the off-grid WECS.

The kinetic energy of a WECS is:

$$E = \frac{1}{2} m v^2 , \tag{1}$$

where m is the mass; v is the velocity.

The power available in wind can be defined as:

$$P = \frac{1}{2} \rho A v^3 , \tag{2}$$

where A is the cross-sectional area of the wind turbine; ρ is the air density.

The coefficient factor C_p for the wind turbine can be expressed as:

$$C_p = P_0 / P. \tag{3}$$

The power converted from the wind speed is expressed as:

$$P_0 = \frac{1}{2} C_p \rho A v^3 . \tag{4}$$

Tip-speed ratio of wind turbine can be expressed as:

$$\lambda = R\omega / v , \tag{5}$$

where R is the radius of the wind turbine; ω is the angular speed of wind turbine.

DFIG d and q axis change in current, it can be expresses as:

$$\frac{\mathrm{d}I_d}{\mathrm{d}t} = -\left(\frac{R_a}{L_d}\right) I_d + \omega_s \frac{L_q}{L_d} I_q + \frac{1}{L_d} U_d ; \tag{6}$$

$$\frac{\mathrm{d}I_q}{\mathrm{d}t} = -\frac{R_a}{L_q} I_d - \omega_s \left(\frac{L_d}{L_q} I_d + \frac{1}{L_q} \psi_p\right) + \frac{1}{L_q} U_q , \tag{7}$$

where R_a is the resistance; L_d is the d-axis inductance; L_q is the q-axis inductance; ω_s is the angular speed of rotor; ψ_p is the excitation flux; U_d is the d-axis voltage; U_q is the q-axis voltage.

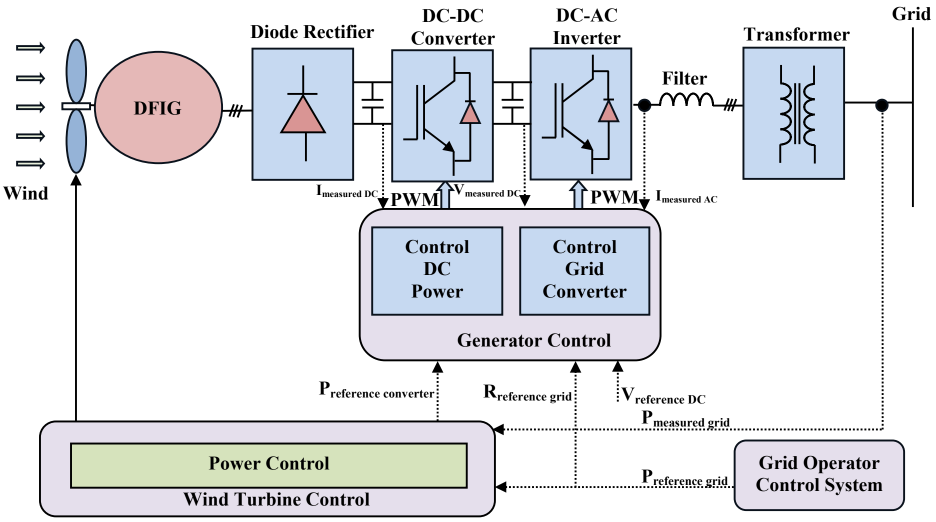

Fig. 1. Off grid WECS

The electromechanical torque produced by the wind turbine can be expressed as:

$$T_e = -1.5\frac{P}{2}\left[\left(\psi_p I_q + I_d I_q\left(L_d - L_q\right)\right)\right]. \tag{8}$$

Three phase voltage transformation of three axis system can be expressed as:

$$U_{ga} = U_{Ia} - L\frac{\mathrm{d}I_a}{\mathrm{d}t} - IR_a ; \tag{9}$$

$$U_{gb} = U_{Ib} - L\frac{\mathrm{d}I_b}{\mathrm{d}t} - IR_b ; \tag{10}$$

$$U_{gc} = U_{Ic} - L\frac{\mathrm{d}I_c}{\mathrm{d}t} - IR_c . \tag{11}$$

Two axis voltage transformation system can be expressed as:

$$U_d = R_a I_d - \omega_s L_q I_q + \frac{\mathrm{d}I_d}{\mathrm{d}t} L_d ; \tag{12}$$

$$U_q = R_a I_q + \omega_s L_d I_d + \frac{\mathrm{d}I_q}{\mathrm{d}t} L_q + E_s . \tag{13}$$

Transformed *d* and *q* axis controller can be expressed as:

$$U_d = e_d - RI_d + \omega L I_q - L\frac{\mathrm{d}I_d}{\mathrm{d}t} ; \tag{14}$$

$$U_q = -R_a I_q - \omega L I_d - L\frac{\mathrm{d}I_q}{\mathrm{d}t} . \tag{15}$$

Simplifying the above two equations final simplified expression can be illustrated as:

$$\begin{bmatrix} U_d \\ U_q \\ U_0 \end{bmatrix} = \sqrt{\frac{2}{3}} \begin{bmatrix} \cos(\omega t - \theta) \\ \sin(\omega t - \theta) \\ 0 \end{bmatrix} , \tag{16}$$

where θ is the estimated angle in *a-b-c* to *d-q* transformation.

An extensive procedure was required to integrate renewable energy into the connectivity of a wind turbine generator. A three-phase full bridge diode rectifier was the first component, and its primary function was to change the alternating current produced by the wind turbine into direct current. This rectifier was essential in guaranteeing a reliable and constant DC output. The DC boost converter came next, and it was in charge of increasing the DC voltage to a level appropriate for effective power transmission. This increase in voltage was required to reduce power losses during the energy transfer to the grid. The three-phase inverter, the last component of this complex system, was created to transform the amplified DC power back into grid-compatible AC. The inverter's function was crucial in ensuring that the electricity produced by the wind turbine could integrate easily into the current grid system. In the end, this networked system enabled the clean, renewable energy produced by the wind turbine to be effectively transmitted to the grid, supplying a dependable source of electricity to power homes and businesses while lowering carbon emissions and dependence on non-renewable energy sources.

Boost converter-fed diode rectifier and inverter system is a complex arrangement designed to efficiently manage power flow in renewable energy applications, particularly in off-grid or hybrid systems. At its core, the boost converter serves to regulate the voltage level of the DC link, ensuring that the system operates within specified voltage limits. The diode rectifier, connected to the DC link, converts AC power from the three-phase source into DC, which is then smoothed and regulated by the boost converter. The three-phase inverter, controlled by PWM techniques, converts the regulated DC power back into AC, suitable for grid or load connection. The PWM control adjusts the switching of the inverter devices to regulate output voltage and frequency, ensuring compatibility with the grid or load requirements. PI controller is typically employed to regulate the DC link voltage. It compares the actual DC voltage (actual V_{dc}) with a reference voltage (reference V_{dc}), adjusting the duty cycle of the boost converter to maintain the desired voltage level. In hybrid systems, a battery has been included in the DC link to store excess energy or provide backup power during periods of low renewable energy generation. The integration of the battery adds flexibility to the system, allowing for improved energy management and enhanced reliability.

Figure 2 illustrates the boost converter with diode and inverter connected system and Fig. 3 shows WECS to load system through diode rectifier and three phase inverter system. In a grid operator control system, power control and wind turbine control are crucial components. Power control involves regulating the output of wind turbines to match grid demand, ensuring grid stability and reliability. This requires real-time monitoring and adjustment of power generation levels to maintain grid frequency and voltage within acceptable limits. Wind turbine control encompasses pitch control, yaw control, and rotor speed regulation to maximize energy capture and minimize mechanical stress. Integrating advanced control algorithms enables efficient coordination between power control and wind turbine control, optimizing energy production while ensuring grid compatibility and reliability.

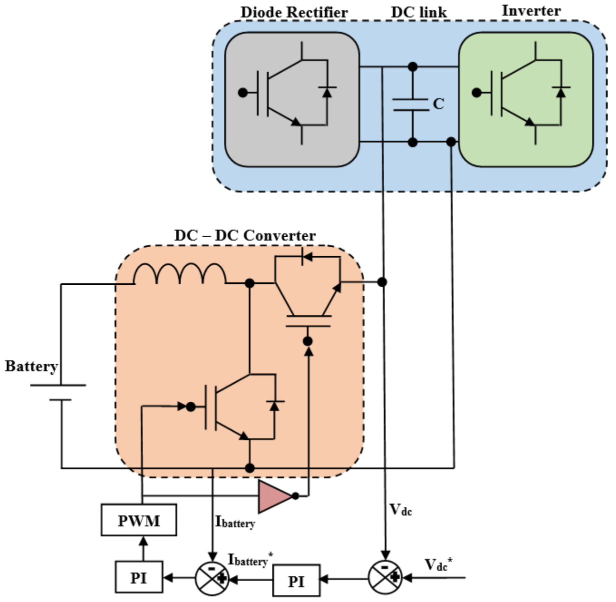

Fig. 2. Boost converter with diode and inverter connected system

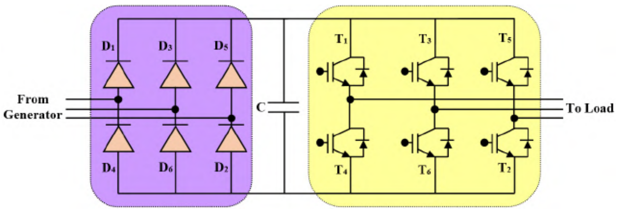

Fig. 3. WECS to load system

The performance of a wind turbine is essential for producing energy efficiently, and the incorporation of a PI controller within its DC-DC converter is a key to optimizing this procedure. A typical control technique called the PI controller modifies the duty cycle of the converter's switching components to control the output voltage. In order to ensure that the wind turbine runs at its peak power for optimum energy extraction, it strikes a balance between the trade-off between transient reaction and steady-state precision. A diode rectifier works with a DC-DC converter to change the changing AC output from the wind turbine generator into a steady DC voltage. As a device for unidirectional current flow, the diode rectifier only permits forward current to pass from the generator to the DC connection. The DC voltage is then converted into AC by the last component, an inverter system, making it eligible for grid connection. A seamless integration with the electrical grid is made possible by the PI controller in the inverter system, which makes sure the output voltage and frequency precisely match the grid's needs. This system, which includes a wind turbine, a DC-DC converter with a PI controller, a diode rectifier, and an inverter, guarantees effective energy conversion, grid synchronization, and overall optimal performance, promoting the use of renewable energy sources and sustainable power generation.

Figure 4 illustrates the interconnection of three phase diode rectifier, boost converter, three phase inverter to load and generator.

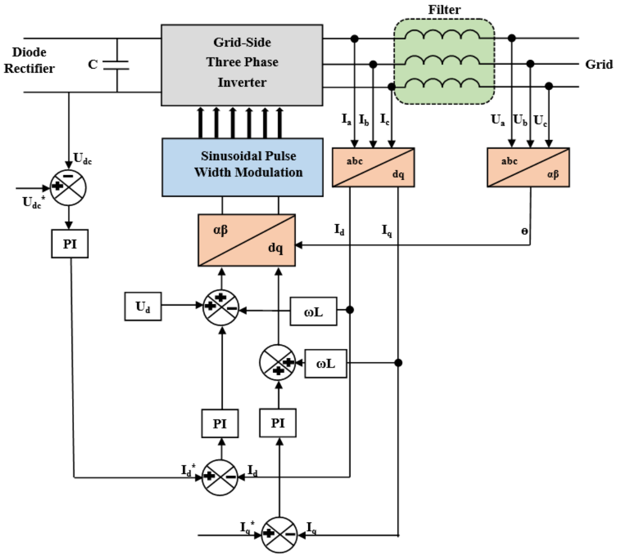

Fig. 4. Three to two axis transformation diode bridge rectifiers to grid integration

3. Results and discussion. WECS is a vital component in harnessing renewable energy from wind sources. Figure 5 displays the relationship between turbine mechanical power and rotor speed across various velocities ranging from 3 m/s to 13 m/s. The rotor current in a DFIG comes from the excitation of the coil, inducing a magnetic field that generates the current.

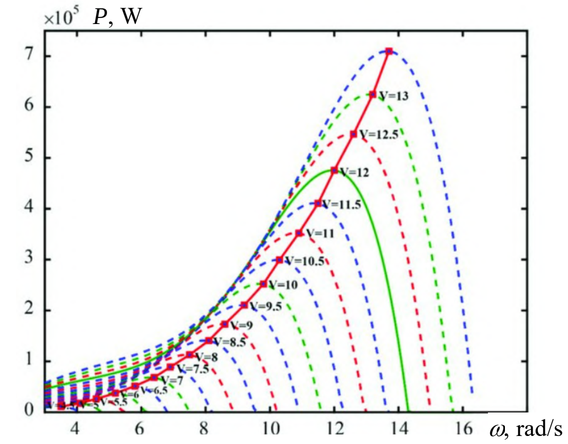

Fig. 5. Turbine mechanical power vs rotor speed at different velocities

Figure 6 provides key operational parameters at a cut-in speed of 1200 rpm, with rotor current at 1.7 A and stator current at 1.3 A.

Figures 7, 8 detail the output voltages of the diode bridge rectifier and DC link boost converter, respectively, crucial for maintaining stable power generation.

Figure 9 illustrates grid phase voltage variations during inductive filter and non-filter conditions, essential for grid integration.

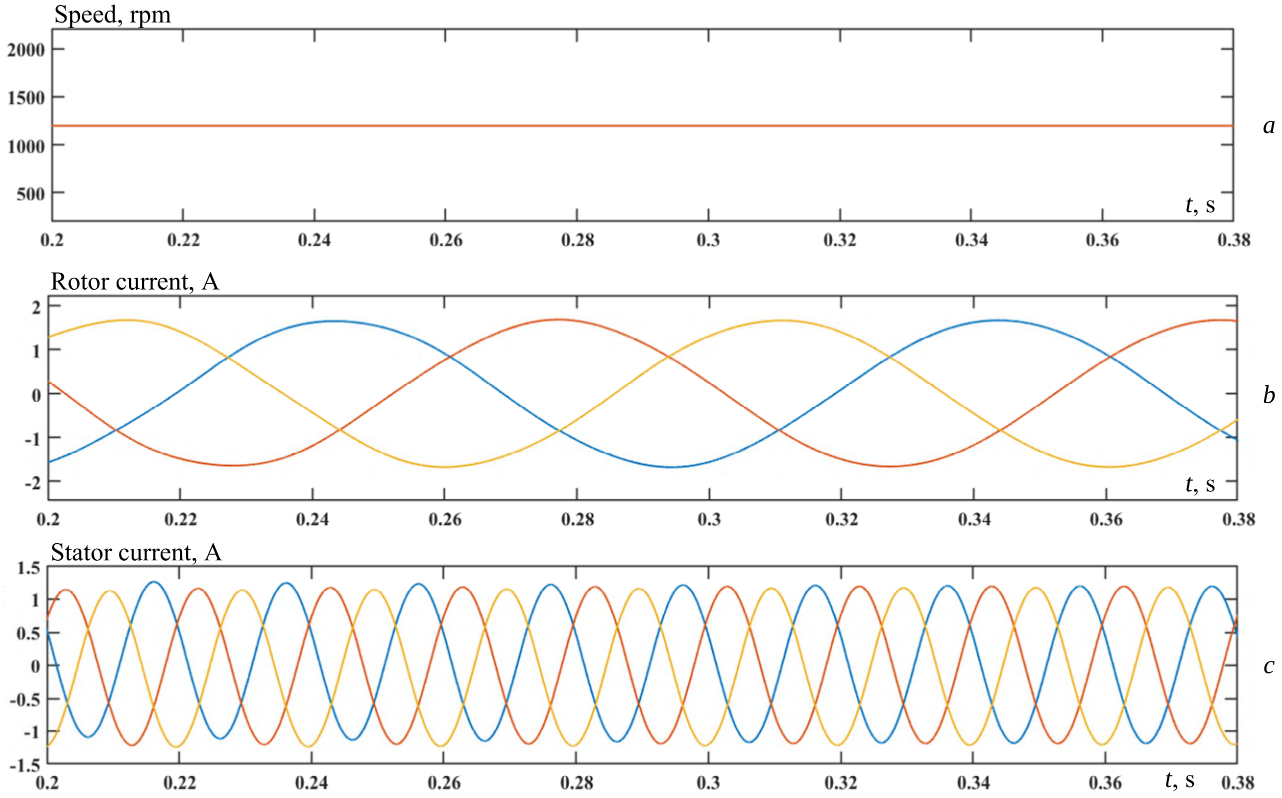

Fig. 6. WECS rotor speed (*a*), rotor current (*b*) and stator current (*c*)

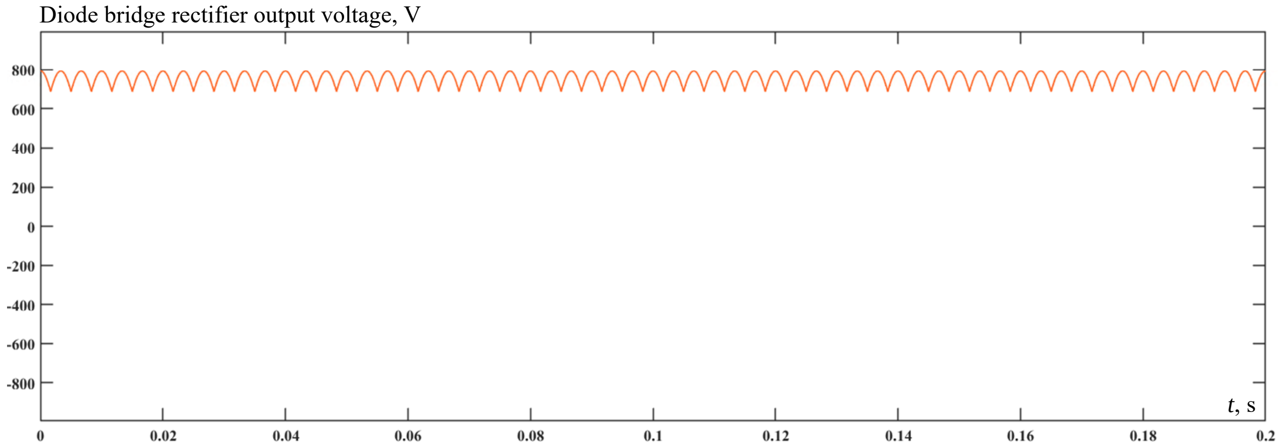

Fig. 7. Diode bridge rectifier output voltage

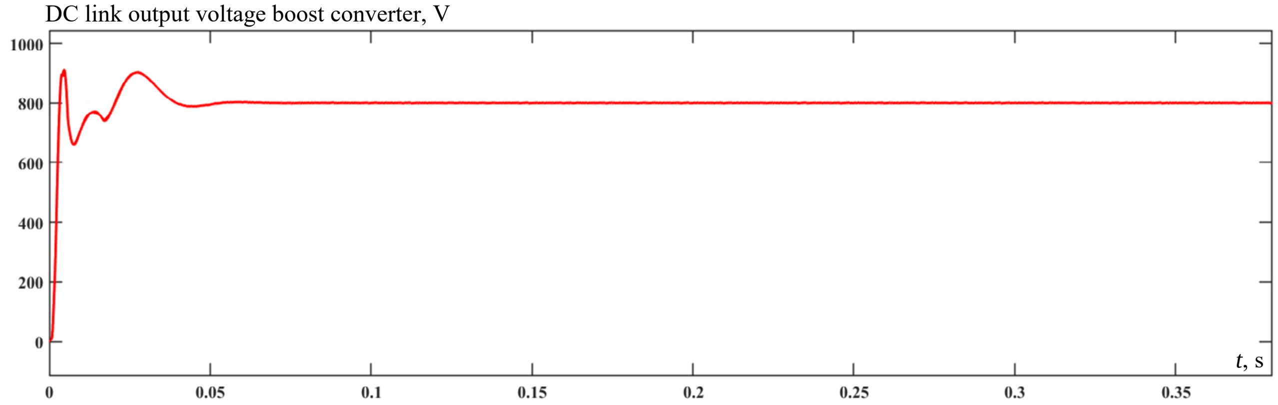

Fig. 8. DC link output voltage boost converter

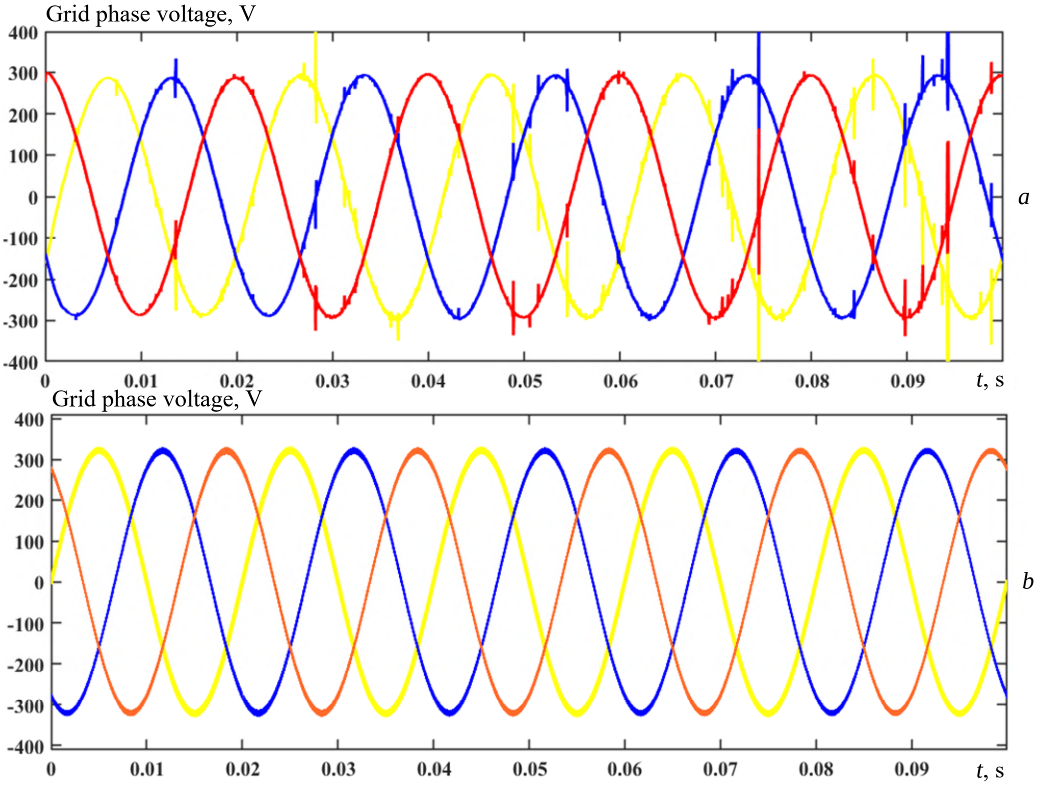

Fig. 9. Grid phase voltage during filter (*a*) and non-filter (*b*)

Figure 10 presents a comparative analysis of voltage gain in the boost converter, ranging from 0.1 to 0.8, crucial for optimizing power conversion efficiency. Meanwhile, while investigating electricity quality solely with a filter isn't groundbreaking, Fig. 11's depiction of THD in the inverter is noteworthy. It illustrates a substantial decrease from 18 % without a filter to 2.3 % with a filter, crucial for ensuring grid compatibility, validating the filter's effectiveness

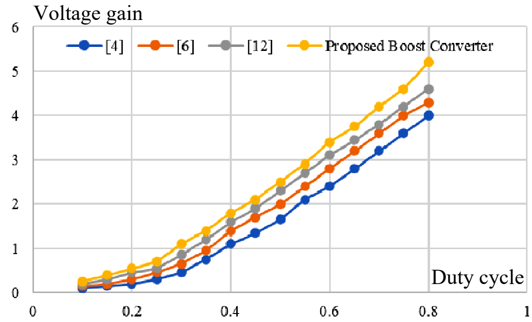

Fig. 10. Comparative analysis of voltage gain of boost converter

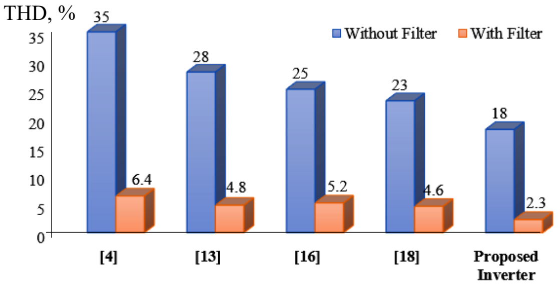

Fig. 11. Comparative analysis of THD in inverter

Table 1 encapsulates essential WECS parameters, including rated power, wind speed, power coefficient and technical specifications like the number of blades, tip speed ratio and gear ratio. Notably, the listed parameters provide a comprehensive overview of the system's capabilities and operational characteristics.

Table 1

WECS parameters

Name	Parameters	Value
DFIG	Rated power, kW	2
	Rated wind speed, m/s	8
	Power co-efficient	0.3
	Number of blades	2
	Tip speed ratio	6
	Cut-in speed, m/s	3
	Cut-in turbine speed, rpm	45
	Cut-in generator speed, rpm	1200
	Rotor winding resistance, mΩ	2.63
	Stator winding inductance, mH	5.6438
	Rotor winding inductance, mH	5.6068
	Magnetizing inductance, mH	5.4749
DC regulated converter	Output voltage, V	400
	Power device	MOSFET
	Switching frequency, kHz	50
	RMS inductor current, A	10.2
	Conduction loss	523.4
Three phase VSI	Power device	IGBT
	Number of devices	6
	On-off frequency, kHz	2.2

4. Conclusions. The integration of optimized control strategies in off-grid wind energy systems represents a significant advancement in addressing the challenges associated with intermittent wind resources and lack of grid connectivity. Through the implementation of advanced control techniques such as predictive control and adaptive algorithms, these systems can effectively enhance power quality by regulating voltage, frequency, and mitigating harmonics. The results obtained from the proposed topology, implemented in MATLAB/Simulink, demonstrate substantial improvements in power quality metrics, including reduced voltage fluctuations and harmonics. This not only ensures smoother operation of off-grid wind energy systems but also minimizes disturbances on the grid, thereby enhancing overall system reliability and performance.

Conflict of interest. The authors declare that they have no conflicts of interest.

REFERENCES

1. Hans F., Borowski P., Wendt J., Quistorf G., Jersch T. Opportunities and Challenges of Advanced Testing Approaches for Multi-Megawatt Wind Turbines. *IEEE Open Journal of Power Electronics*, 2024, vol. 5, pp. 323-335. doi: https://doi.org/10.1109/OJPEL.2024.3364973.

2. Kazmi S.H.H., Viafora N., Sorensen T.S., Olesen T.H., Pal B.C., Holboll J. Offshore Windfarm Design Optimization Using Dynamic Rating for Transmission Components. *IEEE Transactions on Power Systems*, 2022, vol. 37, no. 3, pp. 1820-1830. doi: https://doi.org/10.1109/TPWRS.2021.3118278.

3. Mehrabankhomartash M., Saeedifard M., Yazdani A. Adjustable Wind Farm Frequency Support Through Multi-Terminal HVDC Grids. *IEEE Transactions on Sustainable Energy*, 2021, vol. 12, no. 2, pp. 1461-1472. doi: https://doi.org/10.1109/TSTE.2021.3049762.

4. Xing L., Wei Q., Li R. An Improved Current-Source-Converter-Based Series-Connected Wind Energy Conversion System. *IEEE Transactions on Industrial Electronics*, 2024, vol. 71, no. 5, pp. 4818-4829. doi: https://doi.org/10.1109/TIE.2023.3283700.

5. Chen H., Xu D., Deng X. Control for Power Converter of Small-Scale Switched Reluctance Wind Power Generator. *IEEE Transactions on Industrial Electronics*, 2021, vol. 68, no. 4, pp. 3148-3158. doi: https://doi.org/10.1109/TIE.2020.2978689.

6. Parimalasundar E., Jayanthi R., Suresh K., Sindhuja R. Investigation of efficient multilevel inverter for photovoltaic energy system and electric vehicle applications. *Electrical Engineering & Electromechanics*, 2023, no. 4, pp. 47-51. doi: https://doi.org/10.20998/2074-272X.2023.4.07.

7. Sujatha M.S., Sreelakshmi S., Parimalasundar E., Suresh K. Mitigation of harmonics for five level multilevel inverter with fuzzy logic controller. *Electrical Engineering & Electromechanics*, 2023, no. 4, pp. 52-56. doi: https://doi.org/10.20998/2074-272X.2023.4.08.

8. Zong H., Zhang C., Cai X., Molinas M. Oscillation Propagation Analysis of Hybrid AC/DC Grids With High Penetration Renewables. *IEEE Transactions on Power Systems*, 2022, vol. 37, no. 6, pp. 4761-4772. doi: https://doi.org/10.1109/TPWRS.2022.3150413.

9. Kumar R., Singh B., Kant P. High Reliable Medium Voltage Drive With Reduced Component Count of Converters. *IEEE Transactions on Industry Applications*, 2023, vol. 59, no. 3, pp. 3627-3638. doi: https://doi.org/10.1109/TIA.2023.3251968.

10. Parimalasundar E., Senthil Kumar R., Chandrika V.S., Suresh K. Fault diagnosis in a five-level multilevel inverter using an artificial neural network approach. *Electrical Engineering & Electromechanics*, 2023, no. 1, pp. 31-39. doi: https://doi.org/10.20998/2074-272X.2023.1.05.

11. Parimalasundar E., Kumar N.M.G., Geetha P., Suresh K. Performance investigation of modular multilevel inverter topologies for photovoltaic applications with minimal switches. *Electrical Engineering & Electromechanics*, 2022, no. 6, pp. 28-34. doi: https://doi.org/10.20998/2074-272X.2022.6.05.

12. Hashimoto J., Ustun T.S., Suzuki M., Sugahara S., Hasegawa M., Otani K. Advanced Grid Integration Test Platform for Increased Distributed Renewable Energy Penetration in Smart Grids. *IEEE Access*, 2021, vol. 9, pp. 34040-34053. doi: https://doi.org/10.1109/ACCESS.2021.3061731.

13. Patil H., Nago Kalkhambkar V. Grid Integration of Electric Vehicles for Economic Benefits: A Review. *Journal of Modern Power Systems and Clean Energy*, 2021, vol. 9, no. 1, pp. 13-26. doi: https://doi.org/10.35833/MPCE.2019.000326.

14. Tang Z., Yang Y., Blaabjerg F. An Interlinking Converter for Renewable Energy Integration Into Hybrid Grids. *IEEE Transactions on Power Electronics*, 2021, vol. 36, no. 3, pp. 2499-2504. doi: https://doi.org/10.1109/TPEL.2020.3018585.

15. Marinescu B., Gomis-Bellmunt O., Dorfler F., Schulte H., Sigrist L. Dynamic Virtual Power Plant: A New Concept for Grid Integration of Renewable Energy Sources. *IEEE Access*, 2022, vol. 10, pp. 104980-104995. doi: https://doi.org/10.1109/ACCESS.2022.3205731.

16. Wen Y., Lu Y., Gou J., Liu F., Tang Q., Wang R. Robust Transmission Expansion Planning of Ultrahigh-Voltage AC–DC Hybrid Grids. *IEEE Transactions on Industry Applications*, 2022, vol. 58, no. 3, pp. 3294-3302. doi: https://doi.org/10.1109/TIA.2022.3160147.

17. Sekhar K.S.R., Chaudhari M.A., Khadkikar V. Enhanced Hybrid Converter Topology for PV-Grid-EV Integration. *IEEE Transactions on Energy Conversion*, 2023, vol. 38, no. 4, pp. 2634-2646. doi: https://doi.org/10.1109/TEC.2023.3287890.

18. Yang R., Shi G., Zhang C., Li G., Cai X. Internal Energy Based Grid-Forming Control for MMC-HVDC Systems With Wind Farm Integration. *IEEE Transactions on Industry Applications*, 2023, vol. 59, no. 1, pp. 503-512. doi: https://doi.org/10.1109/TIA.2022.3205569.

Received 10.02.2024
Accepted 15.04.2024
Published 20.08.2024

S. Muthukaruppasamy [1]*, Associate Professor,*
R. Dharmaprakash [2]*, Professor,*
S. Sendilkumar [3]*, Professor,*
E. Parimalasundar [4]*, Professor,*
[1] Department of Electrical and Electronics Engineering,
Velammal Institute of Technology,
Anna University, Panchetti, Chennai – 601204, India,
e-mail: mksamy14@yahoo.com (Corresponding Author)
[2] Department of Electrical and Electronics Engineering,
Panimalar Engineering College, Chennai – 600123, India
e-mail: rdharmaprakash@yahoo.co.in
[3] Department of Electrical and Electronics Engineering,
S.A. Engineering College, Chennai – 641021, India,
e-mail: sendilkumar2009@gmail.com
[4] Department of Electrical & Electronics Engineering,
Mohan Babu University (Erstwhile Sree Vidyanikethan Engineering College), Tirupati, AP – 517102, India,
e-mail: parimalasundar.e@mbu.asia

How to cite this article:
Muthukaruppasamy S., Dharmaprakash R., Sendilkumar S., Parimalasundar E. Enhancing off-grid wind energy systems with controlled inverter integration for improved power quality. *Electrical Engineering & Electromechanics*, 2024, no. 5, pp. 41-47. doi: https://doi.org/10.20998/2074-272X.2024.5.06

UDC 621.3.013 https://doi.org/10.20998/2074-272X.2024.5.07

V.Yu. Rozov, S.Yu. Reutskiy, D.Ye. Pelevin, K.D. Kundius

Magnetic field of electrical heating cable systems of the floors for residential premises

Problem. *In order to effectively protect public health from the magnetic field of electric heating cable systems of the floors, it is necessary to reduce it to a safe level. However, this requires careful study of the magnetic field.* ***The purpose*** *of the work is to develop a mathematical model and a verified methodology for calculating the magnetic field of electric heating cable systems of the floors in residential premises, and assessment of compliance of the magnetic field with the normative level.* ***Method.*** *A methodology for calculating the magnetic field of electric heating cable systems of the floors in residential premises has been developed.* ***Scientific novelty.*** *Based on Bio-Savar's law and the principle of superposition, an analytical model of the magnetic field of electric heating cable systems of the floors and its calculation method was created. The magnetic field of the coaxial heating cable is determined, taking into account the value of its maximum eccentricity. The experimentally substantiated correctness of the obtained theoretical statements, which is confirmed by their coincidence with the results of the experiment with a spread of less than 7 %.* ***Practical significance.*** *A verified methodology for calculating the magnetic field of electric heating cable systems of the floors was proposed and an assessment of compliance of their magnetic flux density with the normative level of 0.5 μT was performed. It is recommended to lay modern two-wire heating cables at a depth of at least 75–100 mm from the floor. With a smaller laying depth, it is recommended to use coaxial heating cables, which have an order of magnitude smaller magnetic field.* References 51, tables 1, figures 11.

Key words: **electric heating cable systems of the floors, magnetic field, modeling and measurement, assessment of compliance with the normative level.**

Проблема. *Для ефективного захисту здоров'я населення від магнітного поля кабельних систем електрообігріву підлог, необхідно його зменшення до безпечного рівня. Однак це потребує ретельного вивчення магнітного поля.* ***Метою роботи*** *є розробка математичної моделі і верифікованої методики розрахунку магнітного поля кабельних систем електрообігріву підлог житлових приміщень, та оцінка відповідності магнітного поля нормативному рівню.* ***Методика.*** *Розроблено методику розрахунку магнітного поля кабельних систем електрообігріву підлог в житлових приміщеннях.* ***Наукова новизна.*** *На основі закону Біо-Савара та принципу суперпозиції створено аналітичну модель магнітного поля кабельних систем електрообігріву підлог та методику його розрахунку. Визначено магнітне поле коаксіального нагрівального кабелю з урахуванням величини його максимального ексцентриситету. Експериментально обґрунтована коректність отриманих теоретичних положень, яка підтверджена їх співпадінням із результатами експерименту з розкидом менше 7 %.* ***Практична значимість.*** *Запропоновано верифіковану методику розрахунку магнітного поля кабельних систем електрообігріву підлог і виконано оцінку відповідності індукції їх магнітного поля нормативному рівню 0,5 мкТл. Рекомендовано прокладати сучасні двожильні нагрівальні кабелі на глибині не менше 0,075–0,1 м від підлоги. При меншій глибини прокладання рекомендовано використовувати коаксіальні нагрівальні кабелі, що мають на порядок менше магнітне поле.* Бібл. 51, табл. 1, рис. 11.

Ключові слова: **кабельні системи електрообігріву підлог, магнітне поле, моделювання та вимірювання, оцінка відповідності нормативному рівню.**

Introduction. Safe and comfortable living of the population in residential buildings is impossible without limiting the level of man-made physical fields [1–3], including the electromagnetic field. One of the most powerful internal sources of electromagnetic field are electric heating cable systems (EHCSs) of floors [4, 5], which are now intensively distributed in the world. Also, like external power grids [6–8], EHCSs create quasi-stationary electromagnetic field of low frequency in residential premises, which is characterized by electric (EF) and magnetic (MF) components that negatively affect a person [6, 8–11]. According to the conclusions of the World Health Organization (WHO), the long-term effect of low frequency MF is more dangerous for public health than EF [12]. The basis for such a conclusion was the discovery at the end of the 20th century of the carcinogenic properties of MF of electrical networks with its weak but long-term effect on the population, and especially on children [13–16]. This led to the development by WHO experts of recommendations to limit the MF flux density of low frequency for the population with 100 μT [17] to the level of 0.2–0.3 μT to reduce the likelihood of cancer [18]. The level of MF flux density of low frequency that is comfortable for residential buildings is also recommended by the international Standard [3] and is in the range of 0.02–0.5 μT. The implementation of these recommendations led to the introduction of stricter national sanitary standards for the MF flux density with frequency of 50–60 Hz [19], stimulated the implementation of a complex of works on the development and implementation of new methods for determining and normalizing MF [3, 20–29].

In Ukraine, the solution of scientific problems of sanitary and hygienic regulation of MF for the population is carried out by the O.M. Marzeev Institute of Public Health of the National Academy of Medical Sciences of Ukraine (formerly the O.M. Marzeev Institute of Hygiene and Medical Ecology of the National Academy of Medical Sciences of Ukraine). In it, under scientific guidance of the famous in the world Ukrainian scientists and hygienists Academician A.M. Serdyuk and Professor Yu.D. Dumanskyi, back in 1975, the need to introduce the maximum permissible level of MF flux density for the population was determined [30]. Finally, this normative for low frequency MF at the level of 0.5 μT was theoretically and experimentally (on animals) substantiated by them in [31]. It meets the current WHO recommendations and formed the scientific basis of the normative document adopted in 2017 [32], according to which (Table 1) the effective value of MF flux density from cable lines at each point of the volume of the residential premises, including the floor (with the exception of the space closer to 0.5 m from the walls), should not exceed the safe level of 0.5 μT.

Table 1

Temporary maximum permissible (normative) levels of the magnetic field above the path of the cable line according to Table 2.3.2 of the regulatory document of Ukraine «Electrical installation regulations» [32]

The territory on which the level of MF of the low frequency is regulated	MF flux density, μT
Inside residential premises	0,5
At a distance of 50 cm from the walls of residential premises and household electrical appliances	3,0* (*used for cables and wiring laid in walls)
On the territory of the residential development zone	10,0
Inhabited area outside the zone of residential development	20,0
Uninhabited area and agricultural land	50,0

The main elements of EHCS (Fig. 1) are resistive heating cables (HCs), which are mounted under the floor surface at a depth h_k from it, and a thermostat with a built-in temperature sensor [5]. HCs are powered by the apartment electrical network and are designed for a nominal current that can reach 15 A [4].

Analysis of the construct execution of HCs [5, 33–42] shows that they are divided into single-wire and two-wire (Fig. 2). Such HCs have different circuits of connection to the power grid (Fig. 3), and create different level of MF. According to [1, 43], the MF flux density of single-wire HCs significantly (more than an order of magnitude) exceeds the MF of two-wire HCs. This limits the use of single-wire HCs in non-residential premises.

For uniform heating of the floor, HCs are laid in the form of a «snake» with a step of 80–120 mm [5]. This makes the distribution of EHCS MF different from the MF of single HCs, which determines its separate analysis. When analyzing the «snake» we present it in the form of a meander (Fig. 3).

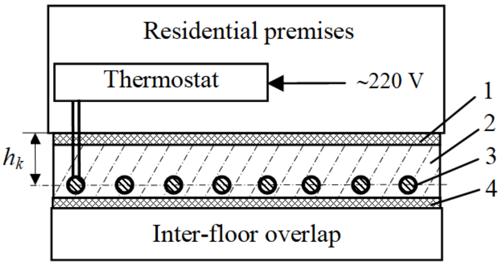

Fig. 1. Typical construction of an electrical heating cable systems (EHCS) (1 – floor covering, 2 – concrete (adhesive) screed, 3 – heating cable (HC), 4 – thermal insulation)

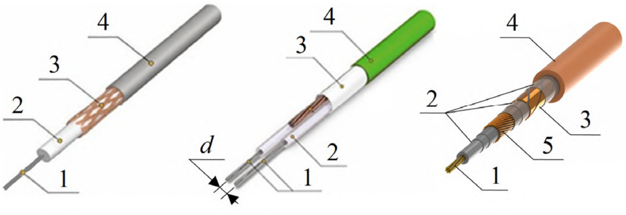

a *b* *c*

Fig. 2. Constructive implementation of HC of various types: single-wire (*a*), two-wire planar (*b*), two- wire coaxial (*c*); (1, 5 – heating (current-conducting) wires, 2 – electrical insulation, 3 – conductive grounding screen; 4 – external electrical insulation)

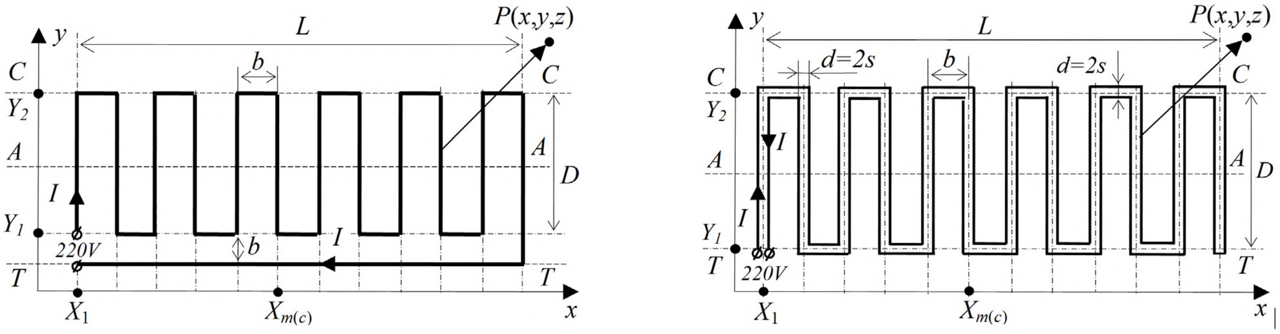

a *b*

Fig. 3. Geometry of laying single- wire (*a*) and two- wire (*b*) EHCS HC in the horizontal plane *XY* under the floor and connection diagrams to the apartment electrical network

It is known that the MF flux density of two-wire HCs, like any electrical network, depends on the distance *d* between the axes of the wires and the current *I* in them [6, 8, 43]. Therefore, two-wire flat (planar) HCs (Fig. 2,*b*) are produced with the technologically minimum possible distance between its wires *d* (1.4 –2.5 mm). However, as will be shown below, the use of such HCs at the standard depth of cabel laying h_k = 0.03–0.05 m (Fig. 1) and a supply current of 10 A leads to a significant excess of MF flux density above the normative level of 0.5 μT.

Normalization of the MF is possible when using coaxial [40] HCs (Fig. 2,*c*), but their MF has not been sufficiently investigated to date. Also, in well-known publications, for example [4, 42–45], the MF of EHCSs with various HCs is not sufficiently considered, there are no verified methods of calculating the MF of EHCSs, a correct assessment of the compliance of the MF flux density of their MF with the current regulations of Ukraine and authoritative international recommendations has not been performed.

The goal of the work is to develop a mathematical model and a verified methodology for calculating the magnetic field of electric heating cable systems of the floors for residential premises, and assessment of compliance with the normative level.

Mathematical models of MF of rectilinear HCs. When building the model, we will accept the following assumptions, which allow us to simplify the simulation, but do not significantly affect its result:

- the length L of the HC is significantly (by an order of magnitude) greater than the distance r to the observation point P, and also from the distance d between the wire axes of two-wire cables, which allows us to consider the HCs as infinitely;
- HCs are modelled by parallel rectilinear conducting wires in the form of current filaments located in horizontal planes;
- HC MF is potential and plane-parallel;
- the influence of external ferromagnetic (electrically conductive) elements and sources of MF of the residential premises, as well as the electrically conductive shield 3 (Fig. 2) of the HC is neglected;
- the voltage of the HC network power supply is sinusoidal.

Single-wire HC. According to the law of full current in integral form [46], the line integral of the strength ***H*** of the MF along a closed circuit is equal to the electric current I through the surface bounded by this circuit:

$$\oint_L (\boldsymbol{H}, \boldsymbol{dl}) = I \,. \qquad (1)$$

Applying (1) to a circle lying on a plane with a radius r and centered at the point through which the infinity conductor passes, we obtain:

$$2\pi r H = I \,. \qquad (2)$$

With the help of (2), we find the dependence of the strength of the MF of a single infinity conductor on its current, the coordinates of the conductor axis (x_c, y_c) and the coordinates of the observation point $P(x, y)$:

$$H(r) = \frac{I}{2\pi\, r^*}, \quad r^* = \sqrt{(x - x_c)^2 + (y - y_c)^2} \,. \qquad (3)$$

From (3) under the conditions $x = r$, $y = 0$, we obtain the known [9, 46] relation that determines the flux density of the MF at a distance r from a single single-wire HC:

$$B_{OK} = \frac{\mu_0}{2\pi}\frac{I}{r}, \ \mu_0 = 4\pi\cdot 10^{-7}\ \text{H/m}. \qquad (4)$$

Two-wire planar HC. It is obvious that the maximum value of MF flux density of a two-wire planar cable located in the horizontal plane XY with the distance between parallel wires d and the currents in them $\pm I$ is distributed along the vertical axis Z. In general, the problem of determining the MF of such a HC can be solved exclusively by numerical methods. However, if we consider the MF only along the Z axis, at a height r from the HC, then the task is significantly simplified due to symmetry. Applying Biot-Savar's law and elementary geometric constructions, similarly to [8], we obtain the following formula for calculating to the MF flux density module of a two-wire planar HC:

$$B_{DPK\ \max} = \frac{\mu_0}{2\pi}\frac{I \cdot d}{\left\{r^2 + (0{,}5d)^2\right\}} \,. \qquad (5)$$

Two-wire coaxial HC. It is known that the MF of an infinity cylindrical conductor is equivalent to the MF of a filamen with the same current passing through the axis of symmetry of such a conductor [10, 47]. Accordingly, in an ideal coaxial HC, the axes of both of its conductors (Fig. 2,*c*) coincide, and their currents are in different directions. Therefore, the MF of these currents is mutually compensated, and for an ideal coaxial HC, its resulting MF outside the conductors will be absent. But during the industrial production of HCs, technological deviations from the symmetrical shape arise. Here, the geometric axis inside the wire of the HC can shift by the value of eccentricity e [48, 49], which characterizes the value of its deviation from the axis of symmetry of the HC. The value of the technological dispersion of the eccentricity of coaxial cables during serial production can be 5–15 % (0.1–0.3 mm) of the ideal distance d between the axis of its central wire and the surface of the cylindrical conductive wire. Therefore, the external MF of a real coaxial HC will coincide with the MF of a conventional two-wire planar HC (5), in which the distance between its wires is equal to the eccentricity value ($d = e$). Taking into account the above, the MF flux density of a real coaxial HC on the basis of (5) can be determined by the relationships:

$$B_{DKK\ \max} = \frac{\mu_0}{2\pi}\frac{Ie}{\left\{r^2 + (0{,}5e)^2\right\}} \,. \qquad (6)$$

Study of MF of different types of HC. We will use the obtained relationships (4)–(6) for the engineering calculation of the MF flux density of the HC as a function of the distance r to the observation point. Here, the value r corresponds to the depth h_k of the HC laying (Fig. 1), which determines the distance from the floor surface to the axis of the HC wires. The calculation results are presented in Fig. 4. The MF flux density of a single-wire HC at the manufacturer's recommended laying depth of 0.03–0.05 m [37–41] is 40–65 µT. This is 80–130 times higher than the normative level of 0.5 µT, which excludes the use of single-wire HCs in residential premises.

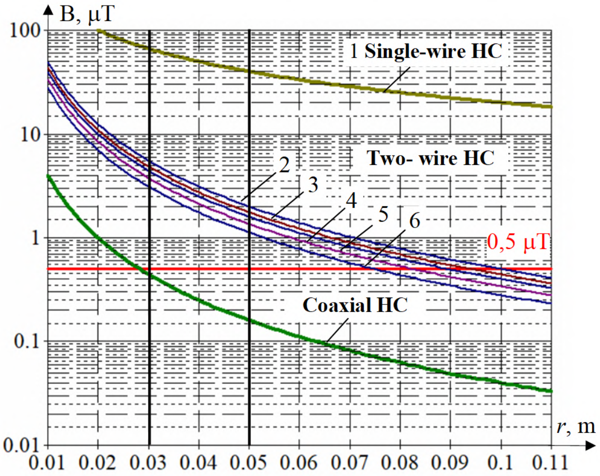

Fig. 4. Calculated values of flux density of MF of different types of rectilinear HCs when at a distance r along the Z axis (two-wire HCs with d: 2 – 2.5 mm; 3 – 2.2 mm; 4 – 2 mm; 5 – 1.7 mm; 6 – 1.4 mm; coaxial HC with e = 0.2 mm); I = 10 A

The MF flux density of two-wire HCs at a laying depth of 0.03–0.05 m, depending on the distance between their wires *d* (Fig. 4) is from 2 to 5.5 μT, which exceeds the normative level of 0.5 μT by 4–11 times.

The MF flux density of the coaxial HC at *e* = 0.2 mm and the standard laying depth of 0.03–0.05 m is (Fig. 4) from 0.16 to 0.45 μT, which corresponds to the normative level of 0.5 μT. Therefore, coaxial HCs, with their eccentricity limited to 0.1*d* (approximately 0.2 mm), can be safely used in residential premises with a standard laying depth.

The results of calculating the MF flux density of real HCs are shown in Fig. 5. They are represented by a planar two-wire HC of the «Arnold Rak 6101-20 EC» type and a coaxial HC of the «Volterm» type at *e* = 0.2 mm and 0.05 mm (curves 2, 3), which was specially provided by the «VOLTERM» Company [40] for testing on the magnetometer stand of the Institute. Analysis of the calculation results (Fig. 5) shows that they correspond to the data in Fig. 4 and the above conclusions.

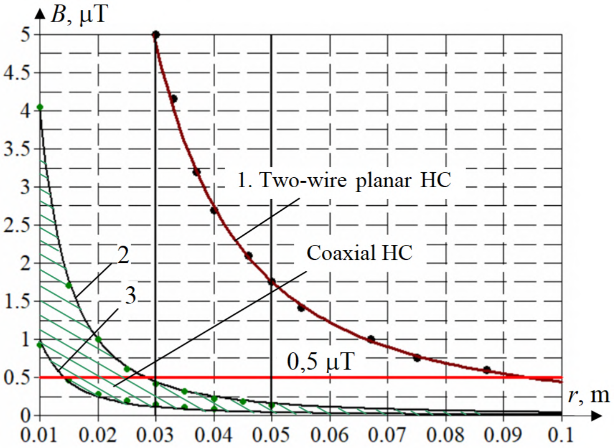

Fig. 5. Calculated ▬▬ and experimental ●●●● values of MF flux density of rectilinear two-wire planar HC type «Arnold Rak 6101-20 EC», *d* = 2.2 mm (1), as well as coaxial HC type «Volterm» (2, 3) with an eccentricity *e* = 0.2–0.05 mm, when moving away from them by a distance *r* along the *Z* axis, *I* = 10 A

Now we will perform a study of the MF flux density distribution of the EHCS with different HCs by the scheme of their laying in accordance with Fig. 3. Such laying changes the spatial distribution of the EHCS MF in comparison with the MF of a single rectilinear HC due to the mutual influence of nearby conductors with a current behind the MF.

Mathematical model of EHCS MF. When building the MF model, we accept the following assumptions: EHCS HCs are modeled by a broken line (meander, Fig. 3) of rectilinear parallel current filaments located in the horizontal plane; quasi-stationary EHCS MF is three-dimensional; the influence of external ferromagnetic (electrically conductive) elements and sources of MF are neglected; the power supply voltage is sinusoidal.

We will perform the simulation using an analytical method based on Biot-Savard's law and the principle of superposition [9, 10, 46, 47] by determining the result in the form of a vector sum of the MF flux density at the observation point *P*(*x*, *y*, *z*) from individual current-carrying conductors.

At a point with a radius vector ***R***, a contour element d*r* with a current *I* generate a MF with MF flux density:

$$\mathrm{d}\boldsymbol{B}(t)=\frac{\mu_0 I}{4\pi R^3}\left[\mathrm{d}\boldsymbol{r}\times\boldsymbol{R}\right], \tag{7}$$

where the vector ***R*** is directed from the location point of the contour element d*r* to the observation point *P*(*x*, *y*, *z*). The total MF of the contour *C* has the MF flux density:

$$\boldsymbol{B}=\frac{\mu_0 I}{4\pi}\int_C\frac{\left[\mathrm{d}\boldsymbol{r}\times\boldsymbol{R}\right]}{R^3}. \tag{8}$$

Consider the MF (Fig. 6,*a*) created by the current *I*, which passes through a straight section between the points $A_n(X_0, Y_1, 0)$ and $A_k(X_0, Y_2, 0)$, i.e., the segment with the current located in the plane *z* = 0 parallel to the *y* axis at a distance *X* from the *y* axis (Fig. 6,*a*). In this case, the contour element is equal to:

$$\mathrm{d}\boldsymbol{r}=\mathrm{d}\eta\boldsymbol{e}_y,\quad Y_1\le\eta\le Y_2, \tag{9}$$

and its coordinates:

$$(X_0,\eta,0),\quad Y_1\le\eta\le Y_2. \tag{10}$$

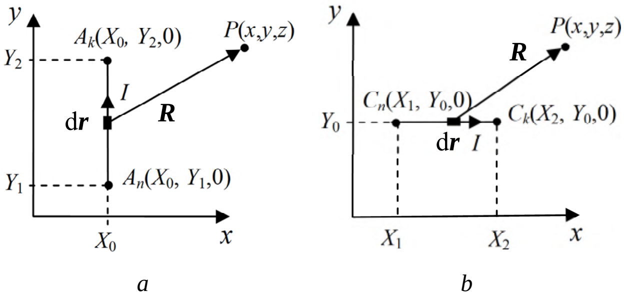

Fig. 6. To determination of the MF flux density of segments with a current located parallel to the *y* (*a*) and *x* (*b*) axes

Then the vector directed from the point where the current element d*r* is located to the observation point *P*(*x*, *y*, *z*) is equal to:

$$\boldsymbol{R}=\left(x-X_0,y-\eta,z\right).$$

The third degree of the distance between the contour element and the observation point:

$$R^3=\left[\left(x-X_0\right)^2+z^2+\left(y-\eta\right)^2\right]^{3/2}. \tag{11}$$

Vector product:

$$\left[\mathrm{d}\boldsymbol{l}\times\boldsymbol{R}\right]=\begin{vmatrix}\boldsymbol{e}_x & \boldsymbol{e}_y & \boldsymbol{e}_z\\ 0 & \mathrm{d}\eta & 0\\ x-X_0 & y-\eta & z\end{vmatrix}=z\mathrm{d}\eta\boldsymbol{e}_x-\left(x-X_0\right)\mathrm{d}\eta\boldsymbol{e}_z. \tag{12}$$

The MF flux density components of a rectilinear segment with current will be written as:

$$B_x=\frac{\mu_0 I}{4\pi}z\int_{Y_1}^{Y_2}\frac{\mathrm{d}\eta}{R^3};\quad B_y=0;\quad B_z=-\frac{\mu_0 I}{4\pi}\left(x-X_0\right)\int_{Y_1}^{Y_2}\frac{\mathrm{d}\eta}{R^3}. \tag{13}$$

In [50] there is a formula for the indefinite integral:

$$\int\frac{\mathrm{d}t}{T(t)^{3/2}}=\frac{4at+2b}{\left(4ac-b^2\right)T(t)^{1/2}};$$

$$T(t)^{1/2}=\left[c+bt+at^2\right]^{1/2}. \tag{14}$$

Using it, we calculate the integral in (13):

$$\int_{Y_1}^{Y_2}\frac{\mathrm{d}\eta}{R^3}=\int_{Y_1}^{Y_2}\frac{\mathrm{d}\eta}{\left[\left(x-X_0\right)^2+z^2+\left(y-\eta\right)^2\right]^{3/2}}=$$

$$= \int_{Y_1}^{Y_2} \frac{\mathrm{d}\eta}{\left[c+(y-\eta)^2\right]^{3/2}} = \int_{Y_1}^{Y_2} \frac{\mathrm{d}\eta}{\left[c+(\eta-y)^2\right]^{3/2}} =$$

$$= \int_{Y_1-y}^{Y_2-y} \frac{\mathrm{d}t}{\left[c+t^2\right]^{3/2}} = \left[\frac{1}{c}\frac{t}{\left[c+t^2\right]^{1/2}}\right]_{Y_1-y}^{Y_2-y} =$$

$$= \frac{1}{(x-X_0)^2+z^2}\left[\frac{Y_2-y}{\left[(x-X_0)^2+z^2+(Y_2-y)^2\right]^{1/2}} - \right.$$

$$\left. - \frac{Y_1-y}{\left[(x-X_0)^2+z^2+(Y_1-y)^2\right]^{1/2}}\right]. \qquad (15)$$

We denote:

$$F(X_0,Y) = \frac{Y-y}{\left((x-X_0)^2+z^2\right)\left[(x-X_0)^2+z^2+(Y-y)^2\right]^{1/2}}.$$

Then the components of the MF will be written in the form:

$$BY_x(X_0,Y_1,Y_2) = \frac{\mu_0 I}{4\pi} z\left[F(X_0,Y_2)-F(X_0,Y_1)\right];$$

$$BY_z(X_0,Y_1,Y_2) = -\frac{\mu_0 I}{4\pi}(x-X_0)\left[F(X_0,Y_2)-F(X_0,Y_1)\right];$$

$$BY_y(X_0,Y_1,Y_2) = 0. \qquad (16)$$

The functions $BY_x(X_0,Y_1,Y_2)$, $BY_y(X_0,Y_1,Y_2)$, $BY_z(X_0,Y_1,Y_2)$ give the components of the MF flux density of a conductor segment parallel to the y axis with a current I at a distance X_0 from the axis.

Consider the MF in the direction of the x axis from the current I passing along the segment between the points $C_n(X_1,Y_0,0)$ and $C_k(X_2,Y_0,0)$ (Fig. 6,*b*). The segment with the current is located in the z = 0 plane, passes parallel to the x axis at a distance Y_0 from the x axis. Performing calculations similar to (9)–(14), we obtain:

$$BX_y(Y_0,X_1,X_2) = -\frac{\mu_0 I}{4\pi} z\left[G(X_2,Y_0)-G(X_1,Y_0)\right];$$

$$BX_z(Y_0,X_1,X_2) = \frac{\mu_0 I}{4\pi}(y-Y_0)\left[G(X_2,Y_0)-G(X_1,Y_0)\right];$$

$$BX_x(Y_0,X_1,X_2) = 0, \qquad (17)$$

where

$$G(X,Y_0) = \frac{X-x}{\left((y-Y_0)^2+z^2\right)\left[(y-Y_0)^2+z^2+(X-x)^2\right]^{3/2}}.$$

The functions $BX_x(Y_0,X_1,X_2)$, $BX_y(Y_0,X_1,X_2)$, $BX_z(Y_0,X_1,X_2)$ give the spatial components of the MF flux density of a conductor segment parallel to the x axis with a current I at a distance Y_0 from the axis.

We will use (16), (17) to determine the calculation relationships of MF of real EHCS of floors, the cable laying schemes for which are presented in Fig. 3.

Calculation relationships for EHCS MF with single-wire HC. The MF flux density at point P from the system of single-wire conductors (Fig. 3,*a*) in the plane z = const, which are parallel to the x and y coordinate axes, is determined by the vector sum of the MF flux density from their straight line segments. Then, according to (16), (17), the components of EHCS MF can be represented as:

$$B_x = \sum_{m=1}^{m=K/2}\left[BY_x(X_{2m-1},Y_1,Y_2)+BY_x(X_{2m},Y_2,Y_1)\right]+$$
$$+BY_x(X_K,Y_1,Y_1-b);$$

$$B_y = \sum_{c=1}^{c=K/2-1}\left[BX_y(Y_2,X_{2c-1},X_{2c})+BX_y(Y_1,X_{2c},X_{2c+1})\right]+$$
$$+BX_y(Y_2,X_{K-1},X_K)+BX_y(Y_1-b,X_K,X_1);$$

$$B_z = \sum_{m=1}^{m=K/2}\left[BY_z(X_{2m-1},Y_1,Y_2)+BY_z(X_{2m},Y_2,Y_1)\right]+$$
$$+BY_z(X_K,Y_1,Y_1-b)+$$
$$+\sum_{c=1}^{c=K/2-1}\left[BX_z(Y_2,X_{2c-1},X_{2c})+BX_z(Y_1,X_{2c},X_{2c+1})\right]+$$
$$+BX_z(Y_2,X_{K-1},X_K)+BX_z(Y_1-b,X_K,X_1), \qquad (18)$$

where $X_m,Y_{1,2}$, K are the coordinates of the ends and the number of segments parallel to the y axis; $X_c,Y_{1,2}$ are the coordinates of the ends of segments parallel to the x axis.

The effective value of the MF flux density of EHCS at the point $P(x,y,z)$ is defined as:

$$\widetilde{B}(P) = \sqrt{B_x^2+B_y^2+B_z^2}, \qquad (19)$$

where the spatial components B_x, B_y, B_z are obtained according to (18).

Calculation relationships for EHCS MF with two-wire HC. The MF flux density at the point $P(x,y,z)$ from the system of two-wire conductors (Fig. 3,*b*) with a distance between the axes of the wires d = 2s, laid out in the plane z = const parallel to the x and y coordinate axes, is determined by the sum of the MF from their rectilinear segments. Then, according to (16), (17), the components of MF flux density of EHCS with two-wire HC can be represented in the form:

$$B_x = \sum_{m=1}^{m=K/2}\left[BY_x(X_{2m-1}-s,Y_1+s,Y_2+s)+\right.$$
$$+BY_x(X_{2m}+s,Y_2+s,Y_1+s)+$$
$$+BY_x(X_{2m-1}+s,Y_2-s,Y_1-s)+$$
$$\left.+BY_x(X_{2m}-s,Y_1-s,Y_2-s)\right]+$$
$$+BY_x(X_K+s,Y_1+s,Y_1-s_1);$$

$$B_y = \sum_{c=1}^{c=K/2-1}\left[BX_y(Y_2+s,X_{2c-1}-s,X_{2c}+s)+\right.$$
$$+BX_y(Y_1+s,X_{2c}+s,X_{2c+1}-s)+$$
$$+BX_y(Y_2-s,X_{2c}-s,X_{2c-1}+s)+$$
$$\left.+BX_y(Y_1-s,X_{2c+1}+s,X_{2c}-s)\right]+$$
$$+BX_y(Y_2+s,X_{K-1}-s,X_K+s)+$$
$$+BX_y(Y_2-s,X_K-s,X_{K-1}+s)+$$
$$+BX_y(Y_1-s,X_K+s,X_K-s);$$

$$B_z = \sum_{m=1}^{m=K/2}\left[BY_z(X_{2m-1}-s,Y_1+s,Y_2+s)+\right.$$
$$+BY_z(X_{2m}+s,Y_2+s,Y_1+s)+$$
$$+BY_z(X_{2m-1}+s,Y_2-s,Y_1-s)+$$

$$
\begin{aligned}
&+BY_z\left(X_{2m}-s, Y_1-s, Y_2-s\right)\Big]+\\
&+BY_z\left(X_K+s, Y_1+s, Y_1-s_1\right)+\\
&+\sum_{c=1}^{c=K/2-1}\Big[BX_z\left(Y_2+s, X_{2c-1}-s, X_{2c}+s\right)+\\
&+BX_z\left(Y_1+s, X_{2c}+s, X_{2c+1}-s\right)+\\
&+BX_z\left(Y_2-s, X_{2c}-s, X_{2c-1}+s\right)+\\
&+BX_z\left(Y_1-s, X_{2c+1}+s, X_{2c}-s\right)\Big]+\\
&+BX_y\left(Y_2+s, X_{K-1}-s, X_K+s\right)+\\
&+BX_y\left(Y_2-s, X_K-s, X_{K-1}+s\right)+\\
&+BX_y\left(Y_1-s, X_K+s, X_K-s\right).
\end{aligned}
\tag{20}
$$

The effective value of MF flux density is determined from (19).

The obtained relationships (18)–(20) make it possible to calculate the MF flux density distribution of EHCS in the case of performing their HC from straight segments – in the form of a rectangular meander (Fig. 3). However, the actual form of HC decomposition can be performed both from practically rectilinear segments [33] and in the form of a «snake» [35] with a radius of curvature of the HC at the level of 0.5*b* (Fig. 10) or less. Outside of the scope of this article, the authors have studied the influence of the shape of decomposition of the top of the HC on the level of EHCS MF, and it is shown that the decomposition in the form of a rectangular meander (Fig. 3) gives the maximum values of MF. This is confirmed by verified curves 1, 3 in Fig. 8, 9. This makes it possible to use the proposed relationships (18)–(20) as universal ones, without taking into account the shape of the peaks of the expansion, to determine the MF flux density of EHCS in the worst case.

Study of EHCS MF with HC of different types. We will use relationships (18)–(20) to determine the MF flux density of EHCS with single-wire and two-wire HCs. Here, we mean that the maximum MF flux density values of the potential EHCS MF in the entire volume of the premisw are concentrated on its floor.

Figure 7 presents a map of the distribution of MF over the EHCS with a single-wire HC, made with dimensions of 1.2×0.8 m and a step of 0.1 m (Fig. 3,*a*). The maximum level of MF flux density (42 μT) occurs at the top of the meander (Fig. 3,*a*) – on the CC line, and above the return wire (TT line). These values practically coincide with the MF of a single rectilinear HC (Fig. 4), which allows us to estimate the maximum values of the MF of this EHCS according to relationship (4). In connection with the significant excess of the normative level of MF, the EHCS with a single-wire HC will not be considered below.

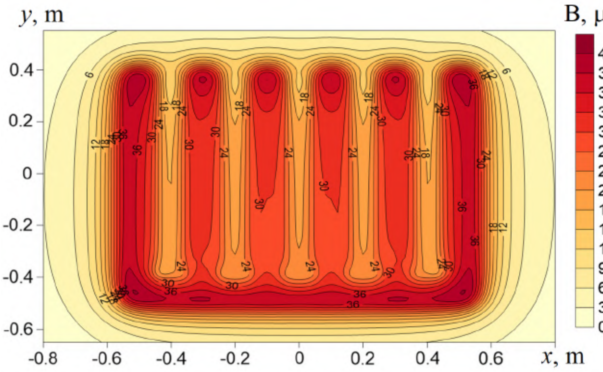

Fig. 7. Calculated values of the MF flux density distribution from EHCS with a single-wire HC type Fenix ASL1P 18 on the floor surface at $h_k = 0.05$ m, $I = 10$ A

The calculated distribution map of EHCS MF with an industrial sample of a two-wire planar HC (Fig. 3,*b*) at $h_k = 0.05$ m with $d = 2.2$ mm is presented in Fig. 8,*a*. Figure 8,*b* shows characteristic graphical dependencies. As can be seen from Fig. 8, the maximum values of the MF flux density of EHCS are 2.16 μT. They take place at the top of the decomposition – along the TT and CC lines (Fig. 3,*b*). These values are greater than the MF of a single HC (Fig. 4) by approximately 15 %.

The calculated distribution map of EHCS MF with an industrial sample of coaxial HC with $e = 0.2$ mm at $h_k = 0.05$ m, made according to Fig. 3,*b*, is presented in Fig. 9,*a*. Figure 9,*b* shows the calculated graphic dependencies. As can be seen from Fig. 9, the maximum values of the MF flux density of EHCS are 0.196 μT, which is significantly less than the normative level of 0.5 μT.

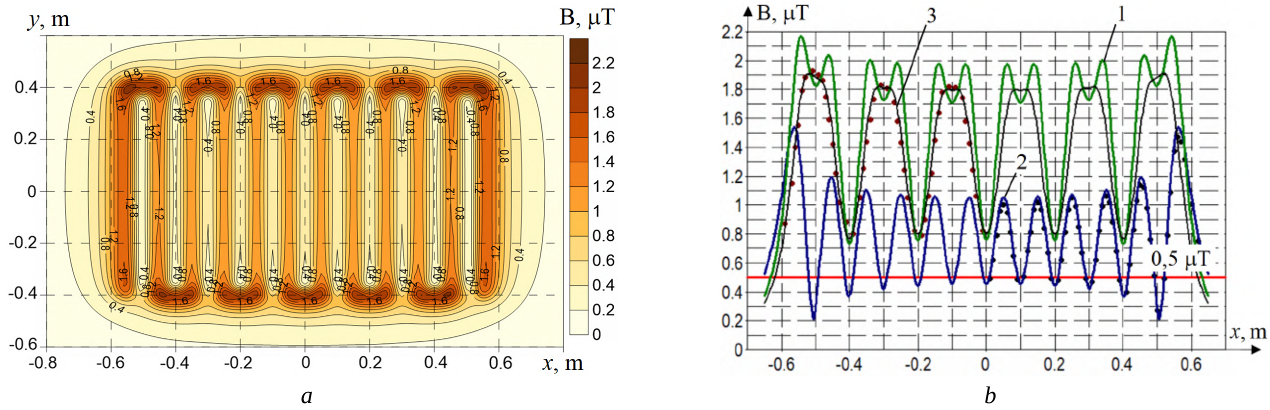

a *b*

Fig. 8. Distribution of MF from EHCS with a two-wire planar HC type Arnold Rak 6101-20 EC ($I = 10$ A, $d = 2.2$ mm) on the floor surface at $h_k = 0.05$ m (EHCS with a rectangular decomposition of HC (Fig. 3,*b*): 1 – along the CC line; 2 – along the AA line); 3 – EHCS with the «snake» decomposition of HC (Fig. 10) along the CC line (Fig. 3,*b*), (▬▬ calculation •••• experiment)

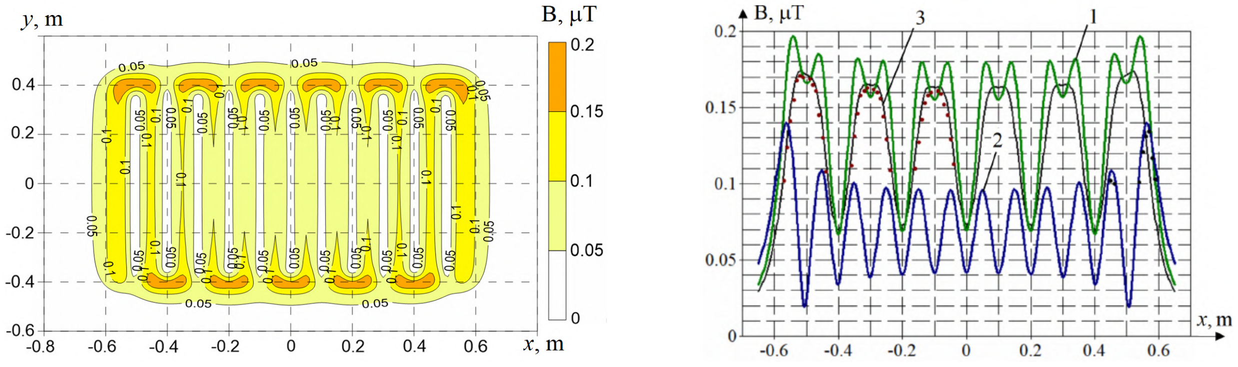

a *b*

Fig. 9. Distribution of MF from EHCS with coaxial HC type «Volterm HR18» (I = 10 A, e = 0.2 mm) on the surface of the floor at h_k = 0.05 m (EHCS with a rectangular decomposition of HC (Fig. 3,*b*): 1 – along the CC line; 2 – along the AA line); 3 – EHCS with the «snake» decomposition of HC (Fig. 10) along the CC line (Fig. 3,*b*), (▬▬ calculation •••• experiment)

Experimental studies of MFs of various types of HC and EHCS based on them. The research was carried out on industrial samples of HC and laboratory models of EHCS based on them at the unique magnetic measuring stand of IPMach of the National Academy of Sciences of Ukraine [26, 27]. Industrial samples of a two-wire planar HC type «Arnold Rak 6101-20 EC» and a coaxial HC type «Volterm HR18» were studied, as well as laboratory models of EHCS based on them, made in accordance with Fig. 3 with dimensions of 1.2×0.8 m and decomposition of the HC with a step of 0.1 m with a snake (Fig. 10). MF flux density measurements were carried out with a certified vector magnetometer type Magnetoscop 1.069 of the Foerster Company (MF flux density measurement range 1 nT–600 mT, error 2.5 %).

Measurement of MF of individual HCs. The results of MF flux density measurements are presented in Fig. 5. For a planar HC, the spread of calculation and experiment results does not exceed 5 %, which confirms the correctness of the developed mathematical models and calculation relationships (18)–(20).

In the process of experimental studies of the «Volterm HR18» type coaxial HC, the inhomogeneity of the distribution of MF flux density along its length was revealed, which at r = 0.03 m varies from 0.16 μT to 0.44 μT. Here, the maximum values of MF flux density according to (6) correspond to the value of eccentricity e at the level of 0.2 mm, and the minimum values of e at the level of 0.05 mm. The spread of the experimental values of the MF flux density by the length of this HC is presented in Fig. 5 in the form of a shaded area between curves 2 and 3. It is significant and indicates the instability of the eccentricity of this HC, which indicates the need to improve the production technology of the coaxial HC by the «Volterm» Company.

Measurement of EHCS MF. Measurements of the MF flux density of EHCS were performed on their laboratory mock-ups (Fig. 10) with the indicated types of HCs. The measurement results are presented in Fig. 8, 9. The spread of calculation and experiment results does not exceed 7 %.

The largest spread occurs at the tops of the EHCS (lines CC, Fig. 3,*b*), which is associated with the difference in the shape of the top of the mock-up (semicircle, Fig. 10) and the calculation model (rectangle, Fig. 3). However, the sspread of the experimental results in comparison with the additionally performed calculation of the MF flux density EHCS by the authors for the case of decomposition of the EHCS vertices according to Fig. 10 in the form of a semicircle with a radius of 50 mm (curve 3 in Fig. 8, 9), also does not exceed 7 %. Therefore, the results of the experiment fully confirm the correctness of the developed mathematical models of EHCS MF (7)–(17) and relations (18)–(20) obtained on their basis.

Fig. 10. Study of the distribution of MF flux density of the EHCS laboratory model with a coaxial HC of the «VOLTERM» type on the magnetometer stand of IPMach of the National Academy of Sciences of Ukraine

Assessment of compliance of EHCS MF with the normative level. On the basis of the verified calculation relationships(18)–(20), the calculation of the maximum values of MF flux density, created by EHCS with modern two-wire planar HCs with d from 1.4 to 2.5 mm and coaxial HCs with eccentricity e = 0.2 mm and e = 0.1 mm eas carried out. The calculation was performed on the surface of the floor of the living premise at different depth h_k of laying the HC and a current of 10 A. The results of the calculation in the form of graphs are presented in Fig. 11.

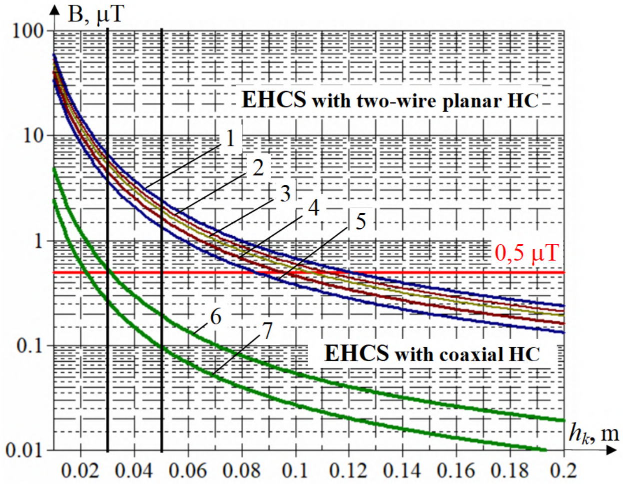

Fig. 11. Calculated by the verified relationships (19), (20) the maximum flux density values of EHCS MF created on the surface of the floor with two-wire planar HCs (d: 1 – 2.5 mm; 2 – 2.2 mm; 3 – 2 mm: 4 – 1.7 mm; 5 – 1.4 mm) and coaxial HCs (6 – e = 0.2 mm; 7 – e = 0.1 mm) with different depth of their laying h_k,, I = 10 A

Analysis of Fig. 11 allows us to state the following. When performing EHCS on the basis of modern two-wire HCs with a minimum distance between wires of 1.4 mm, the maximum value of MF flux density on the floor of residential premises is 3.75–1.3 μT with a laying depth of 0.03–0.05 m and a current of 10 A This is 7.5–2.6 times higher than the maximum permissible level of MF flux density of 0.5 μT. Therefore, the safe use of EHCS based on modern two-wire HCs is achieved only when their laying depth is more than 0.085–0.1 m, or in the case of limiting their current and, accordingly, thermal power.

The reduction of EHCS MF is also possible by installing between the EHCS and the floor of the room a continuous electromagnetic shield, for example, made of welded conductive aluminum sheets 1.5–2 mm thick. But with the expected MF shielding factor at the level of 1.5–2.5 units [51], the cost of such a shield will exceed the cost of EHCS.

Performing EHCS on the basis of coaxial HCs with an eccentricity $e \leq 0.2$ mm at a laying depth of 0.03–0.05 m allows to reduce their MF flux density to the normative level of 0.5 μT. Therefore, the widespread introduction of coaxial HCs is an effective method of solving the problem of reducing possible risks to the health of the population and ensuring their comfortable living in residential premises.

It is also advisable to further improve the design and production technology of coaxial HCs to limit their maximum eccentricity to 0.1 mm and ensure its stability in operating conditions.

Conclusions.

1. On the basis of the Bio-Savar's law and the principle of superposition, an analytical model of the magnetic field of electric heating cable systems of the floors for residential premises and a methodology for calculating the magnetic flux density based on it have been developed.

2. Verification of the developed mathematical model and technique of calculating the magnetic field was carried out through experimental studies of laboratory layouts of electric heating cable systems with industrial samples of various types of heating cables. The measurements confirmed the coincidence of the results of the calculation and the experiment with a spread of no more than 7 %.

3. The magnetic field of the coaxial heating cable was studied and the method of its calculation was proposed, taking into account the maximum value of the eccentricity of its central wire.

4. An assessment of the compliance of the magnetic field in the residential premises with the normative level of 0.5 μT when using electric heating cable systems with different heating cables was carried out, and based on which:

a) an excess of the maximum permissible level of magnetic flux density on the floor of residential premises by 2.6–7.5 times was found when using modern two-wire planar heating cables with a minimum distance between the wire of 1.4 mm at the depth of their laying of 0.05–0.03 m and a current of 10 A;

b) it is shown that the safe use in residential premises of modern planar two-wire heating cables with a current of 10 A requires an increase in the depth of their laying to 0.085–0.1 m.

c) to reduce possible risks to the health of the population and ensure their comfortable living, it is recommended to use coaxial heating cables in residential premises, which create an order of magnitude smaller magnetic field than modern two-wire planar heating cables.

Conflict of interest. The authors declare no conflict of interest.

REFERENCES

1. Brune D., Hellborg R., Persson B.R.R., Pääkkönen R. Radiation at home, outdoors and in the workplace. *Scandinavian Science Publisher*, 2001, 547 p.

2. *Non-Ionizing Radiation, Part 1: Static and Extremely Low-Frequency (ELF) Electric and Magnetic Fields.* IARC Monographs on the Evaluation of Carcinogenic Risks to Humans, 2002, no. 80, p. 395.

3. *Standard of Building Biology Testing Methods: SBM−2015.* Germany: Institut fer Baubiologie + Ekologie IBN, 2015, 5 p. Available at: https://buildingbiology.com/building-biology-standard (Accessed 01 February 2024).

4. Milutinov M., Juhas A., Pekarić-Nađ N. Magnetic field of electrical radiant heating system. *Safety Engineering*, 2017, vol. 7, no. 2, pp. 61-65. doi: https://doi.org/10.7562/SE2017.7.02.03.

5. *DBN V.2.5-24:2012. State building regulations of Ukraine. Electrical cable scorching system.* Kyiv, Minrehionbud Publ., 2012. 81 p. (Ukr).

6. *SOU-N EE 20.179:2008. Calculation of electric and magnetic fields of power lines. Methodology (with changes) (in the edition of the order of the Minenergvugillya dated July 1, 2016, no. 423).* Kyiv, Minenergvugillya Ukraine Publ., 2016. 37 p. (Ukr).

7. Conti R., Giorgi A., Rendina R., Sartore L., Sena E.A. Technical solutions to reduce 50 hz magnetic fields from power lines. *2003 IEEE Bologna Power Tech Conference Proceedings*, 2003, vol. 2, pp. 1016-1021. doi: https://doi.org/10.1109/PTC.2003.1304685.

8. *SOU-N MEV 40.1-37471933-49:2011. Design of cable lines up to 330 kV. Guideline (in the edition of the order of the Minenergvugillya dated January 26, 2017 no. 82).* Kyiv, Minenergvugillya Ukraine Publ., 2017. 168 p. (Ukr).

9. Nesterenko A.D. *Introduction to Theoretical Electrical Engineering*. Kyiv, Naukova Dumka Publ., 1969. 351 p. (Rus).

10. Shimoni K. *Theoretical Electrical Engineering (translation from German)*. Moscow, Mir Publ., 1964. 774 p. (Rus).

11. *DSNiP 3.3.6.096-2002. State sanitary standards and rules for working with sources of electromagnetic fields (order of the Ministry of Health (MoH) of Ukraine dated December 18, 2002 no. 476)*. Kyiv, MoH Publ., 2003. 16 p. (Ukr).

12. *World Health Organization. Electromagnetic fields and public health. Exposure to extremely low frequency fields*. Available at: https://www.who.int/teams/environment-climate-change-and-health/radiation-and-health/non-ionizing/exposure-to-extremely-low-frequency-field (Accessed 01 February 2024).

13. Tognola G., Chiaramello E., Bonato M., Magne I., Souques M., Fiocchi S., Parazzini M., Ravazzani P. Cluster Analysis of Residential Personal Exposure to ELF Magnetic Field in Children: Effect of Environmental Variables. *International Journal of Environmental Research and Public Health*, 2019, vol. 16, no. 22, art. no. 4363. doi: https://doi.org/10.3390/ijerph16224363.

14. Wertheimer N., Leeper E. Electrical wiring configurations and childhood cancer. *American Journal of Epidemiology*, 1979, vol. 109, no. 3, pp. 273-284. doi: https://doi.org/10.1093/oxfordjournals.aje.a112681.

15. Kheifets L., Ahlbom A., Crespi C.M., Draper G., Hagihara J., Lowenthal R.M., Mezei G., Oksuzyan S., Schüz J., Swanson J., Tittarelli A., Vinceti M., Wunsch Filho V. Pooled analysis of recent studies on magnetic fields and childhood leukaemia. *British Journal of Cancer*, 2010, vol. 103, no. 7, pp. 1128-1135. doi: https://doi.org/10.1038/sj.bjc.6605838.

16. Green L.M., Miller A.B., Villeneuve P.J., Agnew D.A., Greenberg M.L., Li J., Donnelly K.E. A case-control study of childhood leukemia in Southern Ontario, Canada, and exposure to magnetic fields in residences. *International Journal of Cancer*, 1999, vol. 82, no. 2, pp. 161-170. doi: https://doi.org/10.1002/(SICI)1097-0215(19990719)82:2<161::AID-IJC2>3.0.CO;2-X.

17. Guidelines for Limiting Exposure to Time-Varying Electric and Magnetic Fields (1 Hz to 100 kHz). *Health Physics*, 2010, vol. 99, no. 6, pp. 818-836. doi: https://doi.org/10.1097/HP.0b013e3181f06c86.

18. Sage C., Carpenter D.O. *BioInitiative Report: A Rationale for Biologically-based Exposure Standards for Low-Intensity Electromagnetic Radiation*. BioInitiative Working Group. 2012. 1479 p. Available at: https://www.infrastructure.gov.au/sites/default/files/submissions/BioInitiative_Working_Group.pdf (Accessed 01 February 2024).

19. *World Health Organization. Exposure limits for low-frequency fields (public). Data by country*. Available at: https://apps.who.int/gho/data/node.main.EMFLIMITSPUBLICLOW?lang=en (Accessed 01 February 2024).

20. Kuznetsov B.I., Nikitina T.B., Bovdui I.V., Voloshko O.V., Kolomiets V.V., Kobylianskyi B.B. Synthesis of an effective system of active shielding of the magnetic field of a power transmission line with a horizontal arrangement of wires using a single compensation winding. *Electrical Engineering & Electromechanics*, 2022, no. 6, pp. 15-21. doi: https://doi.org/10.20998/2074-272X.2022.6.03.

21. Kuznetsov B.I., Kutsenko A.S., Nikitina T.B., Bovdui I.V., Kolomiets V.V., Kobylianskyi B.B. Method for design of two-level system of active shielding of power frequency magnetic field based on a quasi-static model. *Electrical Engineering & Electromechanics*, 2024, no. 2, pp. 31-39. doi: https://doi.org/10.20998/2074-272X.2024.2.05.

22. Rozov V.Y., Reutskiy S.Y., Kundius K.D. Protection of workers against the magnetic field of 330-750 kV overhead power lines when performing work without removing the voltage under load. *Electrical Engineering & Electromechanics*, 2024, no. 4, pp. 70-78. doi: https://doi.org/10.20998/2074-272X.2024.4.09.

23. Rozov V.Y., Reutskyi S.Y., Pelevin D.Y., Kundius K.D. Approximate method for calculating the magnetic field of 330-750 kV high-voltage power line in maintenance area under voltage. *Electrical Engineering & Electromechanics*, 2022, no. 5, pp. 71-77. doi: https://doi.org/10.20998/2074-272X.2022.5.12.

24. Rozov V.Y., Pelevin D.Y., Kundius K.D. Simulation of the magnetic field in residential buildings with built-in substations based on a two-phase multi-dipole model of a three-phase current conductor. *Electrical Engineering & Electromechanics*, 2023, no. 5, pp. 87-93. doi: https://doi.org/10.20998/2074-272X.2023.5.13.

25. Rozov V.Yu., Rezinkina M.M., Dumanskiy Yu.D., Gvozdenko L.A. The study of man-caused distortions in the geomagnetic field of residential and industrial buildings and to identify ways to reduce them to a safe level. *Technical Electrodynamics. Thematic Issue «Problems of Modern Electrical Engineering»*, 2008, chapter 2, pp. 3-8. (Rus).

26. Rozov V.Yu. To the 40th anniversary of the Science and Technology Center of Magnetism of Technical Objects of the NAS of Ukraine. *Technical Electrodynamics*, 2010, no. 3, pp. 74-80. (Rus).

27. Baranov M.I., Rozov V.Y., Sokol Y.I. To the 100th anniversary of the National academy of sciences of Ukraine – the cradle of domestic science and technology. *Electrical Engineering & Electromechanics*, 2018, no. 5, pp. 3-11. doi: https://doi.org/10.20998/2074-272X.2018.5.01.

28. Rozov V.Yu., Getman A.V., Petrov S.V. Magnetism of space-craft. *Technical Electrodynamics. Thematic Issue «Problems of Modern Electrical Engineering»*, 2010, chapter 2, pp. 144-147. (Rus).

29. Rozov V., Grinchenko V., Tkachenko O., Yerisov A. Analytical Calculation of Magnetic Field Shielding Factor for Cable Line with Two-Point Bonded Shields. *2018 IEEE 17th International Conference on Mathematical Methods in Electromagnetic Theory (MMET)*, 2018, pp. 358-361. doi: https://doi.org/10.1109/MMET.2018.8460425.

30. Dumanskiy V.Yu., Serdyuk A.M., Los' I.P. *The influence of electromagnetic radiation on humans*. Kyiv, Zdorovye Publ., 1975. 180 p. (Rus).

31. Dumanskiy V., Bitkin S., Didyk N., Dumanskiy Yu., Nikitina N., Mizyuk M., Bezverkha A., Zotov S., Tomashevskaya L., Semashko P., Lyashenko V., Galak S., Medvedev S. Hygienical ground of requirements to placing and exploitation of cable busses of electricity transmission and their equipment in the conditions of modern municipal building. *Hygiene of populated places*, 2015, no. 66, pp. 20-29. (Ukr).

32. *Electrical installation regulations*. Kharkiv, Fort Publ., 2017. 760 p. (Ukr).

33. *SunTouch Heating Mat Kits*. Available at: https://www.flooringsupplyshop.com/category/suntouch-heating-mats-kits-119 (Accessed 01 February 2024).

34. *Arnold Rak*. Available at: www.rak-waermetechnik.de (Accessed 01 February 2024).

35. *Hemstedt*. Available at: https://www.hemstedt.de (Accessed 01 February 2024).

36. *Handbook for Comfortable Warm Floors. nVent Raychem*. 2022. 48 p. Available at: https://www.nvent.com/sites/default/files/acquiadam_assets/2022-08/RAYCHEM-TH-EU1001-Floorheating-EN.pdf (Accessed 01 February 2024).

37. *ELEKTRA Heating Cables. Installation manual*. 72 p. Available at: https://elektra.pl/download/ru/electrical-heating-systems/floor-heating/heating-cables-VCD/vcd7_vcd10_vcd17_heating_cables_manual.pdf (Accessed 01 February 2024).

38. *Woks. PJSC «Odeskabel».* Available at: https://woks.ua/ua (Accessed 01 February 2024).
39. *Indoor Cable Floor Heating Systems. Application manual*. 2016. 52 p. Available at: https://assets.danfoss.com/documents/89845/AB213486470188en-010101.pdf (Accessed 01 February 2024).
40. *VOLTERM Coaxial Heating system*. Available at: https://volterm.com.ua (Accessed 01 February 2024).
41. *3HeatTech. Radiant Floor Heating Cable*. Available at: https://www.heattechproducts.com/electric-radiant-floor-heating-cable-kits (Accessed 01 February 2024).
42. Ambartsumyants K. Heating cables: construction and applications. (Rus). Available at: https://aw-therm.com.ua/nagrevatelnye-kabeli-konstrukciya-i-primenenie (Accessed 01 June 2024).
43. Manilov A.M., Krasnozhon A.V., Tovstiuk S.O. Assessment of the magnitude of the magnetic field of cable heating of residential and industrial premises from the point of view of its safety for people. *Promelektro*, 2022, no. 3-6, pp. 32-36. (Ukr). Available at: https://pdf.lib.vntu.edu.ua/books/2022/EP/Promelektro-3-6-2022.pdf (Accessed 01 February 2024).
44. Thieblemont H., Haghighat F., Moreau A. Thermal Energy Storage for Building Load Management: Application to Electrically Heated Floor. *Applied Sciences*, 2016, vol. 6, no. 7, art. no. 194. doi: https://doi.org/10.3390/app6070194.
45. Gołębiowski J., Forenc J. The influence of side thermal insulation on distribution of the temperature field in an electrical floor heater. *Przegląd Elektrotechniczny*, 2016, no. 12, pp. 271-277. doi: https://doi.org/10.15199/48.2016.12.68.
46. Stratton J.A. *The Theory of Electromagnetism*. Moscow, Gostehizdat Publ., 1948. 520 p. (Rus).
47. Smythe W.R. *Static and Dynamic Electricity.* McGraw-Hill, New York, 1968. 623 p.
48. Kyessayev A.G. Impact on the transmission parameters eccentricity and ellipticity RF coaxial cables. *Bulletin of the National Technical University «KhPI». Series: Energy: Reliability and Energy Efficiency*, 2013, no. 59, pp. 62-69. (Ukr).
49. Bezprozvannych G.V., Boyko A.M., Kessaev O.G. Influence of constructive and technological defects on coaxial radio-frequency cable impedance. *Electrical Engineering & Electromechanics*, 2013, no. 2, pp. 57-61. (Ukr).
50. Dwight H.B. *Tables of Integrals and Other Mathematical Data*. 4th ed. The Macmillan Company, 1972. 336 p.
51. Del Pino López J.C., Cruz Romero P., Dular P. Parametric analysis of magnetic field mitigation shielding for underground power cables. *Renewable Energy and Power Quality Journal*, 2007, vol. 1, no. 5, pp. 519-526. doi: https://doi.org/10.24084/repqj05.326.

Received 27.03.2024
Accepted 22.05.2024
Published 20.08.2024

V.Yu. Rozov[1], *Doctor of Technical Science, Professor,*
Corresponding member of NAS of Ukraine,
S.Yu. Reutskiy[1], *PhD, Senior Researcher,*
D.Ye. Pelevin[1], *PhD, Senior Researcher,*
K.D. Kundius[1], *PhD,*
[1] Anatolii Pidhornyi Institute of Mechanical Engineering Problems of the National Academy of Sciences of Ukraine,
2/10, Pozharskogo Str., Kharkiv, 61046, Ukraine,
e-mail: vyurozov@gmail.com (Corresponding Author);
sergiyreutskiy@gmail.com; pelevindmitro@ukr.net;
kundiuckateryna@ukr.net

How to cite this article:
Rozov V.Yu., Reutskiy S.Yu., Pelevin D.Ye., Kundius K.D. Magnetic field of electrical heating cable systems of the floors for residential premises. *Electrical Engineering & Electromechanics*, 2024, no. 5, pp. 48-57. doi: https://doi.org/10.20998/2074-272X.2024.5.07

UDC 537.52 + 621.3 https://doi.org/10.20998/2074-272X.2024.5.08

M.I. Boiko, A.V. Makogon

Features of distribution of electric field strength and current density in the reactor during treatment of liquid media with high-voltage pulse discharges

***Purpose**. Development and use of a mathematical model of the stages of formation of high-voltage pulse discharges in gas bubbles in the discharge gap «rod-plane» to identify the features of the electric field intensity distribution in the reactor and determine the current density in the load during disinfection and purification of liquid media by high-voltage pulse discharges and find the most rational treatment. **Methodology**. To achieve this goal, we used computer modeling using the finite element method as a method of numerical analysis. An experimental reactor model was created that takes into account the dynamics of discharges in gas bubbles in water. The equations describing the system include the generalized Ampere equation, the Poisson equation and the electric displacement equation, taking into account the corresponding initial and boundary conditions, as well as the properties of materials. The dependence of the potential of a high-voltage electrode on time has the form of a damped sinusoid, and the specific electrical conductivity in a gas bubble is a function of time. Processes occurring at the front of the voltage pulse from 0 to 20 ns are considered. **Results**. It is shown that with an increase in conductivity and high-voltage potential to amplitude values in a gas bubble, the electric field strength in the water layer in the reactor reaches 70 kV/cm, and it is in the water layer that there is a strong electric field. The calculations show that already by 19th ns the density of conduction currents in water prevails over that of displacement currents. At the same time, additional inclusions in the water significantly affect the distribution of electric field strength and current density, creating a significant difference in their values at the boundaries of the interface between the bubble, conductive element and water. **Originality**. A simulation of the dynamics of transient discharge processes in a gas bubble and a layer of water with impurities was carried out, including an analysis of the distribution of the electric field strength and current density in a system with rod-plane electrodes in the phase transition section of a gas bubble-water. This approach allows us to reveal the features of processes in reactors and to investigate the influence of phase transitions on the distribution of electrophysical quantities. **Practical value**. Computer simulations confirm the prospect of using nanosecond discharges generated in gas bubbles within a volume of water for widespread industrial use and are of great interest for further experimental and theoretical research.* References 25, figures 9.

Key words: **reactor, electric field strength, conductivity current density, displacement current density, discharge in a gas bubble in water, inclusion in water.**

***Мета.** Розробка та використання математичної моделі стадій формування високовольтних імпульсних розрядів у газових бульках в розрядному проміжку «стрижень-площина» для виявлення особливостей розподілу напруженості електричного поля в реакторі і визначення густини струму в навантаженні при знезаражуючій обробці і очищенні рідких середовищ високовольтними імпульсними розрядами та знаходження найбільш раціональних режимів обробки. **Методика.** Для досягнення поставленої мети ми використовували комп'ютерне моделювання за допомогою методу скінченних елементів як методу чисельного аналізу. Створено модель експериментального реактора, що враховує динаміку розрядів у газових бульках у воді. Рівняння, що описують систему, включають узагальнене рівняння Ампера, рівняння Пуассона і рівняння електричного зміщення, з урахуванням відповідних початкових і граничних умов, а також властивостей матеріалів. Залежність потенціалу високовольтного електрода від часу має форму затухаючої синусоїди, а питома електропровідність у газовій бульці є функція часу. Розглянуто процеси, що протікають на фронті імпульсу напруги від 0 до 20 нс. **Результати.** Показано, що зі зростанням провідності та високовольтного потенціалу до амплітудних значень у газовій бульці, напруженість електричного поля в шарі води в реакторі досягає значень 70 кВ/см, і саме в шарі води існує сильне електричне поле. З розрахунків випливає, що біля 19-ої нс, густина струмів провідності у воді вже перевершує густину струмів зміщення. При цьому додаткові включення в воді істотно впливають на розподіл напруженості електричного поля та густини струму, створюючи значне збільшення в їх значеннях на границях розділу середовищ між бульбашкою, провідним елементом та водою. **Наукова новизна.** Проведено моделювання динаміки швидкоплинних процесів розряду в газовій бульці та шарі води з домішками, включно з аналізом розподілу напруженості електричного поля і густини струму в системі з електродами «стрижень-площина» в ділянці фазового переходу газова булька-вода. Цей підхід дозволяє розкрити особливості процесів в реакторах і дослідити вплив фазових переходів на розподіл електрофізичних величин. **Практична цінність.** Комп'ютерне моделювання підтверджує перспективу застосування наносекундних розрядів, що генеруються в газових бульках усередині об'єму води, для широкого промислового використання і становлять великий інтерес для подальших експериментальних і теоретичних досліджень.* Бібл. 25, рис. 9.

Ключові слова: **реактор, напруженість електричного поля, густина струмів провідності, густина струмів зміщення, розряд у газовій бульці у воді, включення у воді.**

Introduction. Modern requirements for wastewater treatment require the development of effective means of destruction of organic substances that are resistant to the action of traditional oxidizers. Another component of the problem is the general requirements of decarbonization of the economy, and the success of their solution also applies to wastewater treatment [1-3]. It is especially important here to avoid long processes of biochemical decomposition of organic substances, accompanied by the formation of CH_4, as a gas that has a significantly higher coefficient of contribution to the greenhouse effect, compared to CO_2. Among the technological alternatives to the traditional technologies of natural and reagent oxidation of compounds contained in wastewater, electrophysical technologies stand out, the tools of which are factors caused by the action of ionizing radiation [4], plasma flows [5], and high-voltage discharges [6]. Prospects for the successful practical implementation of each of the indicated directions, in that the resource for their optimization consists in establishing ways of more fully using the energy of the field effect on the object of destruction (bacteria, viruses, organic compounds) and establishing the role of concomitant factors generated as a result of high-voltage electric discharges in water (acoustic pulses, local temperature increases, secondary radiation). Thus, during the treatment of wastewater by methods based on high-voltage electric discharges, various physical and chemical processes occur: the formation of oxidants, including hydroxyl radicals, ozone, the occurrence of shock waves, ultraviolet radiation, strong electric fields [7-12]. The hydroxyl radical OH^- itself acts as a natural oxidant, exhibits high biocidal activity, is capable of effectively destroying pollutants, inactivating bacteria, viruses, yeast, and oxidizing organic and inorganic compounds [13-15].

The strong electric field in the discharge accelerates the electrons, increasing their ability to ionize atoms and molecules, which leads to an avalanche-like increase in the number of free charge carriers, increasing the current, causing more efficient gas ionization and the formation of more active particles. Under the influence of strong pulse electric fields, the breaking of chemical bonds in molecules can occur, as well as their dissociation, which leads to an increase in the number of free atoms and radicals that can participate in chemical reactions [16]. Also, electric fields, the action of which lasts from micro to nanoseconds with strength of the order of 10-100 kV/cm in the form of pulses of electric field strength of various shapes, effectively inactivate microorganisms, while the primary color, taste, and nutritional value of juices, wines, and dairy products are preserved after their processing [17-21]. In our works [21-23], it was substantiated that the effectiveness of the high-voltage discharge action significantly increases under the condition of injection into the discharge zone of a flow of air bubbles.

The complexity of rapid discharge processes makes it difficult to fully understand the dynamics of the discharge inside the bubble and the water layer, namely, how the electric field strength and current density are distributed in the reactor in the area of the phase transition between gas bubble and water using experimental studies.

The goal of the article is to develop and use a mathematical model of the stages of formation of high-voltage pulse discharges in gas bubbles in the "rod-plane" discharge gap to identify the features of the electric field strength distribution in the reactor and determine the current density in the load during disinfection and cleaning of liquid media with high-voltage pulse discharges and finding the most rational processing modes.

Description of the mathematical model of a reactor for wastewater treatment using high-voltage discharges in gas bubbles in it. Figure 1 shows a model of an experimental reactor for water treatment using discharges in gas bubbles in Cartesian coordinate systems (the dimensions along the axes are given in mm).

The boundary 7-8-9 and 5-11 is a system of copper electrodes (σ = $6\cdot10^7$ S/m): high-voltage rod electrode with radius of curvature of 0.5 mm, low-voltage flat electrode. The gas is supplied to the area of the high-voltage electrode 1, where discharges occur directly. Electrode 1 is fixed in the dielectric housing 4 (ε = 2.3, $\sigma = 1\cdot10^{-12}$ S/m). The interelectrode space contains a gas bubble 2 (ε = 1) and a model water solution 3 (ε = 81, σ = 0.125 S/m).

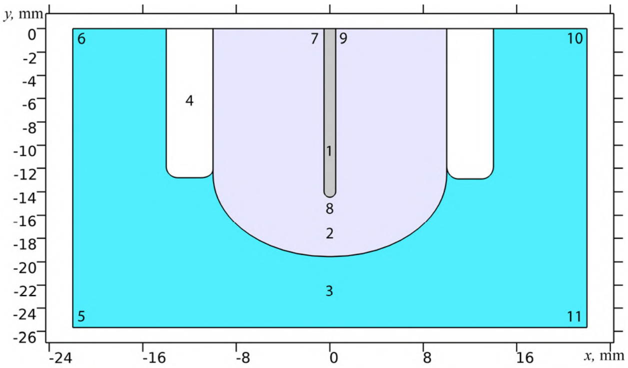

Fig. 1. Model of a reactor for wastewater treatment using high-voltage discharges in gas bubbles in water

The finite element method was used during computer modeling of the formation and development over time of a pulse electrical discharge in a gas bubble inside water.

The initial system of equations:

$$\begin{cases} \boldsymbol{J} = \sigma\cdot\boldsymbol{E} + \partial\boldsymbol{D}/\partial t; \\ \boldsymbol{E} = -\nabla V; \\ \boldsymbol{D} = \varepsilon_0\cdot\varepsilon\cdot\boldsymbol{E}, \end{cases} \quad , \qquad (1)$$

where $\boldsymbol{J}$ is the total current density, σ is the specific electrical conductivity of the material, $\boldsymbol{E}$ is the electric field strength, ε_0 is the dielectric permittivity of the vacuum, ε is the relative dielectric permittivity of the material, $\boldsymbol{D}$ is the electric displacement vector of the dielectric, and V is the electric scalar potential.

In the calculation domain, the condition of continuity of the current is fulfilled: $\nabla\boldsymbol{J} = 0$.

The superimposition of the spatial mesh in the domain of the high-voltage electrode and the gas bubble-water phase transition in the reactor is shown in Fig. 2. A triangular mesh with typical element sizes from $8.8\cdot10^{-4}$ mm to 0.44 mm is set in the entire domain.

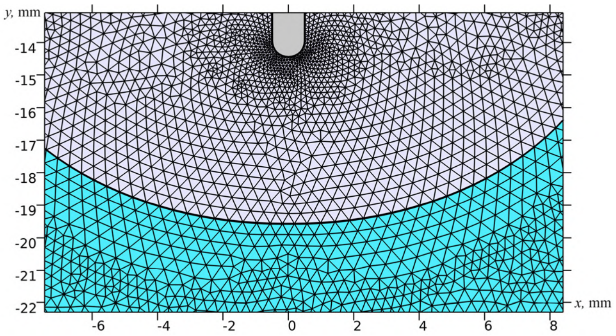

Fig. 2. Superimposition of a spatial mesh in the domain of the gas bubble-water phase transition

Dependence of the potential of the high-voltage electrode on time (boundary 7-8-9) in Fig. 3,*a* has the form of a decaying sinusoid, which is an approximation of the obtained experimental oscillograms of Fig. 3,*b*.

Figure 3,*b* shows experimental oscillograms of nanosecond discharges in gas bubbles in water [23]. The voltage amplitude (curve 1) reaches 30 kV, and the current amplitude (curve 2) – 100 A, the scale along the time axis is 50 ns/div. The scale along the process axis for current oscillograms is 32 A/div, and for voltage oscillograms – 7.9 kV/div.

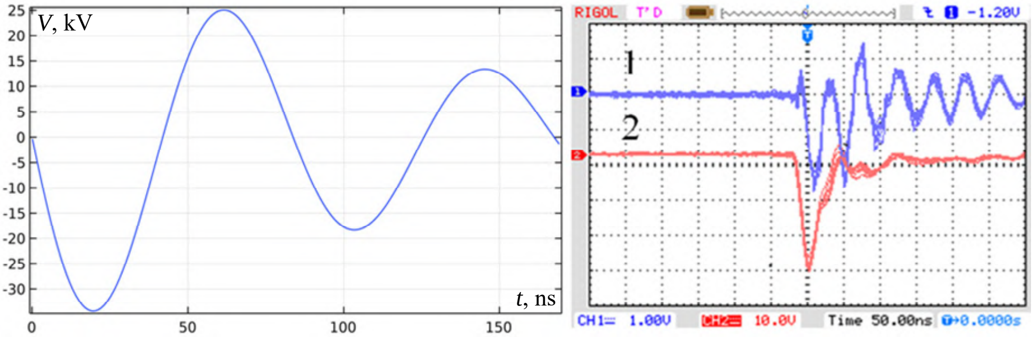

a *b*

Fig. 3. Model and experimental pulses in the reactor: *a* − dependence of the potential of the high-voltage electrode on time; *b* − oscillograms of nanosecond pulses: 1 − voltage pulse, 2 − current pulse

The potential of the low-voltage electrode $V = 0$ (boundary 5-11).

The calculation was performed in the time domain from 0 to 170 ns, with a time step of 0.1 ns.

At zero time, the voltage at all points in the reactor is $V_0 = 0$.

At the boundary 5-6-7, 9-10-11 of the calculation domain, the boundary condition of electrical isolation is set:

$$\boldsymbol{n}\cdot\boldsymbol{J} = 0, \tag{2}$$

where ***n*** is the vector normal to the surface through which the current passes, ***J*** is the current density vector.

This boundary condition means that electric current does not flow across boundaries. The projection of the current density vector on the normal to the surface describes the current density flowing perpendicular to this surface. If the projection is equal to 0, then this indicates the absence of a current perpendicular to the surface. This state corresponds to the boundary conditions of isolation, where charge transfer does not occur at the interface of two media. The potential distribution must be continuous at the interface and the same on both sides of the interface.

Specific electrical conductivity was determined in the model as a function of time to illustrate the influence of ionization processes occurring in the gas bubble under the action of an electric field (Fig. 4).

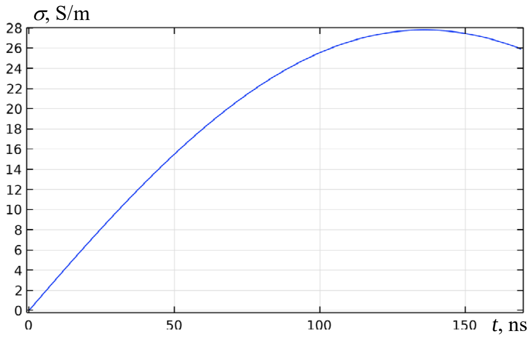

Fig. 4. Specific electrical conductivity in a gas bubble as a function of time

In Fig. 4, specific electrical conductivity changes as follows. At the zero moment of time, the specific electrical conductivity of the gas bubble is 2 orders of magnitude lower than that of water. Gas is a dielectric and contains almost no free charges, so its conductivity is low. On the other hand, wastewater has conductivity due to various ions and minerals dissolved in it, which are carriers of electrical charge and can easily conduct current. As the potential of the high-voltage electrode increases, the electric field strength increases, which activates the movement of free electrons in the bubble. These electrons ionize neutral gas atoms, generating additional free charges. Thus, the number of free charges increases dramatically, which significantly increases gas conductivity. In the model, the conductivity of gas becomes greater than that of water by about 52 times.

Simulation results and their discussion. The processes taking place at the front of the voltage pulse from 0 to 20 ns, when the potential on the high-voltage electrode increases from 0 to the amplitude value, are considered.

In the model, the vector ***E*** in two-dimensional space is represented as $\boldsymbol{E} = (E_x, E_y)$, where E_x is the component of the vector along the x-axis, and E_y is the component of the vector along the y-axis. Thus, to calculate the length of the vector ***E***, we take the square root of the sum of the squares of its components. After calculating the length of the vector, we get the modulus of the electric field strength.

Figure 5 shows the distribution of the y-component of the electric field strength in the reactor.

Figure 5 demonstrates that at the initial moments of time on the (front) of the pulse, the electric field strength near the rod reaches 22 kV/cm, and that with the growth of the bubble conductivity and high-voltage potential to amplitude values, the electric field strength on the water layer reaches 62 kV/cm.

In addition, impurities are introduced into the model water in the reactor, which may be present in the water being treated and contribute to the distribution of the electric field strength and current density, the intersection of which in the plane where the calculations are carried out has the shape, for example, of moist air bubbles in the form of circles with diameter of 1 mm ($\varepsilon = 1$, $\sigma = 0.01$ S/m), copper particles in the form of a square with side of 1 mm and specific electrical conductivity of $1{\cdot}10^7$ S/m.

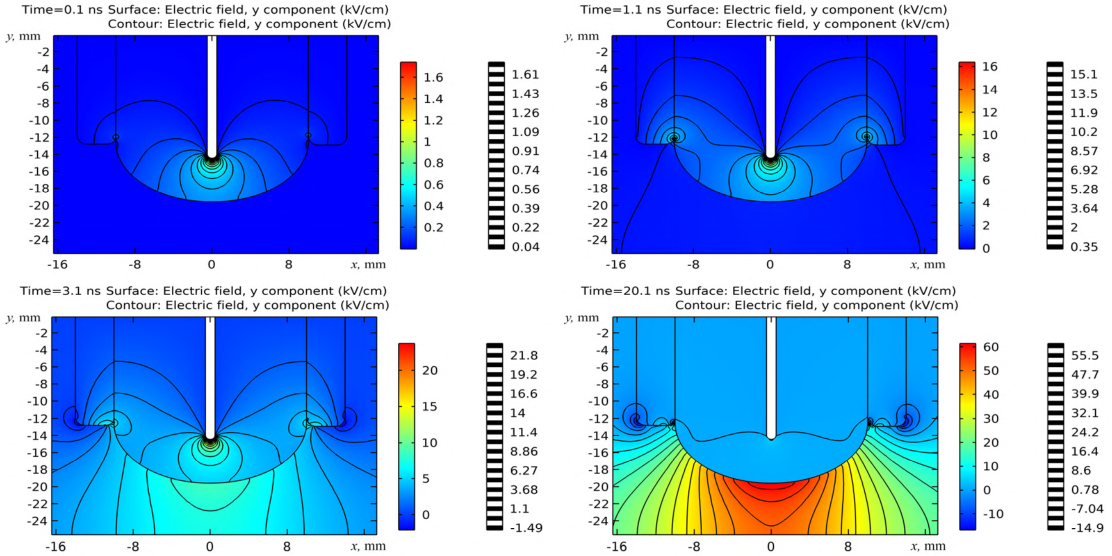

Fig. 5. Distribution of the *y*-component of the electric field strength in the reactor

Figure 6 shows the distribution of the electric field strength with additional impurities in water at the time of 20.1 ns.

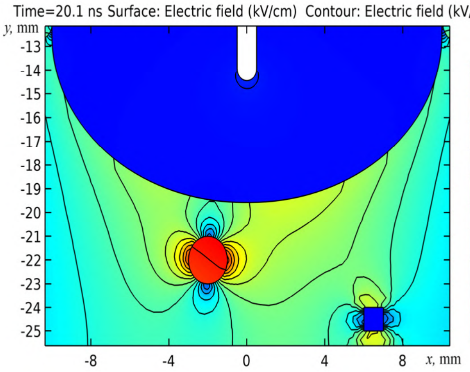

Fig. 6. Distribution of electric field strength in a reactor with impurities in water

Figure 6 demonstrates the distribution of the electric field strength in the Cartesian coordinate system. Here, at 20.1 ns, the electric field strength in the gas bubble of moist air in water reaches 102 kV/cm, in the water layer itself – up to 70 kV/cm. A gas bubble in water is a dielectric. At the interface with water, the electric field strength increases sharply, being distributed inversely proportional to the ratio of relative dielectric permittivities. At the time of 20.1 ns, it can be observed that the value of the electric field in the bubble and in the water at the interface of the media differs by a factor of 10 in some directions.

Modeling of the pre-breakdown distribution of the electric field strength at the specific conductivity of the bubble (in the domain of the high-voltage electrode) of $1 \cdot 10^{-5}$ S/m is shown in Fig. 7.

The process of forming a discharge in a gas bubble can be divided into two stages: *pre-breakdown*, when the gas bubble acts as a dielectric at the initial moments of the process, and *breakdown*, when the gas bubble goes into a conductive state. Due to the increase in the electric field strength, the ionization processes are started and the conductivity increases sharply. The breakdown moment strongly depends on the electric field strength amplitudes, which are affected by the radius of curvature of the rod electrode and the electrical strength of the medium in the discharge gap. During a nanosecond pulse in the gas bubble (Fig. 7), the following electric field strength values were obtained: near the rod – 82 kV/cm, in the bubble itself – up to 40 kV/cm at time of 5.1 ns. The picture of the processes during the breakthrough period itself is similar to the picture of the electric field strength distribution in Fig. 6 according to the specific electrical conductivity of the bubble of $1 \cdot 10^{4}$ S/m, where it is shown that a strong electric field exists precisely in the water layer. A copper particle also distorts the electric field in water (up to 60 kV/cm). Such a distortion can additionally lead to the development of high-intensity factors, microparticles in water.

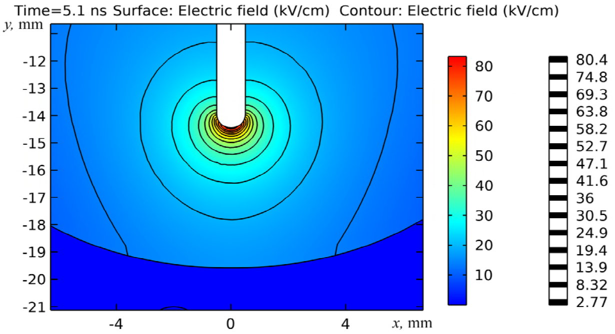

Fig. 7. Distribution of electric field strength in the domain of the high-voltage electrode according to the specific electrical conductivity of the gas bubble of $1 \cdot 10^{-5}$ S/m

When a strong electric field exists in water itself, various physicochemical phenomena occur there, such as ionization, dissociation of water molecules into hydroxyl radicals and hydrogen, as well as the formation of gas microbubbles with characteristic dimensions of $10^{-6} – 10^{-5}$ m as in water, as well as in the domain of its contact with the plasma and metal electrodes [24], where microdischarges such as partial discharges occur in gas inclusions in solid dielectrics. At the interface of two dielectrics with different dielectric permittivities, the electric field generates a mechanical force that is directed perpendicular to the interface and directed toward the dielectric with a lower dielectric permittivity. This force acts regardless of the direction of the electric field strength [25]. We meant that viruses and the membranes of the cells of microorganisms in the treated water are also the dielectrics with a relative dielectric permittivity $\varepsilon = 2 – 4$. During contact of this membrane with water in strong electric field, its sharp increase occurs, which can reach 60 kV/mm. Such an increase in the electric field strength on inhomogeneities in the treated water triggers additional processes of impact ionization by electrons. Collectively, this ultimately leads to a higher degree of disinfection and purification of wastewater.

Figure 8 shows the distribution of conductivity current density.

Up to 20 ns, the conductivity current density near the rod reaches 320 A/cm^2, in the water itself 50-70 A/cm^2, the presence of additional inclusions leads to a 10 time increase in the current density values at the interface between the water medium and these inclusions.

Figure 9 shows the simulation of displacement currents in water.

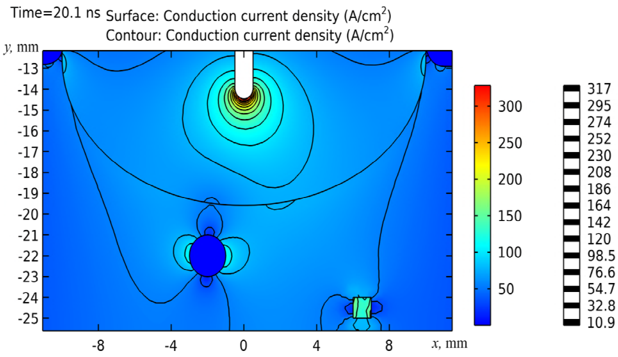

Fig. 8. Distribution of conductivity current density in a sewage treatment reactor

The displacement current density is estimated as a value directly proportional to the rate of change of electrical induction. In Fig. 9, the maximum density of displacement currents in water reaches 62 A/cm^2 at time of 4.1 ns. Further, it follows from the calculations that up to approximately 19 ns after the start of the discharge process, the conductivity currents in water become larger compared to the displacement currents.

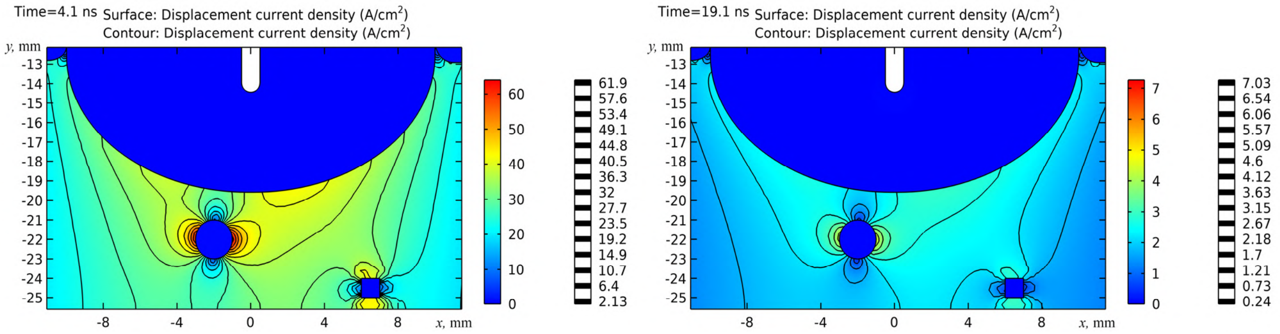

Fig. 9. Modeling of displacement currents in water in a reactor for wastewater treatment

Conclusions.

1. Calculations show that with the growth of conductivity and high potential in the gas bubble to amplitude values, a strong electric field (with strength of up to 70 kV/cm) is created in the water layer. At the same time, additional inclusions contribute to the distortion of the electric field. The values of the electric field strengths in the bubble, conductive inclusion, and water can differ by a factor of 10.
2. At the beginning of the discharge process in the reactor, when there is no gas discharge plasma in the gas bubble near the high-voltage electrode, and the bubble is a dielectric, the moment of breakdown start depends strongly on the amplitude of the electric field strength, which is affected by the radius of curvature of the rod electrode, and the electrical strength of the discharge gap. The higher the rate of voltage rise and the smaller the radius of curvature, the higher the breakdown strength in the nanosecond time range can be obtained (up to 82 kV/cm).
3. In the nanosecond time range, the conductivity current density near the rod exceeds the density in the water itself by 5 or more times, reaching values of 300 A/cm^2 or more. At the same time, additional inclusions also introduce a distortion of the current densities at the interface of the media with a 10-time increase. It follows from the calculations that already approximately by 19th ns after the start of the discharge process, the density of conductivity currents in water exceeds the density of displacement currents.
4. High-voltage nanosecond discharges, which are created in gas bubbles inside the volume of water or in a gas environment near the water surface, have good prospects for wide industrial use in disinfection, wastewater treatment, decarbonization of the economy and are of great interest for further experimental and theoretical research.

Conflict of interest. The authors declare no conflict of interest.

REFERENCES

1. Doorn M.R.J., Towprayoon S., Vieira S.M.M., Irving W., Palmer C., Pipatti R., Wang C. Wastewater treatment and discharge. *2006 IPCC Guidelines for National Greenhouse Gas Inventories*, 2006, 28 p.

2. He Y., Li Y., Li X., Liu Y., Wang Y., Guo H., Hou J., Zhu T., Liu Y. Net-zero greenhouse gas emission from wastewater treatment: Mechanisms, opportunities and perspectives. *Renewable and Sustainable Energy Reviews*, 2023, vol. 184, art. no. 113547. doi: https://doi.org/10.1016/j.rser.2023.113547.

3. Ranieri E., D'Onghia G., Lopopolo L., Gikas P., Ranieri F., Gika E., Spagnolo V., Ranieri A.C. Evaluation of greenhouse gas emissions from aerobic and anaerobic wastewater treatment plants in Southeast of Italy. *Journal of Environmental Management*, 2023, vol. 337, art. no. 117767. doi: https://doi.org/10.1016/j.jenvman.2023.117767.

4. Bojanowska-Czajka A. Application of Radiation Technology in Removing Endocrine Micropollutants from Waters and Wastewaters – A Review. *Applied Sciences*, 2021, vol. 11, no. 24, art. no. 12032. doi: https://doi.org/10.3390/app112412032.

5. Yusuf A., Amusa H.K., Eniola J.O., Giwa A., Pikuda O., Dindi A., Bilad M.R. Hazardous and emerging contaminants removal from water by plasma-based treatment: A review of recent advances. *Chemical Engineering Journal Advances*, 2023, vol. 14, art. no. 100443. doi: https://doi.org/10.1016/j.ceja.2023.100443.

6. Sato M. Environmental and biotechnological applications of high-voltage pulsed discharges in water. *Plasma Sources Science and Technology*, 2008, vol. 17, no. 2, art. no. 024021. doi: https://doi.org/10.1088/0963-0252/17/2/024021.

7. McQuaid H.N., Rutherford D., Mariotti D., Maguire P.D. Generation and delivery of free hydroxyl radicals using a remote plasma. *Plasma Sources Science and Technology*, 2023, vol. 32, no. 1, art. no. 015005. doi: https://doi.org/10.1088/1361-6595/acb07f.

8. Gou X., Yuan D., Wang L., Xie L., Wei L., Zhang G. Enhancing ozone production in dielectric barrier discharge utilizing water as electrode. *Vacuum*, 2023, vol. 212, art. no. 112047. doi: https://doi.org/10.1016/j.vacuum.2023.112047.

9. Joubert V., Cheype C., Bonnet J., Packan D., Garnier J.-P., Teissié J., Blanckaert V. Inactivation of Bacillus subtilis var. niger of both spore and vegetative forms by means of corona discharges applied in water. *Water Research*, 2013, vol. 47, no. 3, pp. 1381-1389. doi: https://doi.org/10.1016/j.watres.2012.12.011.

10. Lukes P., Clupek M., Babicky V., Sunka P. Ultraviolet radiation from the pulsed corona discharge in water. *Plasma Sources Science and Technology*, 2008, vol. 17, no. 2, art. no. 024012. doi: https://doi.org/10.1088/0963-0252/17/2/024012.

11. Zeng M.J., Qu Z.G., Zhang J.F. Negative corona discharge and flow characteristics of a two-stage needle-to-ring configuration ionic wind pump for temperature and relative humidity. *International Journal of Heat and Mass Transfer*, 2023, vol. 201, art. no. 123561. doi: https://doi.org/10.1016/j.ijheatmasstransfer.2022.123561.

12. Boshko I., Kondratenko I., Zabulonov Y.L., Charnyi D.V., Onanko Y., Marynin A., Krasnoholovets V. The study of treatment of water with a high concentration of cod by pulse dielectric barrier discharge on the surface of the liquid. *Geochemistry of Technogenesis*, 2020, vol. 32, no. 4, pp. 65-70. doi: https://doi.org/10.15407/geotech2020.32.065.

13. Khan Z.U.H., Gul N.S., Sabahat S., Sun J., Tahir K., Shah N.S., Muhammad N., Rahim A., Imran M., Iqbal J., Khan T.M., Khasim S., Farooq U., Wu J. Removal of organic pollutants through hydroxyl radical-based advanced oxidation processes. *Ecotoxicology and Environmental Safety*, 2023, vol. 267, art. no. 115564. doi: https://doi.org/10.1016/j.ecoenv.2023.115564.

14. Gershman S., Mozgina O., Belkind A., Becker K., Kunhardt E. Pulsed Electrical Discharge in Bubbled Water. *Contributions to Plasma Physics*, 2007, vol. 47, no. 1–2, pp. 19-25. doi: https://doi.org/10.1002/ctpp.200710004.

15. Yasuoka K., Sato K. Development of Repetitive Pulsed Plasmas in Gas Bubbles for Water Treatment. *International Journal of Plasma Environmental Science and Technology*, 2009, vol. 3, no. 1, pp. 22-27. doi: https://doi.org/10.34343/ijpest.2009.03.01.022.

16. Raizer Yu.P. *Gas Discharge Physics*. Berlin, Springer, 1991. 449 p.

17. Zare F., Ghasemi N., Bansal N., Hosano H. Advances in pulsed electric stimuli as a physical method for treating liquid foods. *Physics of Life Reviews*, 2023, vol. 44, pp. 207-266. doi: https://doi.org/10.1016/j.plrev.2023.01.007.

18. Mohamed M.E.A., Eissa A.H.A. Pulsed Electric Fields for Food Processing Technology. *Structure and Function of Food Engineering*, 2012, pp. 275-306. doi: https://doi.org/10.5772/48678.

19. Bahrami A., Moaddabdoost Baboli Z., Schimmel K., Jafari S.M., Williams L. Efficiency of novel processing technologies for the control of Listeria monocytogenes in food products. *Trends in Food Science & Technology*, 2020, vol. 96, pp. 61-78. doi: https://doi.org/10.1016/j.tifs.2019.12.009.

20. Martinez J.M., Delso C., Alvarez I., Raso J. Pulsed electric field-assisted extraction of valuable compounds from microorganisms. *Comprehensive Reviews in Food Science and Food Safety*, 2020, vol. 19, no. 2, pp. 530-552. doi: https://doi.org/10.1111/1541-4337.12512.

21. Boyko N.I., Makogon A.V. Generator of high-voltage nanosecond pulses with repetition rate more than 2000 pulses per second for water purification by the discharges in gas bubbles. *Technical Electrodynamics*, 2018, no. 4, pp. 37-40. doi: https://doi.org/10.15407/techned2018.04.037.

22. Boyko N.I., Makogon A.V. High voltage plant with 3 MW pulse power for disinfection flow of water by nanosecond discharges in gas bubbles. *Technical Electrodynamics*, 2020, no. 5, pp. 80-83. doi: https://doi.org/10.15407/techned2020.05.080.

23. Boyko N.I., Makogon A.V. The micro- and nanosecond discharges in gas bubbles for water disinfection and purification. *Electrical Engineering & Electromechanics*, 2019, no. 3, pp. 50-54. doi: https://doi.org/10.20998/2074-272X.2019.3.08.

24. Korobeinikov S.M. *Preliminary processes in rare dielectrics under the influence of pulsed voltage have been proven*. Candidate of Technical Sciences Thesis. Novosibirsk, 1983. 24 p. (Rus).

25. Poplavko Yu.M. *Physics of Dielectrics*. Kyiv, NTUU «KPI» Publ., 2015. 572 p. (Ukr).

Received 19.02.2024
Accepted 13.05.2024
Published 20.08.2024

M.I. Boiko[1]*, Doctor of Technical Sciences, Professor,*
A.V. Makogon[2]*, PhD, Senior Researcher,*
[1] National Technical University «Kharkiv Polytechnic Institute»,
2, Kyrpychova Str., Kharkiv, 61002, Ukraine,
e-mail: qnaboyg@gmail.com
[2] Institute of Electrophysics & Radiation Technologies
National Academy of Sciences of Ukraine,
28, Chernyshevsky Str., Kharkiv, 61002, Ukraine,
e-mail: artemmak1991@gmail.com (Corresponding Author)

How to cite this article:
Boiko M.I., Makogon A.V. Features of distribution of electric field strength and current density in the reactor during treatment of liquid media with high-voltage pulse discharges. *Electrical Engineering & Electromechanics*, 2024, no. 5, pp. 58-63. doi: https://doi.org/10.20998/2074-272X.2024.5.08

UDC 621.3.013 https://doi.org/10.20998/2074-272X.2024.5.09

J. Bendik, M. Cenky, J. Paulech, V. Goga

Analytical solution of conductor tensile force in asymmetrical spans used in overhead power lines and substations with influence of tension insulators

Introduction. *Designing electrical substations involves analyzing the horizontal tensile force in flexible tension conductors under varying temperatures. These temperature changes affect the conductor's length and forces.* ***Problem.*** *Existing methods for calculating horizontal tensile force in conductors often focus on symmetric spans or require complex finite element modeling (FEM), which is impractical for routine substation design. Asymmetric spans with tension insulators present a more complex challenge that current solutions do not adequately address.* ***Purpose.*** *Universal analytical solution and algorithm for calculating the horizontal tensile forces in conductors in asymmetric spans with tension insulators used in power substations or short overhead power line spans. The solution is designed to be easily implementable in software without requiring complex tools or extensive FEM.* ***Methodology.*** *The methodology involves deriving an analytical solution based on the catenary curve formed by the conductor between attachment points at different heights. The analysis includes calculating the conductor's length for a given tensile force and using a state change equation to determine forces under new temperature conditions. Validation is performed using FEM calculations.* ***Results.*** *The proposed solution was validated against FEM models with varying height differences (5 m and 15 m) and conductor temperatures (–30 °C, –5 °C, +80 °C). The results showed a minimal error (less than 0.15 %) between the analytical solution and FEM results, demonstrating high accuracy.* ***Originality.*** *This paper presents a novel analytical solution to the problem of calculating tensile forces in asymmetric spans with tension insulators. Unlike existing methods, our solution is straightforward and easily implementable in any programming language.* ***Practical value.*** *The solution is practical for routine design tasks in electrical substations or short overhead power lines. Especially in power substations, accurate tensile forces are needed not only for mechanical design and sag calculations but also for calculating the dynamic effects of short-circuit currents.* References 23, tables 4, figures 3.

Key words: **substation, asymmetrical span, tension section, state change.**

Вступ. *Проєктування електричних підстанцій включає аналіз горизонтальної сили, що розтягує, в гнучких натяжних провідниках при різних температурах. Ці зміни температури впливають на довжину провідника та сили.* ***Проблема.*** *Існуючі методи розрахунку горизонтальної сили, що розтягує, у провідниках часто орієнтовані на симетричні прольоти або вимагають складного моделювання методом скінченних елементів (FEM), що непрактично для звичайного проєктування підстанцій. Асиметричні прольоти з натяжними ізоляторами є складнішим завданням, яке існуючі рішення не вирішують належним чином.* ***Мета.*** *Універсальне аналітичне рішення та алгоритм розрахунку горизонтальних сил, що розтягують, у проводах несиметричних прольотів з натяжними ізоляторами, що застосовуються на силових підстанціях або коротких прольотах повітряних ліній електропередачі. Рішення розроблено таким чином, щоб його можна було легко реалізувати в програмному забезпеченні, не вимагаючи складних інструментів або моделювання методом FEM.* ***Методика*** *передбачає отримання аналітичного рішення на основі контактної кривої, утвореної провідником між точками кріплення на різній висоті. Аналіз включає розрахунок довжини провідника для заданої розтягуючої сили і використання рівняння зміни стану для визначення сил в нових температурних умовах. Перевірка здійснюється з використанням розрахунків методом FEM.* ***Результати.*** *Запропоноване рішення було перевірено на моделях FEM з різною різницею висот (5 м та 15 м) та температурою провідника (–30 °C, –5 °C, +80 °C). Результати показали мінімальну помилку (менше 0,15 %) між аналітичним рішенням та результатами FEM, демонструючи високу точність.* ***Оригінальність.*** *У цій статті представлено нове аналітичне рішення задачі розрахунку зусиль, що розтягують, у несиметричних прольотах з натяжними ізоляторами. На відміну від існуючих методів, наше рішення є простим та легко реалізованим будь-якою мовою програмування.* ***Практична цінність.*** *Вирішення практично для рутинних завдань проєктування електричних підстанцій або коротких повітряних ліній електропередачі. Точні сили, що розтягують, необхідні, особливо на силових підстанціях, не тільки для механічного проєктування та розрахунку провисання, але і для розрахунку динамічних ефектів струмів короткого замикання.* Бібл. 23, табл. 4, рис. 3.

Ключові слова: **підстанція, несиметричний проліт, натяжна ділянка, зміна стану.**

Introduction. One of the basic calculations in the design of overhead power lines (OPL) and electrical substations is the analysis of the horizontal tensile force acting on the tensioned current-carrying conductor in various temperature states [1, 2]. These temperature states result from the natural cooling and heating of the conductor due to ambient temperature, induced wind, irradiation, currents in the conductors, etc. [3]. As a result of a change in conductor temperature, the length of the conductor and the forces acting on the conductor also change. These forces need to be analyzed in the design phase to ensure long-term safe operation and prevent unwanted damage or breakage of the conductors [4]. For this purpose, a tensioned conductor's state change equation is used. The state change equation makes it possible to determine the forces acting in the conductor in any second state given the known value of force and temperature in the defined first state [5].

This article deals with a general problem of horizontal tensile force calculation in a stranded conductor connected at two points with rigid insulators at both span ends, typically used for busbars in power substations. For spans where the weight of the conductor is much higher than the insulators' weight, the tension insulator's influence and the number of conductors in the bundle can be neglected for calculating the horizontal tensile force F_h acting on the conductor. These are typical tension sections of OPL and long spans [6, 7].

Long spans are typically characterized by the condition where the mass of the insulators is considerably less than that of the conductor, resulting in the formation of an almost ideal catenary shape when the span is observed. Solution for long span mechanics is well described in [8] or in [5] by state change equation for long spans and is widely used in power line design practice today [8]. Conversely, assessing the catenary curve for short spans is a more intricate task due to the substantial influence of insulator weights at the span ends [9]. Short spans are typical, for example:

- short tension sections of OPL (approx. less than 150 m);
- dead end of OPL and their connection to an electrical substation;
- tensioned sections in electrical substations, busbars, spans with termination on transformers (Fig. 1).

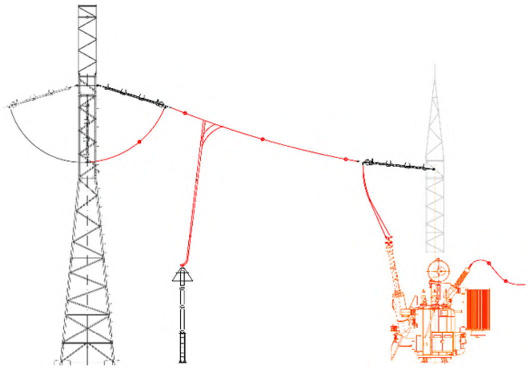

Fig. 1. Example of a short asymmetric span in an electric substation

The mentioned examples of short spans are, in most cases, asymmetrical, which mean that the heights of the suspension points of the insulators are different. Results of mechanical calculations of asymmetric short spans are practically necessary for the following:

- design of tensioned spans [10, 11];
- control of deflections and permitted distances between conductive parts in electrical substation [12];
- calculation of dynamic effects of short-circuit currents in electrical substations [13–15];
- dynamic line rating implementation of OPL or electrical substations [16, 17];
- determination of the intensity of electric field [18];
- determination of magnetic flux density [19, 20].

A symmetric solution to the problem without considering bundle conductors was processed in [8]. An extended solution of the symmetrical span under the influence of bundle conductors is presented in [9].

Solution for asymmetric span win tension insulators using the Finite Element Method (FEM) is presented in [21]. The authors proposed an iterative process based on the mutual calling of MATLAB and ANSYS software. Although it is a valid solution to the problem, it can only be rarely applied in substation design practice due to the need for complicated FEM modelling and complex software.

In another paper by the same group of authors from 2022, they presented a more general solution of the state change equation with the influence on non-uniform load. Authors presented the application of their solution on ultra-high voltage OPL sag calculations [22].

In [23] was presented software for sag-tension substation calculation. Their solution was again purely symmetric. These few studies represent the only relevant sources of information on the topic. We therefore consider it necessary to provide a straightforward solution to the mentioned problem.

The goal of the paper is to presents a clear, comprehensible and universal analytical solution to the mechanics of unsymmetrical spans with consideration of tension insulators. The presented solution is easy software implementable in any programming language and does not require complex tools and programs. The solution was validated using FEM, and the results show a high agreement of the analytical results with the numerical model.

Methodology. Consider a stranded aluminum conductor steel reinforced (ACSR) conductor connected between attachment points (AP I and AP II) and sagged with a horizontal tensile force F_h, and ignoring the insulators. The conductor shapes itself in a catenary curve. If points AP I and AP II are at the same heights, the span is considered a symmetric span. Most spans are asymmetric and have insulators on both ends, which cannot be omitted in the calculation in case of short spans, approximately under 150 m. Figure 2 shows a general short asymmetrical span with tension insulators. The investigated system consists of two attachment points for insulators (API I and API II) and two attachment points of conductors (APC I and APC II, Fig. 2), on the opposite sides of the span. We assume identical rigid insulators on both ends.

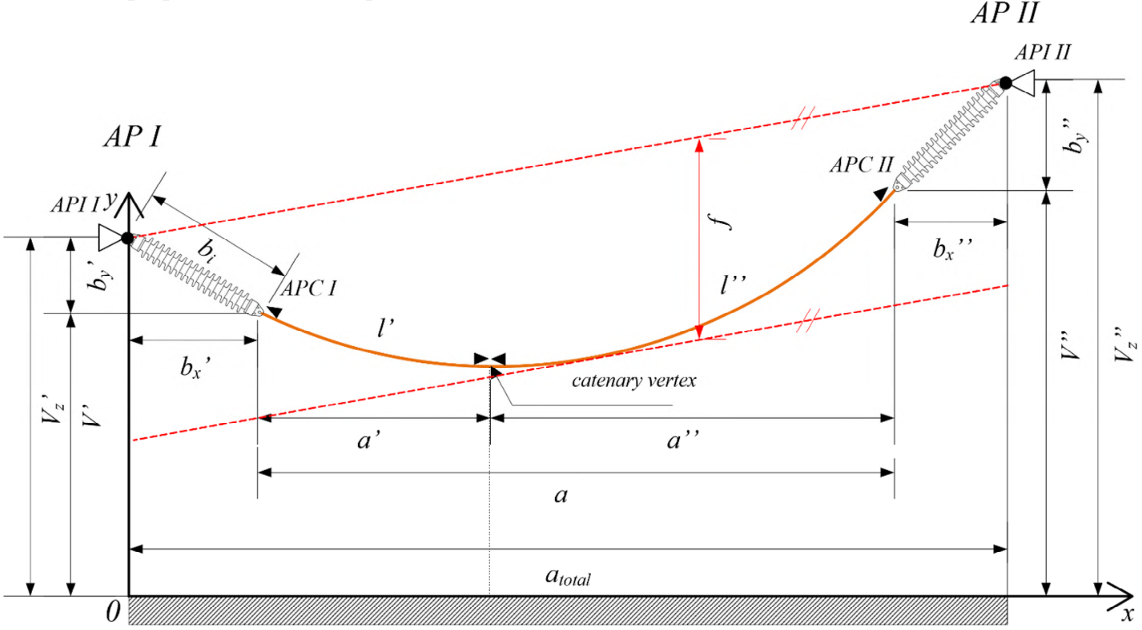

Fig. 2. General short asymmetrical span with tensile insulators

Typical conductor used for tensioned busbar in substations is ACSR conductor. The conductor is freely attached to the insulator on both sides, forming a natural cattery curve with a defined parameter c. Distance from the APC I to the vertex of the catenary is a'. Similarly, a'' equals the distance from the vertex to the APC II.

Total span length a_{total} is a known parameter and equals length from the API I to the API II. Table 1 shows the list of known parameters.

Table 1

Known parameters of the span

Symbol	Description
V_z'	Height of insulator placement at APC I
V_z''	Height of insulator placement at APC II
b_i	Insulator length
W_i	Insulator weight
n_b	Number of conductors in a bundle
a_{total}	Span length with insulators
α	Thermal coefficient of conductor expansion
E	Young modulus of elasticity of the conductor
S	Cross-section of the conductor
w_c	Conductor unit weight
F_h	Horizontal tensile force in a single conductor

We assume that horizontal tensile force F_h acting in a conductor is a known defined parameter. From this, a catenary parameter c is given as:

$$c = \frac{F_h}{w_c n_b g}, \tag{1}$$

where g is the gravitational acceleration.

The analytical solution, state equations calculation, of the presented system, consists of two steps:

- calculation of the length of the conductor for a given F_h;
- calculation of state change equation for a set of state quantities.

Length of the conductor. In general, without considering a specific attachment point, it applies that in a steady state, the sum of the torques of the given system, the insulator and the conductor equals zero (Fig. 3).

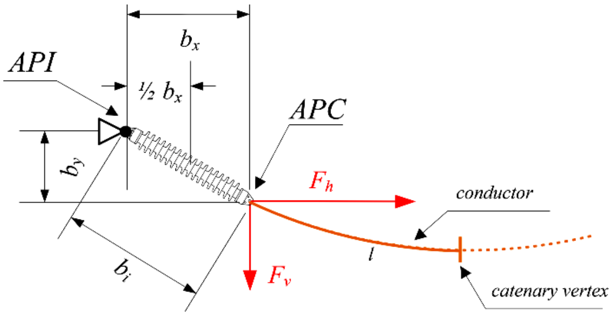

Fig. 3. Forces acting on the conductor on a one side of the span

In such a case, the insulator of length b_i and weight W_i settles in a position with horizontal deflection b_x and vertical deflection b_y. We can write the torque condition as follows:

$$F_v b_x - F_h n_b b_y = 0, \tag{2}$$

where F_v is the vertical force and F_h is the horizontal force acting on the conductor; n_b is the number of conductors in the bundle; F_v is the function of the length of the conductor l and insulator properties.

F_v equals the sum of the weight of the conductor acting on the length from the APC to the vertex of the catenary and the weight of the insulator acting on half the length of the insulator projection b_x. The weight of the conductor is considered as the weight of the conductor per unit of length F_v as a function of l equals:

$$F_v(l) = \frac{1}{2} W_i g + w_c z n_b l g. \tag{3}$$

Torque condition now equals:

$$\left(\frac{1}{2} W_i + w_c l\, n_b\right) b_x g - F_h b_y = 0. \tag{4}$$

The length of the insulator b_i equals by Pythagorean theorem:

$$b_i^2 = b_x^2 + b_y^2. \tag{5}$$

The equations (4), (5) represent two equations with two unknown parameters. Their positive solutions for insulator deflections, b_x b_y, as a function of F_v are given following equations:

$$b_x(F_v) = \frac{b_i F_h n_b}{\sqrt{(F_h n_b)^2 + F_v^2}}; \tag{6}$$

$$b_y(F_v) = \frac{b_i F_v}{\sqrt{(F_h n_b)^2 + F_v^2}}; \tag{7}$$

For clarification, all quantities related to AP I have a superscript «'» and all quantities related to AP II have a superscript «''». For the sake of simplicity, the relations for AP I will be presented in the following section. The vertical component of the conductor force F_v' at APC I is a sum weight force of the insulator and conductor at length l' (Fig. 2):

$$F_v'(l') = g\left(\frac{1}{2} W_i + w_c n_b l'\right). \tag{8}$$

Similarly, F_v'' at APC II. Solving the length of the conductor is an iterative calculation when in the first step, a random estimate is made for the deflection of the insulators b_x', b_x'' and b_y' and b_y'' (e.g. $b_x' = b_x'' = b_i$ and $b_y' = b_y'' = 0$). The length of the conductor span is given as:

$$a(b_x', b_x'') = a_{total} - (b_x' + b_x''). \tag{9}$$

The heights of the suspension points of conductors V' in APC I and V'' in APC II are equal to the difference in the height of the AP I insulator and the vertical deflection of the insulator:

$$V'(b_y') = V_z' - b_y'. \tag{10}$$

Similarly, V'' at APC II. The horizontal distance from the APC I to the vertex of the catenary a' equals:

$$a'(V', V'', a) = a - c \cdot \left[\operatorname{arcsinh}\left(\frac{V'' - V'}{2c \cdot \sinh\left(\frac{a}{2c}\right)}\right) + \frac{a}{2c}\right]. \tag{11}$$

Horizontal distance from the APC II to the vertex of the catenary a'' equals:

$$a''(a') = a - a'. \tag{12}$$

Length of the catenary l_t' from the APC I to the vertex of the catenary equals:

$$l_t'(a') = c\sqrt{\sinh^2\left(\frac{-a'}{c}\right) + 1} \cdot \operatorname{tgh}\left(\frac{a'}{c}\right). \tag{13}$$

Similarly, l_t'' at APC II. As a result of the force F_h, the length of the conductor will contract. The total conductor lengths l' will be equal after this shortening:

$$l'(l'_t) = l'_t - \frac{F_h l'_t}{E \cdot S}, \tag{14}$$

where E is the Young modulus of elasticity; S is the cross-section of the conductor.

Similarly, l'' at APC II. Now, it is possible to determine the vertical force acting in both attachment points $F'_v(l')$ $F''_v(l'')$ from (8). From the vertical forces, the new insulator deflections, b_x' b_x'' equation (6) and b_y' and b_y'', equation (7) are determined.

The calculation is repeated until the difference between newly calculated deflection equals or exceeds user-defined precision ε. The length of the conductor is then calculated as follows:

$$\begin{gathered} l(a', a) = -c\sqrt{\sinh^2\left(\frac{a-a'}{c}\right)+1} \cdot \operatorname{tgh}\left(\frac{a'-a}{c}\right) + \\ + c\sqrt{\sinh^2\left(\frac{a'}{c}\right)+1} \cdot \operatorname{tgh}\left(\frac{a'}{c}\right) \end{gathered}. \tag{15}$$

General form of state-change equation. Subscript 0 defines the primary state, and subscript 1 defines a new state of the conductor. The calculation assumes that the span parameters are known (Table 1) together with the force F_{h0} at the conductor temperature ϑ_0. The calculation aims to determine the horizontal tensile force in the new state of the conductor, which is characterized by a change in state variable ϑ_1.

Change in conductor temperature from ϑ_0 to ϑ_1 causes change in the length of the conductor Δl_ϑ:

$$\Delta l_\vartheta = l_0 \alpha (\vartheta_1 - \vartheta_0), \tag{16}$$

where l_0 is the length of the conductor at state 0 and α is thermal coefficient of expansion. Change of conductor length due to temperature, Δl_ϑ, results in a change in conductor sag and, therefore, a change in horizontal tensile force in the conductor. This change of force causes the opposite change in the conductor length Δl_F:

$$\Delta l_F = \frac{l_0}{E \cdot S}(F_{h0} - F_{h1}). \tag{17}$$

The total change in conductor length is equal to:

$$\Delta l = l_1 - l_0; \tag{18}$$

$$\Delta l = \Delta l_\vartheta - \Delta l_F. \tag{19}$$

By combining (18), (19) with (16), (17) we get general state change equation of the conductor:

$$l_0\left(\alpha(\vartheta_1 - \vartheta_0) + \frac{1}{E \cdot S}(F_{h1} - F_{h0})\right) + l_0 - l_1 = 0. \tag{20}$$

Calculation. The following iterative algorithm is used to calculate the conductor length. Known parameters are listed in Table 1 together with the force F_{h0} at conductor temperature ϑ_0. The iterative algorithm consists of the following steps:

1) calculate the length of the conductor l_0 in state 0;

2) make the initial guess of $F_{h1}^{(k)} = F_{h0}$, where k iteration step equals $k = 0$;

3) calculate the length of the conductor $l_1^{(k)}$ in state 1;

4) calculate the steady state equation error $U_\varepsilon^{(k)}$:

$$U_\varepsilon^{(k)} = l_0\left(\alpha(\vartheta_1 - \vartheta_0) + \frac{1}{E \cdot S}\left(F_{h1}^{(k)} - F_{h0}\right)\right) + l_0 - l_1^{(k)}; \tag{21}$$

5) compare error results:

$$\left|U_\varepsilon^{(k)}\right| \le \varepsilon. \tag{22}$$

- If (22) is True then $F_{h1}^{(k)}$ is the resulting force in state 1 and calculation is over.
- If (22) is False then continue to 6).

6) define new $F_{h1}^{(k+1)}$ according following rules:

- If $k = 0$ then $\Delta F_{h1} = 0.9 \cdot F_{h1}^{(0)}$;
- If $k \neq 1$ then $\Delta F_{h1} = 0.5 \cdot F_{h1}^{(k)}$;
- If $U_\varepsilon^{(k)} > 0$ then $F_{h1}^{(k+1)} = F_{h1}^{(k)} - \Delta F_{h1}$;
- If $U_\varepsilon^{(k)} < 0$ then $F_{h1}^{(k+1)} = F_{h1}^{(k)} + \Delta F_{h1}$.

7) increment k and repeat from step 3).

Validation and results. Presented analytical solution for the general state change equation of conductor with tensile insulators on both ends was validated by calculating identical problem using FEM. FEM model was prepared as a transient structural analysis representing the process of assembling and tensioning the conductors (or bundled conductors) for a defined span in the gravitational field, respecting all given material properties and boundary conditions of the model. The model consists of a fine mesh of link elements that can form ideal sag from the mathematical and physical point of view. In addition, the model involves the link elements for insulators and auxiliary damping elements that ensure a converged model state in time. Result comparison was made for the following models:

- two height differences, ΔV: 5 m and 15 m;
- three temperatures in state 1: –30 °C; –5 °C; +80 °C;
- single conductor and three conductor bundle arrangement.

ACSR conductor 758-AL1/43-ST1A was considered in the calculation. This is a typical, most common ACSR conductor used in a substation in Slovak and Czech Republic region. In all models and calculations, the span length a_{total} was 30 m and force in primary state F_{h0} was 4500 N. Temperature at state 0 was –5 °C. A summary of the model and conductor parameters are in Table 2.

Table 2

Conductor and span specification

Quantity	Value	Unit
b_i	6.64	m
w_c	2.432	kg/m
W_i	425	kg
F_{h0}	4.5	kN
S	801.2	mm^2
a_{total}	30	m
ΔV	5; 15	m
n_b	1; 3	–
α	$2.11 \cdot 10^{-5}$	1/°C
E	62300	MPa
ϑ_0	–5	°C
ϑ_1	–30; –5; +80	°C

Tables 3, 4 show the results of calculated horizontal tensile force in state 1 for different ΔV, temperatures and number of conductors in the bundle. For all calculations, the error of the analytical solution to the FEM was determined as:

$$error = \left|\frac{F_{h1_{FEM}} - F_{h1_{an}}}{F_{h1_{FEM}}} \cdot 100\right|. \tag{23}$$

Table 3

Comparison of horizontal tensile forces in the conductor, ΔV = 15 m, determined using FEM and analytical solution of the state equation

n_b	ϑ_1, °C	F_{h1FEM}, N	F_{h1an}, N	*error*, %
1	–30	4524.89	4525.31	0.009
	–5	4499.23	4500.00	0.017
	80	4414.87	4416.79	0.043
3	–30	4632.08	4638.67	0.142
	–5	4497.11	4500.00	0.064
	80	4111.94	4106.47	0.133

Table 4

Comparison of horizontal tensile forces in the conductor, ΔV = 5 m, determined using FEM and analytical solution of the state equation

n_b	ϑ_1, °C	F_{h1FEM}, N	F_{h1an}, N	*error*, %
1	–30	4518.26	4518.13	0.003
	–5	4499.92	4500.00	0.002
	80	4438.90	4439.67	0.017
3	–30	4585.83	4586.12	0.006
	–5	4499.71	4500.00	0.006
	80	4238.50	4239.01	0.012

Discussion. FEM itself also contains a certain amount of error, because the conductor or bundle of conductors is not considered a continuous continuum, but a finite link of elements representing the conductor. This error can be seen in $F_{h1\mathrm{FEM}}$ for temperature in state 1–5 °C. The expected value is 4500 N because no actual change of conductor state happened. However, the resulting values of F_h in state 1 are approximately 0.002–0.06 %. We consider this error to be insignificant, but it is necessary to keep it in mind when comparing it with the analytical solution.

As can be seen from the results, the analytical solution achieves a minimal insignificant error compared to the solution of the problem using FEM. The error of the analytical solution is at the level of the internal error of the FEM calculation itself. Results also show that error rises with a higher difference of attachment points. Again, the value of this error is in the order of 0.1 %, which is considered highly tolerable.

The primary benefit of the analytical solution in practical applications is its speed. This solution can be readily integrated into the software tools that designers currently use. Conversely, addressing the issue of asymmetrical spans with tension insulators through the FEM method is time-consuming and inefficient for project planning in real-world scenarios.

Conclusions.

1. We have presented a comprehensive analytical solution to the mechanics of asymmetrical spans with the influence of rigid tension insulators on both ends witch are typically. These are the typical tensioned spans used in electrical substations, short overhead power line sections or dead end of overhead power line and its connection to an electrical substation. Our analytical approach is valuable for a range of applications, including the project phase of tensioned spans, the control of deflections and permitted distances between conductive parts in electrical stations, the calculation of dynamic effects of short-circuit currents in electrical substations, and the implementation of dynamic line ratings in electrical substations.
2. The presented solution is easily implementable in any programming language and does not require complex tools or software.
3. We validated this solution by comparing it with finite element method calculations, and the results showed a high agreement between the analytical results and the numerical model.
4. Overall, this work contributes to a better understanding of the mechanics of overhead power lines and tensioned busbars in electrical substations, especially in cases involving non-uniform load distribution and the influence of tension insulators.
5. It offers a valuable tool for engineers and designers in power transmission and distribution, facilitating more accurate and reliable designs for these critical infrastructure components.
6. The motivation for publishing our solution is the lack of a solution to the problem that is understandable and easily implementable in software.
7. The presented work and issues can be expanded in the future by implementing insulator chains connected in series instead of single rigid ones.

In summary, this analytical solution provides engineers and designers with a practical and efficient method for calculating the horizontal tensile force in conductors equipped with tension insulators in overhead power lines and electrical substations.

Conflict of interest. The authors declare no conflict of interest.

REFERENCES

1. Al-Qarni A.S., Ramdas S.K. Voltage Sag Assessment and Mitigation Techniques of a Solar PV Integrated 110 kV/13.8 kV Saudi Substation. *European Journal of Engineering and Technology Research*, 2022, vol. 7, no. 6, pp. 56-63. doi: https://doi.org/10.24018/ejeng.2022.7.6.2902.

2. Santos G.R., Zancul E. A framework to assess the impacts of digital electrical substations. *Smart Energy*, 2023, vol. 12, art. no. 100125. doi: https://doi.org/10.1016/j.segy.2023.100125.

3. Rácz L., Németh B., Göcsei G., Zarchev D., Mladenov V. Performance Analysis of a Dynamic Line Rating System Based on Project Experiences. *Energies*, 2022, vol. 15, no. 3, art. no. 1003. doi: https://doi.org/10.3390/en15031003.

4. Gaspar J., Cruz T., Lam C.-T., Simões P. Smart Substation Communications and Cybersecurity: A Comprehensive Survey. *IEEE Communications Surveys & Tutorials*, 2023, vol. 25, no. 4, pp. 2456-2493. doi: https://doi.org/10.1109/COMST.2023.3305468.

5. *CIGRE-B2.12.3. 324-Sag-Tension Calculation Methods for Overhead Lines*. 2016. 91 p.

6. Pavon W., Inga E., Simani S., Nonato M. A Review on Optimal Control for the Smart Grid Electrical Substation Enhancing Transition Stability. *Energies*, 2021, vol. 14, no. 24, art. no. 8451. doi: https://doi.org/10.3390/en14248451.

7. Krasnozhon A.V., Kvytsynskyi A.O., Buinyi R.O., Dihtyaruk I.V., Krasnozhon O.V. Study of the influence of the parameters of modern grounding wires on the value of power losses in them for overhead power lines of 330-750 kV. *Electrical Engineering & Electromechanics*, 2023, no. 6, pp. 77-83. doi: https://doi.org/10.20998/2074-272X.2023.6.14.

8. Kiessling F., Nefzger P., Nolasco J.F., Kaintzyk U. *Overhead Power Lines: Planning, Design, Construction*. Springer Science & Business Media, 2003. 759 p.

9. Bendik J., Cenky M., Eleschova Z., Belan A., Cintula B., Janiga P. Influence of Tension Insulators and Bundle Conductors on Sag of Conductors in Substations. *2022 22nd International Scientific Conference on Electric Power*

Engineering (EPE), 2022, pp. 1-5. doi: https://doi.org/10.1109/EPE54603.2022.9814112.

10. Wang X., Hong Z., Min Q., Zou D., Zhao X., Xie Q. Seismic performance analysis of double electrical equipment system connected by flexible conductors. *E3S Web of Conferences*, 2024, vol. 522, art. no. 01024. doi: https://doi.org/10.1051/e3sconf/202452201024.

11. Redmond J. Revit 3D Modeling Optimizes Substation Design. *2022 IEEE Rural Electric Power Conference (REPC)*, 2022, pp. 84-87. doi: https://doi.org/10.1109/REPEC55671.2022.00023.

12. Musgrave D., Bellaschi P., Berry L., Brader D., Byron R., Crouch G., Dolan P., Fiero D., Finley G., Hertig G., Maneatis J., Shoun P., Supplee G., Taylor E., Zanzie C. Minimum Line-To-Ground Electrical Clearances for EHV Substations Based on Switching Surge Requirements. *IEEE Transactions on Power Apparatus and Systems*, 1972, vol. PAS-91, no. 5, pp. 1924-1930. doi: https://doi.org/10.1109/TPAS.1972.293520.

13. *International Standard IEC 60865-1:2011 - Short-circuit currents - Calculation of effects - Part 1: Definitions and calculation methods*. Oct. 24, 2011. 102 p.

14. Stenzel D., Librandi M.D., Witzmann R., Schmidt J.M., Milic V. Substation Topology Planning: Impact on Voltage Stability and Short-circuit Current. *2023 IEEE Belgrade PowerTech*, 2023, pp. 01-06. doi: https://doi.org/10.1109/PowerTech55446.2023.10202737.

15. Piechocki P., Frackowiak R., Dombek G., Chmielewska I. Estimation of Short Circuit Duration for the Assessment of Dynamic Effects in Distribution Substations with Flexible Conductors. *Energies*, 2020, vol. 13, no. 4, art. no. 970. doi: https://doi.org/10.3390/en13040970.

16. Verma A., Swarup K.S. Dynamic line rating considering short term reliability and convergence time. *Energy Systems*, 2023. Article in Press. doi: https://doi.org/10.1007/s12667-023-00592-1.

17. Reich K., Weissnar R., Puffer R. Investigation of the dynamic rating of tubular busbars in substations. *Elektrotechnik Und Informationstechnik*, 2020, vol. 137, no. 8, pp. 455-459. doi: https://doi.org/10.1007/s00502-020-00847-0.

18. Koliushko D.G., Rudenko S.S., Tyutyuma S.O., Vorobiov B.V. Determination of the electric field strength of high-voltage substations. *Electrical Engineering & Electromechanics*, 2023, no. 5, pp. 63-68. doi: https://doi.org/10.20998/2074-272X.2023.5.09.

19. Boumous S., Boumous Z., Anane Z., Nouri H. Comparative study of 220 kV overhead transmission lines models subjected to lightning strike simulation by using electromagnetic and alternative transients program. *Electrical Engineering & Electromechanics*, 2022, no. 4, pp. 68-74. doi: https://doi.org/10.20998/2074-272X.2022.4.10.

20. Kuznetsov B.I., Nikitina T.B., Bovdui I.V., Voloshko O.V., Kolomiets V.V., Kobylianskyi B.B. The method of multi-objective parametric design of magnetic field active canceling robust system for residential multy-story buildings closed to double-circuit overhead power lines. *Electrical Engineering & Electromechanics*, 2023, no. 2, pp. 27-36. doi: https://doi.org/10.20998/2074-272X.2023.2.05.

21. Zhang R., Zhao X., Shen G., Yao J. Finite element simulation of wire's sag considering tension insulator string. *Energy Reports*, 2022, vol. 8, pp. 101-108. doi: https://doi.org/10.1016/j.egyr.2021.11.018.

22. Zhang R., Li J., Zhao X., Yao C. Study on the sag of ultra high voltage conductor with large-tonnage tension insulator string. *Energy Reports*, 2022, vol. 8, pp. 394-404. doi: https://doi.org/10.1016/j.egyr.2022.05.091.

23. Quintana J., Garza V., Zamudio C. Sag-tension calculation program for power substations. *2016 IEEE PES Transmission & Distribution Conference and Exposition-Latin America (PES T&D-LA)*, 2016, pp. 1-4. doi: https://doi.org/10.1109/TDC-LA.2016.7805629.

Received 25.02.2024
Accepted 19.04.2024
Published 20.08.2024

J. Bendik [1]*, PhD, Associate Professor,*
M. Cenky [1]*, PhD,*
J. Paulech [2]*, PhD,*
V. Goga [2]*, PhD, Associate Professor,*
[1] Slovak University of Technology in Bratislava,
Faculty of Electrical Engineering,
Institute of Power and Applied Electrical Engineering,
Ilkovicova 3, Bratislava, 84105, Slovakia,
e-mail: jozef.bendik@stuba.sk (Corresponding Author);
matej.cenky@stuba.sk
[2] Slovak University of Technology in Bratislava,
Faculty of Electrical Engineering,
Institute of Automotive Mechatronics,
Ilkovicova 3, Bratislava, 84105, Slovakia,
e-mail: juraj.paulech@stuba.sk; vladimir.goga@stuba.sk

How to cite this article:
Bendik J., Cenky M., Paulech J., Goga V. Analytical solution of conductor tensile force in asymmetrical spans used in overhead power lines and substations with influence of tension insulators. *Electrical Engineering & Electromechanics*, 2024, no. 5, pp. 64-69. doi: https://doi.org/10.20998/2074-272X.2024.5.09

UDC 621.3.013 https://doi.org/10.20998/2074-272X.2024.5.10

A. Nid, S. Sayah, A. Zebar

Power fluctuation suppression for grid connected permanent magnet synchronous generator type wind power generation system

Introduction. *Weather changes lead to create oscillations in values of power extracted from renewable energy resources (RERs). These power oscillations pose significant challenges in RERs integration process with the power grid systems, through its effects on power system stability. Many studies have been performed in various methods to mitigate the output power fluctuation of wind power generation system (WPGS).* ***Purpose.*** *This study focuses on increasing the mitigation rate of the output power fluctuation of WPGS caused by the rapid wind speed changes during wind gusts. Superconducting magnetic energy storage (SMES) system through its properties represents an effective solution for the WPGS power fluctuation issue. WPGS and SMES systems are linked to power grid system through the point of common coupling (PCC).* ***Methods.*** *This paper proposes two robust controllers for controlling the SMES system. The first controller is a Fuzzy Logic Controller (FLC), which has been utilized for controlling the power exchange between the SMES coil and the PCC of the utility grid. While the second controller is a PI controller, which have been utilized to regulate the voltages between the two sides of the PCC and the DC link capacitor in the SMES system. The proposed controllers have been constructed so that can make the SMES system absorb/deliver the real power instantaneously from/toward PCC according the wind speed changes. MATLAB/Simulink has been utilized to simulate the system under study and test the performance of proposed controllers. In addition, two different wind speed scenarios have been used in the simulation.* ***Practical value.*** *Results of simulation have proven the effectiveness of proposed controllers so that the active power fluctuation delivered to utility grid can be reduced by up to 89 %.* References 31, tables 4, figures 9.

Key words: **wind power generation system, power grid system, superconducting magnetic energy storage, fuzzy logic control.**

Вступ. *Зміни погоди призводять до коливань значень потужності, що надходять з відновлюваних джерел енергії (RERs). Ці коливання потужності створюють серйозні проблеми у процесі інтеграції RERs з енергосистемами через їх вплив на стабільність енергосистеми. Було проведено велику кількість досліджень різних методів пом'якшення коливань вихідної потужності системи вітрогенерації (WPGS).* ***Мета.*** *Це дослідження спрямоване на підвищення ступеня пом'якшення коливань вихідної потужності WPGS, викликаних швидкими змінами швидкості вітру під час поривів вітру. Система надпровідного накопичення магнітної енергії (SMES) завдяки своїм властивостям є ефективним вирішенням проблеми коливань потужності WPGS. Системи WPGS та SMES пов'язані з енергосистемою через точку загального підключення (PCC).* ***Методи.*** *У цій статті пропонуються два робастні контролери для управління системою SMES. Перший контролер є контролером нечіткої логіки (FLC), який використовувався для управління обміном енергії між котушкою SMES і PCC енергосистеми. У той час як другий контролер є ПІ-регулятором, який використовувався для регулювання напруг між двома сторонами PCC і конденсатором кола постійного струму в системі SMES. Пропоновані контролери були сконструйовані таким чином, щоб система SMES могла миттєво поглинати/передавати реальну потужність від/до PCC відповідно до змін швидкості вітру. MATLAB/Simulink використовувався для моделювання досліджуваної системи та перевірки продуктивності пропонованих контролерів. Крім того, при моделюванні використовувалися два різні сценарії швидкості вітру.* ***Практична цінність.*** *Результати моделювання довели ефективність пропонованих контролерів, що дозволяють знизити до 89 % коливання активної потужності, що подається до енергосистеми.* Бібл. 31, табл. 4, рис. 9.

Ключові слова: **вітроенергетична система, система електромережі, надпровідний магнітний накопичувач енергії, керування на нечіткій логіці.**

Abbreviations

DFIG	Doubly Fed Induction Generator	PWM	Pulse-Width Modulation
ESS	Energy Storage System	RER	Renewable Energy Resource
FLC	Fuzzy Logic Controller	SMES	Superconducting Magnetic Energy Storage
MF	Membership Function	SC	Superconductor
PMSG	Permanent Magnet Synchronous Generator	VSC	Voltage Source Converter
PV	Photovoltaic	WPGS	Wind Power Generation System
PCC	Point Of Common Coupling		

Introduction. Nowadays, with climate changes and the appearance of global warming, RERs have become increasingly used, unlike solar energy [1, 2]. RERs are environmentally friendly because of their low carbon emissions, whereas conventional generation sources with high carbon emissions have serious environmental impacts. The most prevalent RERs are wind, biomass and PV solar [3, 4]. Due to its high efficiency, WPGS has the fastest growth rate among other forms of power generation. However, the major disadvantage of the WPGS is that the amount of generated power depends entirely on the wind speed, so the output power of the WPGS will fluctuated. Therefore, the stability of the power grid system will be influenced. In addition the output power fluctuations of the WPGS can affect directly the power transfer capability, voltage and frequency stability profiles at the power grid system's connection point, knowing that the voltage and frequency deviation values are of major importance for measuring the level of the power grid stability [5]. In order to ensure a more reliable and economical energy to the customers, ESSs such as flywheels [6], batteries [7, 8], pumped hydro [9, 10], super capacitor [11], etc., are widely used in renewable power generation systems. ESSs are essential elements that have a significant role in solving the mentioned WPGS issues. This can be achieved through the charging and discharging features of the ESS, which ensure a more power balance between RER and loads. Nevertheless, battery and flywheel ESSs have some drawbacks, such as their very slow responses to compensate the power fluctuation as well as short lifetimes and low efficiency [12].

Currently, SMES system is considered one of the most optimal choices for solving the above-mentioned issues by mitigating the output power fluctuation of the WPGS. SMES systems present many advantages such as high efficiency, long lifetime, short time delay during the charging/discharging processes, lower power losses especially at standby operation, very fast response time, and low maintenance requirements [13].

Several studies related to SMES applications in renewable power generation systems have been reported in the literature. Some of these works have focused on installing SMES systems at PCC to improve the performance of WPGS during voltage sag/swell on the power system side [14]. In [15] a SMES device has proposed to power fluctuation suppression and active filtering in PV microgrid. The application of high temperature superconducting devices in a distribution grid for mitigating issues associated with the large-scale penetration of renewable energy has been studied in [16]. In [17] a new effective technique has developed to improve the performance of DFIG-based WECS during wind gust using a high temperature SC. The performance of a battery/SMES hybrid ESS used in a hybrid power system with fuel cells and RERs under an unknown load profile was discussed in [18]. Authors in [19] have proposed the SMES units controlled by self-tuned algorithm in order to smooth out the output power of wind plants. For a more reliable grid connection of superconducting wind turbine generators, authors in [20] have suggested a cooperative strategy integrated with a SMES device and two modified wind turbine generator controls. On the other hand, a new hybrid PV SMES system controlled by a PID fuzzy controller has been studied in [21] in order to minimize the oscillation of the PV extracted power.

The goal of the paper is increasing the mitigation rate of the output power fluctuation of WPGS caused by the rapid wind speed changes during wind gusts.

This paper proposes two robust controllers for SMES systems in order to smooth out the power provided by a WPGS based on PMSG integrated with utility grid. The first controller is a FLC which operates with a DC-DC chopper circuit for controlling the power exchanged between the SMES coil and the PCC of the utility grid. The second controller is a PI controller whose role is to attempt to keep the voltages between both the PCC sides and DC link capacitor sides of the VSC according to the rated values of the SMES system. This is for giving a flexible and rapid exchange of real power as well as to satisfy requirements of coupling the SMES system with the PCC on the utility grid. The wind speed fluctuations are taken into consideration during the implementation of the proposed controllers. The purpose of these controllers is to make the SMES system capable of absorbing energy from WPGS during situations where wind speed is higher than its rated value, while it is delivering the stored energy in SMES coil during situations where wind speed is lower than its rated value. This strategy can help of smoothing out the power fluctuations of WPGS based on PMSG integrated with the utility grid and make the power steady.

Basic topology and dynamic models. In this work, the wind turbine based on PMSG is used as WPGS. The basic topology of the system under study and the SMES system is shown in Fig. 1, which contains of wind turbine, PMSG, rectifier, boost converter, inverter, two-step up transformers, filter, SMES system (SC coil, DC-DC chopper, VSC, filter) and the utility grid.

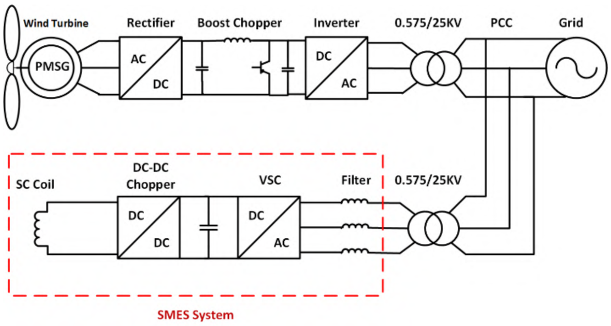

Fig. 1. Basic topology of the system under study and the SMES system

Modeling of wind turbine. The wind turbine is a mechanical machine, which has the ability of transforms the kinetic energy of the wind into mechanical rotational energy that can be exploited by the PMSG. The output power of a wind turbine can be expressed as follows [22]:

$$P_w = \frac{1}{2}\rho\pi R^2 V_w^3 C_p(\lambda,\beta), \qquad (1)$$

where P_w is the mechanical power, which is generated by the wind turbine; ρ is the air density; R is the blade radius; V_w is the wind speed; C_p is the power coefficient, which is a function of both tip speed ratio λ and blade pitch angle β.

The tip speed ratio λ of the rotor can be defined as follow [22]:

$$\lambda = V_r R / V_w\,, \qquad (2)$$

where V_r is the rotor speed.

The power coefficient C_p is given by [22]:

$$C_p(\lambda,\beta) = 0.73\left(\frac{151}{\lambda_i} - 0.58\beta - 0.002\beta^{2.14} - 13.2\right)\cdot e^{\frac{-18.4}{\lambda_i}}\,, \qquad (3)$$

where λ_i is calculated as [22]:

$$\lambda_i = \frac{1}{\dfrac{1}{\lambda + 0.02\beta} - \dfrac{0.003}{\beta^3 + 1}}\,. \qquad (4)$$

Modeling of PMSG. PMSG transforms the mechanical rotational energy to electrical energy that can be exploited for supplying the loads. Table 1 shows the used PMSG parameters in this work. The voltage of stator along the direct and quadrature (d–q) axes are written as follows [23]:

$$v_{ds} = R_s i_{ds} + L_d\frac{\mathrm{d}i_{ds}}{\mathrm{d}t} - \omega_e L_q i_{qs}\,; \qquad (5)$$

$$v_{qs} = R_s i_{qs} + L_q\frac{\mathrm{d}i_{qs}}{\mathrm{d}t} + \omega_e\lambda_m + \omega_e L_d i_{ds}\,; \qquad (6)$$

$$\omega_e = p\omega_r\,. \qquad (7)$$

The mechanical dynamic equations of the PMSG can be written as follows [23]:

$$J\frac{\mathrm{d}\omega_r}{\mathrm{d}t} + D\omega_r = T_m - T_e\,; \qquad (8)$$

where the electromagnetic torque developed can be given by [23]:

$$T_e = \frac{3}{2}p\cdot\left[(L_d - L_q)\cdot i_{ds}i_{qs} - \lambda_m i_{qs}\right]. \qquad (9)$$

The real and reactive power, respectively, are given in *d*–*q* frame by the following equations [24]:

$$P_{pmsg} = \frac{3}{2} \cdot \left[v_{sd} i_{sd} + v_{sq} i_{sq} \right]; \tag{10}$$

$$Q_{pmsg} = \frac{3}{2} \cdot \left[v_{sq} i_{sd} - v_{sd} i_{sq} \right], \tag{11}$$

where λ_m is the magnetic flux of the PMSG; ω_e is the electrical angular speed of PMSG; ω_r is the rotational rotor speed of the turbine's shaft; i_{sd}, i_{sq} are the *d*- and *q*- axis stator currents of PMSG; *J* is the moment of inertia of PMSG; L_s is the synchronous inductance of the PMSG; *p* is the pole pair number of the PMSG; P_{pmsg}, Q_{pmsg} are the real and reactive powers of PMSG; R_s is the stator resistance of PMSG; T_m, T_e are the mechanical and electromagnetic torque of PMSG; v_{ds}, v_{qs} are the *d*- and *q*-axis stator voltages of PMSG.

Table 1

Parameters of the PMSG

Parameter	Value
Nominal power, MW	1.5
Nominal stator voltage, V	575
Nominal frequency, Hz	50
Number of pole pairs	48
Generator inductance in the *d* frame, p.u	0.85
Generator inductance in the *q* frame, p.u	0.85
Generator stator resistance, p.u	0.0012
Flux of the permanent magnets, p.u	0.65

SMES system and proposed controllers.

SMES system. As depicted in Fig. 2, the proposed SMES system contains a coupling transformer, a filter, bidirectional VSC-based IGBT switches, a DC link capacitor, a DC–DC chopper-based IGBT switches and SC coil. To adapt and achieve an optimal power exchange between both of power grid and SMES coil sides, power electronic converters (bidirectional VSC, DC-DC chopper) must be linked between them. SMES system parameters are chosen in such a way that they can effectively address the power fluctuations of the WPGS-based PMSG. Table 2 shows the proposed SMES system parameters.

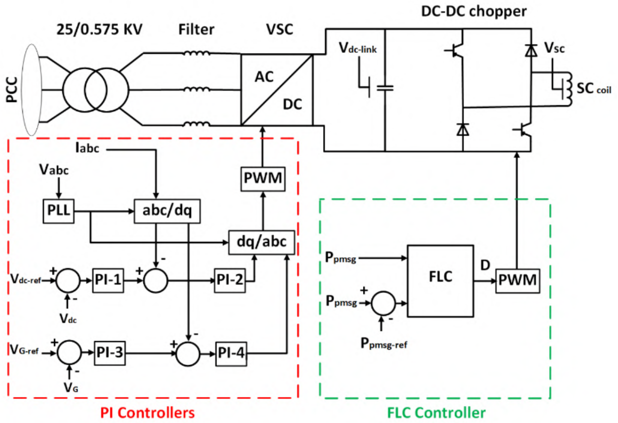

Fig. 2. The structure of the proposed SMES system with its controllers

Type-D chopper shown in Fig. 2 is a type of DC–DC converter that can controls the charge and discharge process of the SC coil. It works by rapidly switching the IGBTs on and off, which in turn controls the amount of exchanged energy between the SC coil and PCC.

Table 2

Parameters of the proposed SMES system

Parameter	Value
Chopper switching frequency, kHz	2
VSC switching frequency, kHz	4
SMES inductance, H	0.5
Filter inductance, mH	0.41
DC link capacitor, mF	15
DC link voltage, kV	1
SMES energy, MJ	0.422
SMES current, kA	1.3

The charged and discharged energy in [J] and the active power in [W], exchanged by the SC coil can be calculated as follows [25]:

$$E_{sc} = \frac{1}{2} \cdot L_{sc} I_{sc}^2; \tag{12}$$

$$P_{sc} = \left(L_{sc} \frac{\mathrm{d}I_{sc}}{\mathrm{d}t} \right) I_{sc} = V_{sc} I_{sc}, \tag{13}$$

where L_{sc} is the self-inductance of SC coil; I_{sc}, V_{sc} are the operating current and voltage of SC coil, respectively.

As shown in Fig. 2, the charge and discharge process of the SC coil is controlled by converting the duty cycle value *D* given by the FLC into pulse signals generated with the PWM block. These pulse signals feed directly to the IGBT switches gates of the DC–DC chopper. So that if the duty cycle is larger than 0.5, the SC coil is in charge mode, while if the duty cycle is less than 0.5 the SC coil is in discharge operation, and it is still in standby mode if the duty cycle is equal to 0.5. The relation between the voltage across the SC coil V_{sc} and the DC-link voltage V_{dc} can be expressed as follows [25]:

$$V_{sc} = (1 - 2D) \cdot V_{dc}; \tag{14}$$

$$I_{dc} = (1 - 2D) \cdot I_{sc}; \tag{15}$$

where I_{dc} is the DC current flowing between a two quadrant DC-DC chopper and VSC; I_{sc} is the DC current of the SC coil.

Bidirectional VSC. Figure 2 shows the connection of VSC circuit in SMES system. VSC is a high-power self-commutated converter, which can be established using 6 IGBT switches. In the VSC, the AC side is linked with a DC side with the ability to transmit power in both sides. Moreover, VSC can operate at a very high-frequency range (2–20 kHz), allowing it to control both real and reactive power whether independently or simultaneously. The DC-link voltage can be maintained at almost steady level of its reference value by the installed DC-link capacitor, that's in order to make the SMES system more effective in the real power exchange with the PCC.

The proposed SMES system controllers. In this paper, two controllers is used to controls the SMES system. The first is an FLC controller, which is designed to control the used type-D chopper, while the second is a PI controller for the VSC converter. The two controllers are represented in Fig. 2.

DC–DC chopper control operation. FLC is a progressing control technique used in several physical systems such as the electrical distribution systems. FLC is cheaper to develop, fast, does not need a mathematical model, robust and simple to use [26–28]. As represented in Fig. 2, the FLC comprises two inputs, as well as an output. The first input is the PMSG output power, while the second input is taken from the result of subtraction between the output of PMSG and its reference value. The duty cycle is taken as an FLC output. MFs of the FLC are depicted in Fig. 3. The triangular MFs type has been used in both fuzzification and defuzzification processes.

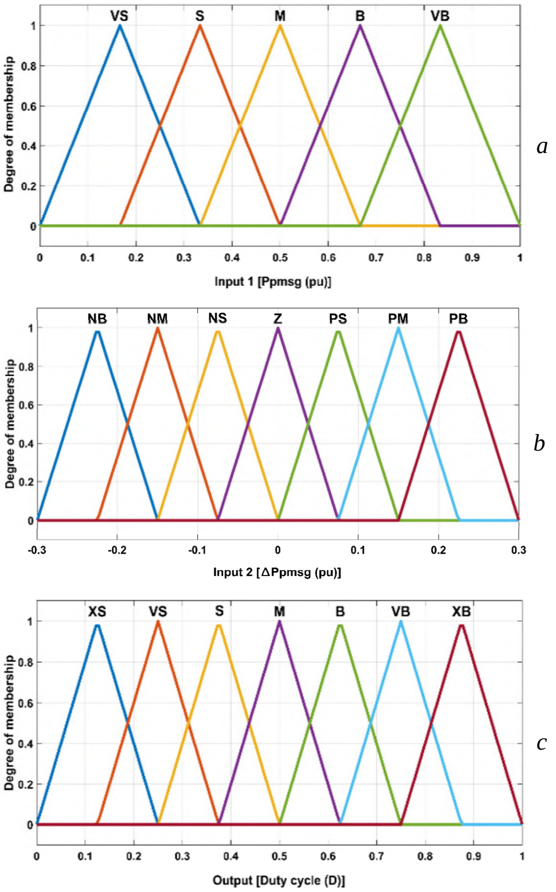

Fig. 3. MFs of inputs/output variables of FLC:
a – input № 1; *b* – input № 2; *c* – output

The triangular MFs can be evaluated as a function of vector ***x*** as follows [29]:

$$f(x,a,b,c)=\max\left(\min\left(\frac{x-a}{b-a},\frac{c-x}{c-a}\right),0\right),\qquad (16)$$

with $a \le b \le c$, where a, c are the coordinates locations of feet of the triangle; b is the coordinate location of the peak; x is the value of the input or output variable.

The fuzzy inference system uses the Mamdani method to build the FLC rules. This strategy depends on IF/ THEN rule to construct the decision table for determining the FLC output values. The FLC output defuzzification process has been achieved using the center of gravity method.

The duty cycle values, which have been considered as the output of FLC in this study, can be evaluated according to the surface graph of Fig. 4.

VSC control operation. As shown in Fig. 3, the VSC control is performed using PI controllers in order to maintain the voltages of AC and DC sides in specified ranges according to predetermined values. The power flow direction between AC and DC sides is determined based on the actual voltages on the two sides of VSC. A phase-locked loop has been employed in PI controllers for coupling the SMES system with both the WPGS system and the power grid, so that it has been used in the VSC voltages synchronization process with grid voltages. The reference currents of *d*-*q* axis can be taken from the subtraction result values of both DC link reference voltage/DC link actual voltage and AC reference voltage/AC actual voltage, respectively. The PI controllers convert the comparison results between the reference currents of *d*-*q* axis and their actual values obtained by the *abc*/*dq* block into controlled voltage signals in *d*-*q* axis. These voltage signals can be converted to three-phase sinusoidal signals by *dq*/*abc* block. These sinusoidal signals are taken as reference voltages, which are utilized by the PWM block to produce PWM pulse signals to feed IGBT switch initiation processes in the VSC converter. The gains of the PI controllers are given in Table 3.

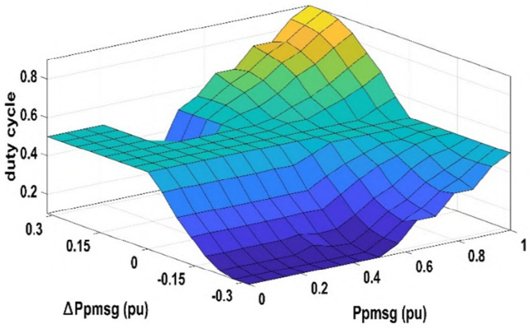

Fig. 4. Surface graph of FLC output variable

Table 3

Parameters of the PI controller

Gains	PI-1	PI-2	PI-3	PI-4
K_p	0.32	0.018	0.16	0.05
K_i	8	247	725	183

Simulation results and discussions. In this part, the proposed controllers for the SMES system were implemented using the MATLAB/Simulink software. As shown in Fig. 5, two wind speed scenarios were used in order to simulate the fluctuations of the power generated by WPGS. In order to verify the effectiveness of the proposed SMES system, significant and sudden changes were chosen for each scenario of wind speed.

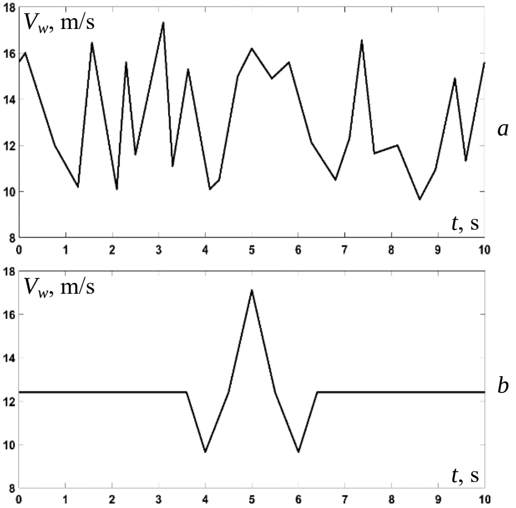

Fig. 5. Wind speed scenarios: *a* – scenario № 1; *b* – scenario № 2

For comparison purposes, simulations were firstly performed without considering SMES system and then by including the proposed SMES system. The rated power value was taken at a V_w = 12.3 m/s, which is considered as the rated speed of wind turbine. Simulation results for duration of 10 s including the active power at PCC and SMES active power are illustrated in Fig. 6, 7, respectively. It is clearly from the first scenario (Fig. 6,*a*) that the real power at the PCC fluctuates between the two limits: 1.31 p.u. and 0.49 p.u. when the SMES system is not installed, while it fluctuates between 1.05 p.u. and 0.96 p.u. limits when the SMES system is installed. Consequently, for scenario №1 the real power fluctuation at PCC is reduced by 89.02 %.

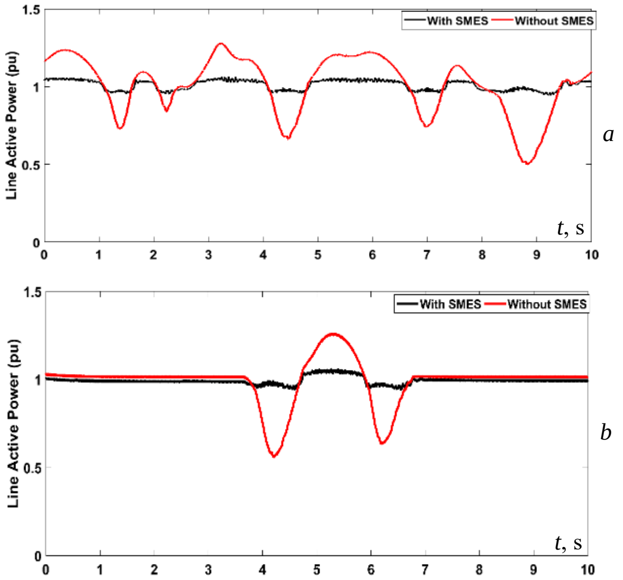

Fig. 6. Response of the active power at PCC during wind gusts: *a* – scenario № 1; *b* – scenario № 2

Likewise, for the second scenario (Fig. 6,*b*) the real power at PCC fluctuates between 1.27 p.u. and 0.56 p.u. limits when the SMES system is not installed, while it fluctuates between the limits 1.05 p.u. and 0.96 p.u. when the SMES system is installed, giving a reduction of 87.32 % in the PCC real power fluctuation. As a result, the findings clearly demonstrate that the proposed SMES system has the capability to decrease the fluctuations of WPGS real power delivered to the power grid.

Besides, it can be seen from Fig. 7 that the direction of SMES real power is directly affected by both the change of real power value produced by WPGS and the wind speed. Therefore, if the output real power of WPGS is more than its rated value, the SMES system absorbs the real power excess from the PCC. On the other hand, if the output real power of WPGS is less than its rated value, the SMES system supplies the power deficiency to the PCC. When the WPGS output real power is equal to its rated power, the SMES system is kept at standby mode.

Figure 8 shows the curve of stored energy in the SMES coil as well as the curve of current flowing through the SMES coil for the two scenarios. It is obvious that the stored energy in the SMES coil and the current flow through the SMES coil are directly dependent on the change of power value produced by the WPGS. Moreover, the proposed SMES system can rapidly exchange energy during charging and discharging process; this is a result of the fast response of the proposed FLC technique.

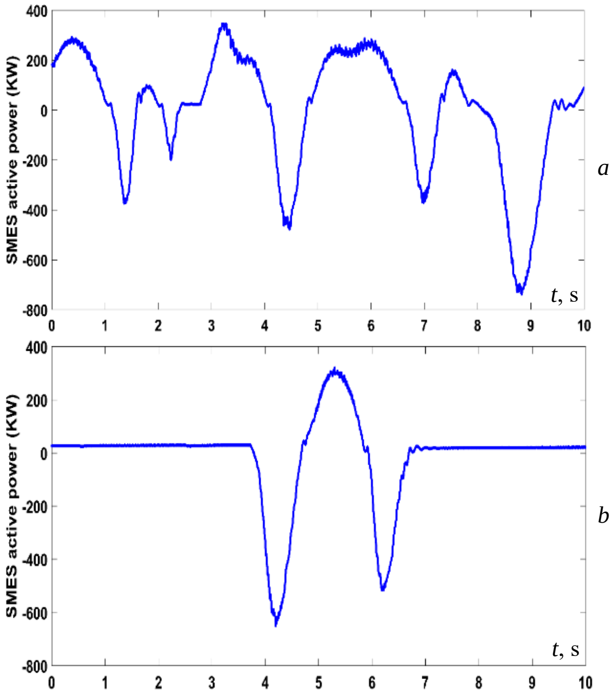

Fig. 7. Response of SMES active power during wind gusts: *a* – scenario № 1; *b* – scenario № 2

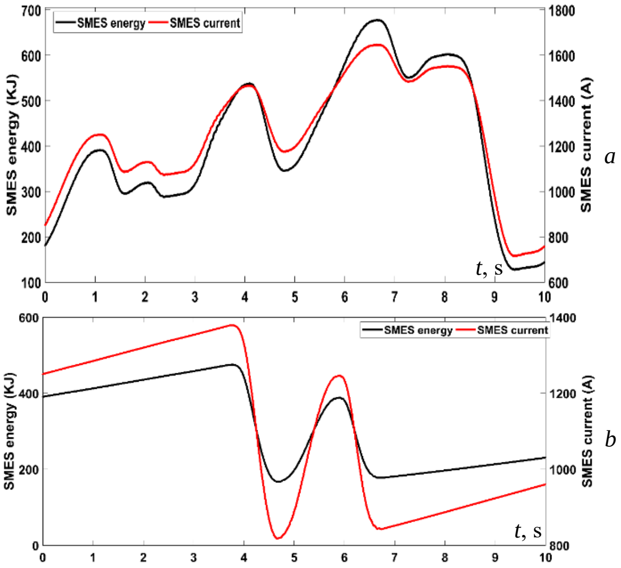

Fig. 8. Behavior of SMES stored energy and current flow through the SMES coil during wind gusts: *a* – scenario № 1; *b* – scenario № 2

Finally, as it can be seen from Fig. 9, the voltage of the SMES DC link capacitor is almost constant and equal to its specified rated value for the two scenarios. This can help in preserving a longer lifetime of the DC link capacitor in the SMES system. These results prove the effectiveness of the proposed PI controllers.

Performance comparison. In order to verify the effectiveness of the proposed SMES system with its controllers, the obtained results of this study are compared with other results reported recently in the literature [30, 31] (Table 4). The comparison includes the SMES capacity used in each study as well as the reduction rate of the real power fluctuations provided by the WPGS. It can be seen from Table 4 that the proposed system gives better reduction rates for the real power fluctuations than those proposed in the recent literature. It is also clear from Table 4 that the proposed SMES has a lower capacity than that published in the recent studies.

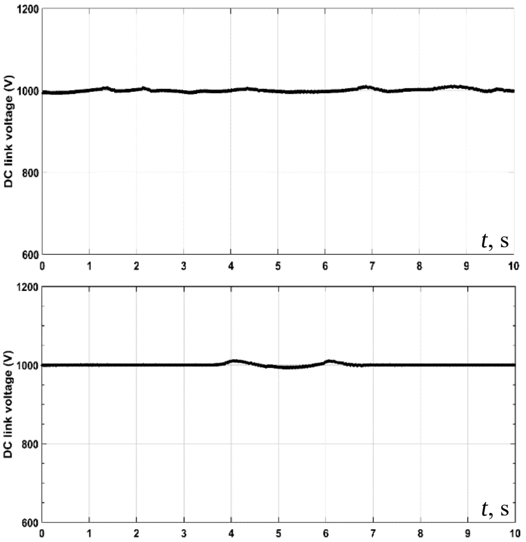

Fig. 9. SMES DC link voltage during wind gusts:
a – scenario № 1; *b* – scenario № 2

Table 4
Comparative study of SMES systems for reduction of power fluctuation generated by WPGS

	9 MW SCIG wind power generation [30]	9 MW DFIG power generation [31]	Proposed: 2 MW PMSG wind power generation
SMES capacity	1 MJ for 2 MW	1.6 MJ for 1.5 MW	0.422 MJ for 1.5 MW
Reduction rate of real power fluctuations for scenario № 1	56.53 %	87.5 %	89.02 %
Reduction rate of real power fluctuations for scenario № 2	53.1 %	71.42 %	87.32 %

Conclusions. In this paper, an effective SMES system with its controllers are proposed to mitigate the fluctuations of power provided by the WPGS based on PMSG integrated with the power grid. The FLC is proposed for controlling the DC-DC chopper circuit, whereas the PI controllers are proposed for controlling the bidirectional VSC circuit. The FLC is designed so that the SMES system can absorb/supply the real power from/to the PCC according to the amount-generated power from the WPGS during wind speed changes. The PI controllers are designed for regulating the voltages on the two sides (PCC and DC link capacitor) of the bidirectional VSC at allowable and predetermined ranges. Simulations were carried out using two different wind speed scenarios. As a result, the following conclusions are drawn:

1. The effectiveness of the proposed PI controllers has proven through the nearly constant at its predetermined value, and avoiding the deep ripples in DC link voltage during the fast charge and discharge processes of SMES coil, consequently this is can help in preserving a longer lifetime of the DC link capacitor.
2. The effectiveness of the proposed FLC has proven by the fast response of the SMES system for absorbing/supplying the real power from/to the PCC during the wind speed changes.
3. The proposed SMES control strategy is found to be very effective in mitigating the real power fluctuations supplied by the WPGS, where the real power fluctuations were significantly reduced by 89.02 % for the first scenario and 87.32 % for the second scenario.

These results contribute to the improvement of the reliability of the WPGS based PMSG.

Conflict of interest. The authors declare that they have no conflict of interest.

REFERENCES

1. Louarem S., Kebbab F.Z., Salhi H., Nouri H. A comparative study of maximum power point tracking techniques for a photovoltaic grid-connected system. *Electrical Engineering & Electromechanics*, 2022, no. 4, pp. 27-33. doi: https://doi.org/10.20998/2074-272X.2022.4.04.

2. Manikandan K., Sasikumar S., Arulraj R. A novelty approach to solve an economic dispatch problem for a renewable integrated micro-grid using optimization techniques. *Electrical Engineering & Electromechanics*, 2023, no. 4, pp. 83-89. doi: https://doi.org/10.20998/2074-272X.2023.4.12.

3. Maradin D. Advantages and disadvantages of renewable energy sources utilization. *International Journal of Energy Economics and Policy*, 2021, vol. 11, no. 3, pp. 176-183. doi: https://doi.org/10.32479/ijeep.11027.

4. Youcef D., Khatir K., Yassine B. Design of neural network fractional-order backstepping controller for MPPT of PV systems using fractional-order boost converter. *International Transactions on Electrical Energy Systems*, 2021, vol. 31, no. 12, art. no. e13188. doi: https://doi.org/10.1002/2050-7038.13188.

5. Said S.M., Salama H.S., Hartmann B., Vokony I. A robust SMES controller strategy for mitigating power and voltage fluctuations of grid-connected hybrid PV–wind generation systems. *Electrical Engineering*, 2019, vol. 101, no. 3, pp. 1019-1032. doi: https://doi.org/10.1007/s00202-019-00848-z.

6. Ghanaatian M., Lotfifard S. Control of Flywheel Energy Storage Systems in the Presence of Uncertainties. *IEEE Transactions on Sustainable Energy*, 2019, vol. 10, no. 1, pp. 36-45. doi: https://doi.org/10.1109/TSTE.2018.2822281.

7. Nayak C.K., Nayak M.R. Technoeconomic analysis of a grid-connected PV and battery energy storage system considering time of use pricing. *Turkish Journal of Electrical Engineering and Computer Sciences*, 2018, vol. 26, no. 1, pp. 318-329. doi: https://doi.org/10.3906/elk-1703-35.

8. Ali Moussa M., Derrouazin A., Latroch M., Aillerie M. A hybrid renewable energy production system using a smart controller based on fuzzy logic. *Electrical Engineering & Electromechanics*, 2022, no. 3, pp. 46-50. doi: https://doi.org/10.20998/2074-272X.2022.3.07.

9. Fan J., Xie H., Chen J., Jiang D., Li C., Ngaha Tiedeu W., Ambre J. Preliminary feasibility analysis of a hybrid pumped-hydro energy storage system using abandoned coal mine goafs. *Applied Energy*, 2020, vol. 258, art. no. 114007. doi: https://doi.org/10.1016/j.apenergy.2019.114007.

10. Bruninx K., Dvorkin Y., Delarue E., Pandzic H., Dhaeseleer W., Kirschen D.S. Coupling Pumped Hydro Energy Storage With Unit Commitment. *IEEE Transactions on Sustainable Energy*, 2016, vol. 7, no. 2, pp. 786-796. doi: https://doi.org/10.1109/TSTE.2015.2498555.

11. Wujong Lee, Hanju Cha. A supercapacitor remaining energy control method for smoothing a fluctuating renewable energy power. *2013 IEEE ECCE Asia Downunder*, 2013, pp. 398-403. doi: https://doi.org/10.1109/ECCE-Asia.2013.6579127.

12. Aly M.M., Mohamed E.A., Salama H.S., Said S.M., Abdel-Akher M., Qudaih Y. A Developed Voltage Control Strategy for Unbalanced Distribution System During Wind Speed Gusts Using

SMES. *Energy Procedia*, 2016, vol. 100, pp. 271-279. doi: https://doi.org/10.1016/j.egypro.2016.10.177.

13. Yao C., Ma Y. Superconducting materials: Challenges and opportunities for large-scale applications. *IScience*, 2021, vol. 24, no. 6, art. no. 102541. doi: https://doi.org/10.1016/j.isci.2021.102541.

14. Seung-Tak Kim, Byung-Kwan Kang, Sun-Ho Bae, Jung-Wook Park. Application of SMES and Grid Code Compliance to Wind/Photovoltaic Generation System. *IEEE Transactions on Applied Superconductivity*, 2013, vol. 23, no. 3, art. no. 5000804. doi: https://doi.org/10.1109/TASC.2012.2232962.

15. Jin J.X., Wang J., Yang R.H., Zhang T.L., Mu S., Fan Y.J., Xing Y.Q. A superconducting magnetic energy storage with dual functions of active filtering and power fluctuation suppression for photovoltaic microgrid. *Journal of Energy Storage*, 2021, vol. 38, art. no. 102508. doi: https://doi.org/10.1016/j.est.2021.102508.

16. Rahman O., Muttaqi K.M., Sutanto D. High Temperature Superconducting Devices and Renewable Energy Resources in Future Power Grids: A Case Study. *IEEE Transactions on Applied Superconductivity*, 2019, vol. 29, no. 2, pp. 1-4. doi: https://doi.org/10.1109/TASC.2019.2895677.

17. Mosaad M.I., Abu-Siada A., El-Naggar M.F. Application of Superconductors to Improve the Performance of DFIG-Based WECS. *IEEE Access*, 2019, vol. 7, pp. 103760-103769. doi: https://doi.org/10.1109/ACCESS.2019.2929261.

18. Bizon N. Effective mitigation of the load pulses by controlling the battery/SMES hybrid energy storage system. *Applied Energy*, 2018, vol. 229, pp. 459-473. doi: https://doi.org/10.1016/j.apenergy.2018.08.013.

19. Qais M.H., Hasanien H.M., Alghuwainem S. Output power smoothing of wind power plants using self-tuned controlled SMES units. *Electric Power Systems Research*, 2020, vol. 178, art. no. 106056. doi: https://doi.org/10.1016/j.epsr.2019.106056.

20. Huang C., Zheng Z., Xiao X., Chen X. Cooperative strategy of SMES device and modified control for cost-effective fault ride-through enhancement and power smoothing of 10 MW class superconducting wind turbine. *Journal of Renewable and Sustainable Energy*, 2020, vol. 12, no. 3, art. no. 033302. doi: https://doi.org/10.1063/1.5143565.

21. Boudia A., Messalti S., Harrag A., Boukhnifer M. New hybrid photovoltaic system connected to superconducting magnetic energy storage controlled by PID-fuzzy controller. *Energy Conversion and Management*, 2021, vol. 244, art. no. 114435. doi: https://doi.org/10.1016/j.enconman.2021.114435.

22. Slootweg J.G., de Haan S.W.H., Polinder H., Kling W.L. General model for representing variable speed wind turbines in power system dynamics simulations. *IEEE Transactions on Power Systems*, 2003, vol. 18, no. 1, pp. 144-151. doi: https://doi.org/10.1109/TPWRS.2002.807113.

23. Soliman M.A., Hasanien H.M., Azazi H.Z., El-Kholy E.E., Mahmoud S.A. An Adaptive Fuzzy Logic Control Strategy for Performance Enhancement of a Grid-Connected PMSG-Based Wind Turbine. *IEEE Transactions on Industrial Informatics*, 2019, vol. 15, no. 6, pp. 3163-3173. doi: https://doi.org/10.1109/TII.2018.2875922.

24. Zine H.K.E., Abed K. Smart current control of the wind energy conversion system based permanent magnet synchronous generator using predictive and hysteresis model. *Electrical Engineering & Electromechanics*, 2024, no. 2, pp. 40-47. doi: https://doi.org/10.20998/2074-272X.2024.2.06.

25. Ali M.H., Park M., Yu I.-K., Murata T., Tamura J. Improvement of Wind-Generator Stability by Fuzzy-Logic-Controlled SMES. *IEEE Transactions on Industry Applications*, 2009, vol. 45, no. 3, pp. 1045-1051. doi: https://doi.org/10.1109/TIA.2009.2018901.

26. Zadeh L.A., Klir G.J., Yuan B. Fuzzy Sets, Fuzzy Logic, and Fuzzy Systems. *World Scientific*. 1996, vol. 6, 840 p. doi: https://doi.org/10.1142/2895.

27. Kaddache M., Drid S., Khemis A., Rahem D., Chrifi-Alaoui L. Maximum power point tracking improvement using type-2 fuzzy controller for wind system based on the double fed induction generator. *Electrical Engineering & Electromechanics*, 2024, no. 2, pp. 61-66. doi: https://doi.org/10.20998/2074-272X.2024.2.09.

28. Aissaoui M., Bouzeria H., Benidir M., Labed M.A. Harmonics suppression in high-speed railway via single-phase traction converter with an LCL filter using fuzzy logic control strategy. *Electrical Engineering & Electromechanics*, 2024, no. 2, pp. 16-22. doi: https://doi.org/10.20998/2074-272X.2024.2.03.

29. Topaloglu F., Pehlivan H. Analysis of the effects of different fuzzy membership functions for wind power plant installation parameters. *2018 6th International Symposium on Digital Forensic and Security (ISDFS)*, 2018, pp. 1-6. doi: https://doi.org/10.1109/ISDFS.2018.8355383.

30. Aly M.M., Abdel-Akher M., Said S.M., Senjyu T. A developed control strategy for mitigating wind power generation transients using superconducting magnetic energy storage with reactive power support. *International Journal of Electrical Power & Energy Systems*, 2016, vol. 83, pp. 485-494. doi: https://doi.org/10.1016/j.ijepes.2016.04.037.

31. Mukherjee P., Rao V.V. Effective location of SMES for power fluctuation mitigation of grid connected doubly fed induction generator. *Journal of Energy Storage*, 2020, vol. 29, art. no. 101369. doi: https://doi.org/10.1016/j.est.2020.101369.

Received 17.09.2023
Accepted 18.03.2024
Published 20.08.2024

A. Nid [1], *PhD Student,*
S. Sayah[1], *Professor,*
A. Zebar[1], *Doctor of Electrical Engineering,*
[1] Department of Electrical Engineering,
Farhat Abbas University, Setif, 19000, Algeria,
e-mail: abdelbasset.nid@univ-setif.dz (Corresponding Author);
samir.sayah@univ-setif.dz; abdelkrim.zebar@univ-setif.dz

How to cite this article:

Nid A., Sayah S., Zebar A. Power fluctuation suppression for grid connected permanent magnet synchronous generator type wind power generation system. *Electrical Engineering & Electromechanics*, 2024, no. 5, pp. 70-76. doi: https://doi.org/10.20998/2074-272X.2024.5.10

UDC 629.1.032 https://doi.org/10.20998/2074-272X.2024.5.11

V.V. Dushchenko, B.G. Liubarskyi, A.O. Masliev, R.A. Nanivskyi, V.G. Masliev, O.M. Ahapov, D.I. Iakunin

Increasing the damping properties of the magnetorheological actuator of the vehicle suspension control system

Introduction. *In accordance with one of the ways of solving the problem of increasing the smoothness of the vehicles, a controlled suspension is proposed, which is created on the basis of the use of «smart» materials – magnetorheological elastomers, the mechanical properties of which, in particular, damping, can be changed with the help of a controlling magnetic field. This is implemented with the help of the magnetorheological actuator of the suspension control system, which has the form of an elastic bushing of the suspension arm, consisting of several electrically connected in series toroid-like coils (with a core of magnetorheological elastomer). The device is powered by current, the value of which is controlled by the operator, or automatically, depending on the road profile and driving mode. Magnetorheological actuators (elastic bushings) are placed in the holes of the suspension levers instead of standard rubber ones and combined with a controlled current source. Thus, the suspension becomes controllable, which makes it possible to set the necessary vibration damping of the vehicle body to increase its smoothness.* ***Problem****. The disadvantage of the previous designs of the magnetorheological actuator is the insufficient amount of the magnetic flux density and the unevenness of its distribution within the elastic bushings. As a result, the damping properties of such controlled suspensions become insufficiently effective, which reduces the possibility of increasing the smoothness of the vehicles.* ***The purpose*** *of the work is to increase the damping properties of the magnetorheological actuator of the vehicle suspension control system, which will increase the control efficiency.* ***The task*** *is to improve the design of the performing magnetorheological device, to carry out calculations and develop a calculation scheme of the study, to determine the average magnetic flux density value and its distribution across the cross-section of the device, to calculate the dependence of the device damping indicator on the magnetic flux density, to compare the damping indicators of the improved device with previously known ones.* ***Methodology.*** *Research tasks were solved on the basis of magnetic field analysis using methods of magnetic field theory and SOLIDWORKS® and FEMM software packages, as well as analysis of the dependence of the damping properties of bushings from magnetorheological elastomers on magnetic flux density. A description of the design and principle of operation of the magnetorheological actuator of the vehicle suspension characteristics control system is given, based on which the calculation scheme was developed.* ***Results.*** *The results of research calculations showed that the average value of magnetic flux density in the proposed design of the device reached 0.85 T, its distribution became fairly uniform, and there were no zones where it was abnormally small. For the first time, the dependence of the damping index on the magnetic flux density of the controlling magnetic field has signs of scientific novelty. It was found that this indicator for the proposed design of the device increased by 22 % compared to previous other designs, which will increase the efficiency of the control system and the smoothness of the vehicle. A positive result was achieved due to the following features of the proposed design of the suspension actuator: the elastic sleeve consists of several coaxially located actuators made of anisotropic magnetorheological elastomer, in which the conglomerates of the ferromagnetic filler during the manufacturing process are located collinear to the direction of the angular deformations of the sleeve and the control magnetic field flux density vector, and the devices have control coils located on their surfaces, which are made of conductive elastic elastomer and electrically connected in a series circuit.* ***Originality****. The control method, previous designs and construction of this controlled suspension are protected by patents of Ukraine.* ***Practical value****. The direction of further research is to optimize the parameters of the control coils in order to reduce the energy consumption for them and to protect them from overheating.* References 20, figures 10.

Key words: **magnetic field, magnetorheological actuator, anisotropic magnetorheological elastomer, control system, vehicle suspension, damping.**

Проблема. *Відповідно до одного із напрямків вирішення проблеми підвищення плавності ходу транспортних засобів, запропоновано керовану підвіску, яку створено на базі застосування «інтелектуальних» матеріалів – магнітореологічних еластомерів, механічні властивості яких, зокрема демпфування, можна змінювати за допомогою керуючого магнітного поля. Це реалізовано за допомогою виконавчого магнітореологічного пристрою системи керування підвіски, який має вигляд пружної втулки важеля підвіски, що складається із декількох електрично поєднаних у послідовне коло тороподібних котушок (з осереддям із магнітореологічного еластоміру). Пристрій живиться електричним струмом, величина якого керується оператором, або автоматично, в залежності від дорожнього профілю та режиму руху. Виконавчі магнітореологічні пристрої (пружні втулки) розміщують у важелях підвіски замість штатних гумових і поєднують із керованим джерелом струму. Таким чином, підвіска стає керованою, що надає можливість встановлювати необхідне демпфування коливань корпусу транспортного засобу для підвищення його плавності ходу. Недоліком попередніх конструкцій виконавчого магіторелогічного пристрою є недостатня величина індукції та нерівномірність її розподілу в межах пружних втулок. Внаслідок цього демпфуючі властивості таких керованих підвісок недостатньо ефективні, що знижує можливості підвищення плавності ходу транспортних засобів.* ***Метою*** *роботи є підвищення демпфуючих властивостей виконавчого магніторелогічного пристрою системи керування підвіски транспортного засобу, що збільшить ефективність керування.* ***Завдання.*** *Удосконалити конструкцію виконавчого магніторелогічного пристрою, провести розрахунки середньої по перерізу пристрою величину індукції магнітного поля та її розподілу, скласти залежність показника демпфування пристрою від індукції магнітного поля, порівняти показники демпфування удосконаленого пристрою з попередніми.* ***Методологія****. Задачі дослідження вирішувалися з використанням методів теорії магнітного поля та програмних пакетів SOLIDWORKS® і FEMM, а також аналізу залежності демпфуючих властивостей втулок з магніторелогічних еластомірів від індукції магнітного поля. Наведено опис конструкції та принцип дії виконавчого магніторелогічного пристрою системи керування підвіски транспортного засобу, на основі чого розроблено розрахункову схему.* ***Результати*** *розрахунків показали, що середня величина індукції магнітного поля у запропонованій конструкції пристрою досягла 0,85 Т, її розподіл став достатньо рівномірний, а зони, де вона аномально мала, відсутні. Складена вперше залежність показника демпфування від індукції керуючого магнітного поля має ознаки наукової новизни. Отримано, що даний показник для запропонованої конструкції пристрою збільшився на 22 % порівняно з попередніми* *конструкціями, що підвищить ефективність системи керування та плавність ходу транспортного засобу. Позитивний результат досягнуто завдяки наступним особливостям запропонованої конструкції виконавчого пристрою: пружна втулка складається із декількох, розташованих співвісно, виконуючих пристроїв з анізотропного магнітореологічного еластоміру, у якого конгломерати феромагнітного наповнювача в процесі виготовлення розташовано колінеарно до напрямку кутових деформацій втулки та вектору індукції керуючого магнітного поля, а котушки керування виконано із струмопровідного пружного еластоміру. Спосіб керування, попередні конструкції та конструкцію даної керованої підвіски захищено патентами України. Напрямки подальших досліджень полягають у оптимізації параметрів котушок керування з метою зниження енергоспоживання та їх захисту від перегріву.* Бібл. 20, рис. 10.

Ключові слова: **магнітне поле, виконавчий магнітореологічний пристрій, анізотропний магнітореологічний еластомір, система керування, підвіска транспортного засобу, демпфірування.**

Introduction. The use of controlled suspensions (CSs) is considered a promising way to solve the problem of improving the smoothness of the vehicles. This is especially relevant for military vehicles, as they move at relatively high speeds on dirt roads and rough terrain. However, known technical solutions of CSs are characterized by complexity, high cost and low reliability. Eliminating these shortcomings is a complex scientific and applied problem, the solution of which is being worked on by experts from all developed countries. One of the variants of the actuator of the CS is a hydro damper filled with a magnetorheological («smart») liquid, the properties of which, in particular, density, change under the influence of the magnetic field. This allows to control its damping properties and influence the smoothness of the vehicle's movement when driving off-road. But the wide distribution of such CSs is restrained by the problem caused by the abrasive action of magnetic particles on the interacting parts of the actuator, which reduces durability, and the instability of the characteristics of the magnetic fluid, which is caused by the sedimentation of the magnetic particles, which reduces the control efficiency and the smoothness of the vehicle's movement. The problem can be solved by using actuator, where the liquid is replaced by a magnetorheological elastomer (MRE), which is devoid of these disadvantages. The use of MRE in the vehicles' CSs was proposed by the authors for the first time – a method and design, confirmed by patents of Ukraine. This work is devoted to the improvement of the magnetorheological actuator (MRA) in order to increase its efficiency. It is intended for military wheeled vehicles, but is also suitable for other vehicles, for example, for electric vehicles with powerful current sources. It is connected to operate for a short time, in addition to the main elastic elements and damping devices of the suspension in case of the need to increase damping when overcoming sections with a difficult road profile on resonant driving modes. This allows to maintain the necessary smoothness of movement, without reducing the speed of movement. In the event of failure of this CS, the vehicle will remain with the usual suspension and will not lose traction. In this way, the urgent tasks of ensuring high reliability of vehicles are also solved.

MREs are a mixture of an elastic matrix (rubber or elastomer) and a ferromagnetic filler, for example, carbonyl iron powder, with a particle size of about 5 μm. The mixture is polymerized and MRE is obtained with a uniform (isotropic) distribution of particles in the matrix, or with an anisotropic one, if the polymerization process is carried out in a magnetic field. At the same time, filler particles form conglomerates in the form of columns, which are located along the lines of the magnetic flux density.

It is known that anisotropic MREs change their elastic and damping properties to a greater extent under the influence of a controlling magnetic field than isotropic ones. This affects the frequency response of the vibrations of the sprung body of the vehicle. An increase in damping causes a decrease in the amplitudes of oscillations and accelerations and, accordingly, in the height of the resonance maximum of the frequency response. An increase in the stiffness of the suspension increases the natural frequency of oscillations of the sprung body on it. This violates its coincidence with the frequency of excitations from unevenness of the road profile and protects against the occurrence of resonant oscillations. Meanwhile, certain problems arise when using MRE, due to the difficulty of obtaining the necessary magnetic flux density of the controlling magnetic field and its uniform distribution within the MRA. A large number of publications, patents and examples of practical application prove the promising direction of solving the problem of increasing the smoothness of the vehicle's movement by using the CS. In this regard, scientific and practical works aimed at improving CSs, in particular, by using MRA in them, improving the damping properties of which this work is aimed at, are relevant.

Analysis of previous studies. In work [1] it is stated that the further improvement of the quality indicators of vehicles due to the improvement of suspension systems requires the application of control of the characteristics of their elastic and damping devices. But traditional materials (metals, composite materials, rubber, elastomers, gases, liquids, etc.) used in these units have exhausted their capabilities to ensure the necessary control of the characteristics of suspension systems. This is due to the immutability of the physical properties and characteristics of these materials, which leads to complex, high-cost and unreliable technical solutions and hinders the introduction of CSs on vehicles.

The authors propose to solve this urgent problem by using alternative materials in the CSs, known in the world as *smart materials*. This will simplify the technology of production of CSs, and will contribute to their implementation on vehicles. At the time, there was a certain spread of CSs, in which the working element is a magnetorheological fluid (MF). Meanwhile, it has significant disadvantages, one of which is the sedimentation of magnetic particles in the liquid. The authors consider several measures to optimize MF deposition from the point of view of the viscosity of the dispersion medium, the suspension strength of the dispersed phase, and innovations in additives. The proposed active mechanism for solving the sedimentation problem promises to improve the performance of MF dampers, even if the sediment persists. But deposition of MF can be reduced only to a certain extent [2].

Another shortcoming of hydro shock absorbers with MF is considered in work [3], which is related to the sensitivity to pulse loads, which is undesirable for impact protection. This causes large damping forces that are transmitted to the vehicle body and pose a serious threat to passengers and mechanical structures. It is reported on the development of a MF hydro shock absorber with low sensitivity to pulse loads. Analytical and experimental studies proved that its sensitivity to impact has decreased.

The work [4] is devoted to testing and modeling the properties of isotropic MRE under the action of static-dynamic compressive loads. On the basis of silicone elastomer, isotropic MREs with different contents of magnetic particles were made. To apply a controlled magnetic field to the MRE during dynamic tests, an electromagnet with magnetic flux density of up to 0.9 T was developed. The «stress-strain» hysteresis loops of manufactured MREs were experimentally obtained under the action of dynamic compressive loads in combination with various static pre-strains. The effect of particle content, strain amplitude, static pre-strain and load frequency on the storage and loss modules of MREs was investigated. The results showed that regardless of the applied magnetic field, the deformation behavior of MREs was in an approximate linear viscoelastic state if the deformation amplitude was less than 7.5 %. Both the absolute and relative effects of MREs increase with increasing particle content and decrease with increasing strain amplitude. Changing the load frequency has almost no effect on MREs. Empirical models are proposed for predicting MRE storage and loss modules as functions of magnetic flux density, magnetic particle content, strain amplitude, frequency, pre-strain, and load. The models can provide effective predictions of storage modules and losses of MREs for the load conditions used in this work.

The work [5] considers the compression characteristics of MRE based on silicon. The developed electromagnet allows for dynamic compression tests up to 300 Hz of samples 40 × 40 × 8 mm in size. Magnetic flux density of about 1 T was achieved, and the predicted increase in the dynamic stiffness of the MRE was obtained. An electromagnet can be used to manufacture and solidify anisotropic MREs.

In work [6], it was noted that MREs have wide possibilities for use in transport as suspension shock absorbers, due to the relatively lower complexity and cost of the structures of absorbing devices based on them, environmental perfection and the absence of disadvantages inherent in MREs. But the authors do not provide the characteristics of MREs and the results of their use.

The work [7] is devoted to obtaining the dependence of the relative magnetic permeability on the concentration of the MRE filler. Its maximum value (6.6) was obtained for 50 % volume concentration of particles. There is no explanation for the increase in magnetic permeability in the work.

The assessment of the influence of the controlling magnetic field on the vibration-isolating properties of MREs was studied in [8] and numerous other works. A significant improvement in the damping properties of MREs under the influence of a magnetic field was revealed.

In [9], it was noted that the known method of producing MRE takes more than a day, since matrices made of natural rubber or silicone rubber require a long time for polymerization. It is proposed to use (poly)dimethylsiloxane as a matrix with its polymerization at a high temperature. This reduces the production time of MRE to 90 minutes. The study of the dynamic properties of MRE produced by the new method gave positive results.

The effect of changing the Young modulus (0.14 – 14.6 MPa) on the physical characteristics of MRE was studied in [10]. The dependence of the damping properties of the composites on the content of particles (7, 10, 14, 21, 31 vol. %) and on the mechanical properties of MRE was also investigated. An increase in damping properties occurs in a certain proportion of magnetic particles, which can be explained by the magnetic exchange between them. Damping properties (hysteresis) are worse in MRE with a higher Young modulus. Irregular participation of MRE magnetic particles in hysteresis was revealed.

In [11], a linear magneto-viscoelastic model for anisotropic MRE is proposed, which allows determining the influence of the magnetic field on the dynamic shear modulus depending on the strength and frequency of the magnetic field. Errors between experimental values and calculations obtained by simulation do not exceed 10 %.

In [12], a method of calculating elastomeric structures that takes into account their features is proposed. In the calculation process, a vector of nodal displacements is found, on the basis of which the fields of deformations and stresses and their values are determined.

Studies of a conical vibration isolator with MRE have proven its effectiveness: it provides reliable vibration isolation due to an increase in the frequency of oscillations by 46.29 % during the control process and control forces up to 75 N. It is noted that vibration isolators with MRE have high energy consumption and unprofitable production [13].

The work [14] presents the results of research on the strain sensor, which was created on the basis of a wire MRE containing a polyurethane sponge with silver nanowires (AgNW), and particles of carbonyl iron and polydimethylsiloxane. The research revealed that the relative change in its resistance reached 91.8 % at a deformation of 20 % when a control magnetic field of 0.428 T was added. There is a prospect of using this material in smart devices, composite electrodes and soft sensors.

The work [15] gives the results of the research of the sensor in the form of a disk (ferromagnetic marker), which is built into a cylindrical MRE. Its 3D displacement is estimated by monitoring the inductance changes of the four inductance coils. Studies of inductance coils revealed its monotonic change and linearity with respect to the applied normal force and shear force. A conclusion was made about the effectiveness of using MRE in sensors.

The results of research on the magnetic field sensor created on the basis of MRE are given in [16]. The sensor can be used to measure uniform magnetic field. The sensor demonstrates a fast response (20 ms) and good magnetic field detection characteristics in the range from 40 to 100 mT.

The work [17] gives the results of research on adaptive absorbers, in which the resonance shift property was used by using MRE. It is known that passive nonlinear absorbers have a wider effective frequency band. The authors combined these two characteristics in a hybrid MRE absorber, which at the same time can shift its own frequency and has a wider absorption band. The results of the research proved that the adaptability of the hybrid absorber is ensured thanks to the MRE.

The analysis of the above studies showed that the dependence of the damping properties of the MRA on the direction of the filler conglomerates on its deformations and on the magnetic flux density vector of the controlling magnetic field is not sufficiently revealed.

In this regard, complex studies were carried out: calculation – by means of computer modelling of the distribution of the magnetic field in the MRA of the suspension of the vehicle, and full-scale – elastic samples from MRE (for comparison of rubber) on a dynamic stand. The samples had a diameter of 20 mm, a central hole with a diameter of 8 mm and a thickness of 10 mm; the content of carbonyl iron (by volume) was 40 %. The frequency of natural oscillations of the mass on these elastic samples was about 2 Hz. Based on the experience presented in [11], the samples were made of MRE with an anisotropic structure: they were polymerized in a magnetic field. The direction of the vector of this field in one part of the samples was orthogonal, and in the other – collinear to the direction of the controlling magnetic field. The damping properties of the samples were evaluated by the averaged relative damping index D

$$D = [\ln(A_1 / A_2)] / 2\pi, \qquad (1)$$

where A_1 and A_2 are the successive amplitudes on oscillograms of natural oscillations.

It was found that with orthogonal direction of the control magnetic field vector (0.6 T) to the direction of sample filler conglomerates, the relative damping index was 0.04 – 0.05, and with collinear 0.071 – 0.083, i.e. much more.

The development and computer modelling of the designs of suspensions of vehicles with MRA was also carried out [18, 19].

Figure 1 shows the visualization of the controlling magnetic field in the form of magnetic lines of force on cross-sections according to the first (*a*) and second (*b*) variants of the elastic suspension hinge with MRA. The controlling magnetic field was created by the current of the control coil *3*, which is located on the outer surface of the MRA. This made it possible to place it in the dimensions of serial hinge *4*, which simplified the replacement of the element from rubber to MRA.

It was found that the flux density of the controlling magnetic field within the MRA (position *2*) is irregularly distributed – it is less than 0.1 T on a large area in the middle, and reaches 0.6 T near the end parts.

This means that about 20 % of the volume of the MRA does not participate in the creation of the damping force, which accordingly reduces the efficiency of the suspension control [10]. Splitting the control coil into two parts in option (*b*) did not significantly change the picture.

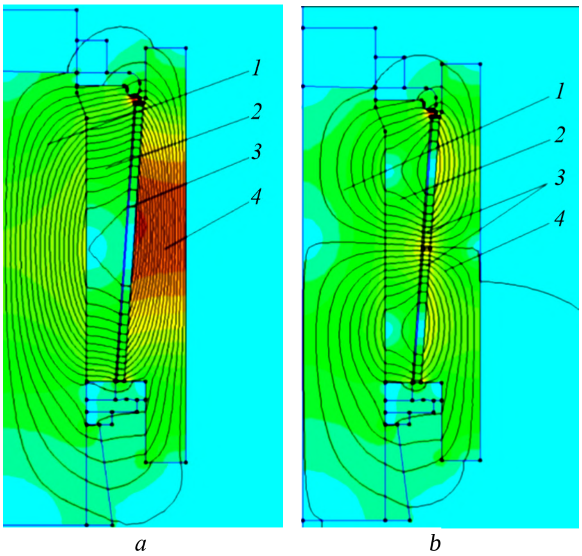

Fig. 1. Visualization of the controlling magnetic field in sections of the MRA according to the first (*a*) and second (*b*) variants of the hinge design: *1* – axis of the hinge; *2* – MRA; *3* – control coil; *4* – hinge

The average magnetic flux density in both variants was about 0.25 T, i.e. significantly less than the magnetic flux density at which the magnetic saturation of the particles of the MRA filler begins. In both variants, it was not possible to direct the magnetic flux density vector of the controlling magnetic field collinearly to the direction of deformations of the MRA: they are orthogonal.

The emergence of «magnetic bridges» from the end parts of the elastic hinge was revealed, where the magnetic flux density exceeded 1 T. Therefore, the adjacent parts of the magnetic circuit reached saturation, which prevented the increase in the magnetic flux density of the controlling magnetic field.

In the third version of the design, the control coil was located from the end of the MRA, which made it possible to increase the number of wire turns in it and, accordingly, the magnetomotive force (MMF) (Fig. 2).

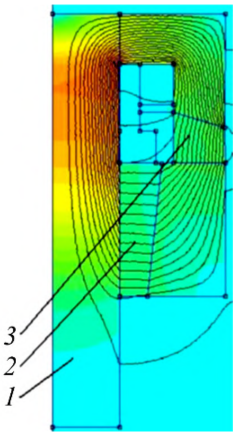

Fig. 2. Visualization of the controlling magnetic field on the MRA according to the third variant of its design: *1* – axis of the hinge; *2* – cylindrical part of the MRA; *3* – end part of the MRA

The MRA is divided into two parts: the first (end) one – in the form of a conical ring, and the second one –

in the form of a conical cylinder on the axis of rotation of the hinge. Collinearity of the vector of the controlling magnetic field and the direction of the conglomerates of magnetic particles has been achieved. This should increase the vibration damping factor to 21 % compared to the isotropic MRA [9, 11].

The study revealed that this MRA excludes parts where the flux density of the controlling magnetic field is too small. Thanks to this, a higher average value (0.6 T) was achieved. But at the same time, it was not possible to achieve collinearity of the flux density vector of the controlling magnetic field, which is tangent to the magnetic field lines, with the direction of deformation of the MRA, which is orthogonal to them.

In all variants, «magnetic bridges» appear on the end parts, which prevents increasing the flux density of the controlling magnetic field. All this required prolonging the search for a more perfect design of the MRA.

Figure 3 shows a scheme of a vehicle suspension with MRA.

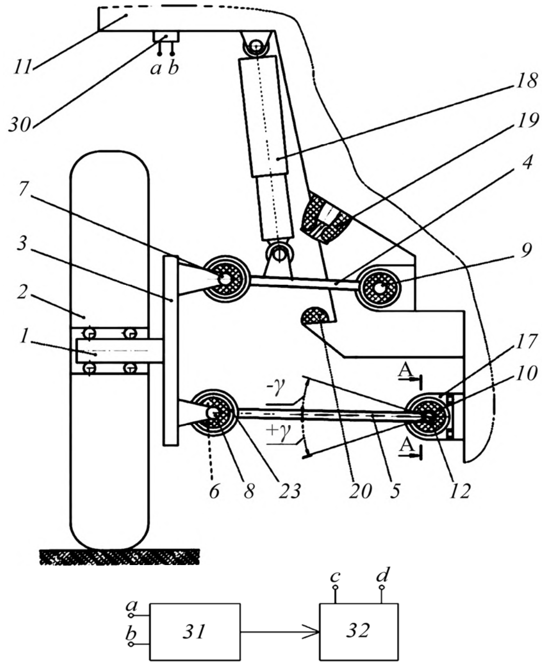

Fig. 3. Scheme of the suspension of the vehicle with MRA: *1* – axle; *2* – wheel; *3* – rotary fist; *4* – upper lever; *5* – lower lever; *6* – MRA; *7* – *10* – axes; *11* – spring-loaded housing; *12* – torsion shaft; *17* – bracket; *18* – hydraulic shock absorber (HA); *19*, *20* – stops; *23* – MRA of the CS; *30* – sensor unit; *31* – control unit; *32* – current source

The goal of the work is to improve the damping properties of the MRA of the vehicle suspension control system by improving its design.

To achieve the goal, the tasks are set:

- to analyze and compare known MRAs and develop a new, improved design;
- to determine the average value and distribution of the flux density of the controlling magnetic field across the MRA cross-section;
- to build the dependence of the MRA damping index on the flux density of the controlling magnetic field;
- to compare the damping indicators of the developed MRA with known structures.

The research methodology consisted in the numerical calculation of the magnetic field arising in the MRE device of the vehicle suspension control system, using the SOLIDWORKS® and FEMM software packages, and the determination of the damping properties of the suspension based on the dependence of the damping index on the flux density of the controlling magnetic field revealed in previous works.

The object of research is an improved MRA, which consists of a coil in the form of a toroid, the core of which is made of anisotropic MRE, and the coil receives current from the power supply unit, while the current value is set by the control unit. This design is protected by a patent of Ukraine [20]. The MRA *23* (Fig. 3) can be installed on axes *7* – *10*.

It should be noted that it is impossible to reproduce an anisotropic MRA with the directions of the filler conglomerates, which coincide simultaneously with all the various deformations of the elastic sleeve during the movement of the vehicle. Therefore, a MRA was created, the direction of the filler conglomerates of which coincides only with the direction of the angular deformations of the elastic sleeves.

Let's consider the operation of the MRA in the CS. The stiffness of the CS is defined as the sum of the stiffnesses of the torsion shaft *12* and MRA *6* brought to the wheel, which can be installed in all (or a certain part) of the hinges of the levers. Damping forces of the HA *18* and MRA *6* are brought to the wheel axis and add up. The controlling magnetic field is created by the current *I* in the control coils *24*, which are electrically connected in a series circuit (Fig. 4–6).

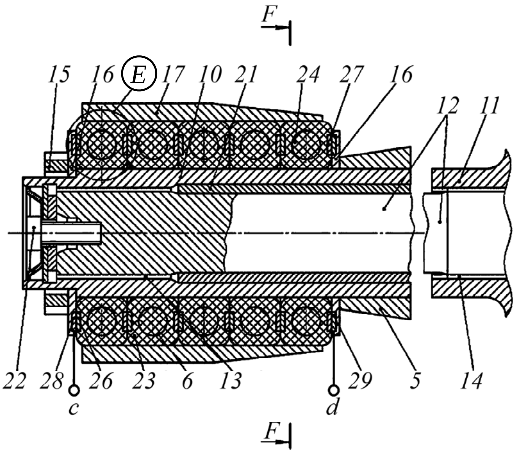

Fig. 4. Section *A-A* (according to Fig. 3): *6* – elastic sleeve from five MRAs; *10* – axis; *11* – spring-loaded housing; *12* – torsion shaft; *13*, *14* – slotted connections; *15* – nut; *16* – washer; *17* – bracket; *21* – sleeve; *22* – bolt fastening; *23* – MRA in the form of a toroid; *24* – control coils; *26* – *29* – contact rings

This field magnetizes the ferromagnetic particles of the MRA filler and they begin to interact with each other, compressing the porous matrix that is located between them. This causes an increase in the frictional forces between the molecular structures in the matrix and, accordingly, the damping forces in the suspension, in proportion to the current *I*.

The process of adjusting the vibrations of the sprung body is as follows. The most dangerous are periodic irregularities that cause resonant oscillations at the corresponding speed of movement. At the same time, wheel *2* moves vertically with a frequency of unevenness and transmits the movement through axis *1* to the fist *3*, upper *4* and lower *5* levers, which rotate relative to axes *7 – 10*, and cause angular deformations ±*γ* of the MRA *6* on these axes (Fig. 3).

The use of anisotropic MRE, in which conglomerates of ferromagnetic filler during the manufacturing process are located collinear to the direction of angular deformations of MRA *6* and the vector of the flux density of the controlling magnetic field, provides the greatest influence on their damping properties (Fig. 6).

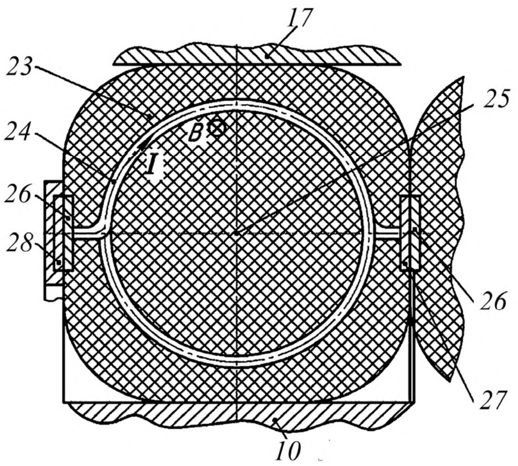

Fig. 5. Unit *E* (according to Fig. 4): arrow *I* indicates the direction of the current in the control coil *24*; ***B*** – magnetic flux density vector; *10* – axis; *17* – bracket; *23* – MRA; *25* – central axis of symmetry of the section of the control coil *24*; *26 – 28* – contact rings

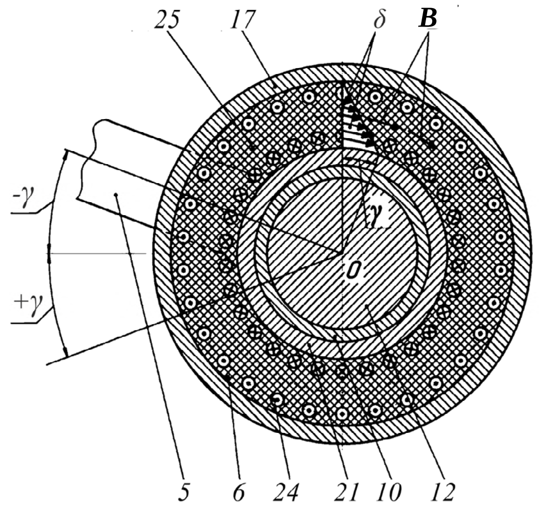

Fig. 6. Section *F-F* (according to Fig. 4): *12* – torsion shaft when it is turned together with the lower lever *5* to the angle *γ*; *δ* – direction of shear deformation; ***B*** – magnetic flux density vector of the controlling magnetic field; *5* – lower lever; *6* – MRA; *10* – axis; *12* – torsion shaft; *17* – bracket; *21* – sleeve; *24* – control coil; *25* – central axis of symmetry of the section of the control coil *24*

The execution of the control coil *24* (Fig. 4, 5) from an elastic current conductor, for example, of polyacetylene, the modulus of elasticity of which is close to the modulus of elasticity of MRE, excludes mutual movement and friction of the contacting surfaces of the control coil *24* with MRE, which will increase the reliability of the device. When the current in the control coils *24* increases, their magnetic field will increase, accordingly, the rigidity and damping of the MRA *6* will increase, which will cause a slight increase in the frequency of the self-oscillations of the sprung body. This frequency will differ from the frequency of following irregularities in the road profile (excitation), as a result of which the amplitudes of resonant oscillations of the sprung body will decrease. Thanks to the control, the damping force in the MRA will also increase, which will be added to the damping force of the HA. This will lead to an improvement in the smoothness of the vehicle.

Research results. To achieve the tasks set, a hypothesis was formulated: *since it is known that coils in the form of toroids concentrate the electromagnetic field in their cores, it can be expected that the toroidal MRA will increase the flux density of the controlling magnetic field, ensure its uniform distribution over the volume and exclude «magnetic bridges».*

The initial data for the research were the drawings of the MRA (Fig. 6), the magnetic characteristics of the hinge steel and MRE filler, the current and the number of turns of the control coil and its geometric parameters:

- the average diameter varied within 70 – 100 mm;
- the diameter of the radial section is 15 mm;
- the diameter of the concentric hole is 8 mm;
- the matrix material – silicone rubber;
- the size of the filler particles is 5 – 10 μm;
- the filler content by volume is 40 %;
- the filler material – carbonyl iron;
- the relative magnetic permeability of the MRA varied within 6 – 8.9.

The operating time of the MRA (time of supplying current to the control coil) was taken to be 10 s, which helped to prevent their overheating. This time is justified by the following. It is known that, according to statistics, a road profile that is difficult from the point of view of smoothness of movement is found on the terrain only periodically, and has 4-6 peaks and depressions in a section 30-50 m long. When hitting the third bump, there is often a breakdown of the suspension and a significant excess of the permissible ergonomic norms of vertical accelerations. As a result, the vehicle's driver is forced to reduce speed sharply. To prevent this, the proposed MRAs of the CS are connected (better automatically, for example, with the help of a sensor of vertical accelerations of the sprung body) only when overcoming a difficult section. At a speed of 8-11 m/s, it will be about 5-7 s. So, the operating time of the MRA with a small margin can be taken as 10 s. This will help to maintain the necessary smoothness of movement without reducing the speed of movement. In case of MRA failure, the vehicle will remain with standard suspension, which will ensure its reliability.

The finite element mesh was created by the FEMM software package in automatic mode with the possibility of its adjustment to clarify the research results. With the use of the SOLIDWORKS® code, the calculation scheme and the problem definition of calculating the magnetic field of the MRA were drawn up (Fig. 7). After setting the parameters, construction materials, as well as forming the winding of the control coil, the FEMM code visualized the magnetic field in the form of lines of force. Examples of calculation results are shown in Fig. 7, 8.

The calculation of the magnetic field was carried out on the cross-section of the generating circle of the toroid, which determines the design of the MRA. It is assumed that the part of the circle of rotation of the toroid according to the thickness of the calculation area is a straight line. Thus, the calculation area becomes cylindrical in shape, the radius of which is determined by the radius of the generating circle of the toroid. Taking into account the assumption, the magnetic field of the toroid can be determined with an axially symmetric formulation of the problem. The axis of symmetry will be tangent to the circle of rotation of the toroid.

Boundary conditions: the magnetic vector potential is zero at the boundary *A*, and periodic boundary conditions are adopted at the boundaries *B* and *C*. In the calculation area, *1* – MRA material, *2* – polyacetylene, which is a winding with a control current, *3* – steel.

Figure 8 shows the calculation area of the MRA. The study revealed that with a current in the winding of 7.18 A, MMF F = 17232 A, current density J = 42 A/mm^2, the distribution of magnetic flux density in the MRA is close to uniform – on average 0.85 T, i.e. the largest among other design variants. Zones where the magnetic flux density does not exceed 0.1 T (which is 2.5 times less than its average value) and «magnetic bridges» (where the magnetic flux density is greater than 1 T and the particles of the filler have reached magnetic saturation) are absent. The current density at the contacts (Fig. 5, items *26* – *28*) is low and amounts to 2.4 A/mm^2, because the contact area is much larger than the cross-sectional area of the winding.

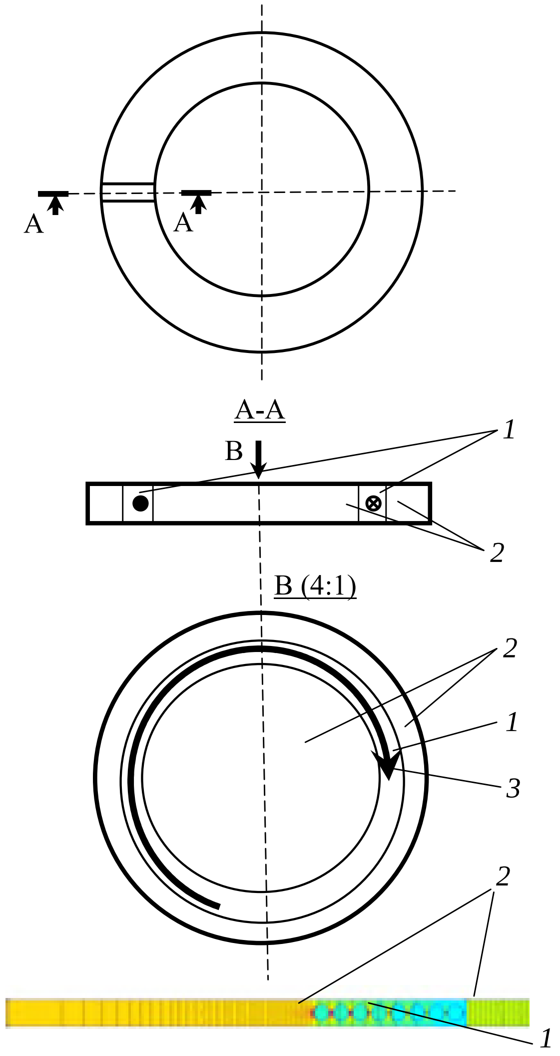

Fig. 7. On the formulation of the problem of calculating the magnetic field: *1* – area with current; *2* – MRA; *3* – current

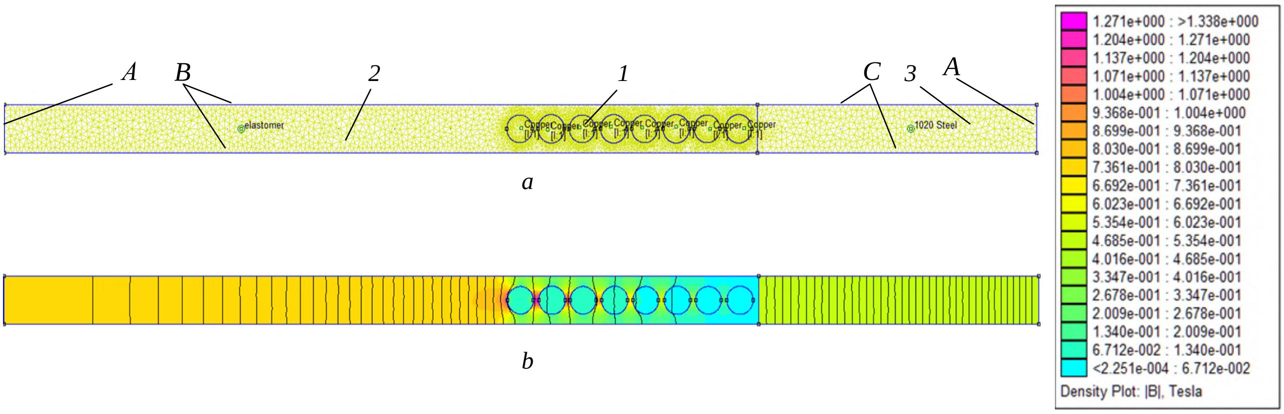

a

b

Fig. 8. Formulation (*a*) and results of solving (*b*) the problem of calculating the magnetic field of the MRA

The MRA coil is fed by current in pulse mode with effective cooling – the role of a radiator is performed by the surface of the components of the undercarriage of the vehicle, which is blown by air. Calculations of overheating of the MRA proved that its temperature does not exceed 45-47 °C during the operating cycle.

The results of the study by means of computer modelling of the dependence of the average flux density of the controlling magnetic field on the average diameter and relative magnetic permeability of the improved MRA are shown in Fig. 9.

As can be seen from Fig. 9, a decrease in the average diameter of the MRA toroid contributes to an increase in the flux density of the controlling magnetic field, and an increase, on the contrary, slightly decreases it. An increase in the relative magnetic permeability is desirable because it proportionally increases the flux density of the controlling magnetic field of the MRA.

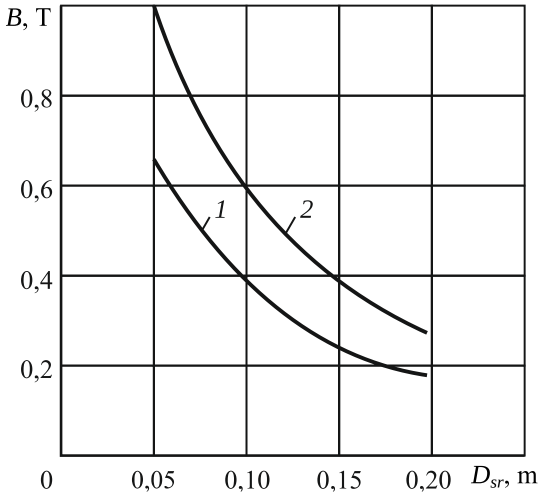

Fig. 9. Dependence of the average flux density of the controlling magnetic field on the average diameter of the MRA and its relative magnetic permeability: *1* – μ = 6; *2* – μ = 8.9

As the MRA filler approaches the state of magnetic saturation, the relative magnetic permeability begins to decrease, which, accordingly, affects the flux density of the controlling magnetic field and the damping properties of the MRA. Therefore, appropriate restrictions are imposed on the MMF and control electric current values.

To evaluate the damping properties of the improved MRA in the form of a toroid, the results of the research presented in [18] were used, where 10 mm thick samples of anisotropic MRE containing 40 % (by volume) filler (carbonyl iron) were experimentally investigated. The direction of the conglomerates in the MRE coincided with the direction of deformation of the samples and the vector of the controlling magnetic field. Since this coincides with the features of the improved MRA, it can be assumed that their damping properties will be sufficiently close to each other.

Taking this into account, the dependencies of the damping index on the flux density of the controlling magnetic field were compiled for the magnetization curves of MRE that are close to the linear parts, when the filler particles have not yet reached magnetic saturation:

$$D = 0{,}038 + 0{,}075B. \tag{2}$$

Therefore, when the flux density of the controlling magnetic field increases to 0.6 T, the relative damping index increases according to the linear law from 0.038 to 0.083, that is, by 2.2 times. At the same time, the amplitudes of mass fluctuations on samples with MRE decreased by half [18].

Using dependence (2), the relative damping index of the MRA D_V in the form of a torus was calculated with the flux density of the controllimg magnetic field B = 0.85 T, which was achieved in it (Fig. 7, 8):

$$D_V = 0{,}102; \tag{3}$$

$$\Delta D_V = 0{,}102 / 0{,}038 = 2{,}68. \tag{4}$$

Thus, the damping factor increased by 2,68 times compared to the case when the controlling magnetic field is absent. This is 22 % more than what was achieved in previous MRA designs (Fig. 1, 2).

Evaluation of the effectiveness of the improved MRA in the form of a torus was carried out by comparing the relative damping index and the force of non-elastic resistance ((N/(m/s) or kg/s)) of two vehicles. The first of them is equipped with a suspension containing elastic hinges made of rubber, and the second one elastic hinges with MRA in the form of a torus.

The damping properties of rubber are not affected by the magnetic field, therefore its relative damping index D_r, obtained during bench tests, is constant and equal to

$$D_r = 0{,}035. \tag{5}$$

The experimentally obtained force of non-elastic resistance of the HA of the standard suspension of one of the vehicles is equal to:

$$\beta_a = 4000 \text{ kg/s}. \tag{6}$$

To determine the force of the non-elastic resistance of the suspension with MRA, we will use the known dependence for the critical resistance coefficient β_k of the oscillating system [kg/s]:

$$\beta_k = 2\cdot(C\cdot m)^{0,5}, \tag{7}$$

where m is the mass involved in oscillations; C is the suspension stiffness.

With the mass m = 2000 kg of the part of the body, which is on one wheel of the vehicle, and the stiffness of the elastic suspension C = 117800 N/m, the critical force of the non-elastic resistance of the suspension with improved MRA β_{kv} will be

$$\beta_{kv} = 2\cdot(117800\cdot 2000)^{0,5} = 30699 \text{ kg/s}. \tag{8}$$

The force of the non-elastic resistance of a vehicle suspension with M without HA β_v

$$\beta_v = 0{,}102\cdot 30699 = 3099 \text{ kg/s}. \tag{9}$$

The force of the non-elastic resistance of the suspension of a vehicle with HA and elastic hinges of levers with MRA β_{av}

$$\beta_{av} = 4000 + 3099 = 7099 \text{ kg/s}. \tag{10}$$

The force of the non-elastic resistance of the suspension of a vehicle with rubber hinges without HA β_r

$$\beta_r = 0{,}035\cdot 30699 = 1074 \text{ kg/s}. \tag{11}$$

The force of the non-elastic resistance of the suspension of a vehicle with HA and elastic hinges of levers made of rubber β_{ar}

$$\beta_{ar} = 4000 + 1074 = 5074 \text{ kg/s}. \tag{12}$$

The relative damping index of the suspension of the vehicle with HA and elastic hinges of levers made of rubber is

$$D_{ar} = (\beta_a + \beta_r) / \beta_k; \tag{13}$$

$$D_{ar} = (4000 + 1074) / 30699 = 0{,}165. \tag{14}$$

The relative damping index of the suspension of the vehicle with HA and elastic hinges of the levers with improved MRA is

$$D_{ar} = (\beta_a + \beta_v) / \beta_k; \tag{15}$$

$$D_{ar} = (4000 + 3099) / 30699 = 0{,}231. \tag{16}$$

Obviously, thanks to the increase of 7099/5074 = 1.4 times the force of the non-elastic resistance of the suspension when it is equipped with an improved MRA, the damping qualities and smoothness of the vehicle are significantly improved.

To evaluate the effectiveness of the control of damping of the suspension of the vehicle, Fig. 10 shows the dependence of the relative damping index on the flux density of the controlling magnetic field for variants of the MEA designs and the standard suspension of the wheeled vehicle.

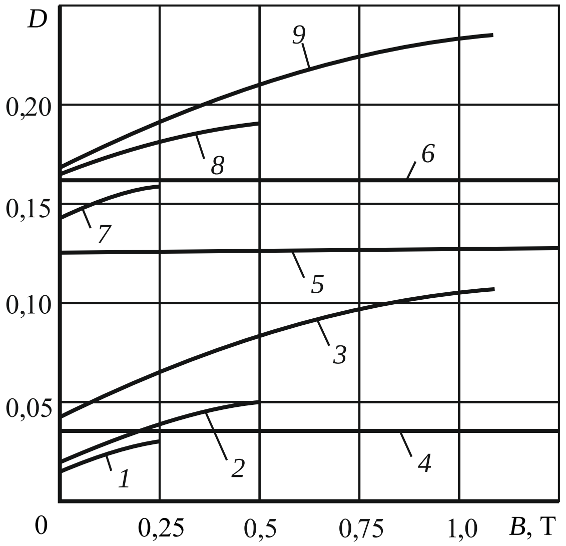

Fig. 10. Dependencies of the relative damping index of the suspension oscillations on the flux density of the controlling magnetic field of the MRA. *Experimental*: *1* – the first and second variants of MRA; *2* – the third variant of the MRA; *3* – improved MRA; *4* – elastic rubber hinges; *5* – HA; *6* – standard suspension with HA and rubber elastic hinges. *Calculated*: suspension with HA and elastic hinges: *7* – according to the first and second variants of the MRA; *8* – according to the third variant of the MRA; *9* – with improved MRA

Graphs in Fig. 10 allow to compare the efficiency of a few vehicles' suspensions. Graph *1* proves that the MRA according to the first and second variants of designs has a relative vibration damping index of no more than 0.03. When installing it to the suspension together with the regular HA (*5*), a relative vibration damping index is no more than 0.16 (*7*) is realized, i.e. at the minimum level of the recommended (0.15 – 0.25) for vehicles. The reasons for this are related to the presence in the MRA of a volume with too little flux density of the controlling magnetic field, «magnetic bridges» on the end parts of the magnetic circuit of the elastic hinge, and the lack of collinearity of the flux density vector of the controlling magnetic field with the directions of the filler conglomerates and deformations of the MRA.

Graph *2* proves that the MRA according to the third variant of the design has a relative vibration damping index of 0.05. When installing it to the suspension together with the standard HA (*5*), a relative vibration damping index of 0.18 (8) is realized, i.e. at the minimum level, The reason for this is the appearance of «magnetic bridges» and the lack of collinearity of the flux density vector of the controlling magnetic field with the directions of deformations and filler conglomerates.

Graph *4* proves that standard rubber elastic hinges reproduce the relative vibration damping index at the level of 0.035. When installing them to the suspension together with the standard HA (*5*), the relative vibration damping index (*6*) is realized at the level of 0.165, that is, almost the minimum recommended. This is confirmed by experimental studies of the movement of vehicles on roads with a heavy profile, in the process of which it was found that there is not enough damping on such roads, and standard HAs overheat [1].

Graph 3 proves that the suspension equipment of the vehicle with an improved variant of the MRA design reproduces the relative vibration damping index at the level of 0.102. When installing the MRA to the suspension together with the standard HA (*5*), a relative vibration damping index of 0.231 (*9*) is realized, which is close to its maximum recommended value (0.25). The reason for this is as follows: collinearity of the flux density vector of the controlling magnetic field with the directions of deformations and conglomerates of the MRA filler is ensured, the controlling magnetic field is concentrated only in the toroid and is regularly distributed throughout its volume, and there are no «magnetic bridges».

An increase in the relative vibration damping index from 0.165 to 0.231 (that is, by 1.4 times) during suspension control should significantly improve the smoothness of the vehicle.

Conclusions.

1. Analysis of the sources revealed that magnetorheological elastomers have certain prospects for use in technical devices. Known designs of magnetorheological actuators (MRAs) of controlled suspensions (CSs) of vehicles have inherent disadvantages: it is impossible to achieve the required value of the flux density of the controlling magnetic field, to direct it along conglomerates of ferromagnetic filler and deformations, and the presence of zones where it is too small, which reduces the efficiency of control of CS.

2. The design of the MRA, which is devoid of the mentioned shortcomings, has been improved and patented, and is made in the form of toroids with control coils made of conductive elastic polymer.

3. It was found that the average value of the flux density of the controlling magnetic field of the improved MRA reaches 0.85 T (that is, the limit where the ferromagnetic filler is just beginning to be magnetically saturated, and the magnetization graph is close to linear, and its relative magnetic permeability is the largest and almost constant), and the zones where the magnetic flux density is too small – absent.

4The dependence of the damping index of MRE samples on the flux density of the controlling magnetic field is built, which allows to predict its damping qualities at the design stage of the CS.

5. The efficiency of suspensions with an improved MRA and with a regular suspension containing elastic hinges made of rubber was compared in terms of the relative damping index. The relative vibration damping index of the vehicle suspension with standard hydraulic shock absorber and elastic lever hinged with improved MRA at the largest control current is 0.231, which is 1.4 times more than that of the standard suspension, which will positively affect the smoothness of the vehicle.

6. The direction of further research is to optimize the parameters of the control coils to ensure their protection against overheating.

Conflict of interest. The authors of the article declare no conflict of interest.

REFERENCES

1. Dushchenko V.V., Masliev A.O. Use of materials intelligent systems at the nodes cushioning prospective military tracked and wheeled vehicles. *Military Technical Collection*, 2016, no. 14, pp. 7-13. (Ukr). doi: https://doi.org/10.33577/2312-4458.14.2016.7-13.

2. Zou Z., Zhang H., Liao C., Wang N., Choi S.-B. Hydrodynamic behaviors of settled magnetorheological fluid redispersion under active dispersing mechanism: simulation and experiment. Smart Materials and *Structures*, 2022, vol. 31, no. 9, art. no. 097001. doi: https://doi.org/10.1088/1361-665X/ac86b0.

3. Deng L., Sun S., Jin S., Li Z., Du H., Zhang S., Li W. Development of a new magnetorheological impact damper with low velocity sensitivity. *Smart Materials and Structures*, 2022, vol. 31, no. 9, art. no. 095042. doi: https://doi.org/10.1088/1361-665X/ac864d.

4. Zhang J., Qiao Y., Zhang M., Zhai P. Magnetorheological behavior of isotropic silicone rubber-based magnetorheological elastomers under coupled static–dynamic compressive loads. *Smart Materials and Structures*, 2022, vol. 31, no. 9, art. no. 095010. doi: https://doi.org/10.1088/1361-665X/ac7d24.

5. Erenchun A., Prieto B., Artetxe G., Gil-Negrete N. Practical design of an electromagnet for the compression characterization of magnetorheological elastomers. *Smart Materials and Structures*, 2022, vol. 31, no. 9, art. no. 095005. doi: https://doi.org/10.1088/1361-665X/ac7bbe.

6. Ahamed R., Choi S.-B., Ferdaus M.M. A state of art on magneto-rheological materials and their potential applications. *Journal of Intelligent Material Systems and Structures*, 2018, vol. 29, no. 10, pp. 2051-2095. doi: https://doi.org/10.1177/1045389X18754350.

7. Bastola A.K., Paudel M., Li L. Magnetic circuit analysis to obtain the magnetic permeability of magnetorheological elastomers. *Journal of Intelligent Material Systems and Structures*, 2018, vol. 29, no. 14, pp. 2946-2953. doi: https://doi.org/10.1177/1045389X18781046.

8. Behrooz M., Wang X., Gordaninejad F. Performance of a new magnetorheological elastomer isolation system. *Smart Materials and Structures*, 2014, vol. 23, no. 4, art. no. 045014. doi: https://doi.org/10.1088/0964-1726/23/4/045014.

9. Dargahi A., Sedaghati R., Rakheja S. On the properties of magnetorheological elastomers in shear mode: Design, fabrication and characterization. *Composites Part B: Engineering*, 2019, vol. 159, pp. 269-283. doi: https://doi.org/10.1016/j.compositesb.2018.09.080.

10. Krautz M., Werner D., Schrödner M., Funk A., Jantz A., Popp J., Eckert J., Waske A. Hysteretic behavior of soft magnetic elastomer composites. *Journal of Magnetism and Magnetic Materials*, 2017, vol. 426, pp. 60-63. doi: https://doi.org/10.1016/j.jmmm.2016.11.048.

11. Agirre-Olabide I., Kuzhir P., Elejabarrieta M.J. Linear magneto-viscoelastic model based on magnetic permeability components for anisotropic magnetorheological elastomers. *Journal of Magnetism and Magnetic Materials*, 2018, vol. 446, pp. 155-161. doi: https://doi.org/10.1016/j.jmmm.2017.09.017.

12. Vasco V.M., Grebenuyk S.M., Reshevskaya E.S. A determination of stress-strain state of elastomeric isolator. *Bulletin of Zaporizhzhia National University. Physical & Mathematical Sciences*, 2015, no. 3, pp. 36-41. (Rus).

13. Wang Q., Dong X., Li L., Ou J. Study on an improved variable stiffness tuned mass damper based on conical magnetorheological elastomer isolators. *Smart Materials and Structures*, 2017, vol. 26, no. 10, art. no. 105028. doi: https://doi.org/10.1088/1361-665X/aa81e8.

14. Erenchun A., Prieto B., Artetxe G., Gil-Negrete N. Practical design of an electromagnet for the compression characterization of magnetorheological elastomers. *Smart Materials and Structures*, 2022, vol. 31, no. 9, art. no. 095005. doi: https://doi.org/10.1088/1361-665X/ac7bbe.

15. Kawasetsu T., Horii T., Ishihara H., Asada M. Flexible Tri-Axis Tactile Sensor Using Spiral Inductor and Magnetorheological Elastomer. *IEEE Sensors Journal*, 2018, vol. 18, no. 14, pp. 5834-5841. doi: https://doi.org/10.1109/JSEN.2018.2844194.

16. Qi S., Guo H., Chen J., Fu J., Hu C., Yu M., Wang Z.L. Magnetorheological elastomers enabled high-sensitive self-powered tribo-sensor for magnetic field detection. *Nanoscale*, 2018, vol. 10, no. 10, pp. 4745-4752. doi: https://doi.org/10.1039/C7NR09129J.

17. Sun S., Yang J., Yildirim T., Du H., Alici G., Zhang S., Li W. Development of a nonlinear adaptive absorber based on magnetorheological elastomer. *Journal of Intelligent Material Systems and Structures*, 2018, vol. 29, no. 2, pp. 194-204. doi: https://doi.org/10.1177/1045389X17733053.

18. Dushchenko V.V., Masliev V.G., Nanivskyi R.A., Masliev A.O. Application of magnetorheological elastomers for performance control of cushioning systems for wheeled vehicles. *Electrical Engineering & Electromechanics*, 2019, no. 5, pp. 50-59. doi: https://doi.org/10.20998/2074-272X.2019.5.09.

19. Dushchenko V., Masliiev A. *Suspension with adjustable stiffness and damping*. Patent UA, no. 110476. 2016. (Ukr).

20. Dushchenko V., Masliiev A., Masliiev V. *Adjustable vehicle suspension*. Patent UA, no. 149223. 2021. (Ukr).

Received 22.09.2023
Accepted 17.03.2024
Published 20.08.2024

V.V. Dushchenko[1]*, Doctor of Technical Science, Professor,*
B.G. Liubarskyi[1]*, Doctor of Technical Science, Professor,*
A.O. Masliev[2]*, PhD,*
R.A. Nanivskyi[3]*, PhD, Assistant Professor,*
V.G. Masliev[1]*, Doctor of Technical Science, Professor,*
O.M. Ahapov[1]*, PhD, Assistant Professor,*
D.I. Iakunin[1]*, PhD, Assistant Professor,*
[1] National Technical University «Kharkiv Polytechnic Institute»,
2, Kyrpychova Str., Kharkiv, 61002, Ukraine,
e-mail: viacheslav.masliiev@khpi.edu.ua (Corresponding Author)
[2] Armed Forces of Ukraine.
[3] Hetman Petro Sahaidachnyi National Army Academy,
32, Heroes of Maidan Str., Lviv, 79026, Ukraine.

How to cite this article:
Dushchenko V.V., Liubarskyi B.G., Masliev A.O., Nanivskyi R.A., Masliev V.G., Ahapov O.M., Iakunin D.I. Increasing the damping properties of the magnetorheological actuator of the vehicle suspension control system. *Electrical Engineering & Electromechanics*, 2024, no. 5, pp. 77-86. doi: https://doi.org/10.20998/2074-272X.2024.5.11

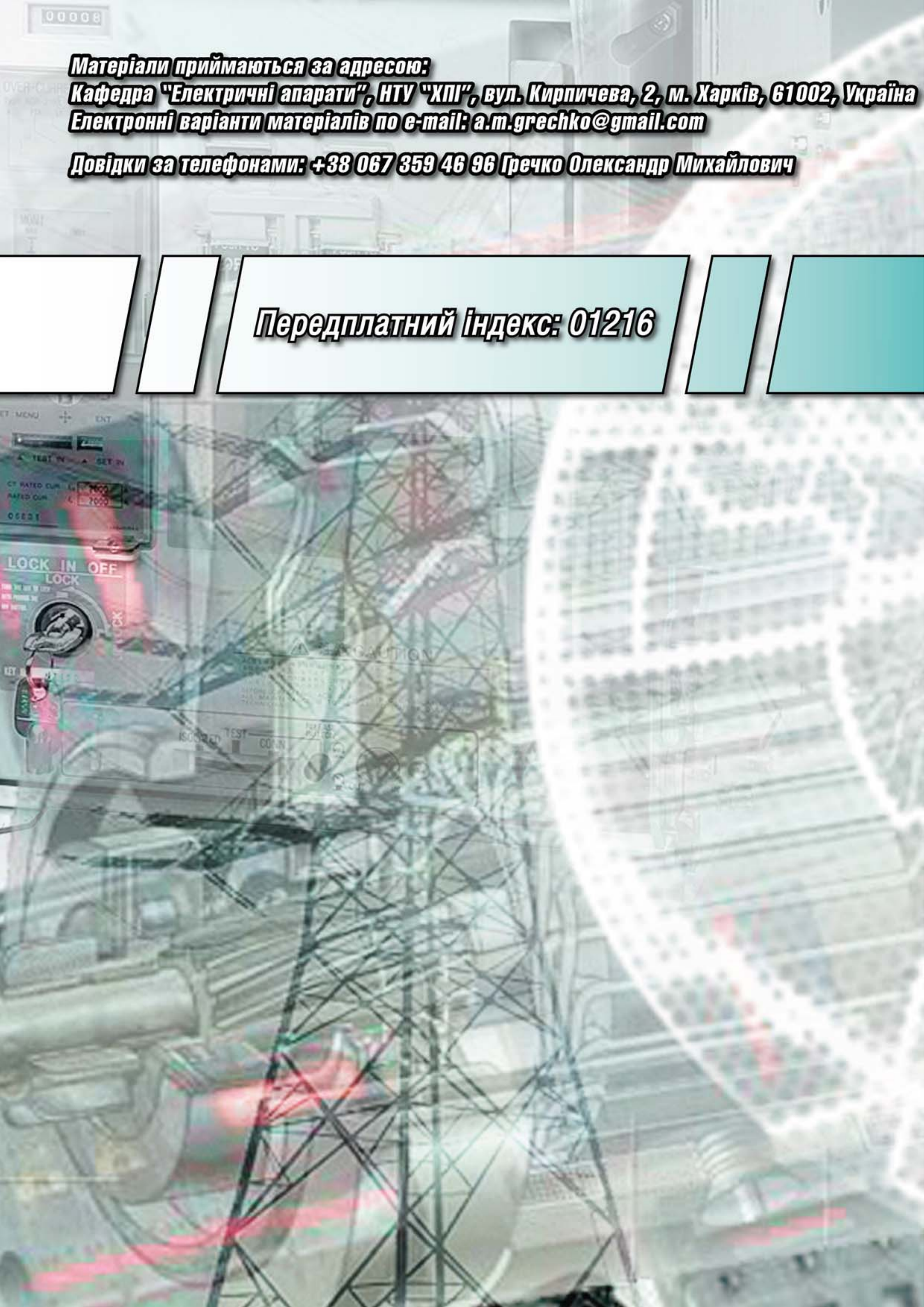

Матеріали приймаються за адресою:
Кафедра "Електричні апарати", НТУ "ХПІ", вул. Кирпичева, 2, м. Харків, 61002, Україна
Електронні варіанти матеріалів по e-mail: a.m.grechko@gmail.com

Довідки за телефонами: +38 067 359 46 96 Гречко Олександр Михайлович

Передплатний індекс: 01216